論文 / 著書情報
Article / Book Information

題目(和文)	室温イオン液体膜内に原子金装飾ポリアニリン/プラチナ複合材 料を使用した小型電流測定ガスセンサー
Title(English)	Miniaturized amperometric gas sensor with atomic gold decorated polyaniline/platinum composites in room temperature ionic liquid film
著者(和文)	AnifatulFaricha
Author(English)	Faricha Anifatul
出典(和文)	学位:博士(学術), 学位授与機関:東京工業大学, 報告番号:甲第12590号, 授与年月日:2023年9月22日, 学位の種別:課程博士, 審査員:中本 高道,小池 康晴,小尾 高史,長谷川 晶一,曽根 正人
Citation(English)	Degree:Doctor (Academic), Conferring organization: Tokyo Institute of Technology, Report number:甲第12590号, Conferred date:2023/9/22, Degree Type:Course doctor, Examiner:,,,,
学位種別(和文)	博士論文
Type(English)	Doctoral Thesis

Miniaturized amperometric gas sensor with atomic gold decorated polyaniline/platinum composites in room temperature ionic liquid film

by

Anifatul Faricha

A thesis submitted to

The Department of Information and Communications Engineering

In partial fulfillment of requirements

for the degree of

Doctor of Philosophy

In the subject of Engineering

Tokyo Institute of Technology

August 2023

Doctoral Committee

Advisor:

Takamichi Nakamoto, Dr. Eng.

Professor, Department of Information and Communication Engineering

Members:

Masato Sone, Dr. Eng.

Professor, Department of Materials Science and Engineering

Yasuharu Koike, Dr. Eng.

Professor, Department of Information and Communication Engineering

Takashi Obi, Dr. Eng.

Associate Professor, Department of Information and Communication Engineering

Shoichi Hasegawa, Dr. Eng.

Associate Professor, Department of Information and Communication Engineering

To my mom & my dad, my brothers, and Mas Zendhi:

thanks for everything

Abstract

The miniaturized amperometric gas sensor (AGS) offers many benefits compared to bulky AGS systems in terms of power consumption, response time, simplicity of chip implementation, etc. However, a tiny sensor suffers from a low signal response. Therefore, the sensor system is required to be redesigned and improved. In this study, the planar electrode and a room-temperature ionic liquid (RTIL) film were used to realize the miniaturized AGS. In addition, to improve the sensitivity, the atomic gold clusters, i.e., Au_2, were decorated at the working electrode made of platinum/polyaniline (Pt/PANI) composites. The butanol isomers were used as the analytes, which have the same chemical formula and molar mass. Based on the results, miniaturized AGS with atomic gold had a higher sensor response than miniaturized AGS without atomic gold. In addition, the AGS array with different potentials at the working electrode achieved high discrimination capability after selecting RTIL films and working potentials based on the pattern separation index.

Acknowledgment

Firstly, I would like to thank my God, Allah SWT, for drawing my beautiful journey, especially this PhD phase. The completion of my PhD supported by many people from different walks of life. I would like to express my deepest gratitude to Prof. Takamichi Nakamoto to accept me as a student in his Laboratory and teaching me patiently. There have been many lessons that I have learned here. This is a precious phase in my life.

Prof. Masato Sone is our collaborator who expert in the material side. I would like to gratitude for all his support, comments, questions, and suggestions during conducting this research. I also would like to thank Assoc. Prof. Tso-Fu Mark Chang from Sone Laboratory for all his critical points during the progress meeting, especially, for clearly pointing out related unstable curves due to the drift issue at the very beginning of applying the RTIL with fixed EC potential which was very beneficial for this research.

Words cannot express my gratitude to Asst. Prof. Parthojit Chakraborty. He has been helping me a lot. He did the training for me at the very beginning, introducing me to the experimental setup and the atomic gold deposition process, and also teaching me to order the chemicals and devices for this research work.

I also would like to thank Prof. Jiri Janata and Dr. Mira Josowicz from Georgia Tech for their guidance and helpful advice for our research.

This research would not have been possible without Yoshida-kun, Okamoto-kun, and Kawakami-kun from Sone Laboratory, who helped to fabricate the polyaniline and recorded the SEM image.

Finally, I am so thankful to Assist. Prof. Dani, Dr. Manuel, Dr. Deng, Dr. Iseki, Kondo-san, Iijima-san, for all their help. In addition, thanks to all members and formers of Nakamoto Lab., and my dormitory roommates (Bora, Jasmine, Nabilah, and Intan), for the cheerful days. Lastly, I would like to thank IT-Telkom Surabaya, especially all lecturers in Electrical Engineering Department.

Tokyo, August 2023

Anifatul Faricha

Contents

Chapter 1

Introduction

1.1 Overview of the gas sensor market

Gas sensor plays an ever-increasing role, it is a device commonly used to detect, monitor, and quantify the presence of the gaseous target compounds like hazardous gases, explosive gases, vapors, toxic gases, volatile organic compounds (VOCs), etc. Gas sensor technologies are broadly applied in many fields, such as the semiconductor industry, heating-ventilation-air-conditioning (HVAC) systems, automotive and transportation, smart cities, medical industry, smart agriculture, security, environmental monitoring, oil and gas industry, etc. The global demand for gas sensors has shown positive growth over the decades. As shown in Figure 1.1, the market size of gas sensors was valued at $ 3.16 billion in 2022 and is predicted to surpass around $ 6.2 billion by 2030. In addition, the compound annual growth rate (CAGR) is projected to grow at 8.81% over the forecast period from 2023 to 2030. The major factors driving the gas sensor demand in markets are the development of miniaturized gas sensors coupled with the improvement of wireless capability, networking, and communication technology, like internet of things (IoT), cloud computing, big data, etc [1–4].

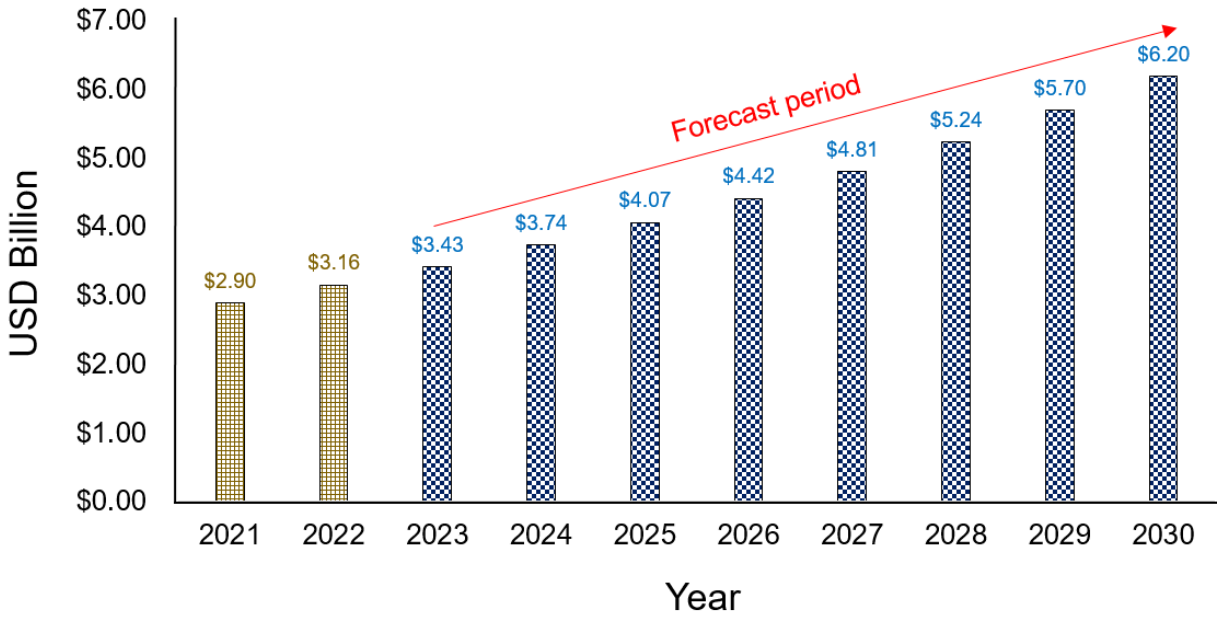

Figure 1.1: Global gas sensor market size from 2021 to 2030 [2]

Figure 1.2 depicts the detailed global gas sensor market report segmentation over the forecast period from 2023 to 2030. The segments covered in the report included connectivity, technology, product (gas type), key market players, and region scopes, i.e., North America, Europe, Asia-Pacific, Latin America, Middle East, and Africa. In 2022, based on the connectivity, the wired gas sensor was favored due to low maintenance cost, and it

dominated the market with a share of 56.5% in the global revenue. On the other hand, although, the loss of internet connection and signal has been the main challenge in wireless gas sensors. However, in modern technology, the wireless gas sensor is expected to drive gas sensors market growth because it offers many benefits such as high flexibility, high portability, and allowing to monitor gas remotely, particularly for hazardous and toxic gases. Furthermore, from the technology perspective, the electrochemical sensor dominated the market with the largest global revenue share around 23.0% in 2022. Less power consumption and high selectivity to particular gaseous targets become the main reasons for the high demand for electrochemical gas sensor type [1–4]. Besides electrochemical gas sensors, other sensor types applied for gas measurement are semiconductor, photo-ionization, infrared, etc, which will be explained in more detail in section 1.2.

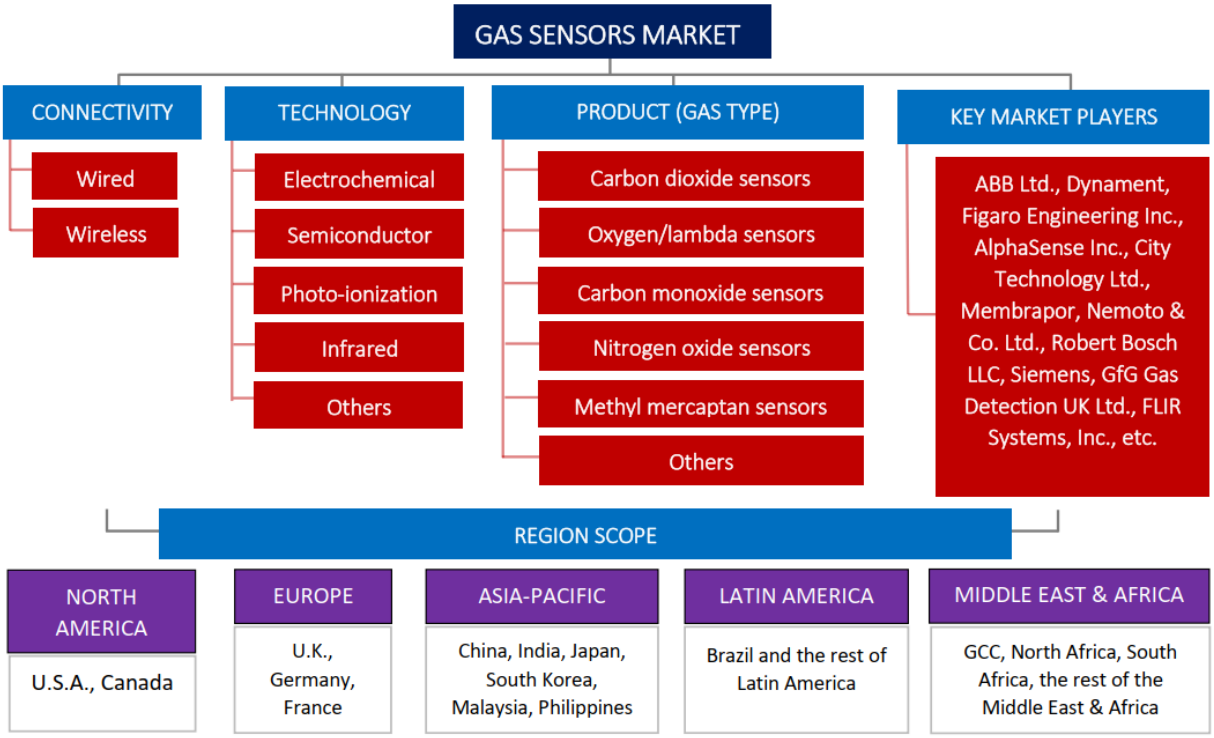

Figure 1.2: Report of the gas sensors market scope over the forecast period from 2023 to 2030 [1–4]

By product, the carbon dioxide (CO_2) sensor was dominant in the market in 2022 and accounted for a market share of around 33%. The CO_2 sensor is generally used to monitor air quality, healthcare, automotive, buildings, etc. In addition, in 2021, TDK company introduced the miniaturized ultra-low power micro-electromechanical system (MEMS) based CO_2 sensor, which was also driving the growth of this segment [5]. Besides CO_2 sensors, the demand for oxygen (O_2) sensors is also high. It is broadly used in HVAC systems, environment monitoring, and other applications. Numerous industries such as chemical, power, fuels, oil, and gas have applied gas sensors to detect various hazardous, combustible, and toxic gases such as carbon monoxide (CO), nitrogen oxide (NOx), hydrocarbons, ammonia (NH_3), methyl mercaptan, and other flammable compounds. The global players of gas sensors are available in Figure 1.2. Furthermore, by region, Asia-Pacific (APAC) dominated the gas sensor market with a global market share of 34.9% in 2022 and will remain to lead the market during the forecast period from 2023 to 2030 [1,2].

1.2 Gas sensor types

1.2.1 Electrochemical sensor

The electrochemical (EC) sensor is one of the oldest branches of chemical sensors and is broadly used in a wide range of applications. This type of sensor uses the electrode as the transducer element and converts the signal information based on the electrochemical reaction between the analyte and the electrode. As shown in Figure 1.3, the EC sensor system can be built using two-electrode or three-electrode configurations. Three kinds of electrodes are required to construct the three-electrode configuration in the EC sensor, i.e., working electrode (WE), counter electrode (CE), and reference electrode (RE). While, in a two-electrode system, only two electrodes are necessary, i.e., WE and an auxiliary electrode (here, the auxiliary electrode can function as both the CE and RE) [6]. Since the two-electrode system uses an auxiliary electrode, hence, its pseudo-reference cannot form a stable reaction and is required to be calibrated to another electrode with known potential; it is called pseudo-reference because its potential varies predictably with conditions (it does not maintain a constant potential). In EC sensors, the three-electrode configuration is generally used instead of the two-electrode configuration because it uses the classical reference electrode forming a well-defined thermo-dynamic reaction to maintain a stable reaction and thus does not require calibrating to another electrode [6].

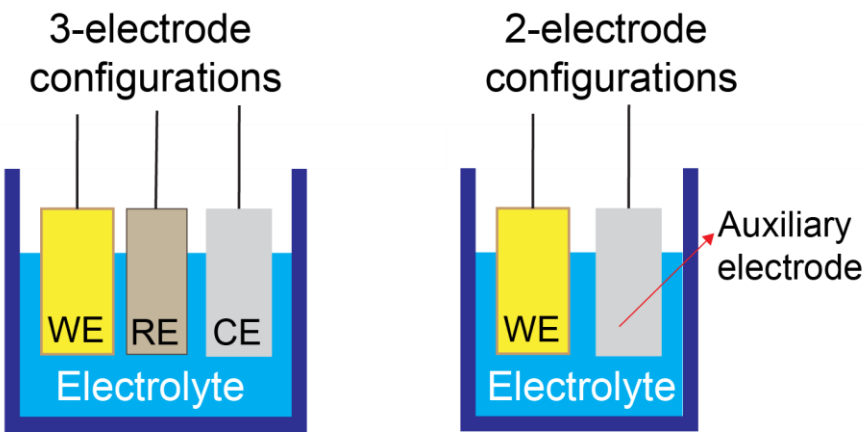

Figure 1.3: The basic electrode configurations in the EC sensor system

Fundamentally, all the electrodes in the EC sensor system are immersed in the electrolyte, which is a conductive medium. Common electrolytes used in EC sensors are aqueous electrolytes, such as sodium hydroxide, sulfuric acid, potassium chloride; nonaqueous electrolytes, such as propylene carbonate with lithium perchlorate, tetrahydrofuran, diethyl carbonate; and solid electrolytes, such as polymer Nafion, NASICON, YSZ, β-alumina, etc. Generally, WE is made from a noble metal that is typically resistant to corrosion, such as platinum or gold. In addition, since many forms of carbon are biocompatible, graphite and glassy carbon are also popular materials for WE. Afterward, CE is needed to complete the circuit and must also be stable during the electrochemical reaction; the platinum electrode is also commonly used for CE in EC sensors. In addition, RE is required to form the stable potential with the electrolyte. The RE should be generally not sensitive to temperature, relative humidity, and other reactants or contaminants; an Ag/AgCl is very often used as RE in the EC sensors, particularly in three-electrode configuration [6].

Generally, EC sensors can be categorized into three classes based on the operating principle or generated signal type, as follows:

1. Amperometric (measure current),
2. Potentiometric (measure voltage),
3. Conductometric (measure conductivity).

The amperometric sensor follows Faraday's law, i.e., the generated current is proportional to the amount of analyte's concentration taking part in the electrochemical reaction by applying either fixed or variable electrode potential. Generally, the relationship between the generated current and the concentration of the analyte is linear [6]. AGS is widely used for monitoring oxygen, CO, hydrogen, etc. The detailed information of AGS will be explained in section 1.3.

Another EC gas sensor is potentiometric. In the potentiometric sensor, the measurements are operated under zero current conditions, the potential is monitored from the open circuit between the two electrodes [6]. The potentiometric sensor follows the Nernst equation, i.e., the monitored potential is typically proportional to the logarithm of the analyte's concentration, the equilibrium state of chemical reactions and diffusion process must be achieved to obtain an accurate signal which is sometimes time-consuming [6]. Ion-selective electrode (ISE) is the popular example of potentiometric sensor, shown in Figure 1.4. ISE uses the ion-selective membrane (ISM) to filter particular ion activities, the potential difference at the equilibrium state governed by ion activity can be described in Nernstian manner against ion concentration [7,8]. In the gas sensing measurement, the ion-sensitive field-effect transistor (ISFET) also follows the basic potentiometric working principle, i.e., ISM coated onto the gate surface to replace the common metallic gate in FET will control the current flow between the source and the drain through ISE potential. The presence of analyte changes the ISE potential due to the electrochemical reaction at ISM. Although, ISFETs offer cost-effective, low energy consumption, and small sensor size can be realized. However, long-term drift, hysteresis, and thermal drift limit the accuracy of ISFETs [9]. In addition, fabricating the ISM for a specific ion requires high cost of experiments, moreover, in most cases, unwanted ions are still able to pass through the membrane, hence, poisoning the electrode and reducing the accuracy [7–9].

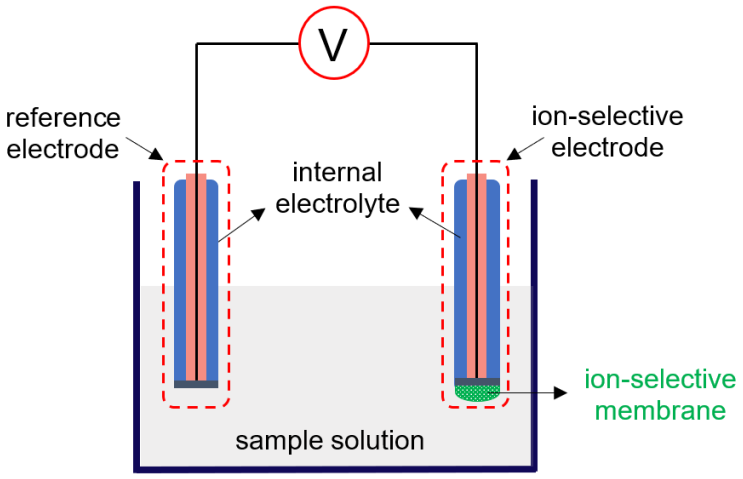

Figure 1.4: Schematic for ion selective electrode (ISE) using potentiometric with 2-electrode configuration

Furthermore, the last EC sensor is conductometric sensor type. Principally, conductometry measures the conductance or conductivity as sensor information, the amount of analyte concentration is determined by the change of conductivity between the pair of electrodes [10]. Compared to the amperometric and potentiometric sensors, the conductometric sensor is very low-cost in their fabrication and has a simple design that consists of two basic elements, i.e., a conducting layer (or solution) and two electrodes. Figure 1.5 depicts the example of using the conductometric sensor for liquid and gas phase measurements. As shown in Figure 1.5.a, in liquid phase measurement, a voltage is applied between two electrodes, then the conductivity generated by a liquid sample is measured. Furthermore, in a gas phase measurement shown in Figure 1.5.b, the electrical conductivity of the sensing layer is changed upon the analytes' exposure under the effect of reactions like diffusion, adsorption, chemical reactions, catalysis, etc. Conductometric gas based on metal oxides (MOs) are also widely used for monitoring environmental gases including CO_2, O_2, H_2, etc [10].

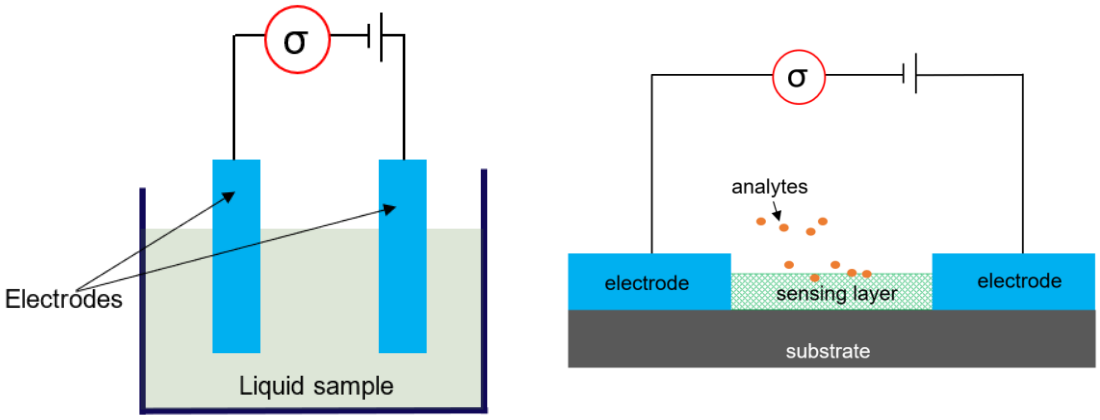

(a) (b)

Figure 1.5: Schematic for conductometric sensor measurement in: (a) liquid phase; and (b) gas phase

Although the conductometric sensor has a simple operating principle theoretically and is inexpensive, its conductance signal interpretation is very difficult [10]. For example, when applying DC voltage, in most cases, instead of measuring the conductance, the resistance is reported as sensor signal since the conductance (G) is the reciprocal of resistance (R), here conductometric is also well-known as chemresistive or chemiresistors [10–12]. Furthermore, when the AC signal is applied, the impedance (Z) is preferred to be reported as the sensor signal than the conductance (G) itself, then, oftentimes the conductometric sensor is called impedimetric sensor although the resistance is just a real part of the impedance [13,14]. In addition, the fundamental equivalency between current and conductance under constant voltage is inherent according to generalized Ohm's law (in Equation 1.1) which oftentimes blurs the line between amperometry and conductometry. Another drawback of the conductometric sensor is ions with similar conductivity would generate the same sensor response.

$$G(\omega) = \frac{I(\omega)}{V(\omega)} \tag{1.1}$$

1.2.2 Quartz crystal microbalance sensor

Quartz crystal microbalance (QCM) is one of the piezoelectric sensors. It is a gravimetric sensor that can detect mass change even at the nanogram level. Typically, the physical structure of the QCM sensor is shown in Figures 1.6.a and 1.6.b, it consists of a quartz plate with electrodes on both sides. Basically, the characteristics of QCM depend on quartz crystal cuts and vibration mode. Among types of quartz crystal cuts, the AT-cut quartz crystal is the most widely used. It has good stability when operating at room temperature and it undergoes a thickness-shear mode of vibration, i.e., the quartz's displacement is perpendicular to the quartz's thickness when voltage is fed up to the device, as illustrated in Figure 1.6.c. The thickness and cuts of quartz crystal determine the natural frequency of QCM. In addition, the electrode material type contributes to the energy trapping to obtain a high Q-factor thus making QCM sensor vibrates very stable [15].

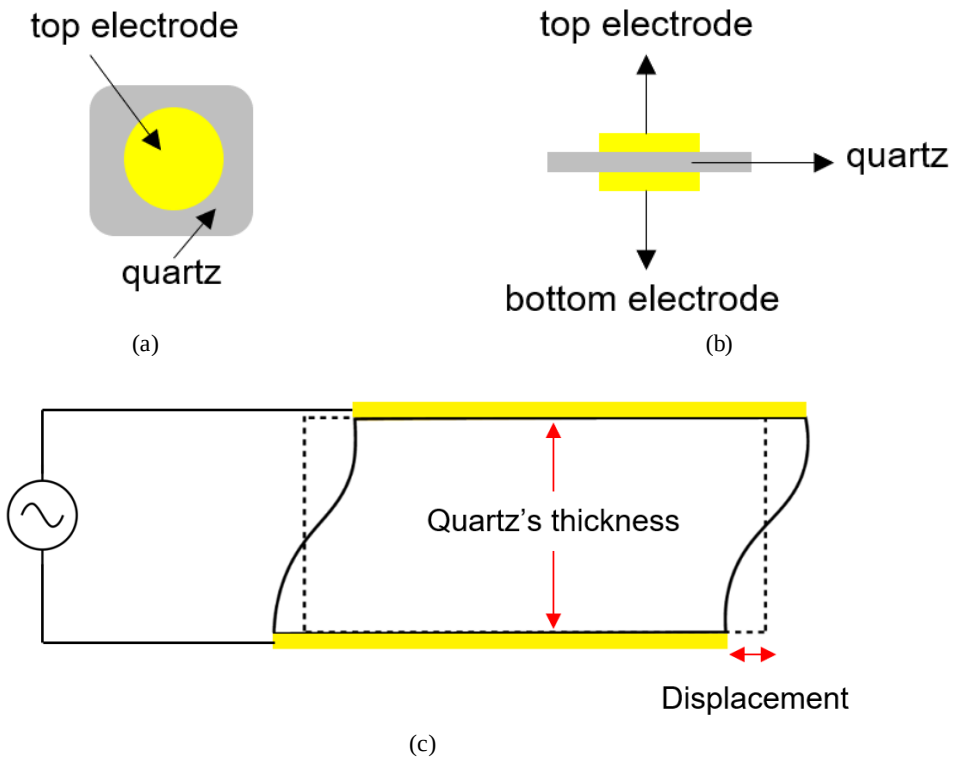

Figure 1.6: Schematic physical layout for QCM sensor: (a) top view; (b) side view; (c) illustration of thickness-shear mode of vibration

The heart of the QCM sensor is a quartz crystal which has an interesting property to oscillate at a defined frequency (called resonance frequency) when an appropriate voltage is applied to those two metal electrodes as shown in Figure 1.7.a. The oscillation frequency can be decreased from the original resonant frequency by the addition of a thin sensing film deposited on the electrode surface. Different sensing material causes different frequency shift as described in Figure 1.7.b; in this case, QCM sensors are very useful for sensing applications such as biosensing, gas sensing, etc. Figure 1.7.c illustrates the gas sensing using QCM coated with a thin sensing film, gas adsorption taking place at sensing film causes mass loading onto the QCM then affects the frequency change of the QCM, as determined by Sauerbrey formula in Equation 1.2.

$$\Delta f = \frac{-2f_0^2 m_f}{A\sqrt{\rho_q \mu_q}} \tag{1.2}$$

where Δf is the frequency change (Hz), f_0 is the resonant frequency (Hz), m_f is the mass change due to adsorption of the gaseous analyte (g), A is the area of active crystal (cm^2), ρ_q is the quartz material density (2.648 g/cm^3), μ_q is the shear modulus of quartz for AT-cut crystal (2.497×10^{11} $g\ cm^{-1}\ s^{-2}$).

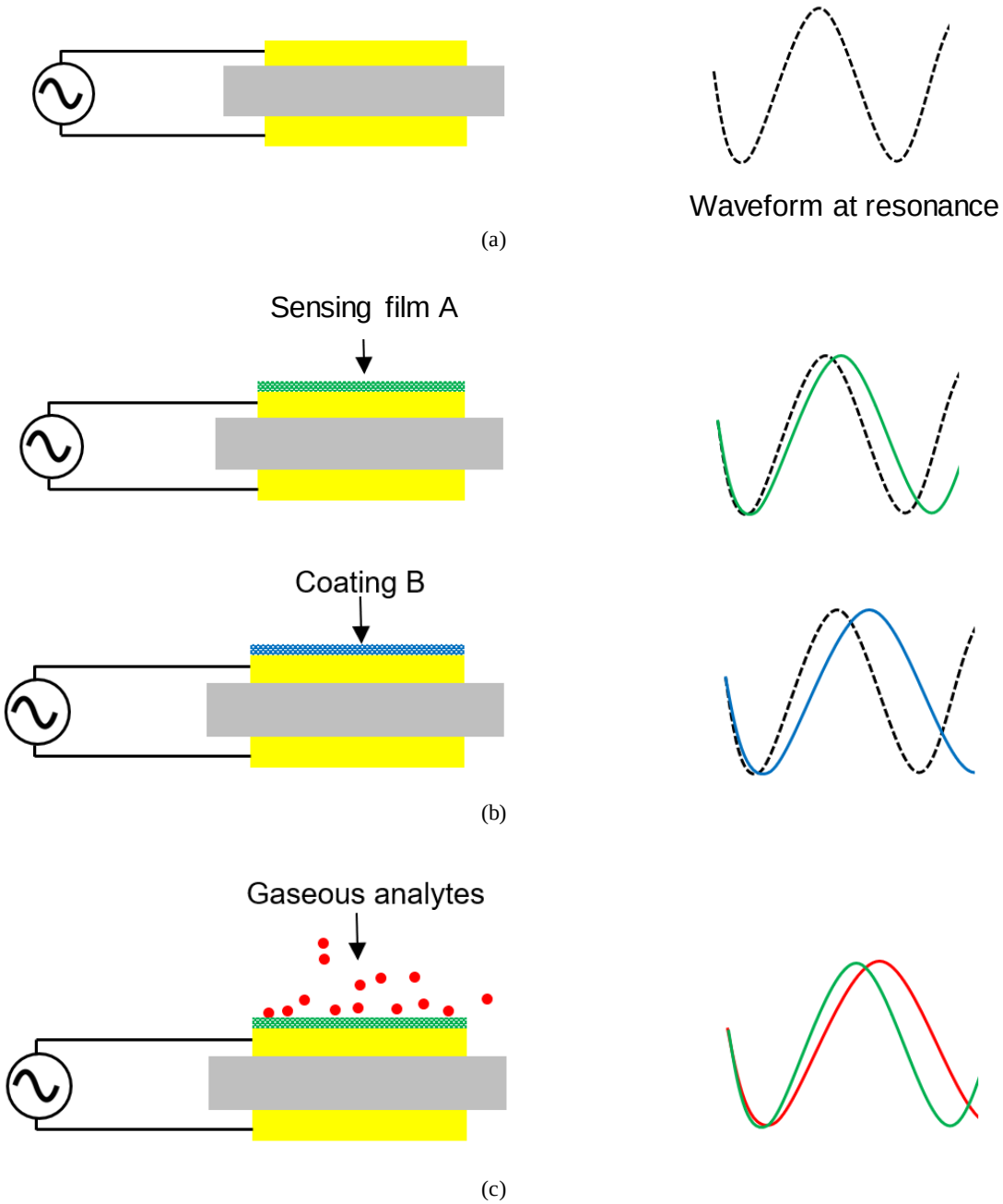

Figure 1.7: Different oscillation frequencies: (a) QCM without sensing layer (the original resonant frequency); (b) different sensing films coated on QCM's electrode resulting in different frequency shift; (c) QCM coated with a thin film applied for a gas sensing measurement

QCM sensors can be found in a wide range of applications due to their high sensitivity and stability. It can also be used together with another sensor type to complement the measurement information, for example, the electrochemical quartz crystal microbalance (EQCM) which combines a QCM sensor and electrochemical cell, as depicted in Figure 1.8. In EQCM, one side of the electrode at QCM which is in contact with the electrolyte is used as the working electrode and as the oscillator circuit [15]. The amount of deposited polymer on the working electrode for the electrochemical cell is easily determined using QCM when calculated through the oscillator circuit. In addition, the dynamic electrochemical reactions during measurement which take place at the working electrode are also able to be monitored precisely since QCM is very mass-sensitive. In Figure 1.8, Hartley Oscillator is used here although the standard oscillator that measures only one parameter of frequency shift cannot be applied due to the interference with potentiosat. In addition, only using frequency shift information is impossible to distinguish between liquid loading and mass loading during EQCM measurement [16]. Therefore, the impedance spectrum information is also measured to separate the mass loading from liquid loading; at each frequency, the impedance is calculated by measuring the current generated from applied potential [16]. If the liquid property is unchanged and mass loading occurs, mass change is obtained from frequency change.

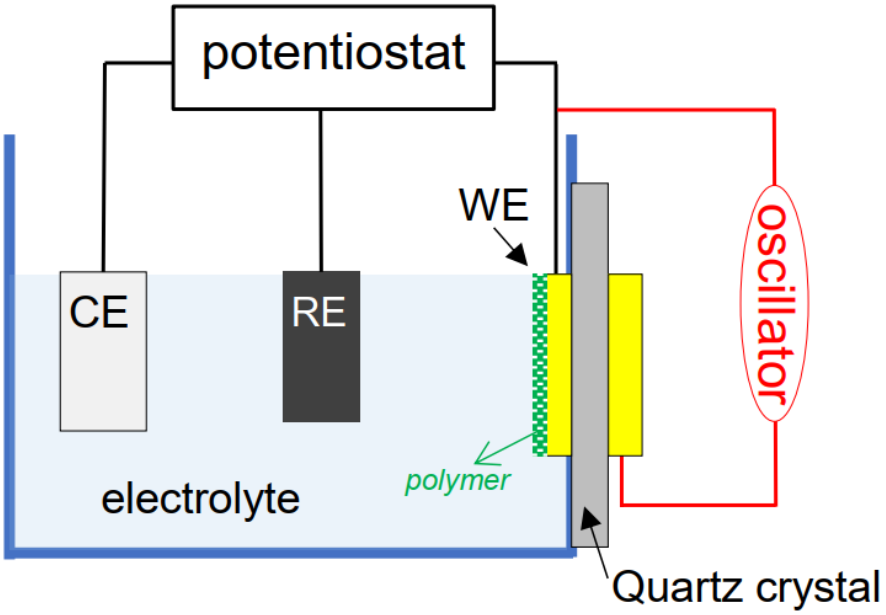

Figure 1.8: Schematic of electrochemical quartz crystal microbalance (EQCM)

Figure 1.9 shows the sensor response from QCMs coated with two sensing films (in black [C4mim][dca] and in red [C4mim][otf]) against four gaseous volatile compounds (VOCs), i.e., hexanol, butyl acetate, 2-hexanone, hexanoic acid; Figure 1.9.a depicts the frequency shift response and Figure 1.9.b shows the resistance response [17]. Although, the response was not too stable, particularly for hexanoic acid which had a long-lasting effect on the coated QCMs [17], however, as shown in Figure 1.9.a and b, the real-time response can be achieved by this sensor type, in addition, each sensing film had certain response against the VOCs. QCM offers many benefits but it is inherently sensitive to humidity which could interfere with its accuracy [18].

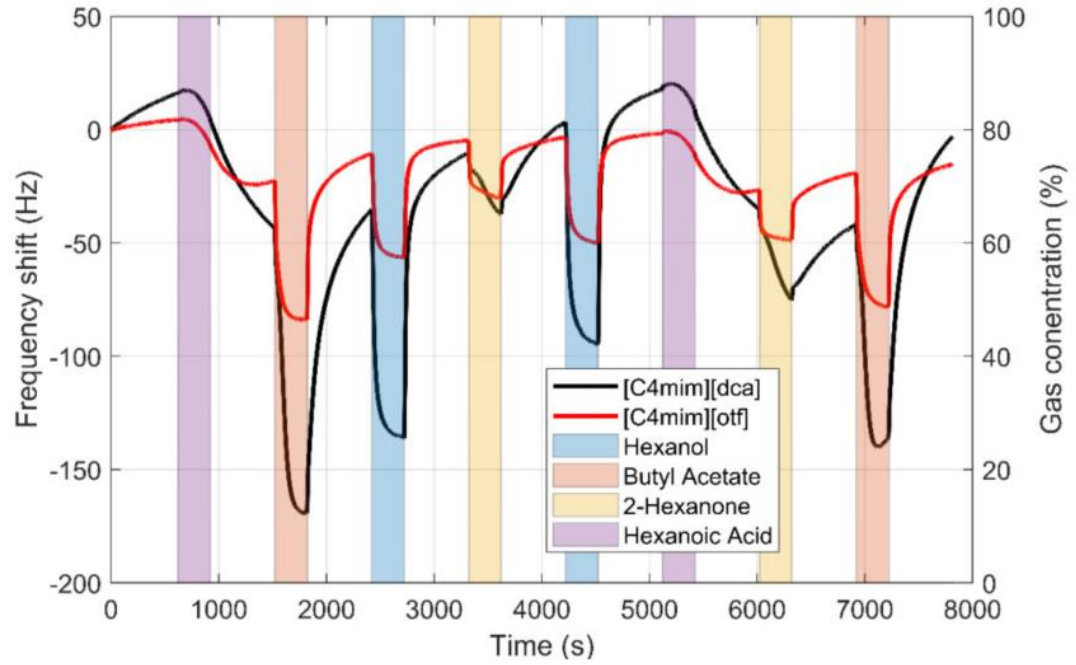

(a)

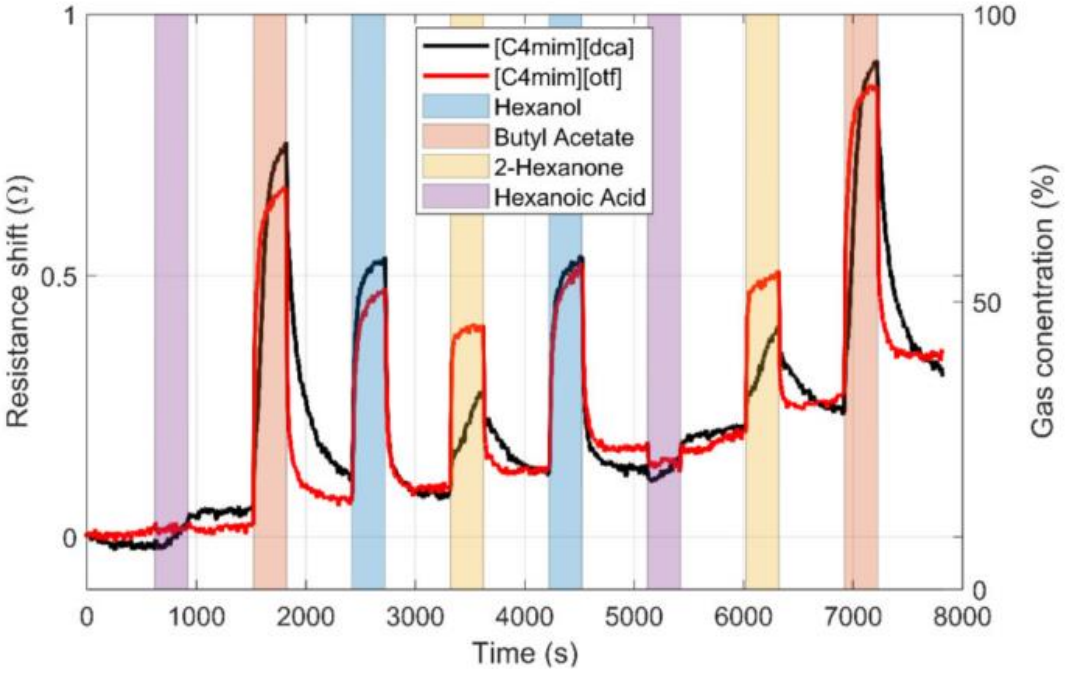

(b)

Figure 1.9: The sensor responses from QCMs coated with [C4mim][dca] and [C4mim][otf] against four VOCs: (a) the frequency shift response; (b) the resistance shift response. Reproduced from [17]

1.2.3 Biosensors

The success of the amperometric glucose enzyme electrode invented by Leland C. Clark Jr., in 1962 inspires many researchers to use the biological element as part of the sensor component, which is well-known as a biosensor [19,20]. Typically, a biosensor consists of two main parts, i.e., bioreceptor and transducer.

The bioreceptor is a biologically derived material which responsible for specifically recognizing the analyte, while the transducer has the role to convert the biorecognition obtained from a bioreceptor to a measurable signal. The bioreceptor can be made from enzymes, deoxyribonucleic acid (DNA), cells, tissue, antibodies, proteins, etc. On the other hand, many transducer types can be used for biosensors such as electrochemical, gravimetric, optical, electrochemiluminescence, etc. Figure 1.10 illustrates the schematic representation of the biosensor [21].

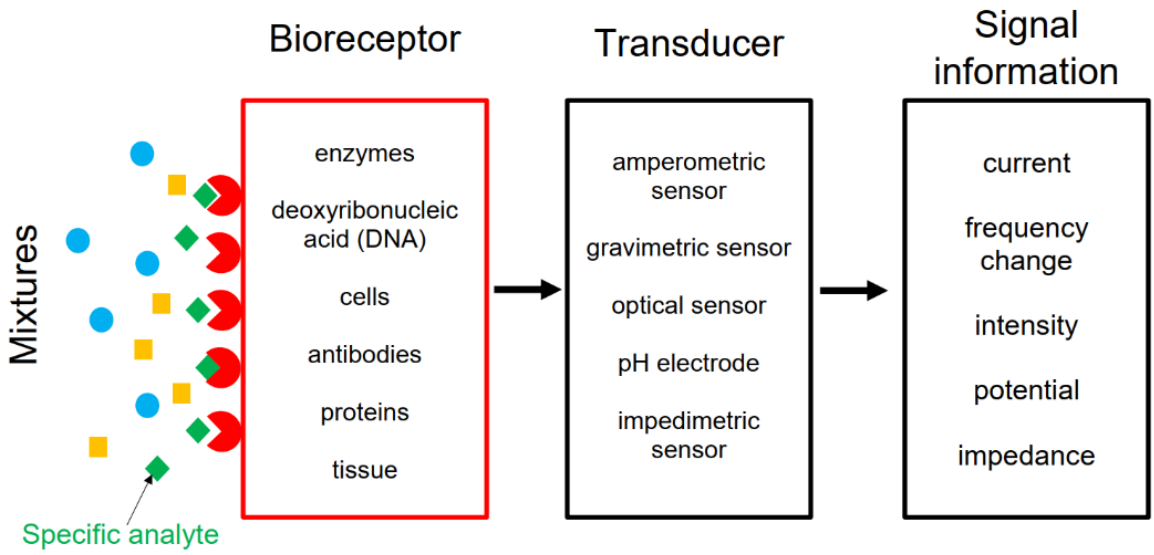

Figure 1.10: Schematic of biosensors

Generally, biosensor has high selectivity; the key is from the bioreceptor selection. The ability of a bioreceptor to recognize a specific analyte in the mixtures becomes the main concern when choosing a bioreceptor, as illustrated in Figure 1.10. Biosensor has a high selectivity because it interacts with certain analyte oriented to its bioreceptor. One of examples is the interaction of an antibody and an antigen. Basically, the antibody acts as a bioreceptor coated on the transducer's surface. Even if a solution contains mixtures of antigen and interferants, the antibody only interacts with the certain antigen [21]. Furthermore, in gas sensing, odorant-binding proteins (OBPs) have been applied for bioreceptor since OBPs reversibly bind odorant molecules [22].

Figure 1.11 shows the selectivity of biosensor using olfactory receptor-derived peptide (ORP), i.e., ORP3 [23]. ORP contains odorant binding sites. It is short peptide fragments derived from odorant receptor (OR); OR is membrane proteins in olfactory for the sense of smell. In Figure 1.11, several gaseous volatile compounds were investigated with 100 ppb concentration, based on the result depicted in Figure 1.11, ORP3 has the highest selectivity against gaseous pheromone 4-vinylanisole (4 VA) among other analytes. Although biosensor offers high selectivity, the primary challenges working with biosensors are also reported, i.e., bioreceptors has short lifetime thus affecting the durability of biosensor, in addition, mostly, bioreceptors are not able to survive at high temperature and have low levels of stability [21].

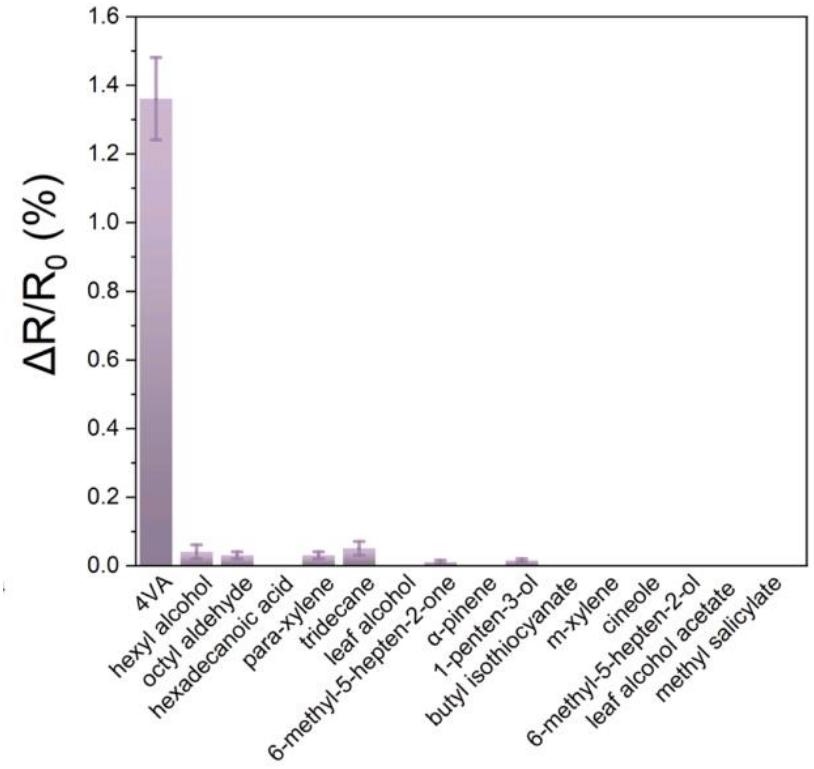

Figure 1.11: Selectivity of the ORP3-sensor to several gases with a concentration of 100 ppb. Reprinted from [23]. Copyright (2023), with permission from Elsevier

1.2.4 Semiconductor gas sensor

One of the most popular gas sensor types is the semiconductor sensor which generally offers a low-cost, long lifetime, and short response time. In semiconductor gas sensors, a semiconducting oxide well-known as metal oxide (MO) becomes the main role because it is used as a sensing material. Different metal oxide materials have been explored to obtain proper sensing material for particular gas sensing measurements. Generally, there are two types of metal oxide semiconductor (MOS), i.e., n-type MOS where electrons are majority charge carriers, such as tin oxide (SnO_2), tungsten oxide (WO_3), zinc oxide (ZnO), titanium oxide (TiO_2), ferric oxide (α-Fe_2O_3); and p-type MOS where holes are majority charge carriers, such as copper oxide (CuO), nickel oxide (NiO), and chromium (III) oxide (Cr_2O_3), etc [24–26].

Principally, in the MOS sensor, the change of the resistance caused by gas exposure on to sensing material is measured as a sensor signal. The surface state of sensing material made from n-type or p-type serves for electron donors or acceptors. For reducing gases (such as H_2, CO, NH_3, CH_4, NO, and so on), the electrons are transferred from reducing gases to the n-type MOS, resulting to a decrease in electron depletion layer then lowering the resistance (or conductivity is increased); the opposite effect for p-type MOS. Furthermore, when exposed to oxidizing gases like NO_2, O_2, CO_2, etc, the resistance is increased for n-type MOS and is decreased for p-type MOS. A microheater is also commonly embedded in the MOS sensor to elevate the temperature at the operating range to obtain the reliable performance of a gas sensor, in addition, at high temperatures, gases like H_2, CH_4, H_2S and others are easy to be oxidized or reduced. Figure 1.12 depicts the schematic of the Taguchi sensor, the most popular MOS gas sensor. In 1971, Taguchi applied

SnO_2 as sensing material at the first commercial sensor using the tubular model as shown in Figure 1.12.a. One of the big MOS gas sensor companies, Figaro Engineering Inc, still sells this type of sensor. The design is renewed along with the sophisticated technology but the main parts are generally same, for example, the MO coated on alumina (ceramic) substrate to realize a miniaturized MOS sensor as depicted in Figure 1.12.b.

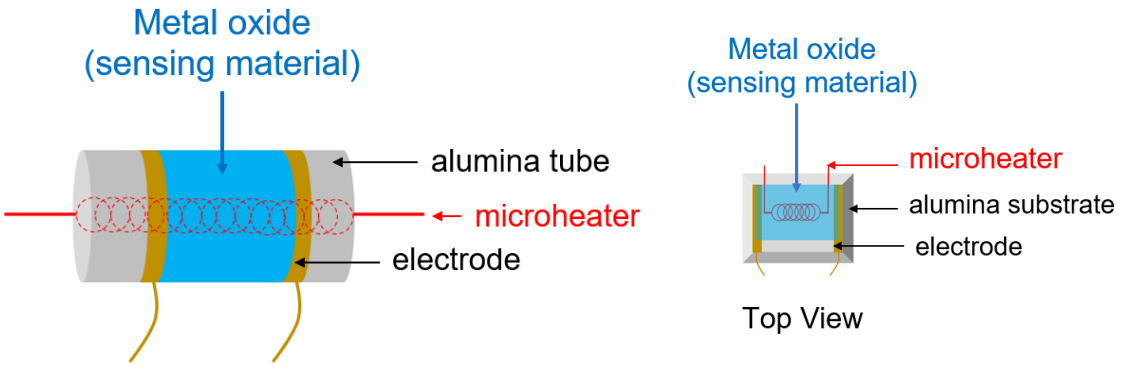

(a) (b)

Figure 1.12: Schematic of Taguchi sensor: (a) tubular model; (b) a thin MO coated on alumina substrate

Figure 1.13 shows response from MOS gas sensors [27]. Three different n-type MOS materials were applied, i.e., SnO_2, ZnO, and SnO_2-ZnO. The oxidizing gas of NO_2 was used as analyte. Figure 1.13.a depicts the response from SnO_2, ZnO, and SnO_2-ZnO towards NO_2 with scanned temperatures from 25-400 °C. According to Figure 1.13.a, the enhanced sensitivity was achieved by SnO_2-ZnO with the optimum temperature was about 100 °C that may be credited to the optimal heterostructures formation for NO_2 measuerements. Furthermore, the dynamic response from SnO_2-ZnO against various concentrations of NO_2 is displayed in Figure 1.13.b, the rise of NO_2 concentrations increases the resistance.

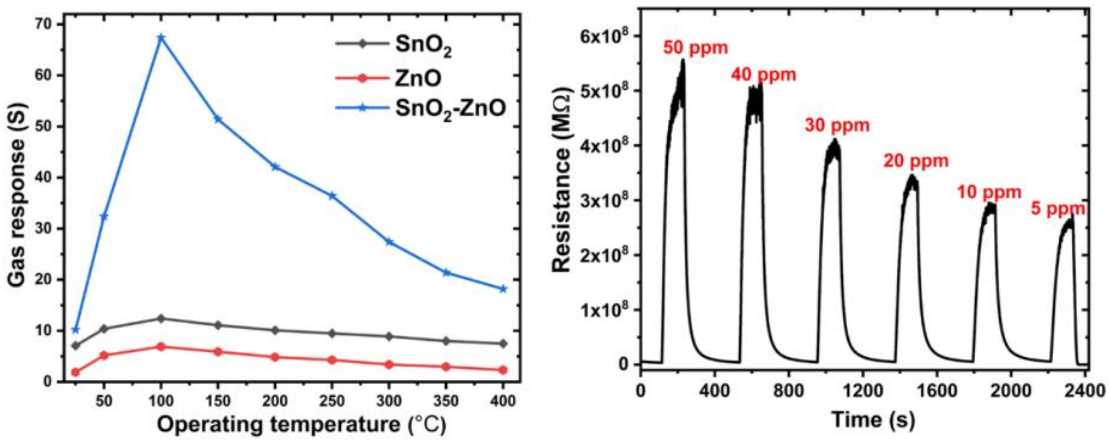

(a) (b)

Figure 1.13: Gas response towards NO_2: (a) sensor response from SnO_2, ZnO, and SnO_2-ZnO at various temperatures; (c) the response from SnO_2-ZnO towards NO_2 at different concentrations. Reproduced from [27]

The MOS sensor is still the main subject until now, especially for nanomaterials. Since the 1980s, different gas sensing materials are intensively explored to boost semiconductor gas sensors. As depicted in Figure 1.14, besides MOS, there are several sensing materials for semiconductor gas sensor like conducting polymers, carbon nanotubes, and in the most recent is 2D materials [26]. Since the 1980s, the conducting polymer (CP) such as polyaniline (PANI), poly(3,4-ethylene-edioxythiopene) (PEDOT), or polypyrrole (PPy), is used as CP and its conductivity can be further improved by adding an impurity like metal doping. Composites between CPs and metal oxides such as SnO_2 and/or TiO_2, results in CP composites to detect CO gas. In the 2000s, carbon nanotube (CNT) has been studied as gas sensing materials, it is a tube made from carbon with diameters in nanometers. CNT can also be made by wrapping a graphene in singe-walled CNT (SWCNT) formed of one sheet, or multi-walled CNT (MWCNT) formed of several sheets. CNTs offer a high surface-to-volume ratio, however the manufacturing process is very costly. CNTs also exhibit slow response and baseline recovery due to the nature of gas adsorption and desorption by these materials. The composites between CNTs with CPs like PANI or PEDOT achieved a good selectivity for ammonia but the baseline recovery was still poor. In the recent years, 2D materials is widely studied. Since the structure is just 2D, highly structured 2D material might have more surface-to-volume ratio which is required to achieve a broader area for reaction thus allowing them to obtain a high sensitivity in gas sensing measurement. Graphene is 2D material and it also can be used for gas sensing material (like in CNTs), thus this fact has opened the high possibility of using 2D materials for semiconductor gas sensor including the hexagonal boron nitride (hBN), transitional metal chalcogenides (TMDs), black phosphorous (BP), and transition metal carbides/nitrides, etc.

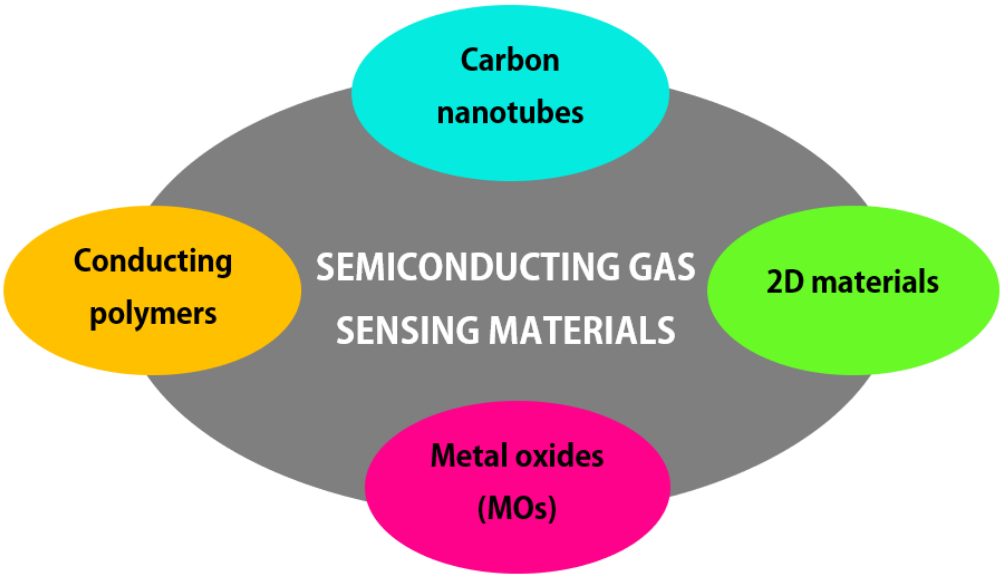

Figure 1.14: Several sensing material types applied in semiconductor gas sensor

The future semiconductor gas sensing relies on diverse types of heterostructure involving many combinations of semiconducting gas sensing materials such as, carbon nanotubes (CNTs), metal oxides (MOs), conducting polymers (CPs), and 2D materials. To summarize each gas sensing material type, a brief

overview of gas sensing materials used in semiconductor gas sensor including the advantages and disadvanges is available in Table 1.1.

Table 1.1. Overview of several semiconducting gas sensing materials [26]

Semiconducting gas sensing materials	Pros	Cons
1. Metal oxides (MOs) n-type: SnO_2, ZnO, TiO_2, WO_3 p-type: CuO, NiO, Cr_2O_3	Low cost, simplicity of use, easy fabrication, ability to sensing various gases, long lifetime, good sensitivity and stability	Cross and poor selectivity, high power consumption, high operating temperature
2. Conducting polymers (CPs) PANI, PPy, PEDOT, etc	Easy synthesis, room temperature operation	Affected by humidity, long-term use causes irreversibility and instability, it has low selectivity and a short lifetime (9-18 months)
3. Carbon nanotubes (CNTs) SWCNTs or MWCNTs made from graphene	High surface-to-volume ratio, good chemical and mechanical stability	Costly synthesis
4. 2D materials Graphene, TMDs, hBN, BP, etc	High surface-to-volume ratio, inherent flexibility	Highly cost fabrication

1.2.5 Photo-ionization Detector (PID)

Photo-ionization detector (PID) is an extremely sensitive device for gas measurement. The available commercial PID in the market offers various models of PID with readings from low parts-per-billion (ppb) up to 10000 part-per-million (ppm) range or higher. The general working principle of PID uses a high energy (E) of ultraviolet (UV) light from a lamp to ionize the gas target. As shown in Figure 1.15, the UV lamp acts as the light source with a certain amount of energy to irradiate the target gas (i.e., neutrally charged molecules) flowing in the ionization chamber. During ionization, the complete energy of the photon ($E = hv$) is transferred to the target gas atom where the amount of irradiated gas atom is decomposed into electron and ion (positively charged fragment). To form the current, the free electrons and ions move to the sensing electrode. The sensing electrode is positive electrode and counter electrode is negative electrode, respectively, whereas, the neutrally charged molecules diffuses out from the chamber. The current after amplification is the output signal where the producing flow of electrical current is proportional to the amount of irradiated target gas concentration [28–30].

PID offers high sensitivity and it can detect many volatile organic compounds (VOCs) but a reference gas must be used for calibration purposes before measuring the gas target, which is time-consuming, generally, its price is very expensive compared to the other gas sensor like the MOS sensor. In PID, the reading of gas target concentration strongly depends on the amount of the irradiated target gas atoms that successfully decomposed, principally UV radiation follows the Gaussian distributions where the center point has the highest intensity distribution as illustrated in Figure 1.15. PID is also sensitive to humidity and other contaminants like dust, and dirt which can lead to lamp fogging thus decreasing the sensitivity and accuracy, therefore when buying a PID, generally, it comes with cleaning kits [28,29].

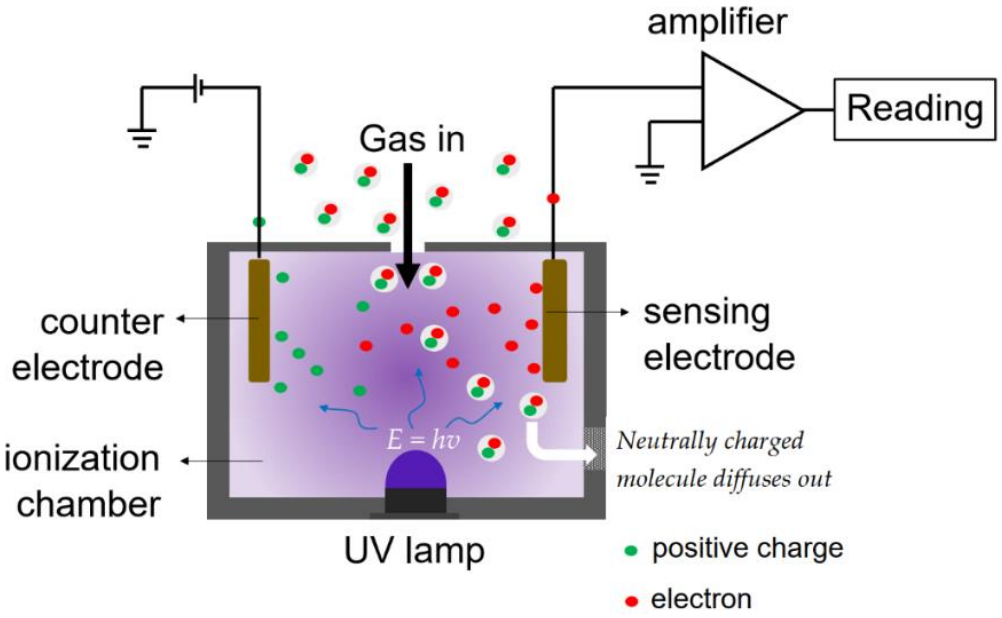

Figure 1.15: The basic sensing mechanism of gas measurement using a photo-ionization sensor

1.2.6 Infrared (IR)

Infrared (IR) is part of the electromagnetic radiation between visible lights and radio waves or microwaves, it has a spectrum wavelength region approximately from 780 nm to 1 mm. Generally, IR is separated into three categories oriented to its region as follows:

1. Near-IR (NIR)

   It has spectral range wavelength above the end of red region (at visible light spectrum) and less than ~2 µm. It produces a less heat.

2. Mid-IR (MIR)

   It has spectral range wavelength approximately 2 to 20 µm. The produced heat in between NIR and FIR. The absorption strength by molecular transition are generally 10 to 1000 times greater than NIR [31].

3. Far-IR (FIR)

   It has spectral range wavelength above ~20 µm and less than the radio waves. It produces the most heat.

The basic working principle of IR as gas sensors are as follows; the IR light is absorbed by gas molecules at a specific wavelength, and the vibrations of atoms held in gas molecules occur when the right wavelength of the IR matches the molecule's natural frequency (resonance), the higher excited IR light (with right wavelength) then the higher the molecules vibration, the wavelength or resonant frequency depending on the mass and number of atoms possessed by molecules as well as the strength and number of the various chemical bonds. In summary, when there is no analyte then there is no absorbance thus the signal output is at a maximum level. However, when the sensor is exposed to the analyte then there is absorbance causing the decreased signal output which gets reduced as analyte concentration increases [31,32].

In the IR gas sensors, the wavelengths from the IR source can be separated spatially using gratings or prisms well-known as dispersive IR or the alternative way uses non-dispersive IR (NIDR) where the

optical filter is applied to transmit only the required wavelength. The NIDR is much more favorable than dispersive IR because most dispersive IR is a very expensive, bulky, long-time measurement, and fragile. In addition, it has been reported by Pierre Jacquinot in 1954 that in separating IR wavelengths, optical filters are 1000 times and up to 100,000 times more efficient than gratings and prisms, respectively [33]. Figure 1.16 shows the schematic of NDIR for gas measurement which consists of an IR source, a reflective gas chamber, and two filtered detectors i.e., detector with active filter and detector with reference filter. The active filter has a particular bandwidth mounted on the detector passing through the IR light absorbed by the analyte, while, the reference detector only allows the IR light that does not interact with analyte and blocks the IR light absorbed by the analyte. The difference of transmitted intensities between active and reference filters mounted on the detector is converted into analyte concentration. The relationship between IR transmittance and analyte concentration is quantitatively described by the Lambert-Beer law determined in Equation 1.3; where, T is the transmittance, I_0 is the initial IR intensity emitted from IR light, I is the intensity generated during analyte exposure, $\in$ is the molar attenuation coefficient, c is the analyte concentration, L is the path length (shown in Figure 1.16).

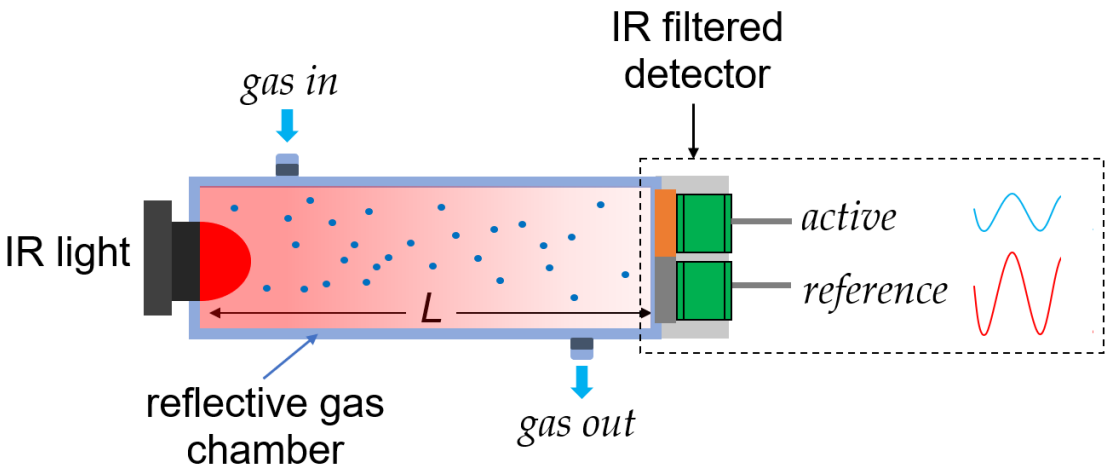

Figure 1.16: The schematic of NDIR gas sensor with two filtered detectors

$$T = \frac{I}{I_0} = e^{-\in cL} \tag{1.3}$$

Besides NDIR, IR radiation is widely applied for other gas measurements such as NIR-spectroscopy for gas analyzers, MIR-spectroscopy for gas phase analysis, MIR-optical gas sensors, or even the powerful gas measurement technology, i.e., Fourier transform infrared (FTIR) spectroscopy where all IR spectrums included and allowing simultaneously multiple gasses measurements, etc. However, IR only interacts with the molecular dipoles which occurred when atoms in molecules are arranged non-symmetrically or the vibrational modes are non-symmetry [34,35]. Therefore, symmetrical molecules such as H_2, O_2, N_2, are not excited by IR because their structure and vibration's mode are symmetry and do not create any dipoles [35].

1.2.7 Summary

In this section, several gas sensor types have been reported. A brief summary of several gas sensor technology regarding the sensor type, signal information, benefits, and drawbacks, are presented in Table 1.2. Furthermore, in the next section, the amperometric gas sensor and related works are discussed.

Table 1.2. Brief summary of several gas sensor types

Type	Signal information	Benefits	Drawbacks	Ref
EC sensor	current, voltage, conductance	low cost and low power consumption	slow response time	[6–14]
QCM sensor	frequency change	fast response, high stability	sensitive to humidity	[15]
Biosensor	biochemical signal	high selectivity	short lifetime, sensitive to temperature, low stability	[19–22]
Semiconductor gas sensor (MOS type)	conductance or resistance	inexpensive, long lifetime, high sensitivity and stability	high power consumption, high operating temperature, cross and poor selectivity	[24–26]
PID sensor	current	high sensitivity and response to many gases	expensive, humidity interference	[28–30]
IR sensor	transmittance	good selectivity, some commercial sensors are relatively inexpensive	only interacts with the molecular dipoles (response limited to analytes)	[31–35]

1.3 Amperometric gas sensor (AGS)

1.3.1 Working principle

Amperometry is an electroanalytical technique that includes voltammetry, constant potential techniques, and coulometry. Amperometry can be applied to quantify the electroactive species in liquid or gas phase measurement. In liquid phase measurement, the analytes are dissolved in liquid electrolyte and all the electrodes are immersed in a common liquid electrolyte. On the other hand, in gas phase measurement, a target gas as an analyte is exposed to the amperometric system. Numerous factors are required to be considered when designing an amperometric sensor for gas phase measurements such as the geometry, the diffusion transport of target gas to reach the electrode, the response time, and the reversibility. Amperometric gas sensor (AGS) is also well-known as voltammetric, polarographic, amperostatic, limiting current, microfuel cell, etc, but the most descriptive name is amperometric because its sensor signal is in a current.

AGS can be built using a simple two-electrodes configuration or three-electrode configuration. A typical AGS using a three-electrode configuration is shown in Figure 1.17. All the electrodes, i.e., working electrode (WE), counter electrode (CE), and reference electrode (RE) are in contact with the electrolyte and connected to the potentiostat circuit. A gas permeable membrane is used to filter the analytes (target gas) to flow into the system as well as to prevent the leakage of the electrolyte [6]. Either constant or variable

potential can be applied to AGS. The electroactive species of analyte in the electrolyte undergoes the redox reaction when a suitable potential is applied. As oriented to Figure 1.17, the oxidation of analyte occurs in anode (WE); at the same time, the reduction of analyte takes place at cathode (CE). The reduction and oxidation reaction that occur on the surfaces of each electrodes can be written in Equation 1.4 and 1.5, respectively. The RE is functioned to avoid the voltage drop and maintain a stable electrochemical reaction [6].

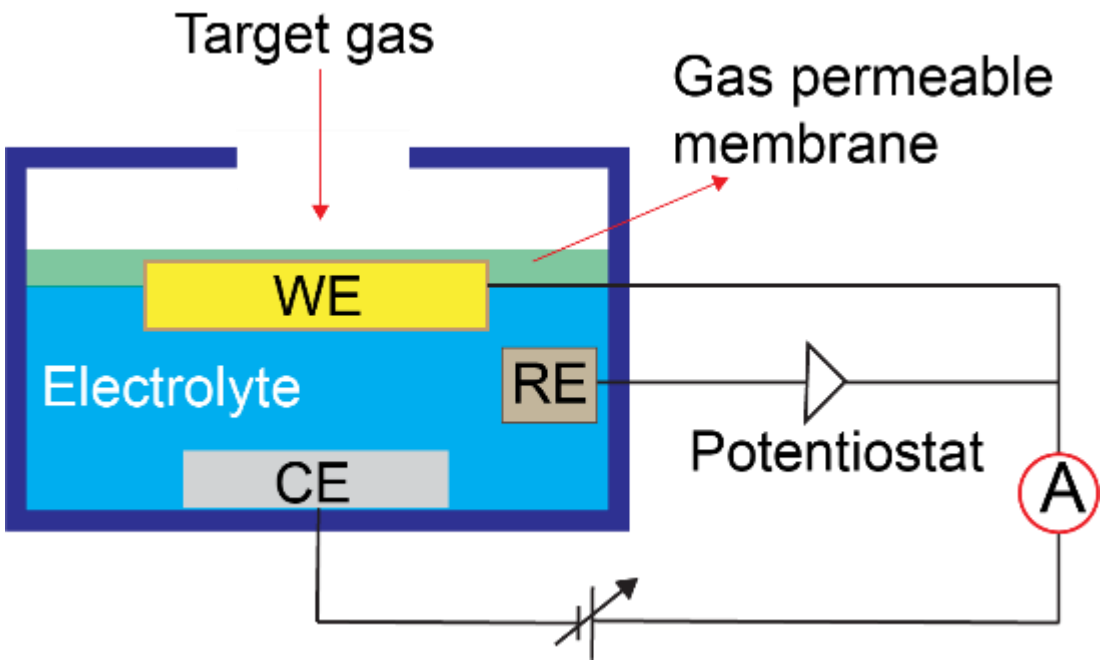

Figure 1.17: Schematic layout of the amperometric gas sensor (AGS) with three electrodes configurations

$$O1^{n+} + ne^- \rightarrow R1 \qquad \text{(reduction at CE as cathode)} \qquad (1.4)$$

$$R2 \rightarrow O2^{m+} + me^- \qquad \text{(oxidation at WE as anode)} \qquad (1.5)$$

The $O1$, $O2$ are oxidized species and $R1$, $R2$ are reduced species. The cathode reaction contributes electrons from CE and combines them with oxidized species ($O1^{n+}$) to generate a reduced species ($R1$). On the contrary, at the anode, the reduced species ($R2$) reacts to generate the oxidized species ($O2^{m+}$) and electrons which are transferred to WE as the anode. The electrons at the WE and the lack of electrons at the CE build the charges on each electrode surface, when the WE and CE are connected through external circuit then those electrons flow from WE to CE. In the AGS system, the Faraday's Law can be illustrated as follows; number of electrons are used (at cathode reaction) or generated (anode reaction) per each analyte molecule, then the charge occurs on each electrode surface which is exactly related to the amount of analyte reacting at the electrodes, afterwards, the current (electron flow in Coulombs/s) is dependent to the rate of the EC reaction, hence the rate of EC reaction at electrode is directly proportional to the amount of analyte concentration, consequently the current is also proportional to the concentration of analyte in AGS system. The common measurements using AGS is by recording the current between WE and CE as a function of the analyte concentration. The AGS generates a sensor response when the target gas contains electroactive

analyte because it diffuses into EC cell, to WE surface, then undergoes the EC reaction that either generates or consumes electrons (i.e., redox reaction).

In AGS, the observed current depends on many parameters and the resultant mathematical expression relating the rate of EC reaction, the analytes concentration, the applied potential on electrodes, can be very complex. To simplify the resulting expression relating the observed current at AGS, a limiting condition (or limiting current) is used which can be divided into two main operating conditions [6]:

1. Condition 1: $r_r \ll r_d$ (r_d controls the limiting current)
2. Condition 2: $r_r \gg r_d$ (r_r controls the limiting current)

where r_r = the rate of the mass transport (i.e., difussion) from the analyte to the electrode surface,
r_d = the rate of the EC reaction at the electrode surface.

In the first condition where $r_r \ll r_d$, the rate of the EC reaction taking place at the electrode surface controls the limiting-current. In this case, the analyte reaches the electrode surface much faster than it is reacted, hence, the concentration at the electrode surface is equal to the concentration in the bulk solution. The limiting current from this condition is derived in Equation 1.6. As shown in the equation 1.6, if all the conditions are conducted in a constant, then the limiting current is proportional to the concentration of analyte with an exponential term including temperature. The limiting current obtained from this condition (i.e., electrode's kinetic control) is not always stable because the degradation of the electrode's catalytic activity and it is not good for a practical AGS.

$$I_{lim} = nFkACexp(\alpha nFE/RT) \tag{1.6}$$

where n is the number of electrons per reacting molecule, F is the Faraday constant, k is the standard rate constant, A is the area of electrode, C is the concentration of the analyte, α is the transfer coefficient, E is the overvoltage of the electrode reaction, R is the gas constant, T is the Kelvin temperature.

In the second condition where $r_r \gg r_d$, the rate of the mass transport from the analyte governs the limiting current. In this case, the rate of reaction in the surface electrode is much faster than the rate of the diffusion transport of analyte. Theoretically, the concentration of analyte at the electrode surface is zero, in other words, every molecule that reaches the electrode surface is immediately reacted or participated in the EC reaction. Therefore, in this condition, the limiting current is further simplified in to Equation 1.7. As determined in Equation 1.7, the limiting current is now governed by the rate of analyte's mass transport to reach the electrode. Therefore, the current is directly proportional to the gaseous analyte concentration which is often preferred by AGS designer since this condition yield a more stable sensor.

$$I_{lim} = k[C]_{gas}, \tag{1.7}$$

where k is the constant rate at which the analyte transports to the electrode surface, C is the concentration of the analyte.

AGS sensors offer numerous benefits such as low cost, low power consumption, stability, selectivity, in some conditions are fast response time. The performance of AGS could be improved in many ways such as by selecting a proper electrolyte, and depositing a catalyst at its working electrode. The high electroanalytical at a modest cost is the important characteristic offered by AGS thus making it a very popular for industrial choice. Moreover, this sensor type is very potential to be miniaturized.

1.3.2 AGS system with aqueous electrolyte

Electrolyte plays an important role in EC cell, it acts as a medium for redox reactions, solubilize the analyte, electron transfer, etc. The electrolyte must be stable chemically and physically under the sensor's working operations. It is a conductive medium that must be in contact with all electrodes and assists in the charge transport in the EC cell. The aqueous electrolyte is in a liquid phase, it is water-based solvents including acids and bases (alkalines). Although the 1970s witnessed different electrolyte improvements such as nonaqueous and solid polymer electrolytes for AGS, the aqueous electrolyte is still favorable even nowadays because it has high conductivity. In addition, typically, an aqueous electrolyte is not sensitive to moisture which contributes to its stability.

In the research and development department or in the university, to improve the performance of AGS, commonly, a working electrode is modified with conducting polymer like polyaniline (PANI), then frequently the aqueous electrolytes are used in the measurement such as the acidic electrolyte, i.e., perchloric acid ($HClO_4$) and base electrolyte, i.e., potassium hydroxide (KOH) [6]. Big company like Figaro Engineering Inc., also still sells AGS with aqueous electrolyte like TGS 5042 for the detection of CO [36]. A very low concentration of mixed alkaline electrolyte that consists of KOH, potassium bicarbonate ($KHCO_3$), and potassium carbonate (K_2CO_3) results in excellent stability in long-term operation even only having two-electrode configurations. In addition, the evaporation rate was minimized by optimizing the sensor's internal structure resulting in the expected lifespan of this product has been extended to 10 years [36,37]. The oxygen sensors products like the O2-A2 and O2-A3 sensors from another big company of Alphasense Inc., are also applying the aqueous electrolyte, and the lifetime of those two products is rated approximately 3 years [38,39]. Typically, the sensor lifespan of AGS with aqueous electrolyte is controlled by the electrode materials, the electrolyte types, and the gas permeable membranes.

Although the AGS with aqueous electrolytes is still popular, the main issue encountered by TGS 5042, O2-A2, O2-A3, and other commercial AGS with aqueous electrolytes from another company, is the same, which is a slow response time. For example, according to the datasheet, the time taken to reach 90% of the steady-state response well known as t_{90} obtained by TGS 5042 and O2-A2 are within 60 s and 15 s, respectively [36–39]. The prolonged response time is due to the presence of the gas permeable membrane that makes it impractical for real-time gas measurement moreover for the rapid change of sensing conditions that occurs within a second or less. Another drawback extensively reported using AGS with aqueous electrolytes is a narrow EC window (operating potential range) which limits the target gasses (analytes) detection since some redox reactions occur at a high electrochemical potential [6,40]. In addition, AGS with aqueous electrolytes has a limited operating temperature range, mostly, aqueous electrolytes are not operating at extreme temperatures due to the evaporation issue, and using aqueous electrolytes in such a condition decreases the sensor's lifespan [6,40]. Lastly, a miniaturized AGS with aqueous electrolyte is hard

to be realized since a gas permeable membrane is indeed necessary and cannot be removed to slow down the evaporation rate and avoid the electrolyte's leakage, as shown in Figure 1.17.

1.3.3 AGS system with room temperature ionic liquid

The miniaturization for AGS is very promising, however, the AGS system must be redesigned. Although since the 1970s, the solid polymer electrolyte (SPE) has been used for AGS, it has a low ionic conductivity at room temperature and it is majorly used in extreme temperatures [6]. Ionic liquid (IL) was first reported in 1914 by Paul Walden. Currently, ILs have been used in many fields as the electrolyte for a miniaturized AGS since only a small amount of IL is required [41]. Conventional electrolytes like aqueous or nonaqueous electrolyte are evaporated or decomposed at extreme temperatures, the high thermal stability and low volatility owned by IL are allowing to operate even at extreme conditions without any losses in concentrations thus ensuring a longer lifetime [40]. In the recent progress of miniaturized AGS operating at room temperature, the room temperature ionic liquid (RTIL) is a promising choice as an electrolyte that offers many benefits: first, it has a wider EC window than aqueous or nonaqueous electrolyte which allows more target gasses to be detected; second, it has low or zero volatility and negligible vapor pressure at room temperature thus membrane-free gas detection can be realized then theoretically, the response time can be much more improved due to removing gas permeable membrane; the last, a thin film using RTIL can be realized for a tiny AGS.

Mostly, the amount of RTIL used in miniaturized AGS in the microliter range. In 2018, Gondosiswanto et.al., applied one µL of hydrophobic RTIL, i.e., 1-butyl-1-methylpyrrolidinium bis(trifluoromethylsulfonyl)imide ([BMP][Ntf2]) on several miniaturized AGS system to measure the oxygen gas at room temperature [41]. As shown in Figure 1.18.a and b, the miniaturized AGS used two different electrodes i.e., macro disk electrode (MDE) and microelectrode array (MEA), where WE, CE, and RE were deposited on a single glass substrate. The MDE and MEA had the same dimensional size of the glass substrate, i.e., 10 × 6 × 0.75 mm. MDE had gold as the WE (diameter, 1 mm) and platinum for both the CE and pseudoreference electrode. MEA had microelectrodes array with 15 pairs of 10 µm electrodes and WE, CE, RE were made of gold. When measuring oxygen, both MDE and MEA applied fix potential of -1.2 V; in MEA, only WE1 was used with WE2 disconnected. Based on the Figure 1.18.c, MEA had higher sensor response than MDE, however, the obtained t_{90} value (the response times to reach 90% of steady-state current density) for MDE and MEA was around after 150 s which was still very slow and required to be improved. In this related works, the RTIL has been already applied to AGS. However, only one RTIL and WE without catalyst were used, the AGS system with catalyst is necessary and explained in more detail in the next section. The improvement of miniaturized sensors can also be achieved from many factors, one of the examples is the RTIL selection. RTIL is made from cation and anion combinations and different cation-anion combinations offer different physical and chemical properties thus technically various RTILs can be made. In addition, the transport properties related to diffusion coefficient, conductivity, and viscosity owned by an RTIL change by different applied temperatures and/or the presence of additives [40,42–44]. The variation of RTIL transport properties with the temperature follows Vogel–Fulcher–Tamman (VFT) equation which is explained in Chapter 2; 2.1.2 Basic property of RTIL (viscosity and conductivity) on page 52.

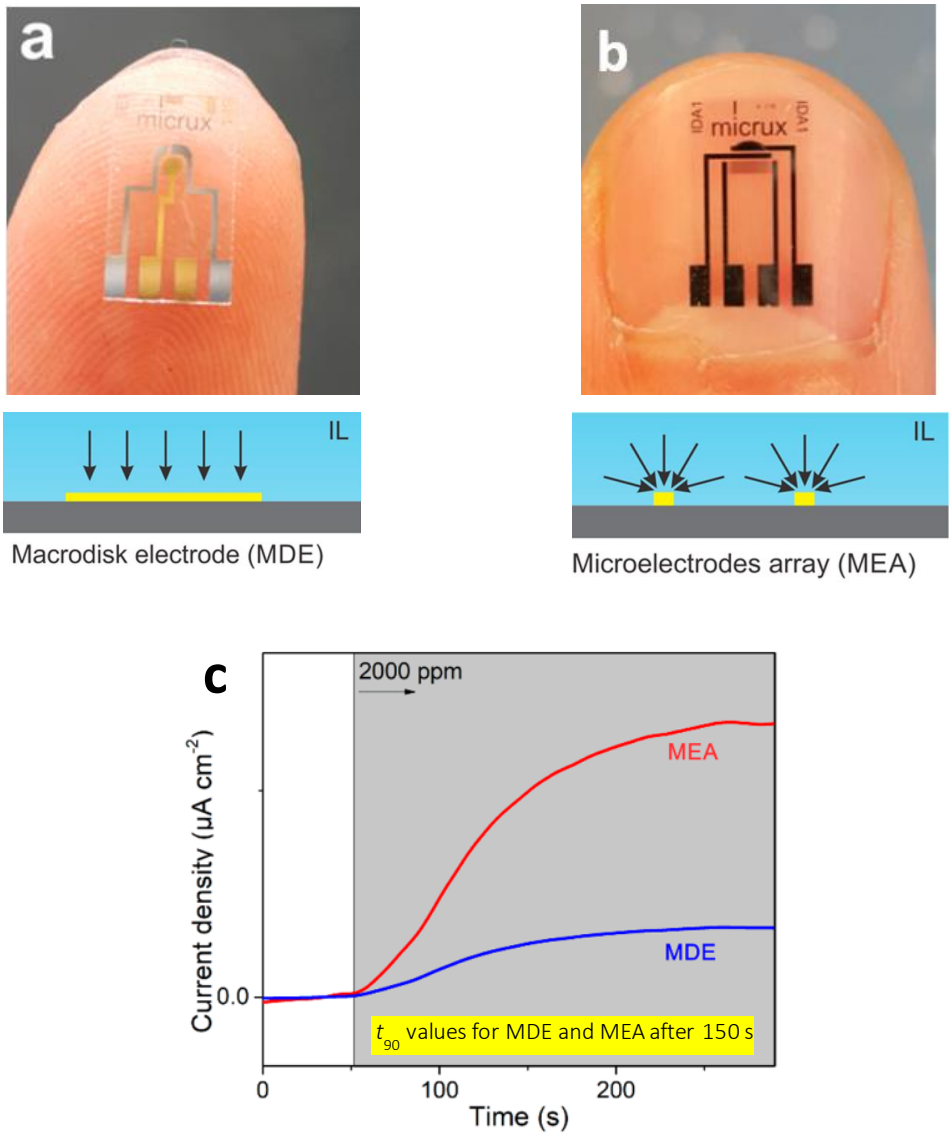

Figure 1.18: Miniaturized AGS system with RTIL: (a) MDE configuration; (b) MEA configuration; (c) the response time of MDE (blue) and MEA (red) for O_2 at 2000 ppm concentration. Reprinted with permission from [41]. Copyright 2017 American Chemical Society

1.3.4 AGS system with catalyst

The working electrode (WE) in the AGS system also plays an important role, as we know that the amperometric sensor signal depends on the rate of the analyte reacting at the electrode surface and the size of the electrode's active area, the smaller the size, the lower the amperometric signal. Therefore, WE is oftentimes modified to improve the sensor performance either for two-electrode or three-electrode configurations. Long-term stability of modified WE is essential by applying a proper modifier. Firmly attached to WE surface and not dissolved in electrolyte are the basic parameters to justify the feasibility of the modifiers applied for WE. A catalyst is frequently used as a modifier, it is a substance that increases the rate of the EC reaction without being consumed, and desirable catalyst should meet several indicators such as compatible, active, selective, stable, and cost [45]. In AGS, a catalyst can be from biology element or metal material which is explained in more detail in the following section.

1.3.4.1 Biological element as catalyst

Enzymes are frequently used as catalysts for modified WE in AGS, moreover, for disease diagnosis using breath analysis. Principally, enzyme only can interact with particular analyte, hence, high selectivity is expected when using enzyme for modified WE in AGS since the target substance can be easily detected. Figure 1.19 shows the fabrication of modified WE with enzyme for gaseous ethanol measurement. As shown in Figure 1.19.a, chromatography paper (ChrPr), a porous material with cellulose fiber, was used as the enzyme supporting layer. The enzyme supporting layer has two different layers, i.e., a mediator layer and an enzyme layer. For the mediator layer, the ChrPr was diped into a PBS containing a reducing mediator (Ferro: $K_4[Fe(CN)_6]$). For the enzyme layer, ChrPr was dipped into a PBS containing two enzymes, alcohol oxidase (AOD) and peroxidase (HRP). Afterward, ChrPr with mediator and ChrPr with enzymes were left to dry at a refrigerator for 12 h at 4 °C, as shown in Figure 1.19.b. Then the enzyme supporting layer consisting of mediator layer and an enzyme layer was placed onto the screen-printed electrodes, as depicted in Figure 1.19c. The measurement setup for gaseous ethanol is depicted in Figure 1.19.d.

Figure 1.20 shows the results for ethanol vapor using the modified electrode with the enzyme supporting layer. As shown in Figure 1.20, there were clear output current curves between ethanol vapor exposure and without ethanol vapor exposure (0 ppm). After ethanol vapor was released at 20 s, the current was produced by the oxidation of ethanol vapor diffused into PBS and approximately 40 s was required for the enzyme reactions to increase, the output current increased linearly for 80 s, finally, it reached a steady state current at 200 s for all concentrations. Although the selectivity is high using enzyme, the reproducibility and stability is very poor. In addition, enzyme has a short lifetime.

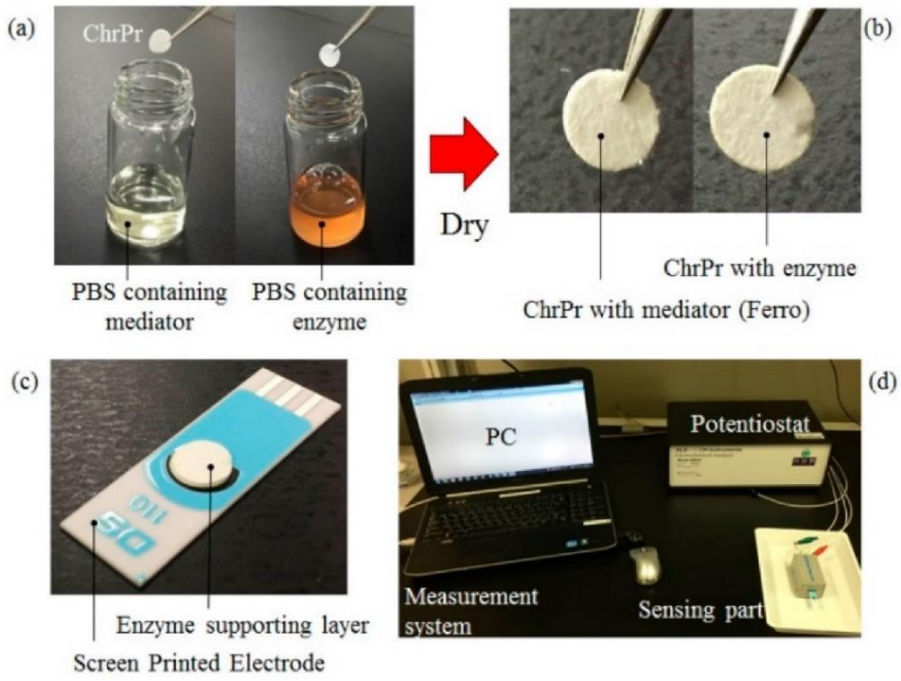

Figure 1.19: Fabrication of modified electrodes with enzymes: (a) ChPrs dipped into the solution containing mediator and enzymes; (b) ChPrs with mediator and enzyme were left to dry; (c) the enzyme supporting layer placed onto screen-printed electrodes; (d) measurement set-up for gaseous ethanol. Reproduced from [46]

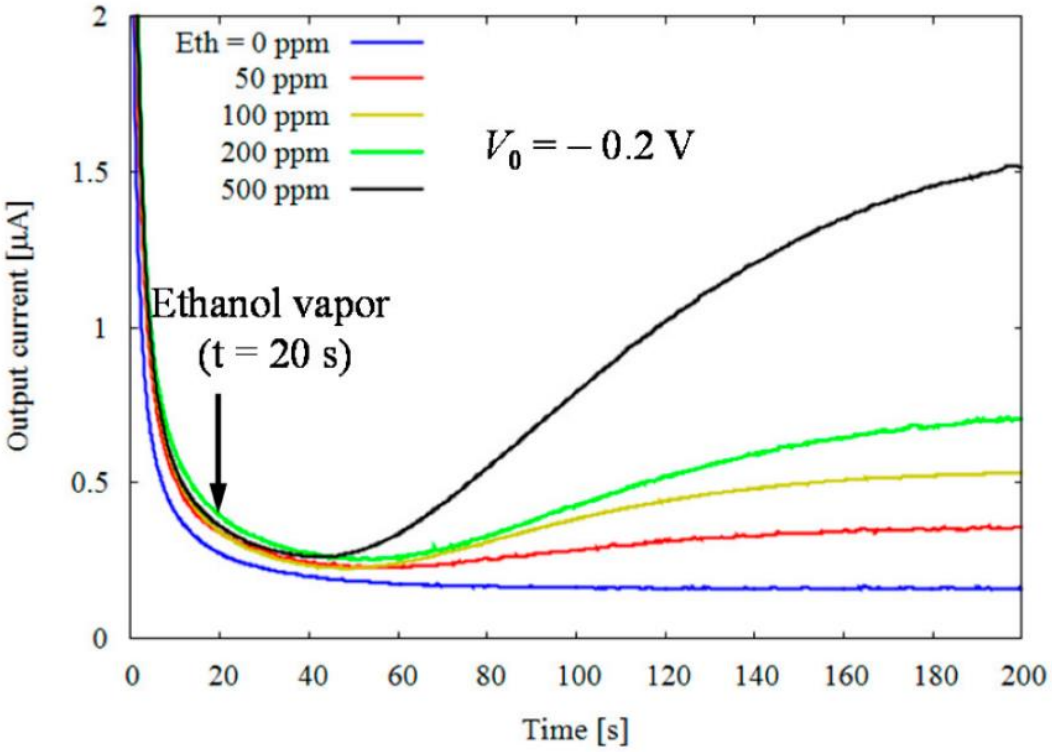

Figure 1.20: The output current from different concentration of ethanol vapor exposure using modified electrode with the enzyme supporting layer, the chronoamperometry measurement was conducted at the voltage of -0.2 V. Reproduced from [46]

1.3.4.2 Metal oxide nanostructures

Metal oxide (MO) was briefly introduced in the previous section 1.2.4. MO has been predominantly solid-state for gas measurement systems with many advantages such as compact size, good sensitivity, low cost, easy fabrication, etc., and yet there is still room for improvement by controlling its morphology, size, or even adding some impurities [47]. Generally, MOs are divided into porous and dense. In dense MO as sensing film, the gas interaction only occurs at the surface of sensing film since the target gas can not penetrate into the sensing film. In porous MO film, the target gas can penetrate into the MO film and interact with the inner grains. In fact, with current technology development, actually, MOs films are inherently produced with a certain porosity. A well-defined and uniform porous structure owned by MO film is desired to enhance the sensing performance as part of the large surface-to-volume ratio. The high surface-to-volume ratio tends to be a good catalyst since a small quantity of a catalyst can be used when catalyzing reactions and can occupy a larger surface area [47]. In this section, several example of MO nanostructures and their gas sensing from the aspects of morphology and particle size is given such as mesoporous metal oxide, metal oxide nanowires, metal oxide nanotubes, and metal oxide nanosheets [47]. In addition, metal nanoparticles doped in metal oxide are briefly introduced.

A. Mesoporous metal oxide

According to the porous size, there are three kinds of porous materials i.e., macro porous with diameter greater than 50 nm, microporous with diameter less than 2 nm, and mesoporous with diameter

between macro and microporous. Figure 1.21 depicts the comparison of field emission scanning electron microscope (FE-SEM) image between traditional tin oxide (SnO_2) and mesoporous SnO_2 (mesoporous SnO_2 was prepared by multi-wall carbon nanotube (MWCNT) method). Theoretically, mesoporous SnO_2 has better gas permeability because it facilitates a region that gas can diffuses in and out through the mesoporous SnO_2 film, thus it has a higher sensor response than traditional SnO_2. Figure 1.22 depicts the comparison sensor response between traditional SnO_2 and mesoporous SnO_2 for ethanol and benzene vapors with concentrations of 70 ppm and 280 ppm, respectively. As shown in Figure 1.22.a, mesoporous SnO_2 has a higher output current than traditional SnO_2 for ethanol vapor, the same result was also obtained for gaseous benzene measurement shown in Figure 1.22.b. The main reason is due to mesoporous SnO_2 having a higher surface-to-volume ratio and better gas permeability than traditional SnO_2. Mesoporous SnO_2 allows the gas reaction not only taking place at the surface but inner region is also active, whereas, the traditional SnO_2 limits on the surface only. In addition, the shapes of the porous in MO films play important role to determine the rate of gas diffusion transport [48].

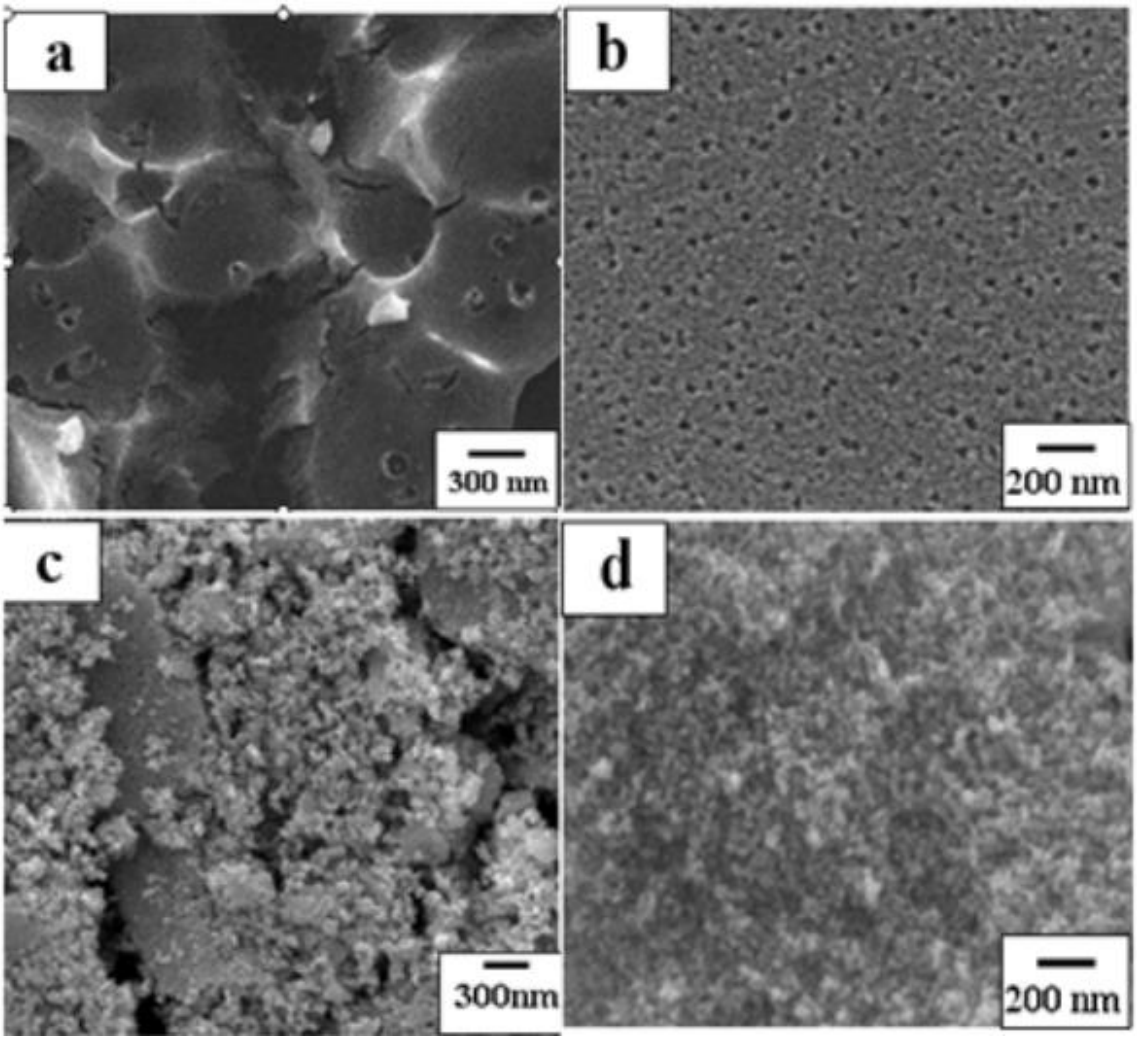

Figure 1.21: The FE-SEM images of: (a), (b) mesoporous SnO_2; (c), (d) traditional SnO_2. Reprinted from [48], Copyright (2010), with permission from Elsevier

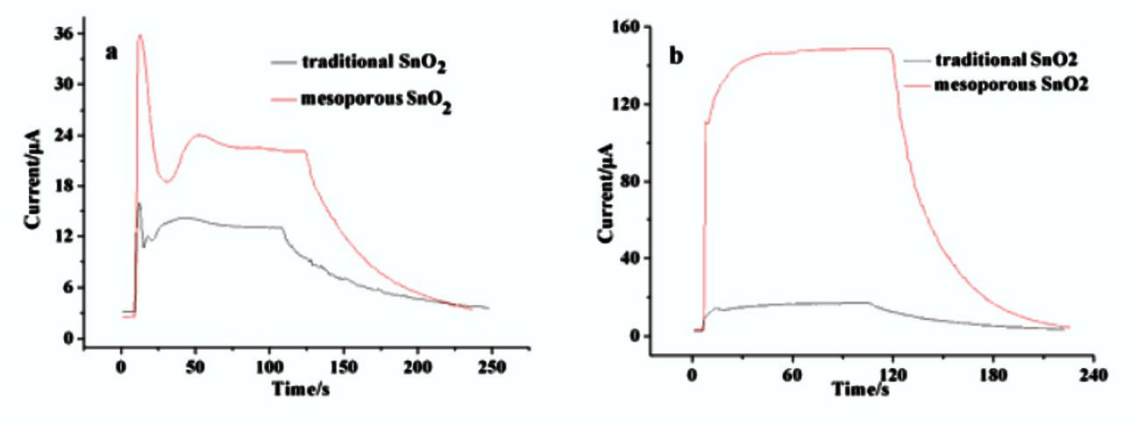

Figure 1.22: The sensor response between mesoporous SnO_2 and traditional SnO_2 for: (a) Ethanol with concentration of 70 ppm; (b) Benzene with concentration of 280 ppm. Reprinted from [48], Copyright (2010), with permission from Elsevier

B. Metal oxide nanowires

Nanowires is one-dimensional MO nanostructure which have been widely used in many fields such as in the gas sensing, food safety, etc. There are many semiconductor nanowires such as SnO_2, In_2O_3, ZnO, TiO_2, etc [47,49]. Nanowires have been attracted due to their high surface-to-volume ratio, and high sensitivity, or even a single nanowire is able to be used for gas sensors. Figure 1.23 shows the image for SnO_2 nanowires. The typical fabricated nanostructure morphologies of SnO_2 nanowires were captured using SEM as shown in Figure 1.23.a, which had diameters around 40 to 65 nm with several microns long. Furthermore, Figure 1.23.b depicts the transmission electron microscopy (TEM) of a single nanowire which would be applied for ammonia gas sensor.

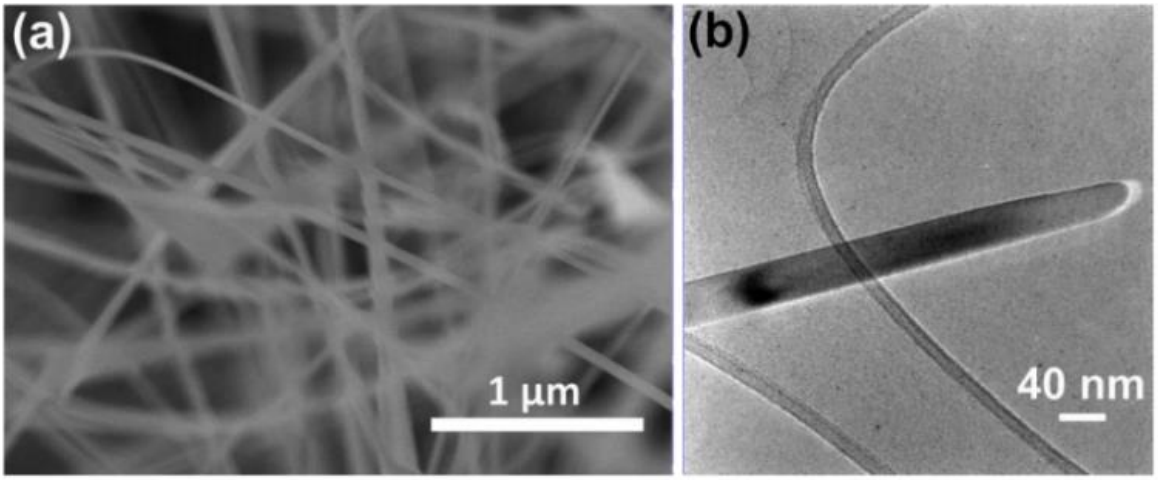

Figure 1.23: Images of SnO_2 nanowires: (a) The SEM image for typical fabricated of SnO_2 nanowires; (b) the TEM image of a single nanowire. Reproduced from [49]

A single SnO_2 nanowire was used for ammonia gas measurement. Figure 1.24 depicts the sensor response and the 3D-model of the gas sensor applying a single SnO_2 nanowire. Figure 1.24.a depicts the

current as a function of time using different ammonia concentrations (e.g., 5 ppm, 3 ppm, 2 ppm, 1 ppm, 0.5 ppm, 0.2 ppm, 0.1 ppm) and different temperatures (e.g., 200 °C, 240 °C, 280 °C, 320 °C, 360 °C). The current increasing as ammonia injected is a typical n-type semiconductor response when interacts with reducing gas like ammonia. The ammonia releases the electrons in the SnO_2 nanowire and thus increases the current flows. As shown in Figure 1.24.a, the increased temperature resulted in a higher current and faster recovery time. Figure 1.24.b shows the sensor responses for gaseous ammonia at several concentrations and five working temperatures, the lowest temperature exhibited the most linear response and the highest temperature tend to saturation. Figure 1.24.c displays the 3D-model of the sensor with a single SnO_2 nanowire (in white) for ammonia gas measurement acting as the bridge between two metal electrodes (in blue). The top SEM image of the sensor is available in Figure 1.24.d.

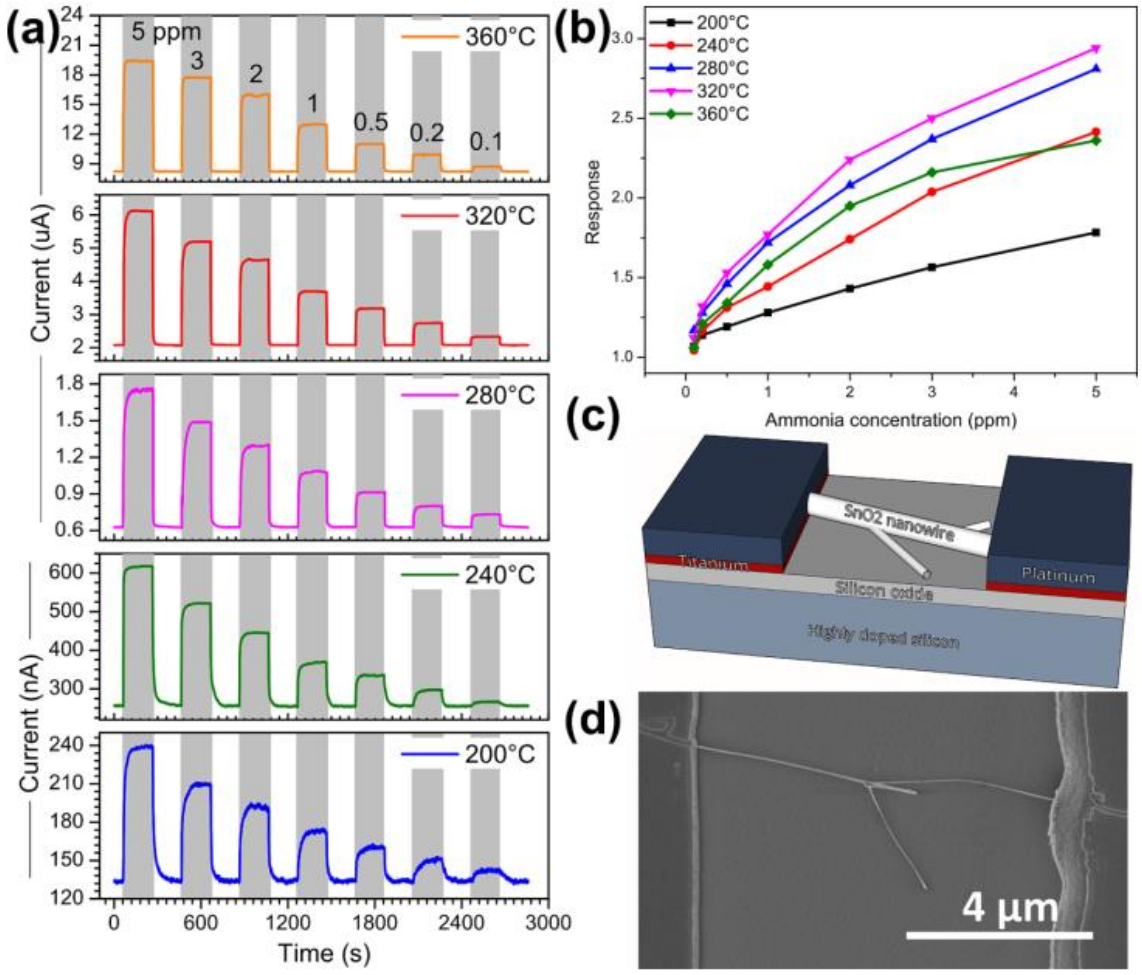

Figure 1.24: A single SnO_2 nanowire applied for ammonia gas measurement: (a) the sensor responses for different concentrations of gaseous ammonia (5 ppm, 3 ppm, 2 ppm, 1 ppm, 0.5 ppm, 0.2 ppm, 0.1 ppm) at different temperatures (200 °C, 240 °C, 280 °C, 320 °C, 360 °C); (b) sensor response as a function various concentration of ammonia with different temperatures; (c) 3D-model of sensor with a single SnO_2 nanowire; (d) the SEM image. Reproduced from [49]

C. Metal oxide nanotubes

Nanotubes are the most widely 1-D nanostructures which possess a higher porosity and larger surface area than nanowires. Hence, it is more favorable to apply nanotubes as gas sensing measurements instead of nanowires [47]. However, it is majorly reported that nanotubes fabrication is much more complicated than nanowires [47]. A porous nanotube offers a higher surface-to-volume ratio than traditional nanotubes, its porosity allows a larger area for gas reaction, for example, the porous SnO_2 nanotubes can be used for VOCs measurements. Figure 1.25 depicts a brief process to fabricate the porous SnO_2 nanotubes using carbon nanotubes (CNTs) as templates. Firstly, the carbon nanotubes (CNTs) with diameter of 20-30 nm were purified. The FE-SEM image of purified CNTs is shown in Figure 1.25.a. Then, SnO_2/CNT nanocomposites were synthesized, their SEM image is depicted in Figure 1.25.b. Afterward, through the chemical and physical process, the porous SnO_2 nanotubes were obtained as shown in Figure 1.25.c, d, the detail procedures to fabricate SnO_2 nanotubes was available in this Ref [50].

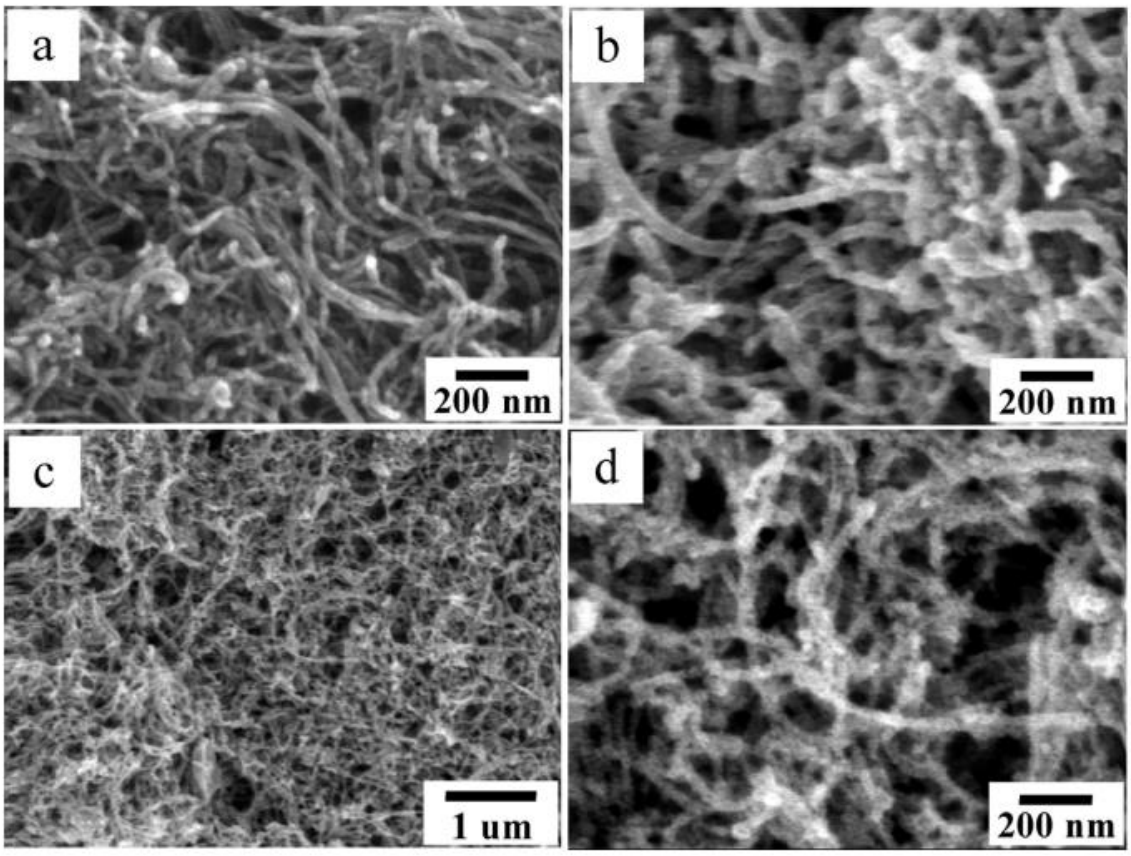

Figure 1.25: The FE-SEM image for: (a) the purified CNTs; (b) SnO_2/CNT nanocomposites; (c), (d) porous SnO_2 nanotubes. Reprinted with permission from [50]. Copyright (2009) American Chemical Society

Figure 1.26 shows various sensor responses from porous SnO_2 nanotubes for several VOCs using different concentrations (e.g., 5 ppm, 10 ppm, 25 ppm, 50 ppm, 75 ppm, 100 ppm, 150 ppm, 200 ppm, 300 ppm, and 400 ppm) at measurement temperature of 200 °C. Figure 1.26.a, b, c, and d depict the sensor responses from porous SnO_2 nanotubes against methanol, propanol, 2-propanol, and acetone, respectively. The good sensing properties were associated to the porous morphology of SnO_2 nanotubes. The different

magnitudes of sensor responses possessed by porous SnO_2 nanotubes against methanol, propanol, 2-propanol, and acetone indicated that porous SnO_2 can be used to detect those VOCs and exhibited a cross-selectivity among those VOCs.

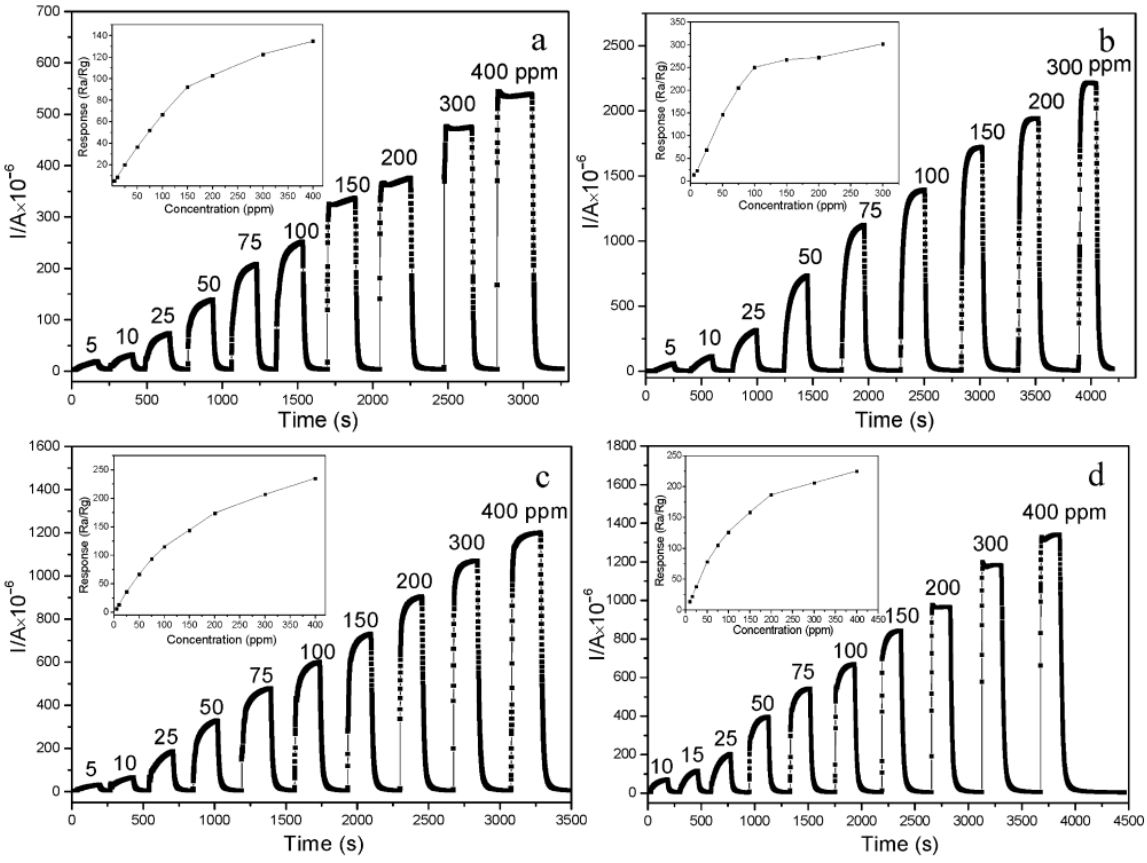

Figure 1.26: The sensor response (current) of porous SnO_2 nanotubes for different concentrations of VOCs: (a) methanol; (b) propanol; (c) 2-propanol; (d) acetone, at 200 °C. The insets show the corresponding sensor response curves. Reprinted with permission from [50]. Copyright (2009) American Chemical Society

D. Metal oxide nanosheets

Nanosheets are two-dimensional metal oxide nanostructure which possess a large surface area. Nanosheets have been also widely used in nanomaterials for gas sensing, different structure of nanosheets performs different results. Figure 1.27 shows SEM images of heterostructures of ZnO nanosheets with Zn foil as a substrate, two different heterostructures were ZnO sheet array/Zn shown in Figure 1.27.a and ZnO free sheet/Zn depicted in Figure 1.27.b. The detail procedures to fabricate those two heterostructures nanosheets can be obtained from this Ref [51]. According to the measurement results, the sensor responses for CO_2 reduction from different scan rates obtained between ZnO sheet array/Zn and Zn/O free sheet/Zn were different shown in Figure 1.28. The ZnO sheet array/Zn had a higher current density (*j*) than ZnO free sheet/Zn indicated that the activity of CO_2 reduction reaction was higher using ZnO sheet array/Zn which was attributed to its morphology of 3D nanosheet array.

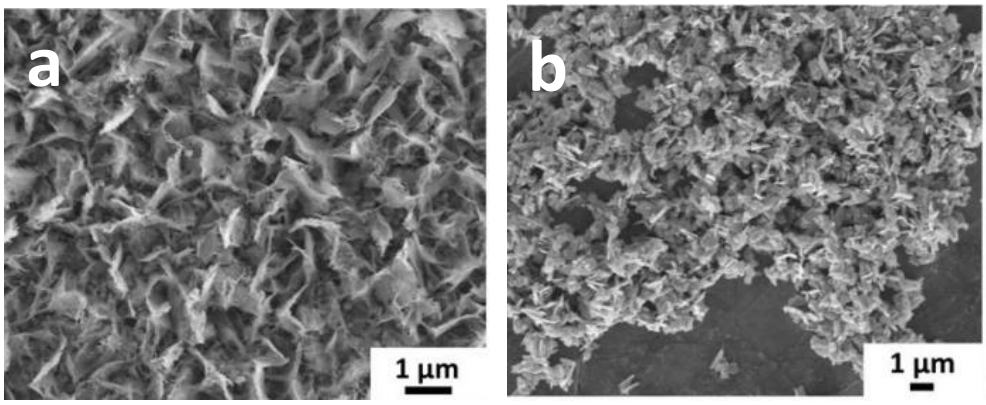

Figure 1.27: The SEM image of heterostructure of ZnO nanosheets: (a) ZnO sheet array/Zn; (b) ZnO free sheet/Zn. Reprinted with permission from [51]. Copyright (2021) American Chemical Society

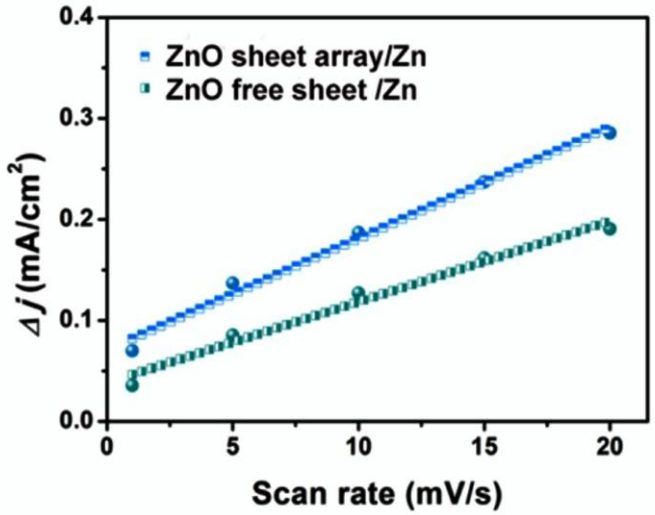

Figure 1.28: The sensor responses for CO_2 reduction reaction with different scan rates obtained from ZnO sheet array/Zn and ZnO free sheet/Zn. Reprinted with permission from [51]. Copyright (2021) American Chemical Society

Although there are many kinds of metal oxide's morphologies such as mesoporous metal oxide, metal oxide nanowires, metal oxide nanotubes, metal oxide nanosheets, etc. The catalytic activity of metal oxide without doping is still considered low. Therefore, the impurities like metal nanoparticles and metal clusters are added to metal oxide to boost the performance.

E. Metal nanoparticles doped in metal oxide

Nanoparticles (NPs) play a notable role for a catalyst. NPs can be categorized as nanocatalysts which promote a faster reaction and increase efficiency due to lowering the activation energy to obtain a high product yield. Compared to a bulk catalyst, nanocatalyst has a larger surface area allowing more active contact with reactant thus a higher reaction rate and catalytic activity can be achieved. Generally, there are two main groups of metal materials used for a catalyst, i.e., noble metal and non-noble metal (Fe, Ni, Co, Cu, etc), in this section, we specifically focused on the effect of noble metal doped in metal oxide. In the

gas sensing application, the common used nanocatalysts of noble metals mainly include gold (Au), platinum (Pt), palladium (Pd), silver (Ag), ruthenium (Ru), rhodium (Rh).

Figure 1.29.a shows the TEM image of Au NPs with an average particle size of ~7 nm decorating the WO_3 nanofibers. According to the reported results, the sensor response obtained by Au/WO_3 nanofibers achieved ~60 times higher than that of pure WO_3 nanofibers towards n-butanol vapor measurement. Figure 1.29.b presents the SEM image of Pt NPs decorating WO_3 micro-belts. Based on the experimental results, the addition of Pt nanocatalysts showed a high remarkably selectivity towards H_2S against other interfering gasses like ethanol, acetone, ammonia, carbon monoxide. Figure 1.29.c depicts the SEM image for Pd decorating the coral-like-ZnO nanosheets. Based on the results, with Pd modification, the improved response to acetone vapor was achieved three times higher and the response/recovery time was about threefold faster than the pristine ZnO.

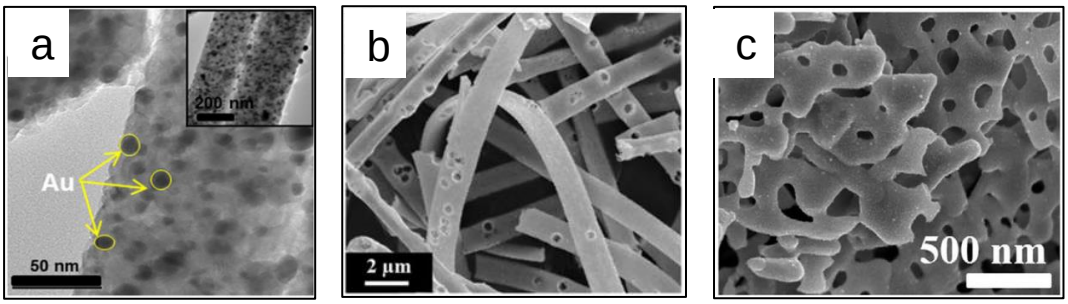

Figure 1.29: Several noble metals doped in metal oxides: (a) TEM image of Au NPs doped in WO_3 nanofibers; (b) SEM image of Pt decorating WO_3 micro-belts; (c) SEM image of porous coral-like Pd-decorated ZnO nanosheets. Reprinted from [52]

Figure 1.30.a shows the TEM image for a single Ag NP doped in the ZnO. According to the results, Ag/ZnO improved the sensing behavior even for a very low gaseous NO_2 concentration at 500 ppb. Figure 1.30.b depicts the image of Ru NPs doped in Co_3O_4. Based on the results, the Ru/Co_3O_4 nanocomposites enhanced gas sensitivity toward ethanol vapor. Figure 1.30.c presents the TEM image for decorated Rh NPs at NiO nanofibers. The outcomes revealed that the enhanced sensor response toward 200 ppm of acetone was 37.9 times higher than the pristine NiO nanofibers sensor. Furthermore, the example for bimetal decorating metal oxide is shown in Figure 1.30.d, the Au-Pt NPs decorated ZnO nanowires. Based on the results, the AuPt-decorated ZnO increased the sensor response towards 20 ppm H_2S four times higher than the pristine ZnO.

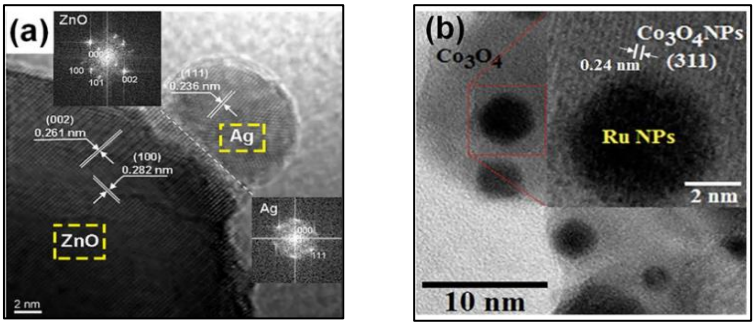

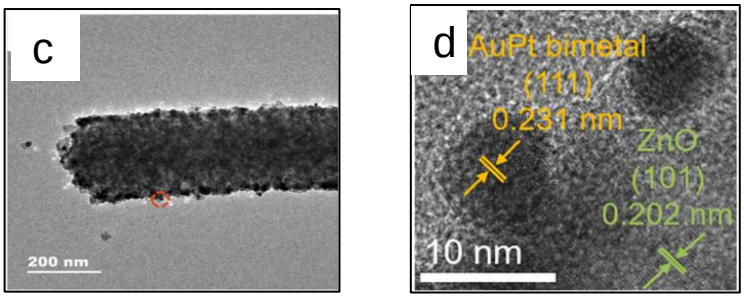

Figure 1.30: Several noble metals doped in metal oxides: (a) TEM image of a single Ag NP decorated on ZnO; (b) image of Ru NPs decorating Co_3O_4; (c) TEM image of Rh NPs decorated NiO nanofibers; (d) TEM image for Au-Pt decorated ZnO nanowires. Reprinted from [52]

Several noble metals nanoparticles doped in various metal oxides have been briefly explained. Noble metals are extensively used for nanocatalysts due to their high electrocatalytic activity and chemical inertness. However, some parameters must be considered to fabricate a good catalyst, for example, the host matrix having good conductivity is required to site the nanocatalyst since the coalescence of two or more nanoparticles oftentimes occurs; in case of metal nanocatalysts doped in the metal oxide, the host matrix is then the metal oxide. Furthermore, the catalytic activities owned by the noble metal catalysts depend on their size, reduction of catalyst size to atomic level shows interesting catalytic properties which are explained in more detail in the following section.

1.3.4.3 Atomic metal catalysts

Over the past few decades, metal nanoparticles (NPs) having diameters less than 100 nm have attracted many researchers because they exhibit different catalytic behavior, moreover, their magnetic, thermodynamic, electrical, optical, and chemical properties differ from metal NPs and bulk metals. In the metal NPs, generally, the catalytic properties are scalable to diameter size. However, in the metal clusters or even lower size (the atomic level), each atom exhibits a unique property due to quantum size effect and geometrical effect [53]. Figure 1.31 illustrates the position between NPs, metal clusters (CLs), and atoms, oriented to their diameter, approximated number of atoms, and molecular geometries [53,54].

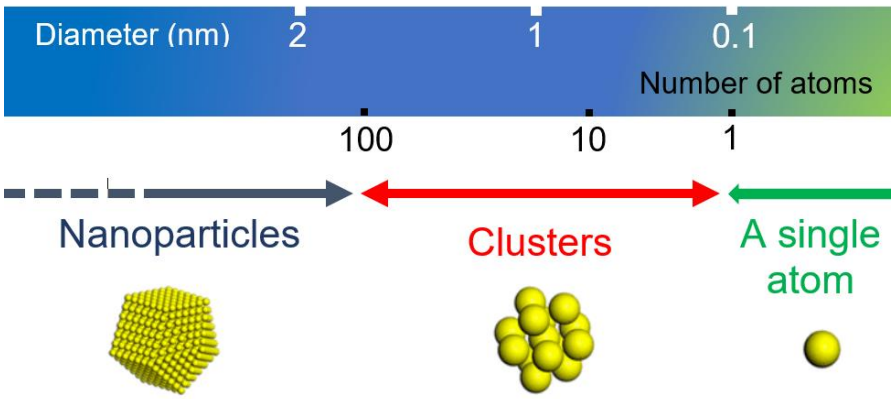

Figure 1.31: The concept of nanoparticles, clusters, and atoms oriented to their geometric, diameter, and number of atoms

Besides, NPs and CLs, a single-atom catalyst (SAC) in which a single atom increases the chemical kinetics, is also popular, moreover, for heterogeneous catalysts. SACs offer great potential to achieve the high rate of catalytic activity and selectivity. Figure 1.32 shows various single noble metal materials for catalysts such as Pd, Pt, Au, Ag, Ru, Rh. Heterogeneous catalyst made from bimetals like alloy, heterostructure, and core-shell are also popular.

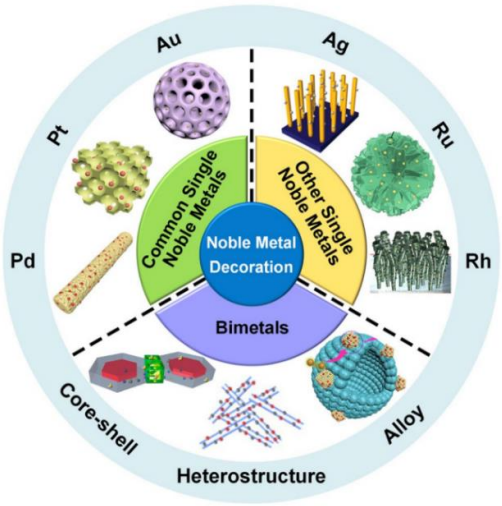

Figure 1.32: Various single noble metals and bimetals used for catalysts in gas sensors. Reprinted from [52]

Figure 1.33 describes the illustration of the a single-atom metal formation. Although bulk metal is conductive material, however, bulk metal like noble gold metal is chemically inert thus it is generally regarded as a poor catalyst. When its size is reduced into metal NPs then the catalytic activity is enhanced. Reducing the size of metal NPs to the atomic metal level where a high density of SACs sited in the host matrix exhibit remarkably catalytic activity properties due to a larger active area undergoing the catalytic reactions.

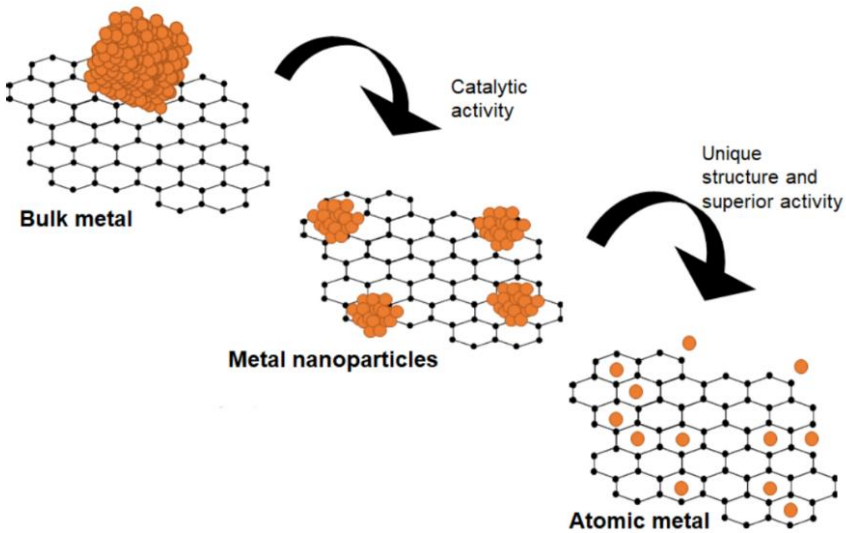

Figure 1.33: Illustrative example of a single-atom metal formation. Modified from [55] with permission from John Wiley and Sons

In 2012, Ilana Schwartz et al., conducted measurements using different atomic gold catalysts at Pt/PANI working electrode that affected the electrooxidation of propanol isomers in KOH [56]. Figure 1.34 shows the unique catalytic activity achieved by several atomic gold decorated Pt/PANI electrodes for 1-propanol (Figure 1.34.a) and 2-propanol (Figure 1.34.b). The cyclic voltammograms (CVs) of several atomic gold electrodes (AGEs) are presented in Figure 1.34.a and b, i.e, Pt/PANI/Au_N where N is the number of the number of atomic gold (N=2-7) in the cluster. As shown in Figure 1.34, each electrode decorated with a particular number of atomic gold clusters exhibited a unique catalytic property, for example the even number of N like AGE-6, AGE-4, AGE-2 exhibited a higher catalytic activity than electrode with odd number of N, i.e., AGE-3, AGE-5, AGE-7.

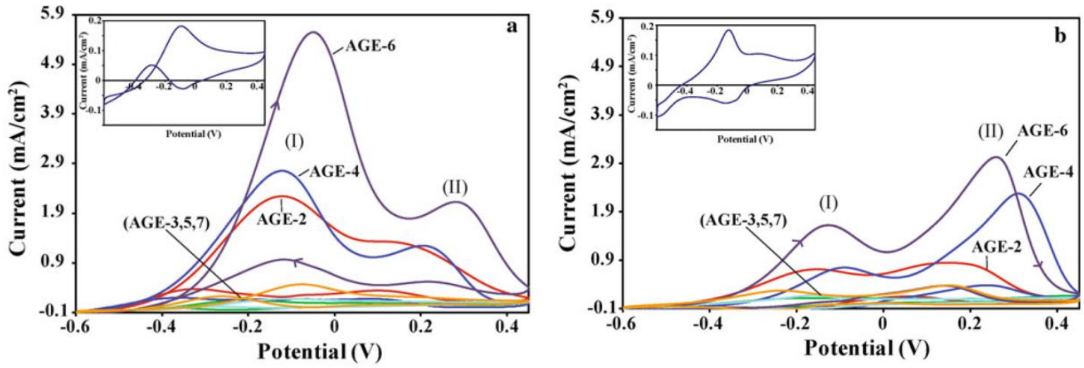

Figure 1.34: The CV curves 0.5 M propanol isomers in 1 M KOH using several electrodes Pt/PANI/Au_N (where N is the number of atomic gold clusters started from 2 to 7): (a) electrooxidation of 1-propanol; (b) electrooxidation of 2-propanol. The panels correspond to N = 0. Reproduced from [56] with permission from Springer Nature

Previously, our group also conducted the effect of atomic catalyst for amperometric sensor. Table 1.3 summarizes the research works conducted by our group. In 2020, the atomic gold deposition system was successfully built in Nakamoto Laboratory; a bulky amperometric sensor of Pt/PANI/Au_N (where N = 1 to 4) was fabricated and used for propanol isomers measurement in KOH shown in Figure 1.35. The CV curve for 1-propanol and 2-propanol using Pt/PANI/Au_N (where N = 1 to 4) are depicted in Figure 1.35.a and b, respectively. As shown in Figure 1.35.a and b, the even number of N like Au_2 and Au_4 exhibited a higher catalytic activity than the odd number of N like Au_1 and Au_3. The bulky Pt/PANI/Au_2 was used for gas sensing measurements for ketones, alcohols, esters, etc. Figure 1.36 shows the representative results for gaseous 1-propanol and 2-propanol using a bulky Pt/PANI/Au_2 in KOH. As shown in Figure 1.36, the propanol isomers were able to be distinguished even different gaseous concentrations loaded; at the forward scan, 1-propanol vapor had the highest peak at negative voltage region (i.e., approximately at -0.18 V shown in Figure 1.36.a) and iso-propanol had the highest peak at positive voltage region (approximately at +0.18 V shown in Figure 1.36.b). In 2021, we moved to a tiny AGS system, the Pt/PANI/Au_2 was successfully fabricated in a miniaturized AGS system and first reported by our group, we also applied RTIL of 1-ethyl-3-methylimidazolium trifluoromethanesulfonate ([EMIM][Otf]) in this system. Afterward, the miniaturized AGS system using Pt/PANI/Au_2 and [EMIM][Otf] were applied for gaseous propanol isomers measurement.

Figure 1.37 shows the comparison of gaseous propanol isomers measurements at different relative concentrations using a miniaturized Pt/PANI/Au_0 and Pt/PANI/Au_2 coated with 50 µL of [EMIM][Otf] and only one fixed EC potential of +1.0 V against reference electrode of Ag/AgCl was explored. Based on the Figure 1.37, for 1-propanol, mostly at different concentrations, Pt/PANI/Au_2 exhibited a higher sensor response (Figure 1.37.b) than Pt/PANI/Au_0 (Figure 1.37.a). For 2-propanol, mostly at different concentrations, Pt/PANI/Au_2 also showed a higher sensor response (Figure 1.37.d) than Pt/PANI/Au_0 (Figure 1.37.c). Based on these results, the Pt/PANI/Au_2 had a higher catalytic activity than Pt/PANI/Au_0. However, the remaining issue was the measurement data collected with time interval of 20 s. In addition, only a single sensor with one RTIL using one EC potential was applied in this measurement. Therefore, a real-time measurement and several RTILs with varying EC potentials are required to be realized and explored.

Table 1.3. Brief summary of research works conducted by our group

Year [ref]	Research works
2020 [57]	▪ Atomic gold deposition system built in the bulky amperometric system using Pt/PANI/Au_N (where N = 1 to 4) ▪ Measurement conducted in aqueous electrolyte (KOH) and target compounds were 1-propanol and 2-propanol
2020 [58]	Bulky AGS system decorated Au_N (where N = 2), i.e., Pt/PANI/Au_2 used for gas measurements for ketones, alcohols, esters, and carboxylic acids in aqueous electrolyte (KOH)
2021 [59]	▪ Fabricating Pt/PANI/Au_2 on a miniaturized AGS system ▪ A dried Ag/AgCl ink was proposed for RE to form a stable reaction ▪ One RTIL was used 1-ethyl-3-methylimidazolium trifluoromethanesulfonate ([EMIM][Otf])
2023 [60]	▪ Miniaturized AGS system decorated Au_N (where N = 2), i.e., Pt/PANI/Au_2 and applying 50 µL RTIL of [EMIM][Otf] were used for gas measurements for 1-propanol and 2-propanol ▪ To obtain a rapid and real-time gas measurement, fixed EC potential was applied (only one fixed EC potential explored)

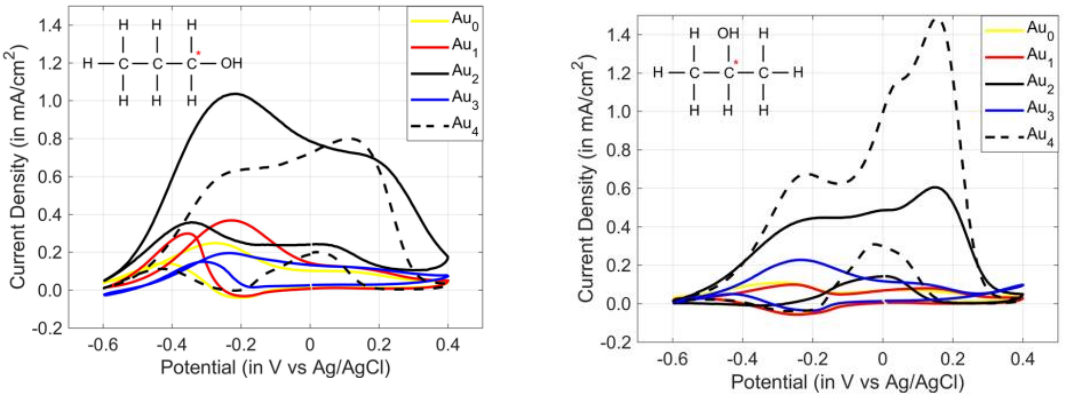

Figure 1.35: CV of a bulky amperometric sensor using Pt/PANI/Au_N (N is the number of atomic gold; N = 0, 1, 2, 3 and 4) for electrooxidation of 0.5 M propanol isomers in 1 M KOH: (a) 1-propanol; (b) 2-propanol. The scan rate was 100 mV/s. Reproduced from [58]

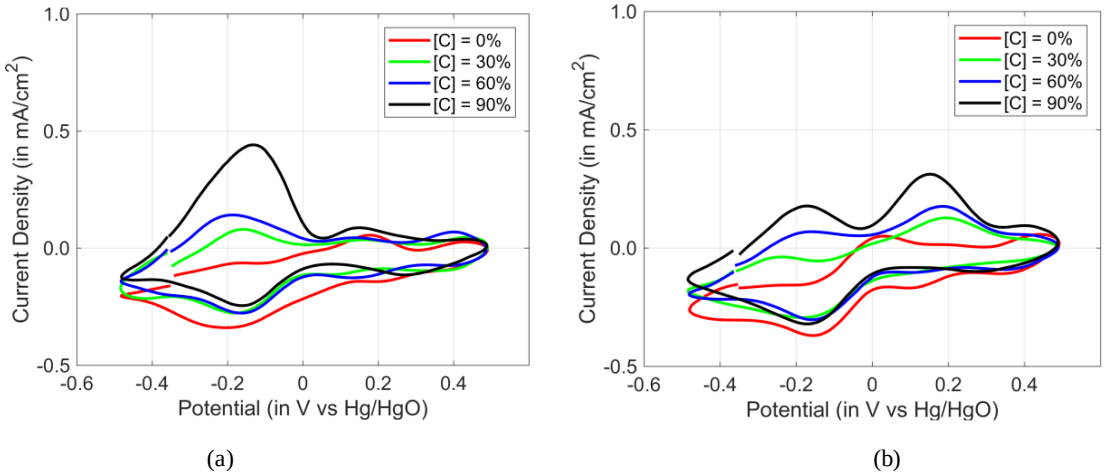

Figure 1.36: The sensor response of 0.5 M propanol isomers using Pt/PANI/Au_2 in 1 M KOH for different concentrations of: (a) n-propanol vapors; (b) iso-propanol vapors. [C] = the concentration percentage of full scale 1600 ppm. The scan rate was 100 mV/s. Reproduced from [58]

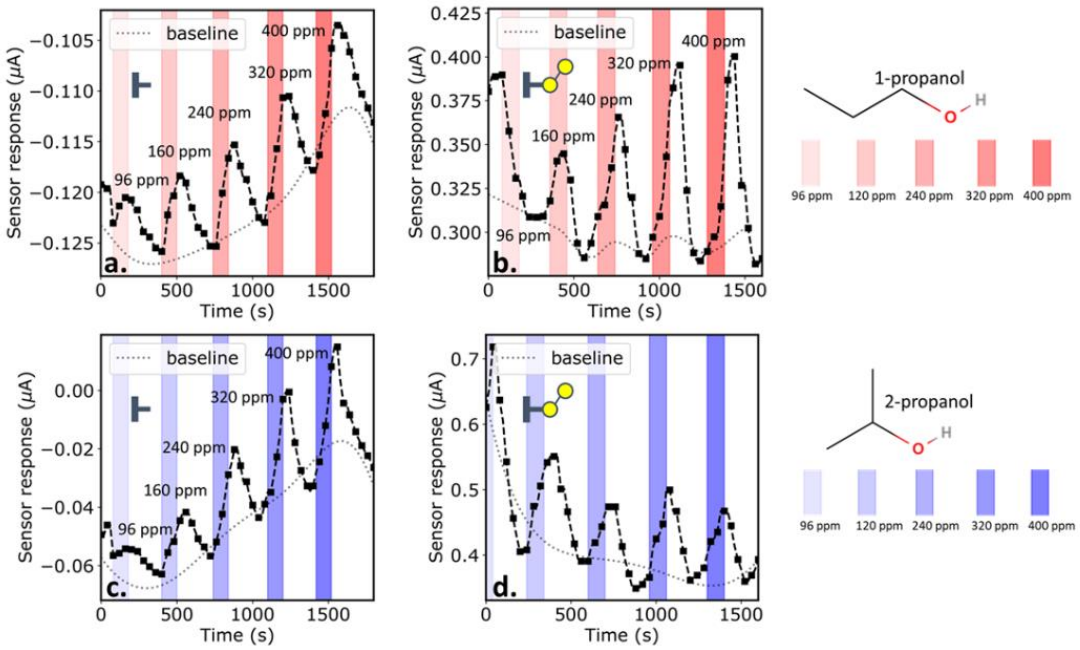

Figure 1.37: The comparison sensor response between Pt/PANI/Au_0 and Pt/PANI/Au_2 coated with 50 µL of [EMIM][Otf] at different relative concentrations (RC % = [0, 20, 40, 60, 80, 100], RC 100% = 400 ppm) of propanol isomers: (a) 1-propanol using Pt/PANI/Au_0; (b) 1-propanol using Pt/PANI/Au_2; (c) 2-propanol using Pt/PANI/Au_0; (d) 2-propanol using Pt/PANI/Au_2. The duration of each gas injection was 100 s. The applied fixed EC potential was +1.0 V against Ag/AgCl. Reproduced from [60]

1.3.5 AGS array

The 1980s witnessed the revolution of microcomputers encouraging the introduction of arrays of amperometric gas sensor (AGS) systems [6]. The AGS array can be made by applying simultaneously several sensing electrodes coupled with a pattern recognition algorithm to quantify and classify the gas mixtures. For example, the AGS array for a gas mixture of O_2, CO, NO_x, and SO_2 measurement employed the sensing electrode made of Nafion/Pt or Au or ceramic plate microelectrodes and backpropagation neural network (BPN) as the pattern-recognition algorithm. The limiting current potentials information for anodic oxidation of NO (on Au), SO_2 (on Pt), CO (on Pt), and cathodic reduction of NO_2 (on Au), O_2 (on Pt) were applied at the sensors array. The system was optimized using BPN algorithm to identify those gases with their concentrations in the mixture. The AGS array technology has been applied for chemical detection of gases which is also well known as electronic nose, and when used in liquid phase known as the electronic tongue [6].

A good selectivity, sensitivity, and stability obtained by the sensor coupled with a sophisticated pattern recognition algorithm are important to realize a reliable AGS array system to quantify and classify the chemical compound composing gas mixture at different loaded concentrations. In terms of selectivity and sensitivity, many works have been conducted to improve the AGS performance such as modifying the sensing electrode, applying several EC potentials, employing different electrolytes or coatings, etc. Since the AGS array requires many sensors, the miniaturizing sensor allows to realize embedding a large sensor in a single AGS array system. The contribution of sensors to discriminate the pattern separation of gases can be evaluated with statistical criterion for example using Wilk's lambda. Furthermore, the supervised learning algorithms can be used to optimize the classification process for example the support vector machine (SVM) optimizes the margin at the discrimination boundary by applying an appropriate kernel function [18].

1.3.6 Summary

In this section, the basic working principle and several related works of amperometric gas sensor (AGS) system have been reported. In the working principle of AGS, the basic redox reactions taking place at AGS system was given. Gas phase amperometric sensor or AGS is different with the liquid phase of amperometric sensor, in AGS, the observed current depends on many factors, the resultant mathematical expression can be very complicated, therefore, the limiting current is generally used to simplify the conditions. Furthermore, a brief summary regarding AGS with aqueous electrolyte, AGS with RTILs, AGS with various catalysts are summarized in Table 1.4.

Table 1.4. Brief summary related works using AGS

Sections	Benefits	Drawbacks	Ref
AGS with aqueous electrolyte	high conductivity, not sensitive to moisture, high stability	slow response (gas permeable membrane), narrow EC window, not operating at extreme temperature, hard to realize the miniaturized AGS, easy evaporate	[36–40]
AGS with RTILs	promising to support miniaturized AGS, a thin film can be made using RTIL, can operate at room temperature (and extreme also), long lifespan, wider EC window, low volatility, negligible vapor pressure, membrane-free gas sensing can be realized, the transport properties (conductivity, viscosity, diffusion coefficient) can be tuned	slow response due to high viscosity	[40–44]
AGS with catalysts			
• *Biological element as catalyst*	high selectivity	slow response and short lifetime	[46]
• *Metal oxide nanostructures*	the morphology and size of MO exhibit different catalytic activity, high surface-to-volume ratio can be achieved by making a porous structure at MO	the catalytic activity is still considered low therefore impurities like metal NPs or CLs are oftentimes added	[45,48–51,61]
• *Metal nanoparticles*	good nanocatalyst	require a host matrix since the coalescence of two or more NPs oftentimes occurs	[47,52]
• *Atomic metal catalysts*	remarkably catalytic activity with unique property due to quantum size e and geometric effect	require a proper host matrix to site the atomic metal	[53–56,58]

1.4 Analytes

To support the green energy and to fulfill the energy demand, biofuels have become the alternative renewable energy source [62,63]. Biofuels can be produced through biomass synthesis such as bio-ethanol, bio-diesel, bio-butanol, etc. Although, bio-ethanol and bio-diesel are frequently used for gasoline and diesel, however, bio-butanol is much preferable because it offers some added benefits when compared to bio-ethanol and bio-diesel, such as a higher energy content, releasing a lesser CO quantities upon the combustion, non-corrosive in nature, usability and ability to blend it in every concentrations with gasoline, etc [62,63]. Butanol has four isomers of which 1-butanol, 2-butanol, and iso-butanol are the most promising candidates for bio-butanol productions [62].

Isomers compounds have exactly same molecular formula and molar mass, therefore, gas measurement using isomers compounds are challenging. In this research the isomers compounds i.e., butanol isomers were selected as analytes. Butanol is a C4-alcohol, all the butanol isomers including 1-butanol, 2-butanol, and iso-butanol have same molar mass of 74.12 g/mol and chemical formula of $C_4H_{10}O$. Table 1.5 provides the detailed information regarding physical and chemical properties of 1-butanol, 2-butanol, and iso butanol. Furthermore, for the molecular structure for those three isomers compounds are depicted in Figure 1.38.

Table 1.5. Physical and chemical properties of 1-butanol, iso-butanol, and 2-butanol [64]

Properties	**1-butanol**	**Iso-butanol**	**2-butanol**
Odour threshold (mg/m^3)	3.078	4.6 (1.5 ppm)	7.69 (2.5 ppm)
Density (kg/m^3)	809 - 811	801 – 803	806 - 808
Boiling point (°C)	118	107.9	initial 98.5 (min) dry point 100.5 (max)
Freezing point (°C)	-89	-108	-115
Viscosity	2.96 mPa x s	3.98 cP	3.54 mPa x s
Vapor pressure (kPa)	0.56	1.17	1.66
Flash point (°C)	33	27.8	23
Other names	n-Butanol, n-Butyl alcohol, n-Butyl hydroxide, etc [65]	2-Methyl-1-propanol, 2-Methylpropyl alcohol, Isopropylcarbinol, etc [66]	sec-Butanol, sec-Butyl alcohol, 2-Butyl alcohol, etc [67]

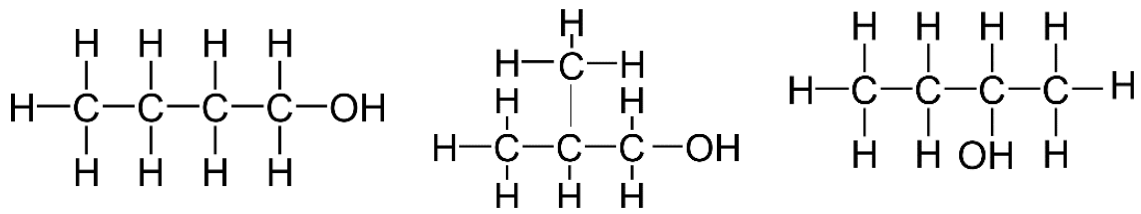

(a) (b) (c)

Figure 1.38: Molecular structure of butanol isomers: (a) 1-butanol; (b) iso-butanol; (c) 2-butanol

1.5 Research purpose

Gas sensors are extensively used in many fields such as in the semiconductor area, industry, HVAC system, pollutant/toxic/volatile gas monitoring, biomedical field, defense, security, etc. Various gas sensor types exist in the market like electrochemical (EC) sensors, semiconductor sensors, photo-ionization (PID) sensors, infrared (IR) sensors, biosensors, quartz crystal microbalance (QCM) sensors, etc. Every sensor has different gas sensing mechanism and offers particular benefits, although many works have been conducted to improve the performance of each gas sensor type, removing the drawbacks completely is impossible.

Important points to realize an odor sensing system are sensitivity, selectivity, and stability. Although semiconductor gas sensor has high sensitivity, its selectivity is not sufficient. Although QCM's selectivity is better than semiconductor, it is still insufficient. Moreover, it is susceptible to humidity interference. On the other hand, biosensor has high sensitivity but its stability is typically poor. Moreover, too high selectivity sometimes makes the range of the detectable gas narrower. EC sensor has higher selectivity than semiconductor or QCM but has lower selectivity than biosensor. Its selectivity is appropriate for detecting many gases with relatively high selectivity. The PID sensor has high sensitivity but does not have selectivity. In addition, a high humidity affected by moisture can reduce PID response. The IR sensor has good selectivity. However, it only interacts with molecular dipoles, thus the gasses having symmetry molecules are not excited by IR.

As shown in Figure 1.39, our research focuses on the EC sensor. Generally, there are three types of EC sensors i.e., potentiometric, conductometric, and amperometric. The potentiometric type offers cost-effective and easy to be operated but the equilibrium state must be achieved to obtain an accurate signal which is time-consuming. The conductometric type offers a simple fabrication and operation but ions with similar conductivity would yield the same sensor response. The amperometric gas sensor (AGS), is one of the popular EC sensors due to offering a high electroanalytical sensor response in a modest cost. Its signal interpretation is well-understood and its sensitivity and selectivity can be varied in many ways such as selecting a proper electrolyte, modifying the sensing electrode, adding impurities at the electrode, etc.

A miniaturized AGS is a promising technology development because it has numerous advantages in terms of power consumption, portability, chip integration, response time, etc. However, conventional aqueous electrolytes commonly used in a bulky AGS cannot be used in a miniaturized AGS due to the evaporation and fluidity issues. In this research, we developed a miniaturized AGS system with room temperature ionic liquids (RTILs) to replace the conventional aqueous electrolyte. The possibility of using RTILs in miniaturized AGS was complemented by another sensor information i.e., QCM coated with the same RTILs to check the solubility of analytes during gas measurement.

Further improvement in our miniaturized AGS system is by modifying its working electrode with catalytic material to enhance the electrocatalytic activity. As shown in Figure 1.39, there are several catalytic materials can be applied such as using biological element, using MO nanostructure, using metal NPs, and using atomic metal. The biological element has short lifetime, the MO nanostructure is still considered to have a low catalytic activity thus metal NPs are frequently added to boost its catalytic activity reactions. When, size of metal NPs is reduced into atomic level, then a remarkably catalytic activity properties is obtained due to a larger active area for catalytic reactions. Therefore, in this research, the atomic gold is selected as catalytic material which doped at our modified working electrode to enhance the sensitivity of the miniaturized AGS system. There has been so far no report of AGS with atomic metal in RTIL film from other research group although AGS with RTIL has been reported.

In our prior works, the atomic gold was used as a catalyst. In a bulky system, the atomic gold clusters (Au_N where N = 1 to 4) were verified through the electrooxidation of propanol isomers. Then, the atomic gold clusters with N = 2 was used to modified the working electrode for a bulky AGS system. Afterward, a miniaturized AGS sensor decorating Au_2 clusters with RTIL was reported the first time by our research group. However, only one RTIL with one fixed EC potential was used. In addition, the target compound was also limited to a lower carbon chain, i.e., propanol isomers with molecular formula of $C_3H_8O_{10}$. Typically, a lower carbon chain provides a higher sensor response than a higher carbon chain.

In this research, the gas measurement using atomic gold doped at a miniaturized AGS system and RTIL films were applied to a higher carbon chain, i.e., gaseous butanol isomers ($C_4H_{10}O$). Several RTILs with different cation-anion combinations were investigated. Furthermore, several fixed EC potentials of each RTIL were explored. In addition, the discrimination capability among butanol isomers was obtained with AGS array by selecting RTIL films and fixed electrochemical potentials at a miniaturized AGS system. The scheme of our research strategy is available in Figure 1.39.

Research strategy

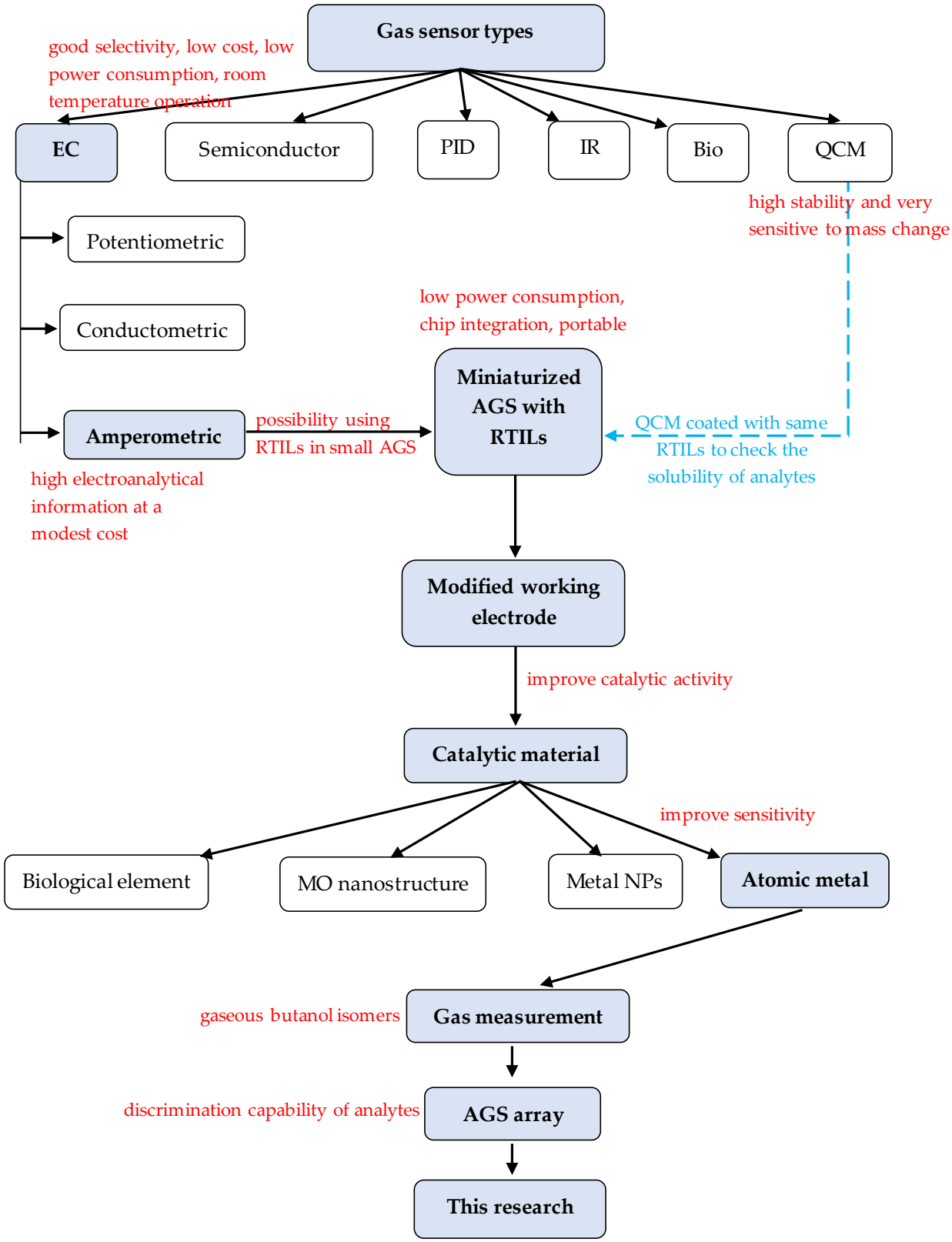

Figure 1.39: The research strategy

1.6 Thesis structure

The scheme of thesis structure in this research is depicted in Figure 1.40 consisting of seven chapters.

Chapter 1 introduces a brief overview of the gas sensor market including the technology, sensor type, key market players, and region scope. Several gas sensor types are also explained as well as the basic working principle, the applications in gas measurement systems, and the benefits and drawbacks. Afterward, the amperometric gas sensor (AGS) is explained in more detail like AGS with aqueous electrolyte, AGS with RTILs, and AGS with catalysts including metal NPs and atomic metal. In addition, the analytes information used in this research is also given. Lastly, the research purpose, research strategy, and thesis structure are also presented in this chapter.

Chapter 2 provides information related to the sensing materials i.e., RTIL and catalytic materials. In this chapter basic structure of RTIL as well as the physical and chemical properties owned by RTILs are explained. In addition, the catalytic materials related to the atomic gold and its host matrix are provided.

Chapter 3 focuses on the methods used in this research which include the experimental setup for depositing sensing films, the gas delivery system, the potentiostat, and the discriminant analysis to assess the separation among analytes numerically.

Chapter 4 gives information regarding sensors using RTIL to develop a miniaturized AGS. In this chapter, several information is provided like the gas measurement system, the RTILs as sensing films coated on miniaturized AGS sensor and QCM sensor, and analyzing their sensor response, furthermore, the sensing element selection and evaluation of gas discrimination capability is also given.

Chapter 5 presents the atomic gold decorating miniaturized AGS with selected RTILs. This chapter gives information related to the PANI polymerization results on miniaturized AGS, the atomic gold deposition results on miniaturized AGS, and the sensor response using modified miniaturized AGS and selected RTILs for gas measurement. In addition, the evaluation of isomers discrimination is also analyzed.

Chapter 6 concludes this research with its key findings.

Chapter 7 provides a glance of the future research to improve the current developed miniaturized AGS system.

Thesis structure

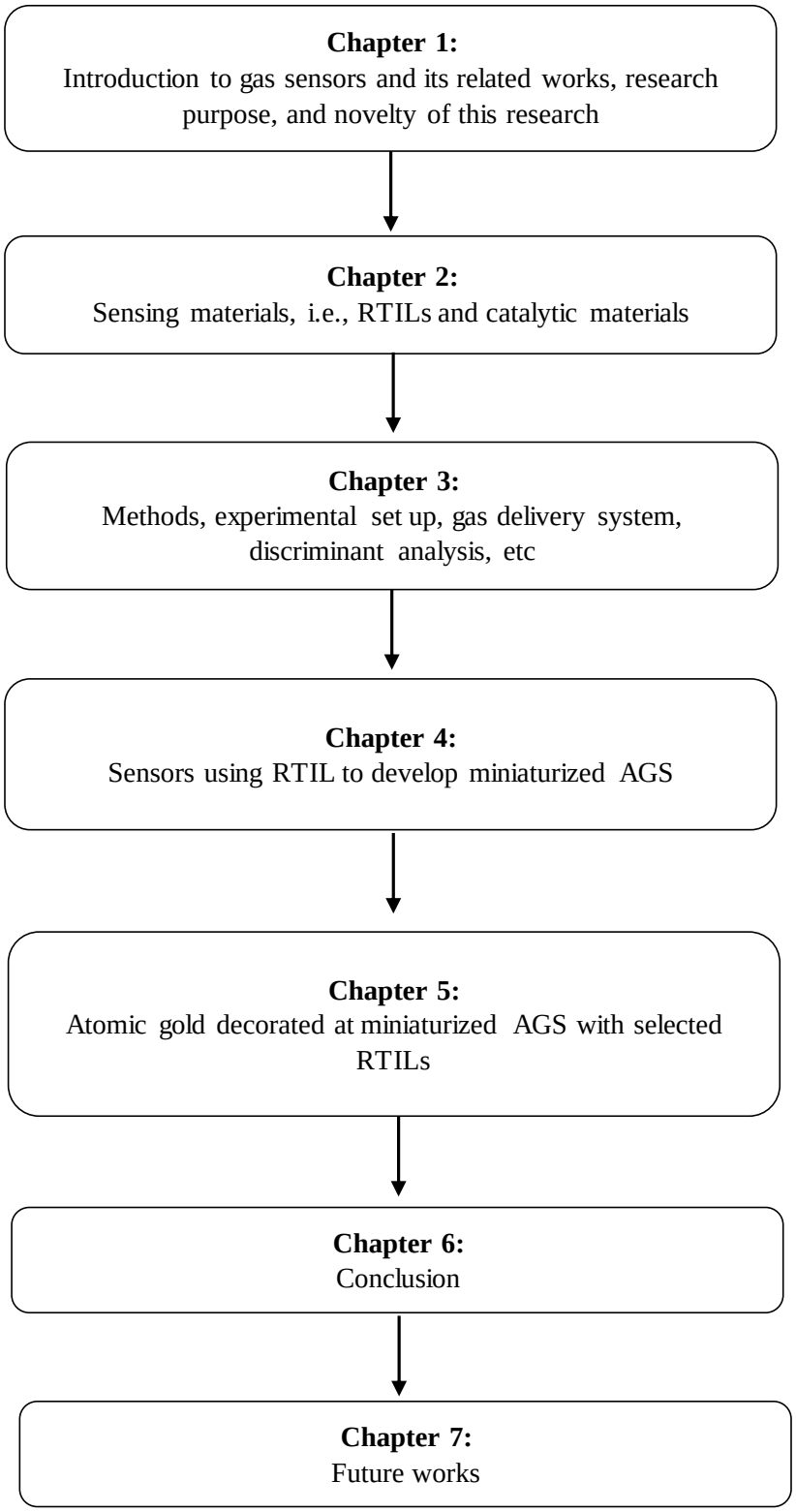

Figure 1.40: The structure of thesis

Chapter 2

Sensing materials

In our research work, the sensor fabrication used a miniaturized amperometric gas sensor (AGS). The applied electrolyte was room temperature ionic liquid (RTILs) to replace the volatile electrolyte. To enhance the sensitivity, the modification of the working electrode at miniaturized AGS was conducted with atomic gold to improve the catalytic properties. In this section, RTILs and catalytic materials are discussed in more detail.

2.1 Room temperature ionic liquids (RTILs)

Ionic liquids are salts that are fluid over a wide temperature range that has been used in many applications, e.g., electrolyte, coating, sensors, enzymatic reaction, drug delivery, gas chromatography materials, solvents, etc [68,69]. The term ionic liquid was introduced in 1914 by Paul Walden who reported the properties of ethyl ammonium nitrate ($[EtNH_3][NO_3]$; the melting point at 12-14 ^oC) [68,70]. Ionic liquids can participate in various attractive interactions such as nonspecific interaction, weak interaction, isotropic interaction (e.g., van der Waals, dispersion, solvophobic forces), strong interaction like Coulombic, specific interaction, and anisotropic interaction (e.g., halogen bonding, dipole-dipole, hydrogen bonding, magnetic dipole, electron pair donor/acceptor interaction) [71]. Room temperature ionic liquids (RTILs) are the vast class of ionic liquids which exist in the liquid state less than 100 ^oC (298 K) [68,70,71]. The basic structure and physicochemical properties of RTILs are explained in the following section.

2.1.1 RTIL structure

RTIL consists of the combination of cation (positively charged) and anion (negatively charged) [68,70]. Typically, RTIL is formed of asymmetric organic cation and organic or inorganic anion [70]. The asymmetry of the cation is preferred because it contributes to lower the melting point. As reported by MacFarlane at al., salts derived from pyrrolidinium and ammonium cations had a "solid" structure at room temperature using a high symmetrical species, whereas, a low symmetry (or asymmetry) formed a "liquid" structure at room temperature [42,68]. Furthermore, the molecular structure of cation and anion commonly used in RTIL is depicted in Figure 2.1.

Cation (positively charged)

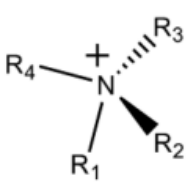

ammonium

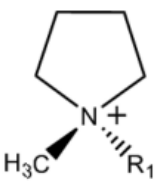

pyrrolidinium

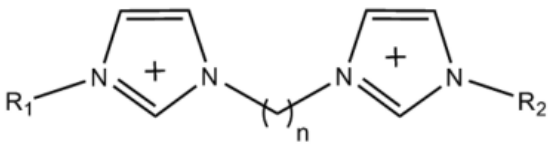

1,3-bis[3-methylimidazolium-1-yl]alkane

phosphonium

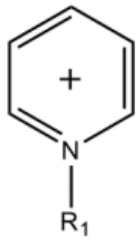

pyridinium

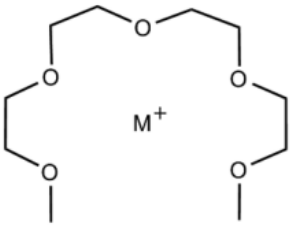

metal (M^+) tetraglyme

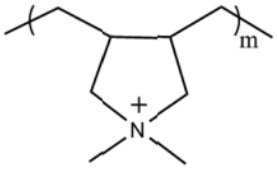

poly(diallyldimethylammonium)

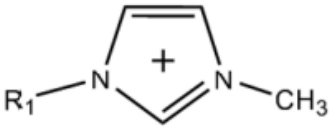

1-methyl-3-alkylimidazolium

Anion (negatively charged)

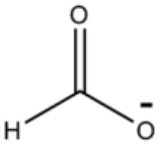

halides

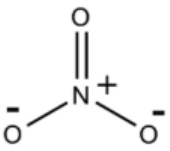

formate

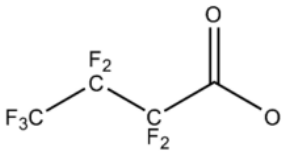

hydrogen sulfate

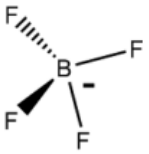

tetrafluoroborate

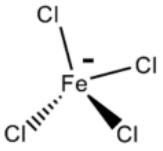

Tetrachloroferrate

tris(pentafluoroethyl)trifluorophosphate

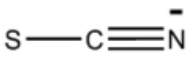

thiocyanate

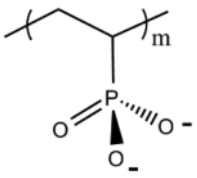

poly(phosphonic acid)

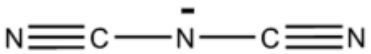

dicyanamide

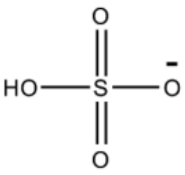

nitrate

hexafluorophosphate

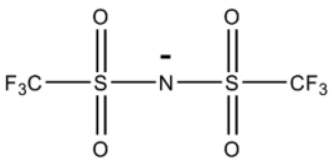

bis(trifluoromethylsulfonyl)imide

Figure 2.1: The chemical structure of cation and anion commonly used in RTIL. Reprinted with permission from [71]. Copyright (2015) American Chemical Society

According to the chemical structure, there are the two most common RTIL types, i.e., protic and aprotic. The protic RTIL is formed via proton transfer from a Brønsted acid and a Brønsted base combination, the H-bond donor and acceptor sites are created in the ions because of proton transfer, it is cost-effective and simple to be made [71,72]. On the other hand, in the aprotic RTIL, the ion formation is formed by the covalent bond formation between two functional group through multistep reactions. The aprotic RTIL is more electrochemically and thermally stable than protic RTIL. Figure 2.2 depicts the example of protic and aprotic chemical structures, for the protic RTILs are 1-ethylimidazolium acetate ([EIM][Ac]) and 1-ethylimidazolium chloride ([EIM][Cl]). Whereas, 1-ethyl-3-methylimidazolium acetate ([EMIM][Ac]) and 1-ethyl-3-methylimidazolium chloride ([EMIM][Cl]) are the example of aprotic RTIL.

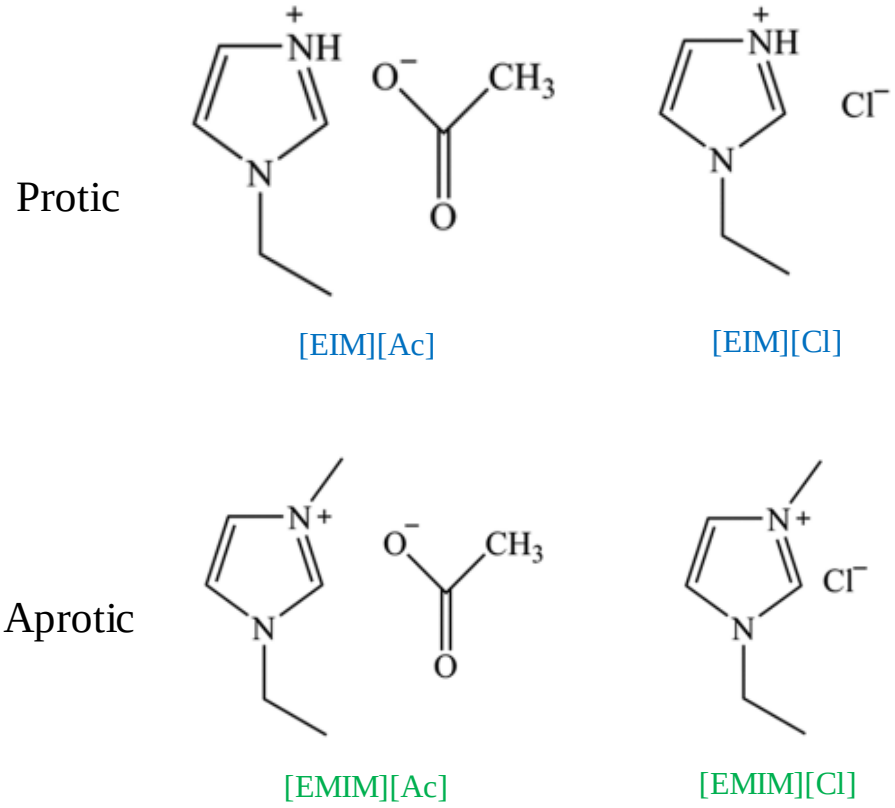

Figure 2.2: The example of protic and aprotic chemical structures. Reprinted with permission from [72]. Copyright (2019) American Chemical Society

2.1.2 Basic property of RTIL

The physical and chemical properties of RTIL are varied depending on the pair of cation and anion combination. Table 2.1 shows the various physical property of melting points influenced by applying different organic and inorganic anions with same organic cation of 1-ethyl-3-methylimidazolium ($[EMIM]^+$). As shown in Table 2.1, although the same $[EMIM]^+$ cation is used, the melting points are varied. The melting point is affected by the type of anions to form an RTIL, i.e., inorganic anions such as chloride $[Cl]^-$, nitrogen dioxide ($[NO_2]^-$), nitrate ($[NO_3]^-$), tetrachloroaluminate ($[AlCl_4]^-$), tetrafluoroborate ($[BF_4]^-$), and organic anions such as trifluoromethanesulfonate ($[CF_3SO_3]^-$), trifluoroacetate($[CF_3CO_2]^-$).

Table 2.1. The $[EMIM]^+$ cation with different anions [69]

Cation-anion pair	Melting point (°C)
[EMIM][Cl]	87
[EMIM][NO_2]	55
[EMIM][NO_3]	38
[EMIM][$AlCl_4$]	7
[EMIM][BF_4]	15
[EMIM][CF_3SO_3]	-9
[EMIM][CF_3CO_2]	-14

The hydrophilic and hydrophobic of RTIL are also varied following the cation-anion combination. Basically, the anions become a major factor that contribute to the water absorption level. Although, cation plays a minor role in hydrophobic-hydrophilic property, typically, the shorter the alkyl chain shows the greater the water absorption. The water absorption of 1-ethyl-3-methylimidazolium ($[EMIM]^+$) is greater than 1-butyl-3-methylimidazolium ($[BMIM]^+$) followed by 1-hexyl-3-methylimidazolium ($[HMIM]^+$) ≅ 1-octyl-3-methylimidazolium ($[OMIM]^+$). Figure 2.3 depicts the hydrophilic and hydrophobic properties from cations and anions [68,69]. Some others RTILs' properties like electrochemical window, conductivity, viscosity, volatility, and thermal stability are explained more detail in the next section.

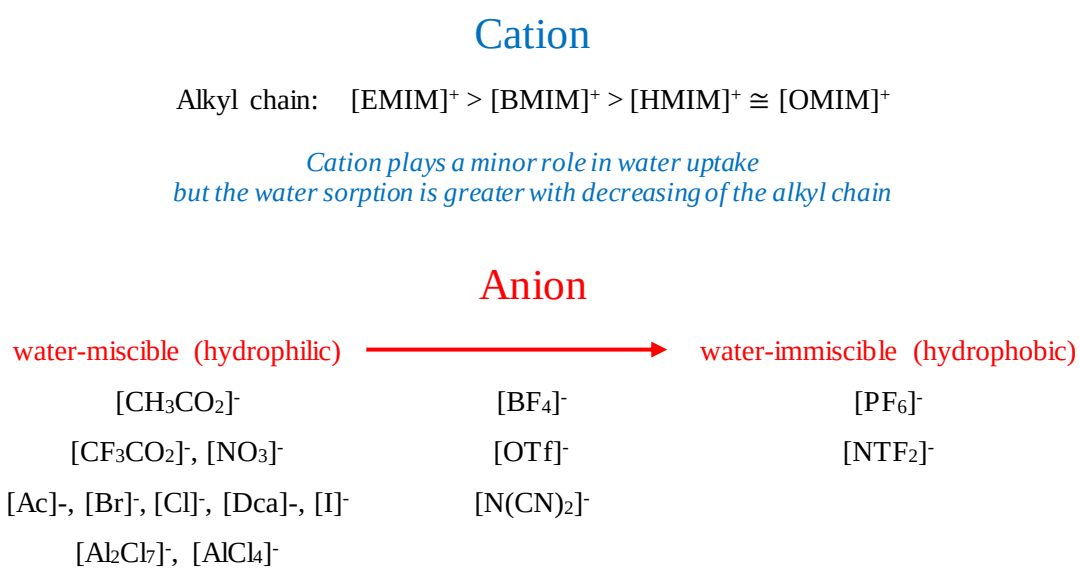

Figure 2.3: The sequence of cation and anion in hydrophilic and hydrophobic properties

A. Electrochemical window

Electrochemical window (ECW) is important criteria to assess the EC properties in electrolyte system. A wider ECW allows a greater analyte to be detected. As determined in Equation 2.1, ECW is defined as the difference between anodic limit potential (V_{AL}) and the cathodic limit potential (V_{CL}) which can be estimated by difference between the highest occupied molecular orbital (HOMO) energy (ε_{HOMO}) and the lowest unoccupied molecular orbital (LUMO) energy (ε_{LUMO}). The value of ECW depends on the cations and anions to determine the V_{AL} and V_{CL} [73,74].

$$\mathrm{ECW} = V_{\mathrm{AL}} - V_{\mathrm{CL}} \tag{2.1}$$

In the experiment, frequently, the length of ECW is altered due to several factors such as materials of the electrodes, water absorption, and temperature. Zhao et.al., studied the dependence of ECW and electrode materials in eighteen protic RTILs. Several working electrodes were applied, i.e., gold (Au), platinum (Pt), boron doped diamond, and glassy carbon (GC) [75]. According to the results, different materials of working electrode (WE) produced different ECW. Figure 2.4 depicts the different ECW from protic diethylamine formic ([DEA][Of]) at 20 °C using Ag wire as the reference electrode with different working electrode materials. According to Figure 2.4, the widest ECW was obtained by GC electrodes, after that boron-doped diamond, then Pt, and the final one was Au. The variation of these ECWs imply that the association of cations and anions along with the electrode materials plays an important role to contribute to the electrochemical stabilities.

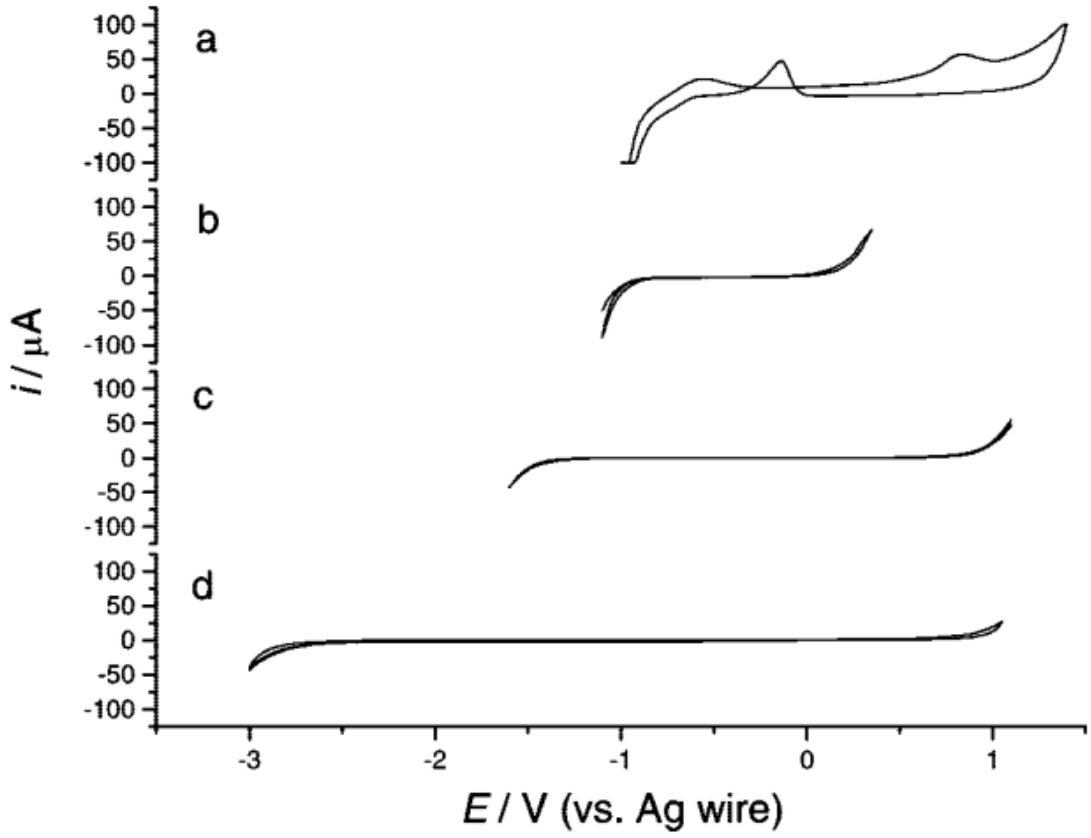

Figure 2.4: Voltammetry potential window for [DEA][Of] using different WE: (a) Pt; (b) Au; (c) boron-doped diamond; and (d) glassy carbon electrodes. Scan rate was 100 mV/s at T = 20 °C. Reprinted with permission from [75]. Copyright (2008) American Chemical Society

Water is considered to be one of the most significant impurities in RTILs and even hydrophobic RTILs can also absorb the water from atmosphere or at certain temperatures [68,76]. A large amount of water absorbed by RTILs leads to the narrow ECW at both cathodic and anodic limits. O'Mahony et.al., studied the effect of water against the ECW at different temperatures using twelve RTILs. Three different

procedures of the measurements were conducted i.e., vacuum-dried, atmospheric, and wet measurements. For the vacuum-dried measurement, the samples of RTILs were purged under a vacuum for 24 hours and stirred at 333 K. For the atmospheric measurement, RTILs as samples were directly used for measurement without any purification or drying. Furthermore, for the wet measurements, the samples were prepared as follows: 1 mL of RTIL and 1 mL of deionized water were mixed through rigorously shaken, then allowed to stand for approximately 24 hours, the wet measurements included three different temperatures, i.e., 298 K, 318 K, and 338 K. Figure 2.5 shows the representative results for the effect of water against the ECW at different temperatures for [EMIM][NTf_2]. As shown in Figure 2.5, the cathodic limits were narrowed by the presence of water content in [EMIM][NTf_2] through the atmosphere and wet conditions, the purged (without adding water content) had the most negative cathodic limit and the widest ECW among others, whereas, the wet conditions at 338 K had the narrowest ECW [76].

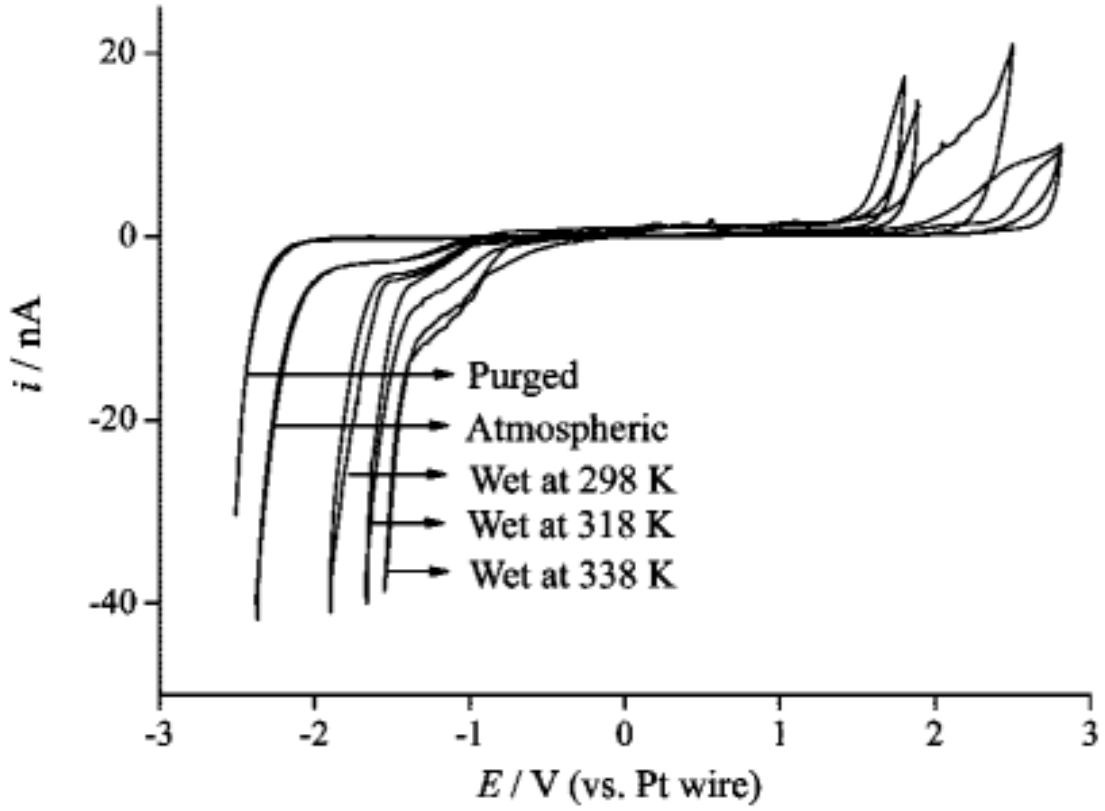

Figure 2.5: ECW from [EMIM][NTf_2] at several conditions, i.e., vacuum-dried (purged), atmospheric, and wet conditions. CV was carried out on 10 µm Pt electrode vs Pt wire (0.3 mm). Scan rate was 100 mV/s. Reprinted with permission from [76]. Copyright (2008) American Chemical Society

Furthermore, the effect of water uptake against the ECW for twelve RTILs in different conditions (vacuum-dried, atmospheric, and wet) are summarized in Table 2.2. As shown in Table 2.2, mostly, the presence of water in RTILs lowered the length of ECW particularly in high temperature. According to O'Mahony et.al., the anions had a large contribution for water uptake and the hydrophobicity adhered to the following trend: $[FAP]^-$ > $[NTf_2]^-$ > $[PF_6]^-$ > $[BF_4]^-$ > halides. As for cations, a long carbon chains enhance the repulsion of water uptake in RTILs due to a reduced polarity [76].

Table 2.2. The effect of water absorption on the ECW for 12 RTILs.

Modified with permission from [76]. Copyright (2008) American Chemical Society

RTIL	ECW (V)				
	Vacuum-dried	Atmospheric	Wet at 298 K	Wet at 318 K	Wet at 338 K
[EMIM][NTf_2]	4.2	2.8	2.6	1.4	0.7
[BMIM][OTf]	4.2	3.3	2.7	1.5	1.3
[BMIM][BF_4]	4.6	2.4	2	2.4	2.3
[BMIM][PF_6]	4.8	3.9	2.6	1.7	1.7
[$P_{14,6,6,6}$][NTf_2]	5.2	3.2	1.8	1.6	0.8
[C_4mpyrr][NTf_2]	4.2	3.0	2.0	2.0	1.2
[HMIM][FAP]	4.6	3.0	2.5	2.4	1.6
[BMIM][NTf_2]	4.3	2.9	2.8	2.4	1.4
[C_4dmim][NTf_2]	4.7	3.3	2.9	2.4	1.4
[$N_{6,2,2,2}$][NTf_2]	4.7	2.3	2.2	1.9	1.7
[BMIM][I]	2.0	1.9	1.6	0.0	0.0
[HMIM][Cl]	3.0	2.9	2.4	2.4	1.4

Vacuum-dried: dried under vacuum for 90 min. Atmospheric: used directly without any attempt at drying or purification. Wet: in a water-sat. atmosphere at temperatures (298, 318, and 338) K.

B. Viscosity and conductivity

Viscosity is important EC property since high viscosities slow down the rate of diffusion-controlled EC reactions and limit some applications [76]. However, RTIL film with high viscosity can be kept on the substrate. The RTIL has higher viscosity compared to aqueous and organic electrolyte, its high viscosity nature is affected by cations and anions. In the imidazolium cation, longer alkyl chain possesses more viscous RTIL. As shown in Table 2.3, [BIMIM][NTf_2] has viscosity of 52 cP, it is more viscous than [EMIM][NTf_2] with the viscosity of 34 cP. Furthermore, the anions also contribute to the RTIL viscosity, for example, $[PF_6]^-$ and $[BF_4]^-$ are much more viscous due to strong HF interactions compared to $[NTf_2]^-$. In addition, the size, shape, and molar mass of the anions affect different viscosity, for example, lighter, smaller, and more symmetric anions result more viscous RTIL. As summarized in Table 2.3, when the same imidazolium cation $[BMIM]^+$ paired with different anions, i.e, $[PF_6]^-$ and $[BF_4]^-$, $[NTf_2]^-$, the viscosities were varied due to the presence of the anions. Based on the Table 2.3, [BIMIM][NTf_2] has the lowest viscosity among [BIMIM][PF_6] and [BIMIM][BF_4].

Table 2.3. Properties of RTILs

Modified with permission from [76]. Copyright (2008) American Chemical Society

RTILs	T = 293 K	
	Viscosity, η (cP)	conductivity, κ (mS/cm)
[EMIM][NTf_2]	34	8.8
[BMIM][NTf_2]	52	3.9
[BMIM][BF_4]	112	1.7
[BMIM][PF_6]	371	1.5

1 cP = 1 mPa·s

The viscosity of RTIL strongly depends on temperature. The Arrhenius equation is often used calculate the relationship between viscosities and temperatures of RTILs but some functional group of RTILs fit better to the Vogel-Tammann-Fulcher (VTF) relationship as determined in Equation 2.2, where η is the viscosity (mPa.s), T is temperature (K), η_0 (mPa.s), X (K), and T_0 (K) are the adjustable parameters for VTF equation. The η_0 is a pre-exponential factor, and T_0 is the ideal glass transition temperature [77–79].

$$\eta(T) = \eta_0 \, exp^{\left[\frac{X}{T-T_0}\right]} \tag{2.2}$$

Conductivity is a vital property for electrolyte. RTIL has intrinsic conductivity since it is purely composed of ions, i.e., cations and anions. The intrinsic conductivity of pure RTIL depends on the ion mobility influenced by ion association, ion size, viscosity, and density [73,76]. In fact, the conductivity change can be attributed almost directly to the viscosity change [76]. As summarized in Table 2.3, [EMIM][NTf_2] has conductivity of 8.8 mS/cm, then a longer cation chain of butyl in RTIL of [BIMIM][NTf_2] dropped the conductivity into 3.9 mS/cm, it has been predicted that the conductivity is reciprocal of the viscosity oriented to the generalized Walden rule [77–79]. Figure 2.6 shows the various conductivities for the imidazolium cation-based RTILs at different alkyl chain length i.e., ethyl (EMIM), butyl (BMIM), hexyl (HMIM), and octyl (OMIM). As observed in Figure 2.6, the conductivities are getting reduced by the increase of the alkyl chain because the longer aliphatic chain has a higher viscosity. The high viscosity reduced the ion mobility thus decreasing the conductivity [73].

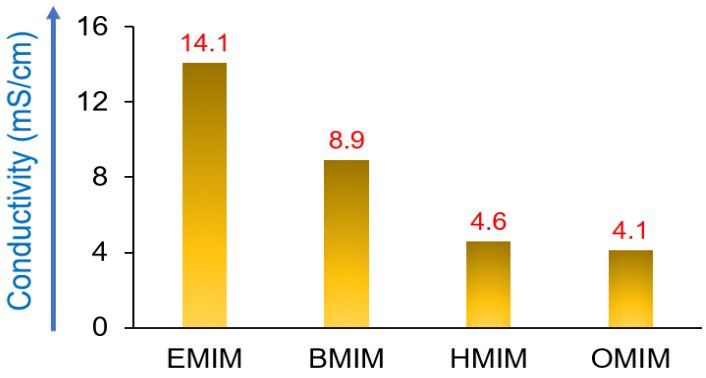

Figure 2.6: The variation of conductivity from several alkyl chain length using imidazolium cation-based RTILs. Reproduced from [73] with permission from the Royal Society of Chemistry

The Walden plot is extensively applied to illustrate the conductivity-viscosity relationship of pure ionic liquids [80]. However, over a wide range of temperatures, the Walden plot oftentimes exhibits deviation, particularly, at increased temperatures, the rapid ion mobility due to dropped viscosity results to elevate the conductivity. Therefore, the variation of ionic liquid conductivity against the temperatures is corrected by the Vogel-Tammann-Fulcher (VTF) relationship with the empirical Equation 2.3 [76,80,81], where κ is conductivity (mS/cm), T is the temperature (K), A, B, and T_0 (K) are empirically adjustable paramaters to fit VTF equation to experimental data.

$$\kappa(T) = \frac{A}{\sqrt{T}} exp^{[-B(T-T_0)]} \quad (2.3)$$

C. Low volatility and high thermal stability

Another advantage intrinsic property of RTIL is low volatility which can be determined by its vapor pressure. Compared to aqueous or organic electrolyte, RTILs have a high vapor pressure due to possessing a strong inter-molecular (ionic) forces. At 293 K, the vapor pressure of water is calculated at 3167.73 Pa, whereas, RTILs only a few mPa [40]. In addition, RTIL can also operate under extreme temperatures without undergoing evaporation. For example, Debbie et.al., used X-ray photoelectron spectroscopy (XPS) to determine the amount of bromide ions in RTIL of 1-butyl-1-methylpyrrolidinium bis(trifluoromethyl-sulfonyl)imide ([C_4mpyrr][NTf_2]) [82]. XPS is generally not applicable for liquids since it applies ultra-high vacuum (UHV) where the aqueous or organic electrolytes can evaporate [40]. In addition, currently, XPS is widely used to characterize RTIL [40].

In 2020, Debora et.al., the atomic mechanisms of gold nanoparticles growth (the gold precursor was sodium tetrachloroaurate (III) dihydrate ($NaAuCl_4 \cdot 2H_2O$)) was recorded in the freestanding thin film of RTIL, i.e., tetrabutylammonium chloride ([Bu_4N][Cl]) using scanning transmission electron microscopy (S-TEM) [83]. The major issue reported using conventional liquid-cell S-TEM is that the electron beam used for irradiation cannot be applied over a long time due to evaporation issues of the liquid, in addition, a thick liquid film along with encapsulation is required to obtain a long measurement process but it limits the achievable spatial resolution, hence, to visualize the motion of an atomic level during particle growth processes is impossible to be achieved. The [Bu_4N][Cl] is very resistant to heat-beam during irradiation compared to aqueous solutions and other imidazolium-based ionic liquids. Therefore, it can survive over long time periods during the measurement. In addition, a thin film of [Bu_4N][Cl] was used to improve the resolution and did not lead to any visible degradation when the beam irradiated the sample although different temperatures were applied as shown in Figure 2.7 and Figure 2.8. Figure 2.7 shows the NPs growth process using measurements conducted at the temperature of 100 °C. Figures 2.8.a and b depict the coalescence process at room temperature and 40 °C, respectively. As shown in Figures 2.8.a and b, many small particles were captured and the motion of individual atoms during particle growth processes could be recorded during the coalescence process. According to these results, applying a thin film of [Bu_4N][Cl] not only enhanced the resolution of S-TEM but also had good thermal stability without undergoing evaporation.

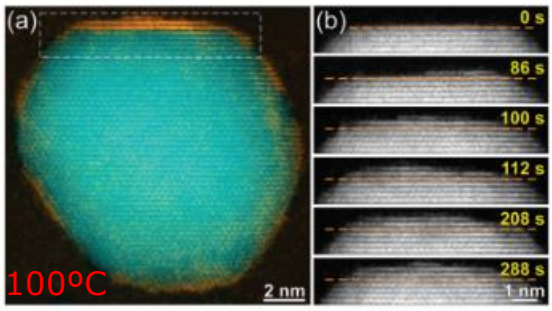

Figure 2.7: NPs growth by monomer attachment: (a) initial particle shape at the beginning (blue), 300 s later (orange); (b) five snapshots captured during the NPs growth. Reproduced from [83] with permission from the Royal Society of Chemistry

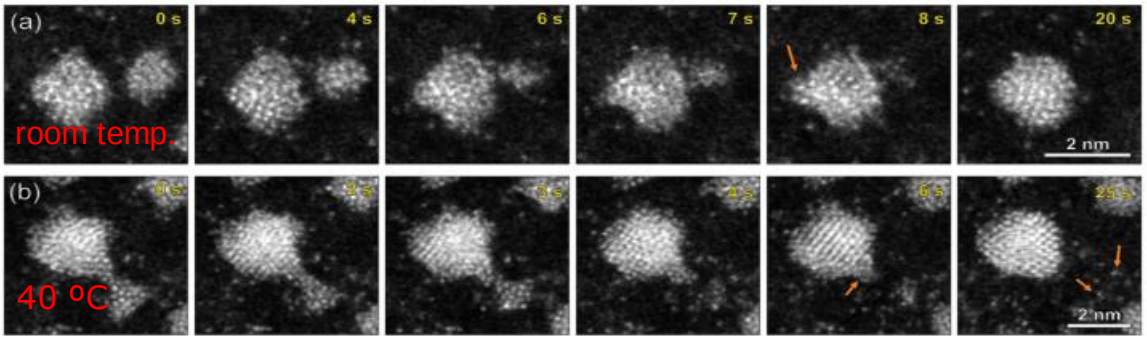

Figure 2.8: The coalescence process: (a) measurement conducted at room temperature; (b) measurement conducted at 40 °C. Reproduced from [83] with permission from the Royal Society of Chemistry

2.1.3 Summary

The basic structure and basic properties of RTIL has been explained. Different cation-anion to form RTIL has different physical and chemical properties such as the melting point, the electrochemical window, the conductivity, the viscosity, the thermal stability and volatility. The melting point plays an important role in electrolyte selection, because RTIL must exist in liquid form during the EC measurement. According to the literature review, although small amount of RTIL was used under extreme temperature, there was no significant degradation of RTIL during the measurement meaning that it performed well without undergoing evaporation and had good thermal stability. In addition, RTIL has a wider EC window than aqueous and nonaqueous electrolyte which allows many gases to be detected since the redox reaction of some gases exist in a high or a low EC potential.

In this research, RTIL was used to subtitute the volatile electrolyte in a miniaturized AGS. In the first stage, in Chapter 4, we check the possibility of using RTIL with different cation-anion in a miniaturized AGS including a higher carbon chain of cation like $[HMIM]^+$. Although diffusion transport is low using a higher carbon chain of cation but it has a higher viscosity which is beneficial to keep its shape. In the experiment, we used potentiostat with the operating voltages from -1 V to +1 V. Therefore, RTILs with ECW more than 2 V were chosen. Furthermore, in the second stage, the selected RTIL oriented to the information obtained from Chapter 4 were explored such as the RTIL having same cation but different anions.

2.2 Catalytic materials

Noble metals like gold (Au), silver (Ag), palladium (Pd), platinum (Pt), ruthenium (Ru), rhodium (Rh), and their bimetal nanocomposites, are frequently used as catalytic materials due to offering a high catalytic activity and chemical inertness. It has been known that the size of the noble metal affects the catalytic activity. The reduction of metal size at the atomic level exhibits remarkably catalytic activity due to a large active area and shows interesting properties due to the quantum and geometrical effect possessed by atoms. In our research work, the noble metal of gold was used as the atomic catalyst. Therefore, this section focuses on atomic gold metal. The basic theory of atomic gold clusters, the fabrication step, the timing diagram, and the experimental results are explained in this section. Furthermore, like nanocatalysts, before depositing the atomic gold catalyst, the host

matrix must be prepared first. The conducting polymer of polyaniline was used as the host matrix for the atomic gold catalyst and is explained in this section first.

2.2.1 Polyaniline

Polyaniline (PANI) is an organic polymer polymerized from an aniline monomer. It is one of the oldest conducting polymers discovered in the mid-19th century. PANI has been extensively applied in various industrial and biomedical fields due to simple fabrication, low cost, biocompatibility, low toxicity, etc [84–87]. PANI exhibits various nanostructures or morphologies such as nanorods, nanoflower, nanogranules, nanospheres, etc, which have different properties and surface-to-volume ratios. Procedure of synthesis condition such as pH, temperature, dopant, solvent, nanocomposite material, chemical oxidation process, the applied EC potential during the polymerization process etc, can affect PANI morphology [69,84]. Figure 2.9 depicts the scanning electron microscopy (SEM) image of different shape of PANI nanostructures oriented to their synthesis conditions. As shown in Figure 2.9, different synthesis procedures applied results in different morphology of PANI such as nanosphere (Figure 2.9.a), nanoflowers (Figure 2.9.b), nanogranules (Figure 2.9.c), nanofibers (Figure 2.9.d), nanotubes (Figure 2.9.e), and nanorods (Figure 2.9.f).

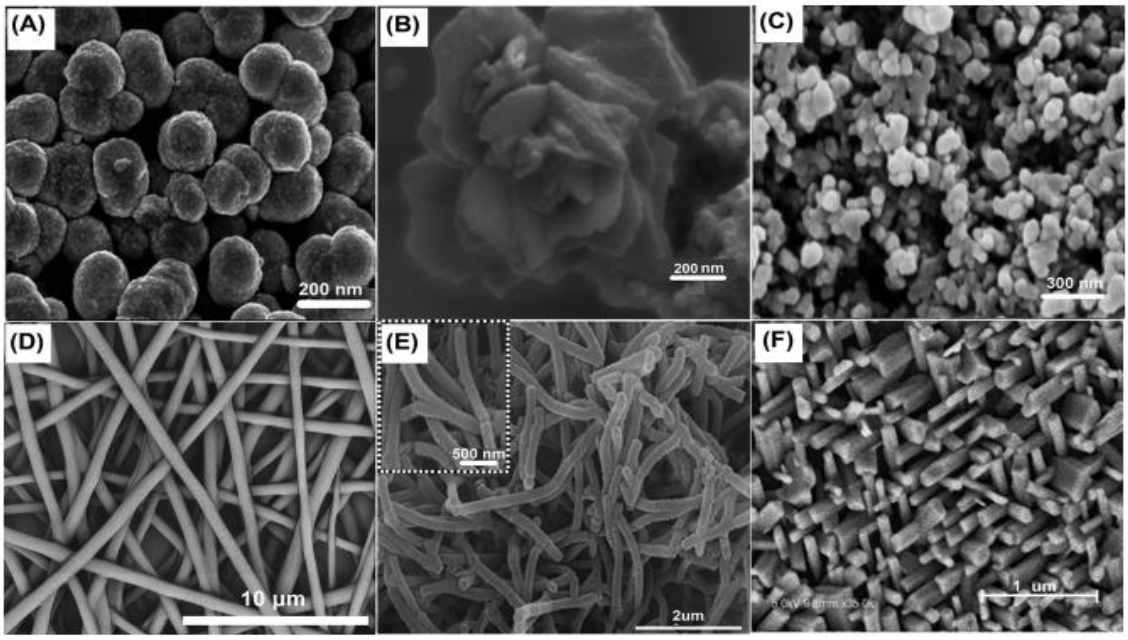

Figure 2.9: SEM images from different shape of PANI morphology: (a) PANI nanosphere synthesized in the acidic sodium carboxymethyl cellulose solution; (b) PANI nanoflowers synthesized in toluene solvent using interfacial polymerization; (c) PANI nanogranules synthesized in the acidic aqueous solution using sonochemistry method; (d) PANI nanofiber synthesized at 0 °C in the acidic aqueous solution using oxidation polymerization followed by electrospinning in 50 mL of $CHCl_3$; (e) PANI nanotubes synthesized by the micelle soft-template procedure in the oxalic acid as a dopant; (f) PANI nanorods synthesized by the ultrasonication. Reprinted with permission from [84]. Copyright (2019) American Chemical Society

Basically, the molecular structure of PANI possess either quinonoid or benzenoid or both types at different proportions [84,87]. According to the reduction-oxidation state, PANI exists in three forms, i.e., leucoemeraldine (Figure 2.10.b), pernigraniline (Figure 2.10.c), and emeraldine (Figure 2.10.d and e). Typically, each form of PANI has different color to indicate its state, leucoemeraldine has yellow color, pernigraniline has purple color. Emeraldine-base (basic condition) has blue color and emeraldine-salt (acidic condition) has dark green color [84]. Thus, there are six forms of polyaniline i.e., leucoemeraldine-salt, leucoemeraldine-base, pernigraniline-salt, pernigraniline-base, emeraldine-salt, emeraldine-base, of which only emeraldine-salt is electronically conducting, all others forms are non-conducting [69,84]. A pure emeraldine-salt (without doping) has the range of electrical conductivity (σ) from 10^{-2} to 10^{0} S/cm.

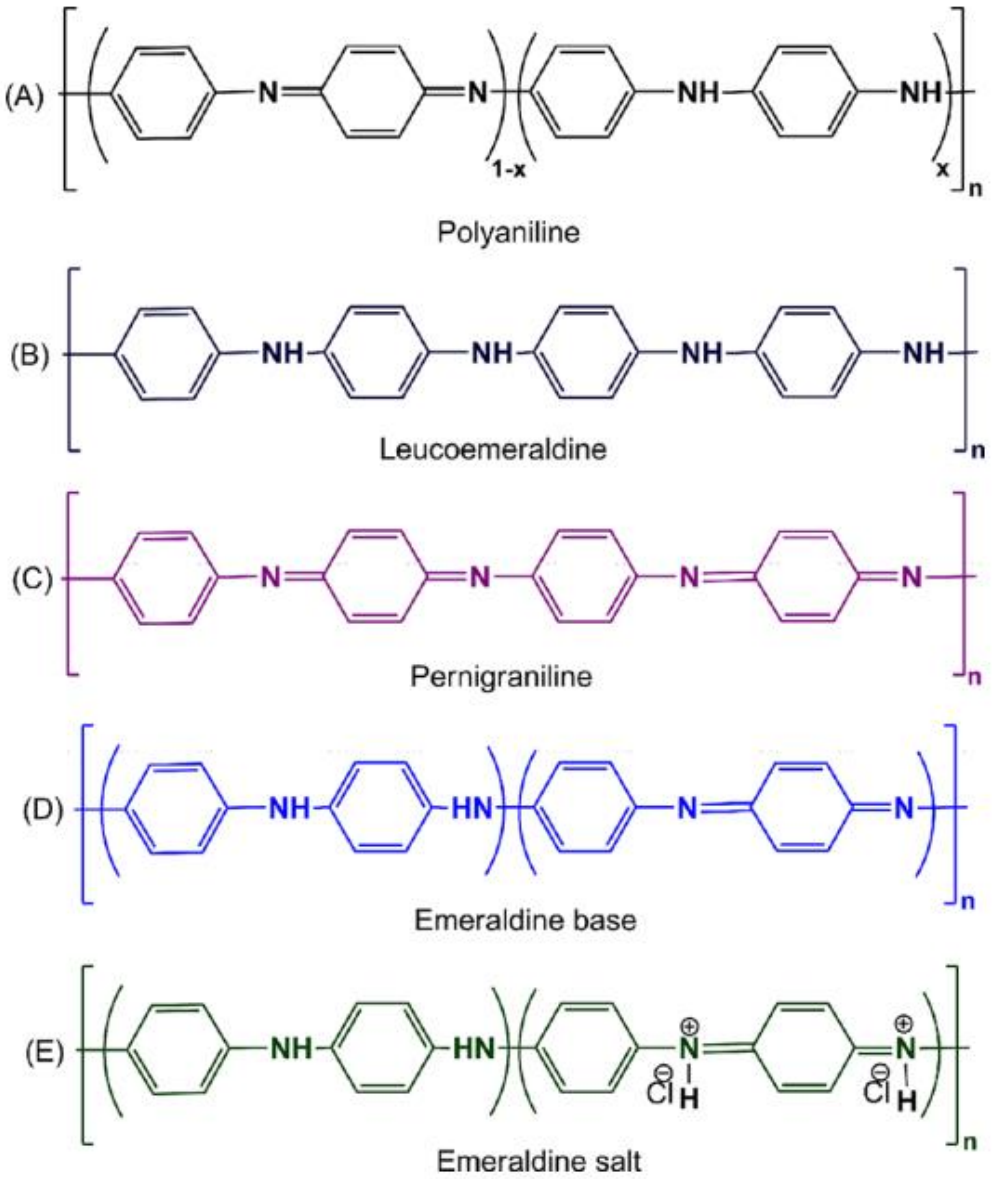

Figure 2.10: The molecular structure of: (a) PANI consisting of reduced (x) and oxidized ($1 - x$) blocks ($0 \leq x \leq 1$); (b) Leucoemeraldine ($x = 1$); (c) Pernigraniline ($x = 0$); (d) Emeraldine base ($x = 0.5$); (e) Emeraldine salt ($x = 0.5$). Reprinted with permission from [84]. Copyright (2019) American Chemical Society

It is well-known that the electrical conductivity of PANI is getting reduced over a long cycle time [69,84]. Copolymerization with another polymer, incorporating nanocomposites with various materials, or doping with a catalyst have been conducted to diminish the aforementioned disadvantage [69,84,87]. The electrical conductivity (σ) of PANI can be much improved with a doping of the emeraldine-base (insulator form, $\sigma \leq 10^{-10}$ S/cm) and formation of emeraldine-salt (conductive form, $\sigma \geq 1$ S/cm) [84]. Generally, for a doping process with PANI, organic and inorganic acidic solutions can be used such as H_2SO_4, HCl, $HClO_4$, H_3PO_4, camphorsulfonic acid, dodecyl-benzenesulfonic acid, and para-toluenesulfonic acid.

Figure 2.11 depicts the typical cyclic voltammetry (CV) curve of PANI in acidic medium of HCl. As shown in Figure 2.11, the two sets redox reactions are recorded. The first redox couple appears between 0 to 0.25 V *vs.* reference electrode of Ag/AgCl which associated to the conversion of fully reduced leucoemeraldine to partially oxidized emeraldine, and the second redox couple takes place between 0.6 to 0.8 V *vs.* reference electrode of Ag/AgCl which related to the conversion of emeraldine to the fully oxidized pernigraniline form. The electrochemical potential of peaks 1 and 1' are independent to the pH change and correspond to expulsion of protons [69,86], whereas, peaks 2 and 2' is strongly dependent to the pH change and responsible to uptake of the anion to the film, and their position and shape strongly depend on the anion type and the acid type [69,86]. PANI also exhibits irreversible degradation when a high voltage is applied, i.e., more than 0.8 V [86,87].

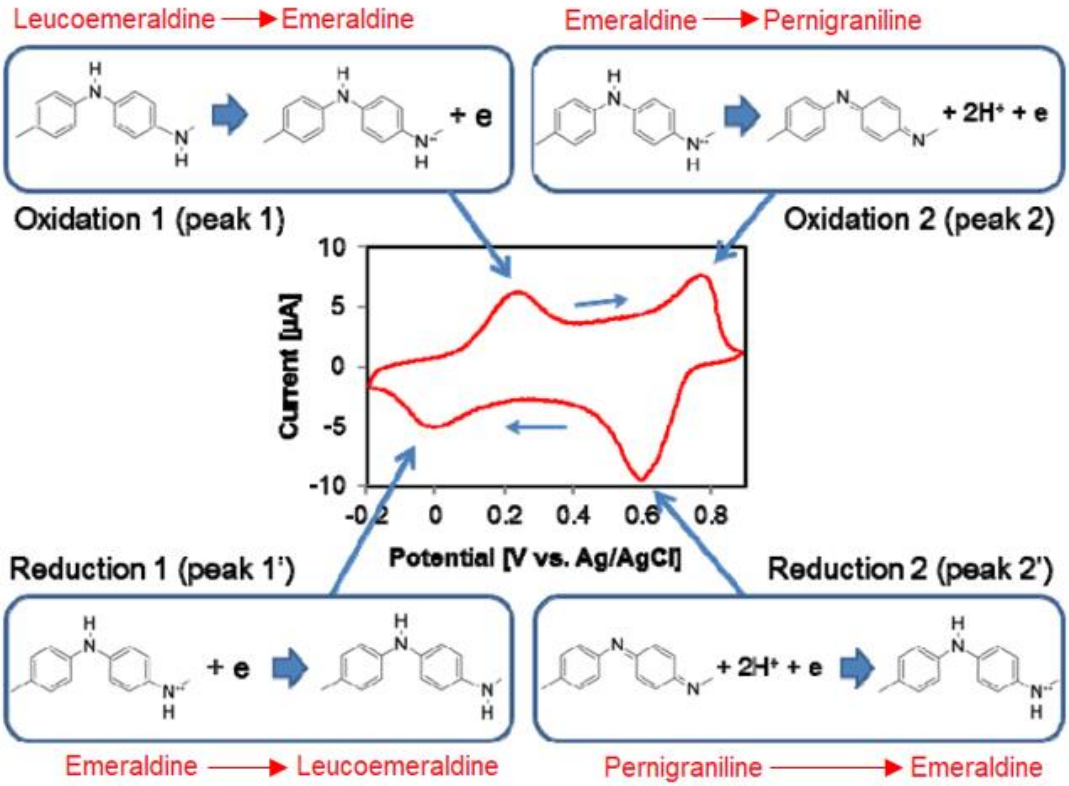

Figure 2.11: The typical cyclic voltammetry (CV) curve of PANI in acidic medium of HCl (pH = 1) showing two sets of redox reactions. Reprinted from [86]

Figure 2.12 illustrates the PANI as a metal binding support matrix in doping process using acidic solution [69]. The incoming metal anion $[A]^-$ resides the vicinity of nitrogen sites and should affect the stretching of N-H frequency in infra-red region (IR) according to the metal size [69,87]. Furthermore, the electrical properties obtained by metal doped PANI depend on several factors, i.e., the macroscopic (e.g., molecular orientation and materials compactness) and microscopic (e.g., level of doping, length of polymer chain, and conjugation) [84].

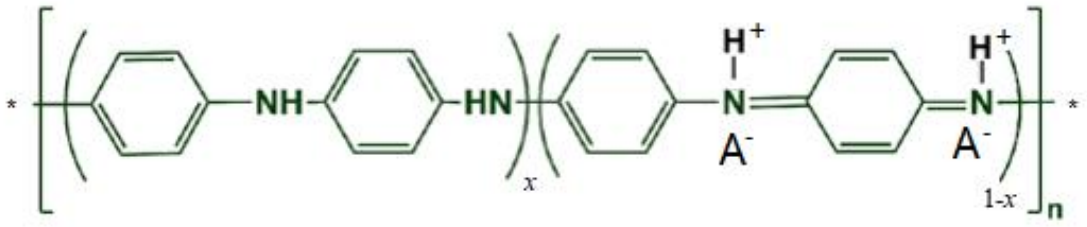

Figure 2.12: The illustration of PANI as host matrix for doped metal in a strong acid, A^- is the incoming metal anion

2.2.2 Atomic gold

A. Basic theory of atomic gold clusters

The atomic gold clusters exhibit remarkably catalytic activity and unique properties due to quantum size effects that have been studied theoretically and experimentally for more than four decades [57,87–90]. The geometrical shape of atomic clusters is one of the factors responsible for their unique property [88,89]. Density-functional theory (DFT) is a popular computational quantum mechanical modeling used in many fields. In this area, DFT is commonly used to determine various possible geometries existing for atomic metal clusters. Figure 2.13 depicts the various equilibrium geometrical structure in anionic, neutral, and cationic for atomic gold clusters using DFT. As shown in Figure 2.13, several possible geometrical structures exist at certain clusters (n), for example when n = 3, then three possible geometrical structures exist in which each geometrical structure possesses particular properties [88].

The energy difference between the highest occupied molecular orbital (HOMO) and lowest unoccupied molecular orbital (LUMO) well-known as HOMO-LUMO gap energy is often used to confirm the formation of atomic metal clusters [57,88]. Theoretically, DFT is extensively used to predict the HOMO-LUMO gap energy of atomic gold clusters (and other atomic metals like silver, copper, etc) that shows the odd-even pattern as depicted in Figure 2.14 [57,88]. Briefly, the gap energy for odd-numbered atomic gold clusters is smaller than the even-numbered atomic gold clusters, this odd-even property is an indirect method to confirm the atomic gold clusters formation. Another way to confirm the atomic gold formation is by using the electrooxidation of propanol isomers in alkaline medium which is explained in the next section after preparation of atomic gold on PANI.

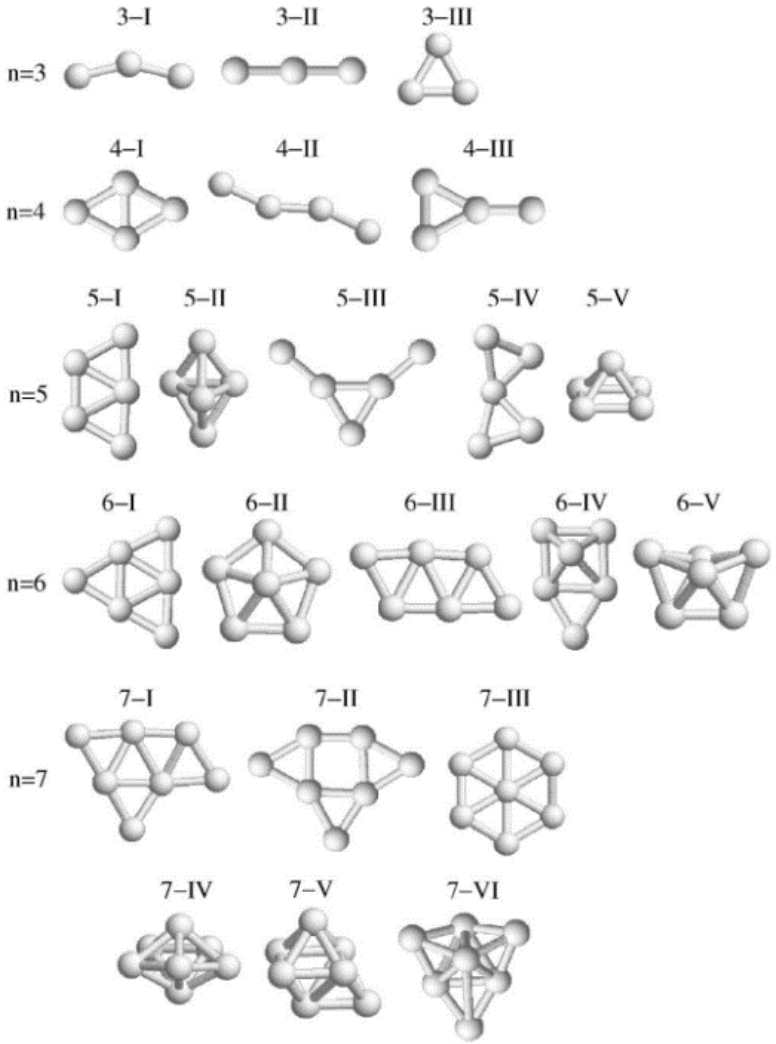

Figure 2.13: The equilibrium of anionic, neutral, and cationic atomic gold clusters where $3 \leq n \leq 7$. The roman numerals identify the different possible geometrical structure. Reproduced from [88]

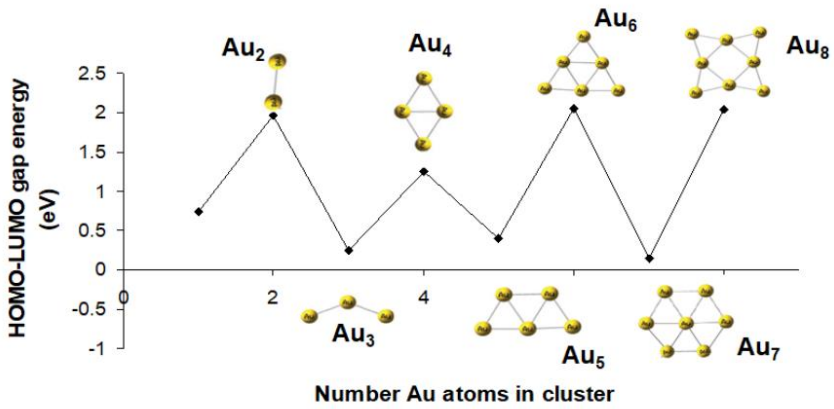

Figure 2.14: The theoretically predicted odd-even pattern from HOMO-LUMO gap energy for atomic gold clusters Au_N where N = 1 to 8. Reproduced from [57]

B. Preparation of atomic gold on PANI

Atom-by-atom growth of Au clusters in PANI using acidic medium ($HClO_4$) is depicted in Figure 2.15. There are several main steps included. Firstly, the PANI must be fully oxidized into pernigraniline form by sweeping the potential from -0.2 V to +0.8 V (I to II). Afterwards, by holding the potential at +0.8 V, the anions of $AuCl_4^-$ (obtained from $KAuCl_4$) is introduced to PANI *in situ* (III). One anion of $AuCl_4^-$ forms a PANI*$AuCl_4^-$ due to high affinity of the PANI to this anion and the excess of the anions of $AuCl_4^-$ are rinsed by $HClO_4$ at +0.8 V (IV). Then, the potential is swept from +0.8 V to -0.2 V leading the reduction of $AuCl_4^-$ to Au (V). Finally, the PANI doped with one Au is achieved. This atomic gold cycle process can be repeated N times to obtain N atomic gold clusters doped in PANI. For example, PANI-Au_2 means that the atomic gold deposition process is repeated twice [57,91].

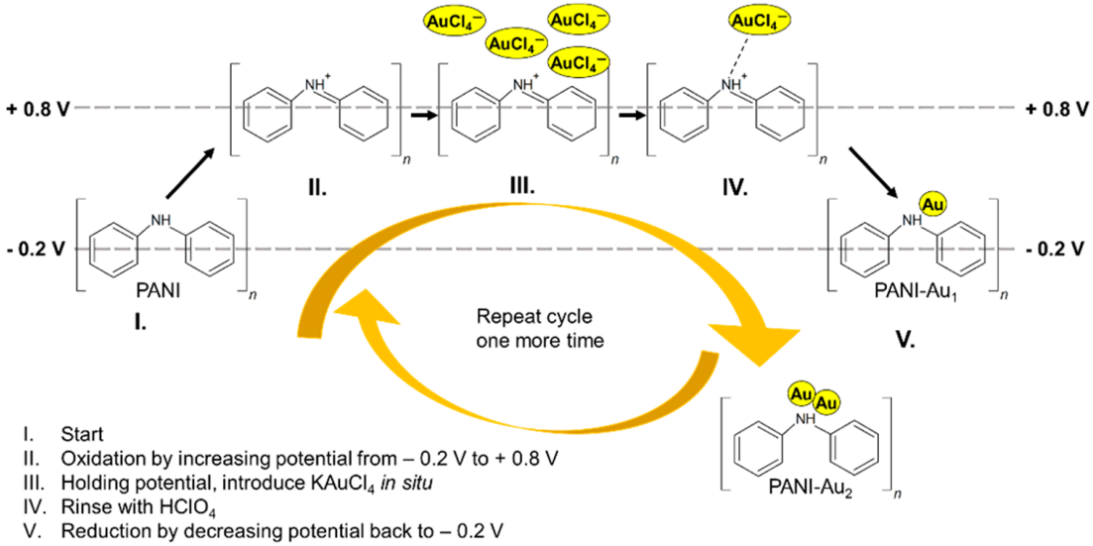

Figure 2.15: The cycle of the atomic gold deposition process in PANI using the acidic medium (HClO4). Reproduced from [91]

Figure 2.16 shows the CV curve of PANI in 0.1 M $HClO_4$ at different conditions. The EC potential was swept from -0.2 V to +0.8 V *vs.* Ag/AgCl reference electrode. According to Figure 2.16, briefly, the two sets redox reactions were recorded at five different conditions, i.e., the CV curve obtained from PANI before deposition (black dash line, I), the CV curve from reduction $AuCl_4^-$ to Au in PANI (red color, II), the CV of PANI-Au_1 (blue color, III), the CV curve from reduction $AuCl_4^-$ to Au in PANI (orange color, IV), and the CV curve of PANI-Au_2 (green color, V). During the formation of PANI-Au_2 or a higher atomic gold clusters deposition, PANI is being held at a prolonged time at +0.8 V (pernigraniline form) which mostly causes the degradation of the polymer indicated by the reduced current density area. The degradation of PANI due to over-oxidation is also observed if the applied potential exceeds 1V vs. SHE [70]. As shown in Figure 2.16, although the current density of PANI-Au_2 in acidic medium (0.1 M $HClO_4$) was decreased meaning that PANI film was degraded. It has been massively reported that the sensing measurement of isomers compound in alkaline medium exhibits a high catalytic activity using PANI-Au_2 than PANI-Au_1. It means the successful formation of Au_2 clusters [57,87,89,91].

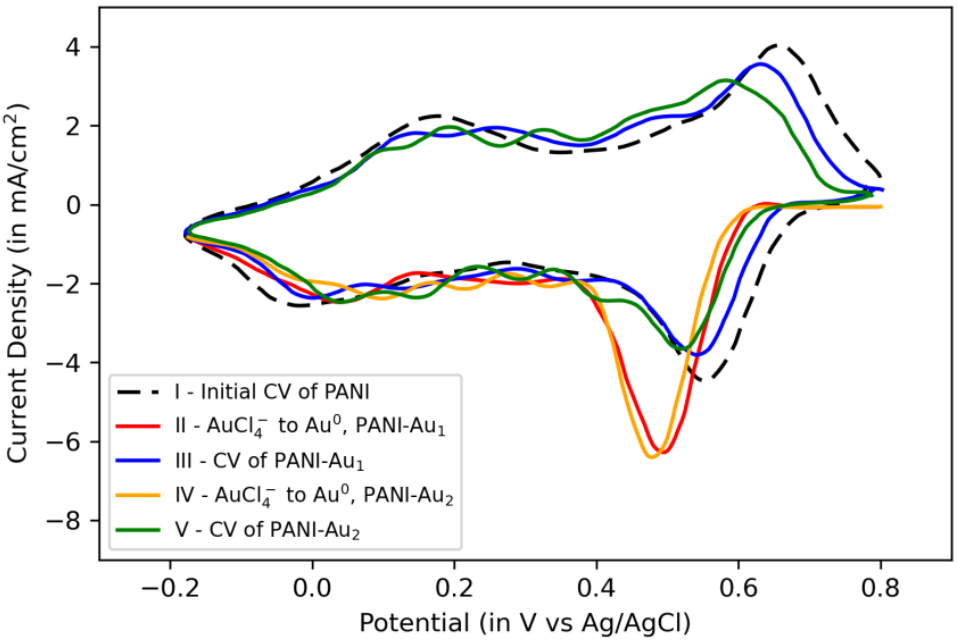

Figure 2.16: The CV of PANI in 0.1 M $HClO_4$ at different conditions: (I) PANI before deposition; (II) Reduction $AuCl_4^-$ to Au in PANI; (III) CV of PANI-Au_1; (IV) Reduction $AuCl_4^-$ to Au in PANI; (V) CV of PANI-Au_2. The scan rate = 20 mV/sec. Reproduced from [57]

C. Odd-even pattern of atomic gold decorated PANI

The effect of atomic gold clusters Au_N (N = 1 to 8) in PANI for electrooxidation of 0.5 M n-propanol (or 1-propanol) in 1 M NaOH is depicted in Figure 2.17. The modified working electrode using Pt/PANI/Au_N was conducted in this measurement. As shown in Figure 2.17, the absence of 0.5 M n-propanol in NaOH exhibits no oxidation peaks although atomic gold clusters were varied from 1 to 8. Furthermore, the presence of 0.5 M n-propanol in 1 M NaOH exhibits a very clear two oxidation peaks (I and II) for the even numbered of atomic gold clusters (except N = 8), and only one peak (I) for odd numbered atomic gold clusters (except N = 7). The first oxidation peak (I) was attributed to platinum, whereas the second oxidation peak (II) was associated to the presence of the atomic gold clusters. The second oxidation peak (II) provides a strong indication that atomic gold clusters sited in PANI which undergoes the electrooxidation for n-propanol in alkaline medium.

Furthermore, the peak current density from the first peak (I) and the second peak (II) *vs.* the number of deposited atomic gold clusters were evaluated and shown in Figure 2.18. As shown in Figure 2.18, the presence of atomic gold clusters can be evaluated from the second peak (II) which exhibits the odd-even pattern, in addition, the HOMO-LUMO gap energy was also calculated. According to Figure 2.18, the HOMO-LUMO gap energy and current density for even-numbered atomic gold clusters were higher than the odd-numbered atomic gold clusters thus confirming the success of atomic gold clusters formation in PANI. When measuring the electrooxidation of 0.5 M n-propanol in 1 M NaOH, the odd-even pattern for current density at the second peak (II) breaks down at N = 8, a possible explanation is that the Au_8 clusters were too large and were not fit into the fibers of PANI matrix then beginning to bridge the distance between the neighboring clusters, and allowing to aggregate (the coalescence process) [83,89].

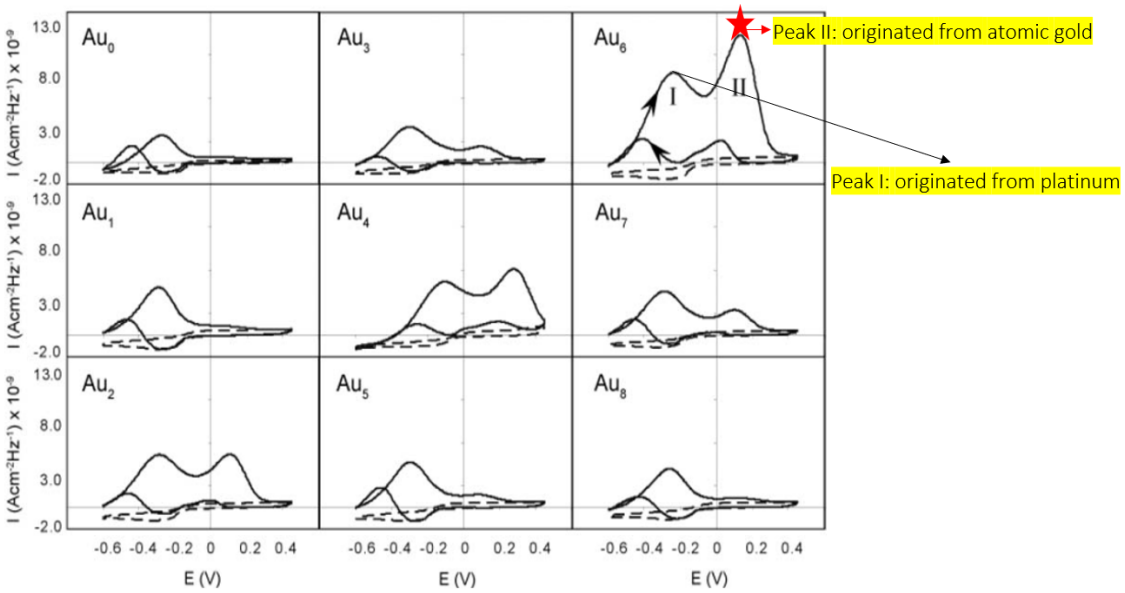

Figure 2.17: The effect of atomic gold clusters Au_N where N = 1 to 8 to PANI of 0.5 M n-propanol in 1 M NaOH (—). The CVs in 1 M NaOH (- - -) are also shown. The CVs are normalized to the mass of PANI from the frequency changes during the deposition on Pt electrode. The scan rate = 20 mV/sec. Ten CVs performed but the last CV shown here. Reproduced from [89]

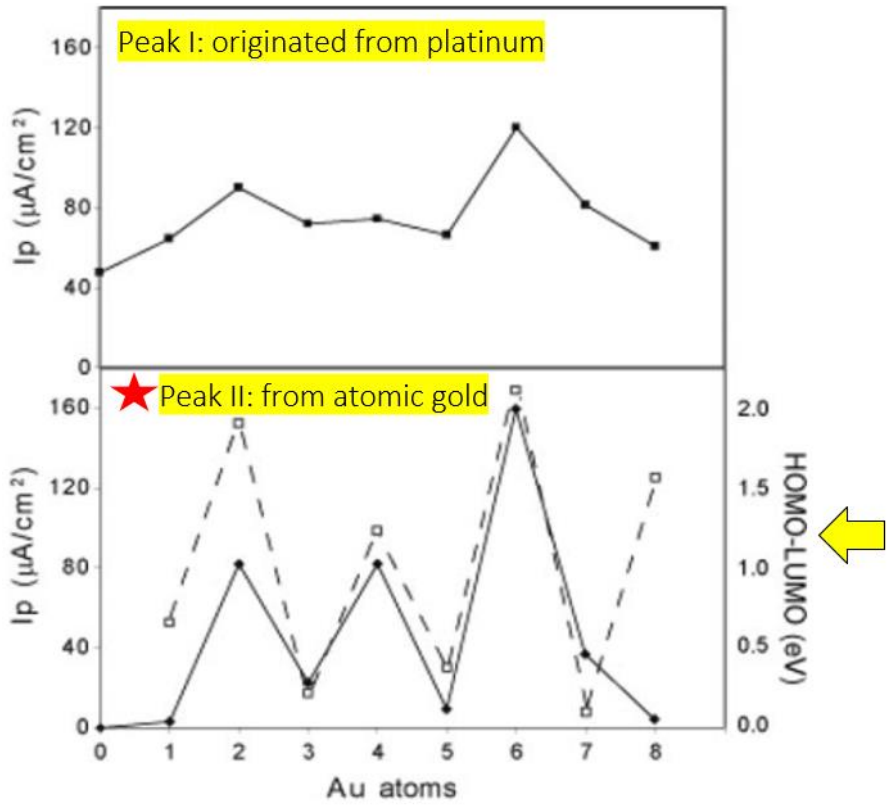

Figure 2.18: Peak current densities (evaluated from Figure 2.17) where (I) is the first oxidation peak and (II) is the second oxidation peak (labeled at Au_6 in Figure 2.17). The dashed line is the calculated HOMO-LUMO gap energy. Reproduced from [89]

It is expected that the atomic gold clusters are reside in the vicinity of nitrogen sites in the PANI chain, hence, the magnitude of N-H stretching frequencies in the infra-red (IR) spectrum region from 3100 to 3500 cm^{-1} should depend on the size and stability of the number of atomic clusters in PANI [89]. The Fourier transform infra-red (FTIR) measurements were taken after cycling in 0.1 $HClO_4$. According to Figure 2.19, the FTIR spectra of PANI/Au_N for N = 0 to 8 from 3100-3500 cm^{-1} showing the N-H stretching vibration. The presence of atomic gold number affects both band intensity and band position at the N-H stretch. The dependence of the peak shift (calculated from band shift) and the peak area (calculated from band area) relative to the band position from Figure 2.19.a are plotted in Figure 2.19.b. As shown in Figure 2.19.b, The peak area showed odd-even pattern where the even numbered atoms had a higher peak area than odd numbered atoms. Furthermore, the peak shifts also had odd-even pattern, i.e., the even numbered atomic gold clusters had a larger shift from the Pt/PANI/Au_0 than the odd numbered atomic gold clusters, except for Au_8. In summary, using FTIR measurements, the odd-even patterns were observed with the even numbered clusters affecting the N-H stretching vibration more strongly than the odd numbered clusters.

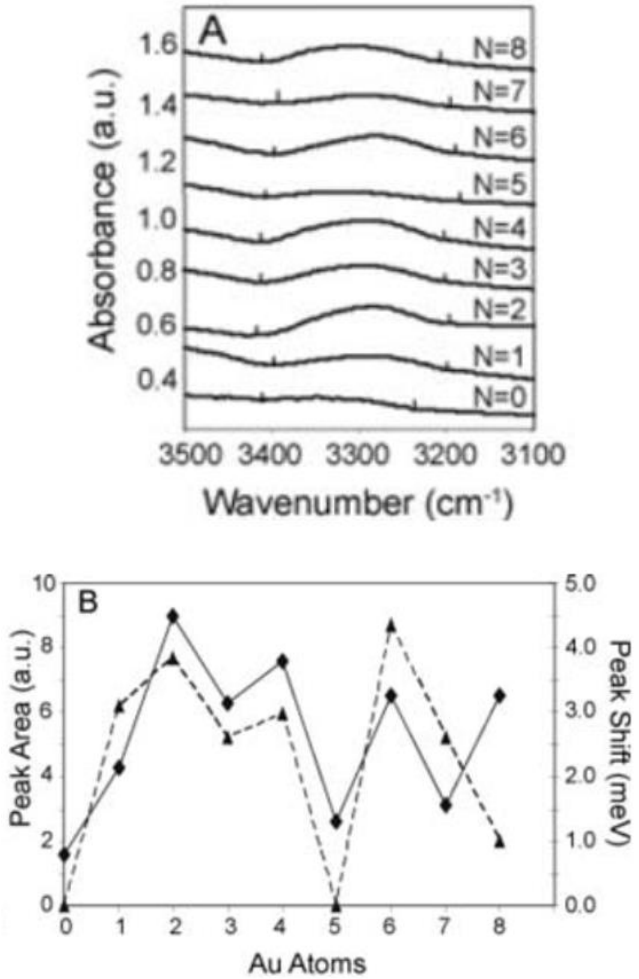

Figure 2.19: The FTIR measurements were recorded after cycling in 0.1 $HClO_4$: (a) FTIR spectra of PANI/Au_N for N = 0–8 showing the N-H stretching vibration at wavenumber of 3100–3500 cm^{-1}; (b) FTIR peak areas (—◆—) and peak shifts (- - -▲- - -) of the peak for the N-H stretching at 3300 cm^{-1} showing an odd-even alternating pattern for PANI/Au_N where N = 0-8. Reproduced from [89]

In our research group, the atomic gold deposition system was successfully conducted in the Nakamoto Laboratory using a bulky EC system. The success of the atomic gold formation in PANI was verified using 0.5 M of 1-propanol and 0.5 M of 2-propanol in 1 M KOH shown in Figure 2.20.a and b, respectively. As shown in Figure 2.20.a and b, the current density were higher for even numbered atoms (N = 2 and 4) than odd numbered atoms (N = 1 and 3) due to HOMO-LUMO gap energy variation [57]. Two peaks occurred, i.e., peak 1 at around -0.2 V attributed to the platinum and peak 2 at around +0.2 V associated to the atomic gold cluster. In the peak current density curve, the odd-even pattern (especially obtained by peak 2 due to the atomic gold cluster) was observed both for 1-propanol and 2-propanol in KOH. Atomic gold clusters with even number showed higher catalytic activity than clusters with odd number of gold atoms. Thus, the atomic gold formation in our laboratory was confirmed.

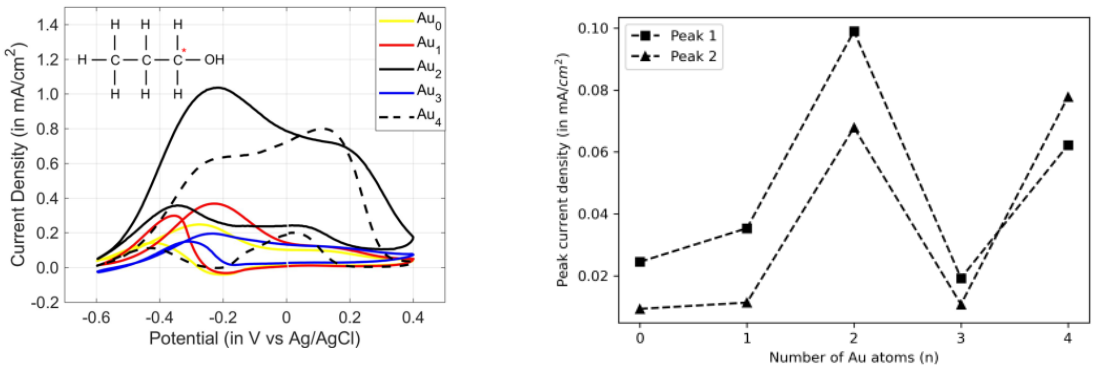

(a)

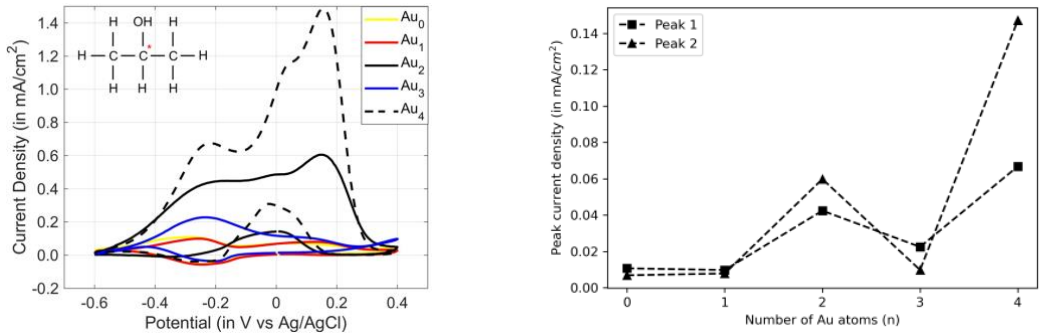

(b)

Figure 2.20: The odd-even pattern observed using Pt/PANI/AuN (N = 0, 1, 2, 3 and 4) in KOH for the electrooxidation of: (a) 1-propanol; (b) 2-propanol. The scan rate was 100 mV/s. Peak 1 = oxidaton peak at around -0.2 V, Peak 2 = oxidation peak at around +0.2 V. Reproduced from [57]

2.3 Summary

In this chapter, two sensing materials have been explained, i.e., RTIL and catalytic materials. To realize a miniaturized AGS sensor in our research indeed requires only small amount of RTIL. The most important information is that RTIL also operates at extreme temperature without undergoing evaporation meaning that although a very small amount of RTIL can be applied in our miniaturized AGS sensor and the common problem like volatility was solved by using RTIL as the electrolyte. In addition, a longer lifetime of the sensor can be realized. In this research, the information of RTIL like the physical and chemical properties are important for selecting RTILs in our research such as the EC window more than 2 V was preferable since our potentiostat has 2 V operating potential window. The different cation-anion of RTILs were applied to check the possibility of applying a high and low viscosity (viscosity is reciprocal to conductivity) of RTILs for a miniaturized AGS.

Furthermore, for catalytic materials, the atomic gold catalyst is the main focus of this research. Like nanocatalysts, the host matrix is required to deposit the atomic gold cluster. Polyaniline was used as the metal binding support matrix for atomic gold clusters. In an acidic medium, polyaniline exists in three redox forms, i.e., leucoemeraldine, pernigraniline, and emeraldine, of which emeraldine salt is the only conducting form. The doping process in PANI must be conducted in an acidic medium. In our research, the atomic gold deposition process using PANI was also conducted in the acidic medium, i.e., $HClO_4$.

To verify the successful atomic gold formation, the electrooxidation of propanol isomers in alkaline medium are oftentimes used, a higher catalytic activity is achieved by even-numbered atomic gold clusters than odd-numbered atomic gold clusters. Afterward, the odd-even pattern of current density (oxidation peak, especially at peak 2 associated to atomic gold formation) due to HOMO-LUMO gap energy variation are commonly used to confirm the success of the atomic gold cluster formation in PANI. The FTIR can also be used to confirm the presence of atomic gold clusters sited in PANI which is expected to affect the N-H vibration depending on the stability and the number of atomic gold clusters.

The Pt/PANI/Au_2 exhibits a high catalytic activity and it can be fabricated using only two cycles of the atomic gold deposition process which is more time-efficient compared a high even-numbered atomic gold cluster. In addition, depositing a high number of atomic gold cluster require PANI being held at a prolonged time at +0.8 V (pernigraniline form) several times leading the irreversible degradation of PANI film. Therefore, in our research, we only fabricated the atomic gold cluster of Au_2 at a miniaturized amperometric gas sensor (AGS).

Chapter 3

Methods

3.1 Introduction

In this chapter, the experimental set-up and discriminant analysis method are explained. The experimental set-up includes the set-up for depositing sensing film such as the method for polyaniline polymerization (conducted in Sone Laboratory), the atomic gold deposition system (e.g., instrumentation, chemicals, and timing diagram), the gas delivery system, and the potentiostat (EVAL-AD5940ELCZ). Furthermore, the discriminant analysis explains the statistical method to evaluate the separation among analytes used in this study.

3.2 Set up for depositing sensing film

3.1.1 Polymerization of Polyaniline (PANI)

In this study, a miniaturized AGS applied the interdigitated array electrode (IDA) as shown in Figure 3.1.a, in which the working electrode (WE), counter electrode (CE), and reference electrode (RE) were made from platinum (Pt) and all electrodes were deposited on a same quartz plate (glass) substrate. The commercial IDA was purchased from BAS Co., Ltd., Tokyo, Japan [92]. The polymerization of polyaniline (PANI) used as support matrix was conducted in Sone Laboratory at Tokyo Institute of Technology, Japan. The PANI polymerized on WE illustrated in Figure 3.1.b., used 0.1 M aniline ($C_6H_5NH_2$) in 2 M tetrafluorobic acid (HBF_4). The PANI electropolymerization applied the Galvanostatic method with a constant current of 0.56 mA for 260 s. The thickness was approximately 0.05 mm.

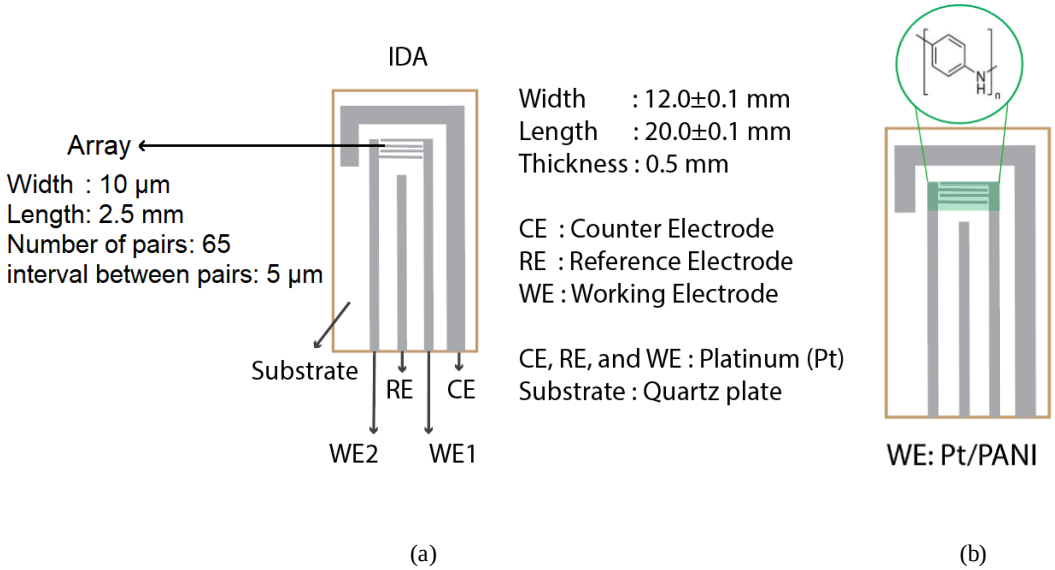

Figure 3.1: The miniaturized AGS: (a) IDA electrode; (b) PANI polymerized on WE. Reprinted from [93]

3.1.2 Atomic metal deposition system

A. Chemicals

There are two kind of chemicals solutions required for atomic gold deposition process, i.e., potassium tetrachloroaurate ($KAuCl_4$) and perchloric acid ($HClO_4$). The $KAuCl_4$ was used as the gold precursor to supply the noble metal of gold. Furthermore, the acidic medium of $HClO_4$ was selected to rinse away the excess of gold anions during the atomic gold doping process. All the chemicals were purchased from the Sigma Aldrich Ltd., Tokyo, Japan and Wako Chemicals Ltd., Osaka, Japan, with purity of 98-99.5%.

B. Atomic gold deposition system

Figure 3.2 shows the atomic gold deposition system along with the schematic layout. The IDA electrode was installed in the chamber where its two WEs, CE, and the external RE of Ag/AgCl were connected to the line of WE, CE, and RE at lab-fabricated potentiostat (based on IC TL074, Texas Instruments, Dallas, TX, USA). The gold precursor was obtained from 0.2 mM $KAuCl_4$. The acidic solution of 0.1 M $HClO_4$ was used to rinse the excess of gold anions during the atomic gold deposition process. Three-way solenoid valve (EXAK-3, Takasago) was used to control the switching between 0.2 mM $KAuCl_4$ and 0.1 M $HClO_4$ coming into chamber and going out from outlet to waste. To obtain a good formation of atomic gold decorated Pt/PANI at WE of IDA, the O-ring was used to remove the leakage of the liquids during the atomic gold deposition process [57,93]. The USB socket was used as connector for IDA as shown in Figure 3.2. It has four pins for IDA's electrode lines, i.e., WE 1, WE 2, RE, and CE. Furthermore, the detailed devices of atomic gold deposition process are explained in the next section.

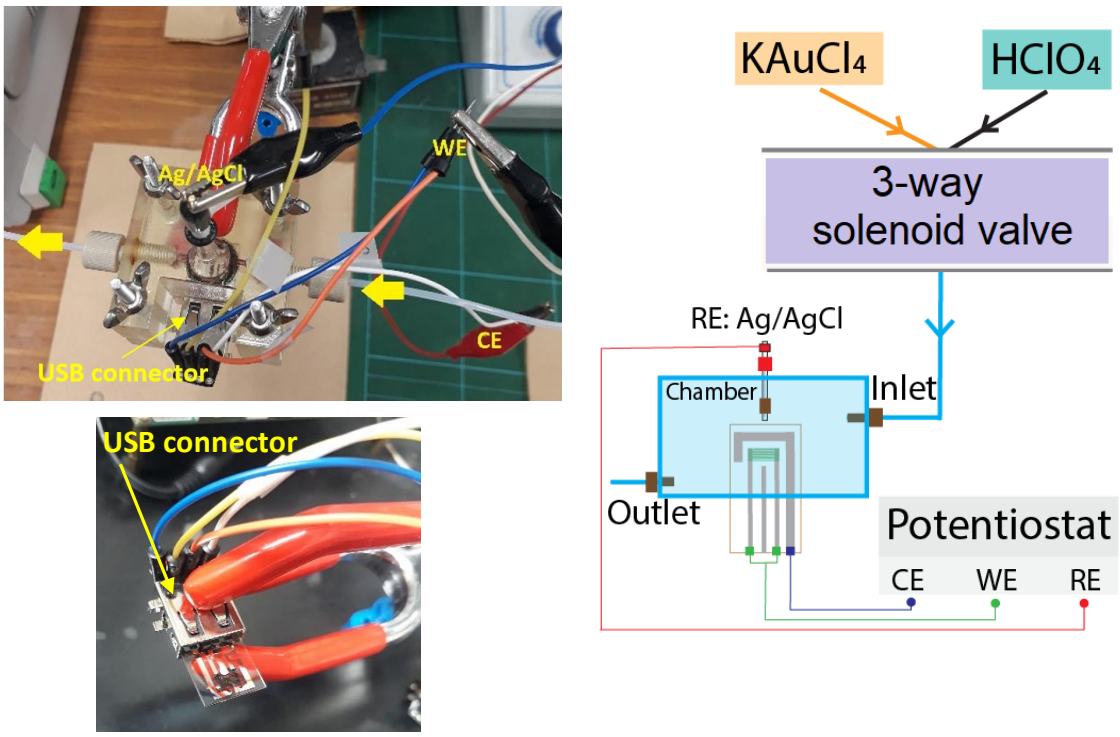

Figure 3.2: The atomic gold deposition system. Reprinted from [93]

C. Chamber

Figure 3.3.a shows chamber used to place the IDA and external reference electrode during the atomic gold deposition process. The 3D printed of acrylic chamber was fabricated in Tokyo Institute of Technology, Japan. Since the reference electrode (RE) of IDA made from Pt thus the external Ag/AgCl reference electrode (RE) is required to maintain a stable reaction during the atomic gold deposition process as shown in Figure 3.3.b. The RE of Ag/AgCl purchased from BAS Co., Ltd., Tokyo, Japan, was isolated in glass tube with the internal solution of 3 M NaCl and it had a constant and defined potential of 195 mV against standard hydrogen electrode (SHE) using reversible hydrogen electrode kit (RHEK) at 25 °C [94,95]. The RE of Ag/AgCl in Figure 3.3.b can be sealed in a small bottle containing 3 M NaCl solution as depicted in Figure 3.3.c to be used for a long period.

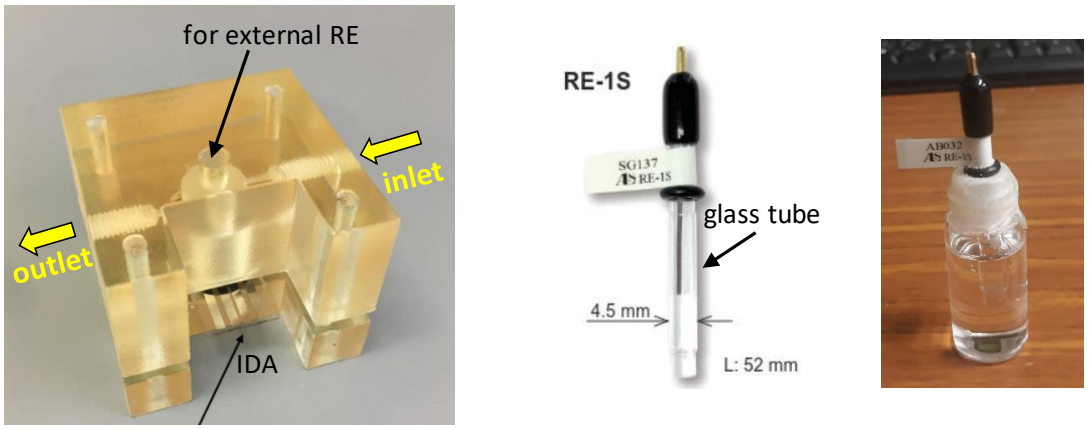

(a) (b) (c)

Figure 3.3: Chamber for atomic gold deposition process: (a) the acrylic chamber; (b) the external RE; (c) sealing the Ag/AgCl in 3 M NaCl solution. Reprinted from [57]

D. Lab-fabricated potentiostat

The potentiostat is an electronic circuit applied to control the voltage difference between a working electrode (WE) and the reference electrode (RE). The working electrode (WE), counter electrode (CE), and reference electrode (RE) are put inside the EC cell or chamber. Figure 3.4.a shows the electronic circuit for lab-fabricated potentiostat mainly used for the atomic gold deposition system. The TL074 quad low-noise JFET-input general-purpose operational amplifier (OP-AMP) from Texas instruments was used. Ideally, no current flows into the input terminals of an OP-AMP, in practice, input bias current (I_{IB}) always occurs and it varies with temperature change, I_{IB} is defined as the average of the current flows into both of input terminals of an OP-AMP ($I_{IB} = (I_{B+} + I_{B-})/2$). The input bias current influences to the resolution of the potentiostat. TL074 has a low input bias current, it has a maximum I_{IB} of 200 pA at 25 °C and 20 nA at 125 °C [96]. As shown in Figure 3.4.a, four integrated circuits (ICs) of TL074 were used, i.e., IC1A, IC1B, IC1C, and IC1D. The IC1A takes sweeping voltage signal for the input which is also reflected at the RE. The current flows between WE and CE through the feedback loop of IC1A. The differential amplifier of IC1B measures the current changes and become the input to IC1D. The IC1D having a gain of 100 is used for to amplify the signal. The IC1C is applied for the offset correction; it is OP-AMP circuit used for subtractor or summer. Figure 3.4.b depicts the printed lab-fabricated potentiostat which is able to measure the currents as

small as 0.1 μA due to backward current from the OP-AMP and background noise from passive components [57]. As shown in Figure 3.4.a, although the WE was connected to ground, the potentiostat controlled the WE potential through the voltage difference between WE and RE. The applied potential fed up to the WE from potentiostat against RE leads the particular EC reaction thus resulting a current flow which can be measured between the WE and the CE. Therefore, the cell potential becomes the controlled variable and the cell current is the measured variable.

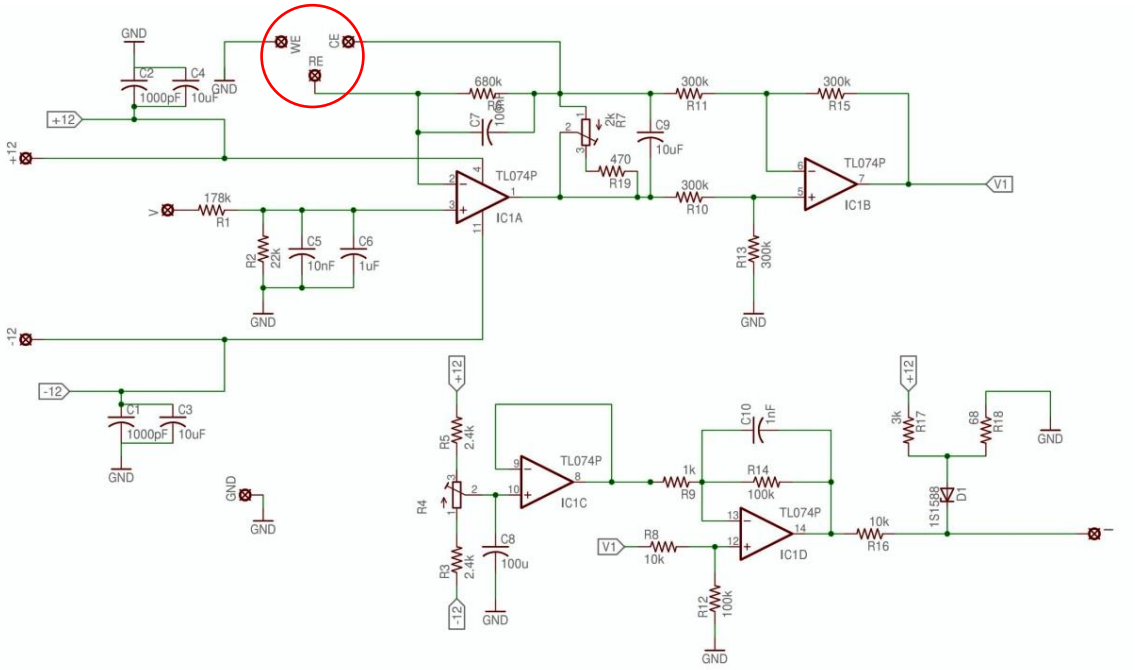

(a)

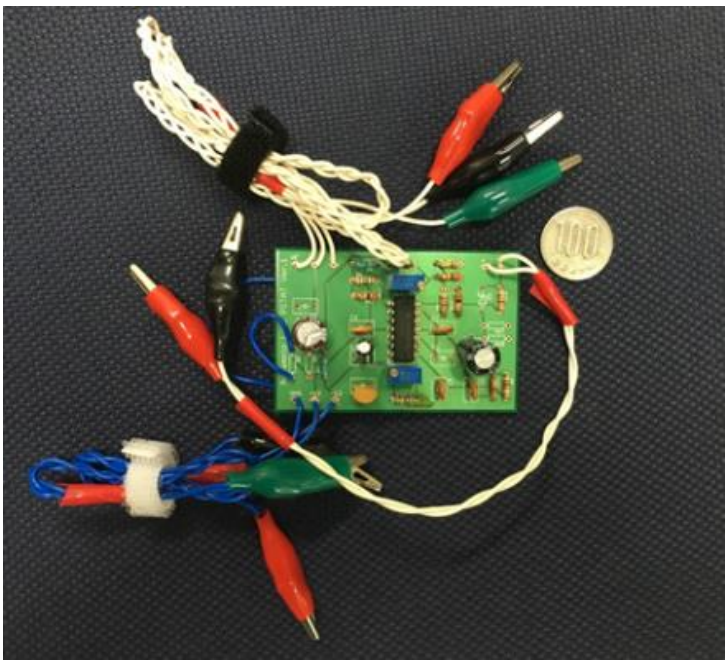

(b)

Figure 3.4: The lab-fabricated potentiostat: (a) the electronic circuit; (b) the image of printed lab-fabricated potentiostat. Reprinted from [57]

E. Instrumentation

Figure 3.5 shows schematic layout and several devices used for the atomic gold deposition process. The detailed descriptive block diagram of atomic gold deposition system is available in Figure 3.5.a. A dual syringe pump (Legato 111, KD Scientific) depicted in Figure 3.5.b, was used in this experiment, it has programmable options (infuse/withdraw) which can accommodate syringes 0.5 μL to 10 mL. The plastic syringe of polypropylene (PP) 10 mL purchased from Terumo, Japan, was placed at Legato 111 syringe pump device to store the $KAuCl_4$ solution. Only a single syringe was used to drive the $KAuCl_4$ into the chamber. This syringe pump was connected to the computer via USB serial interface.

Another solution, i.e., $HClO_4$ was necessary to rinse the excess of gold anions from $KAuCl_4$. The peristaltic pump (13-876-2, Fisher Scientific) as depicted in Figure 3.5.c was used to inject the $HClO_4$ solution through the tube of flexible hose (Tygon Tube, LMT-55 Saint Gobain) placed inside the pump casing. The automatic on/off switch from peristaltic pump for $HClO_4$ was controlled through relay circuit using Arduino depicted in Figure 3.5.d which connected to computer via USB serial as shown in Figure 3.5.a.

Two different tubes (Tygon Tube, LMT-55 Saint Gobain) containing $KAuCl_4$ and $HClO_4$ were connected to a three-way solenoid valve as shown in Figure 3.5.a. Three-way solenoid valve driven by voltage of 12 V (EXAK-3, Takasago) shown in Figure 3.5.d was used to control the flows between $KAuCl_4$ and $HClO_4$ alternately. The automatic on/off state from 3-way solenoid valve was controlled through transistor array using Arduino which connected to computer via USB serial.

Furthermore, a function generator (AFG1022, Tektronix) depicted in Figure 3.5.f was used to control the applied potential to the WE accurately and it was connected to the computer via USB serial. Various voltage signal waveforms were drawn using buttons and stored in the device's memory at the function generator. For the atomic gold deposition process, the generated waveforms from the function generator were fed up to the potentiostat circuit which had three wires, i.e., WE, RE, and CE. During the atomic gold process, the applied voltage (V) and the current as sensor information (I) were measured using an A/D converter (9201 and cDAQ-9171, National Instruments) which connected to the computer. All the measurements were controlled and taken using a Serial-USB protocol inside a MATLAB script file (2019a, Mathworks). The Arduino and MATLAB program were available in this Ref [57] and in the Appendix (in this thesis).

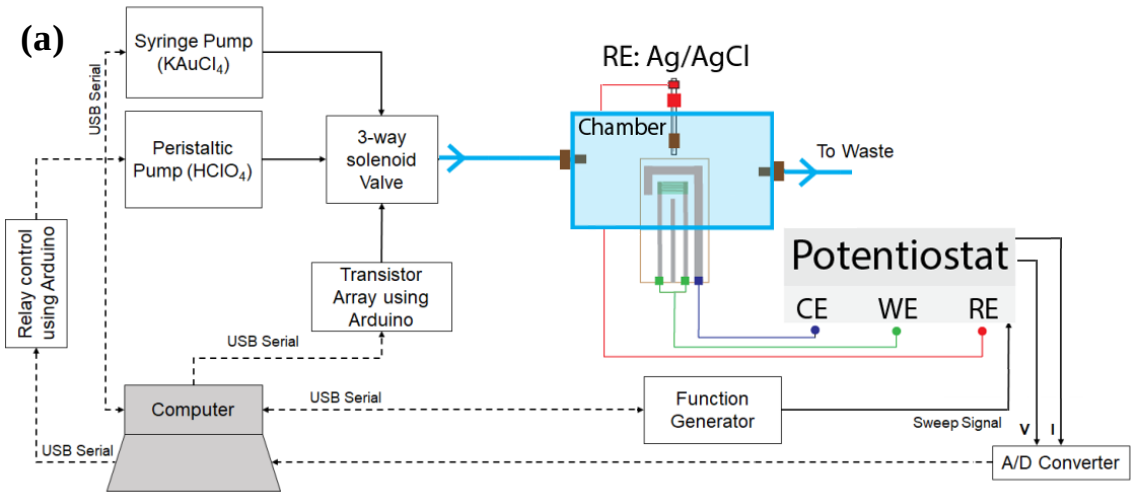

(b) (c)

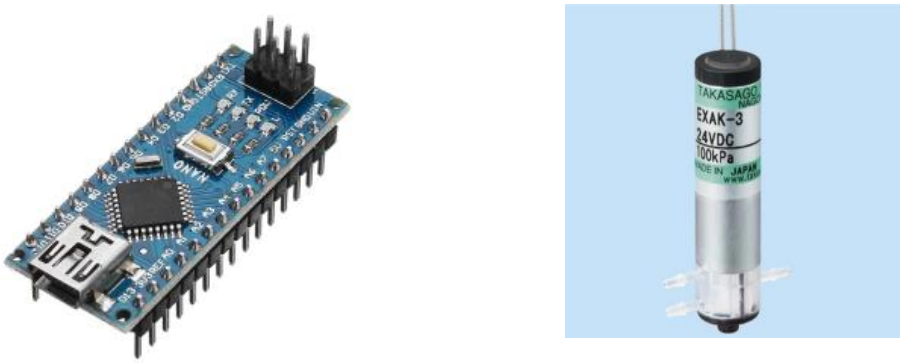

(d) (e)

(f)

Figure 3.5: (a) Layout of atomic gold deposition system; (b) syringe pump; (c) peristaltic pump; (d) three-way solenoid valve; (e) arduino; (f) function generator. Reprinted from [57]

F. Timing diagram

In this study, the atomic gold clusters of Au_N with N = 2 was used to decorate the Pt/PANI at WE using IDA electrode, the timing diagram process is depicted in Figure 3.6. Firstly, the chamber was cleaned

using 0.1 M $HClO_4$ for 300 s. After that, the IDA electrode, external RE were installed into the chamber where all the electrodes were in contact with 0.1 M $HClO_4$. The three cyclic voltammograms (CVs) scans were conducted with sweeping the potentiostat from –0.2 V to +0.8 V back and forth at a scan rate of 20 mV/s. Then, the sweeping potential was held at +0.8 V to obtain the fully oxidized PANI into pernigraniline form; here, the flow of 0.1 M $HClO_4$ was switched off temporally, the 0.2 mM $KAuCl_4$ was flowing into the chamber around 60 s to from PANI*$AuCl_4^-$, after that the 0.2 mM $KAuCl_4$ was switched off alternated with 0.1 M $HClO_4$ flow to rinse the excess of gold anions around 800 s. Then the potential was swept from +0.8 V to -0.2 V leading the reduction of $AuCl_4^-$ to Au, thus PANI/Au_1 formation was obtained. The three CVs were conducted to record the PANI formation after gold deposition process at a scan rate of 20 mV/s. These steps were repeated once again to obtain the PANI/Au_2 formation followed by closing stage to reach the potential at 0 V [57,93].

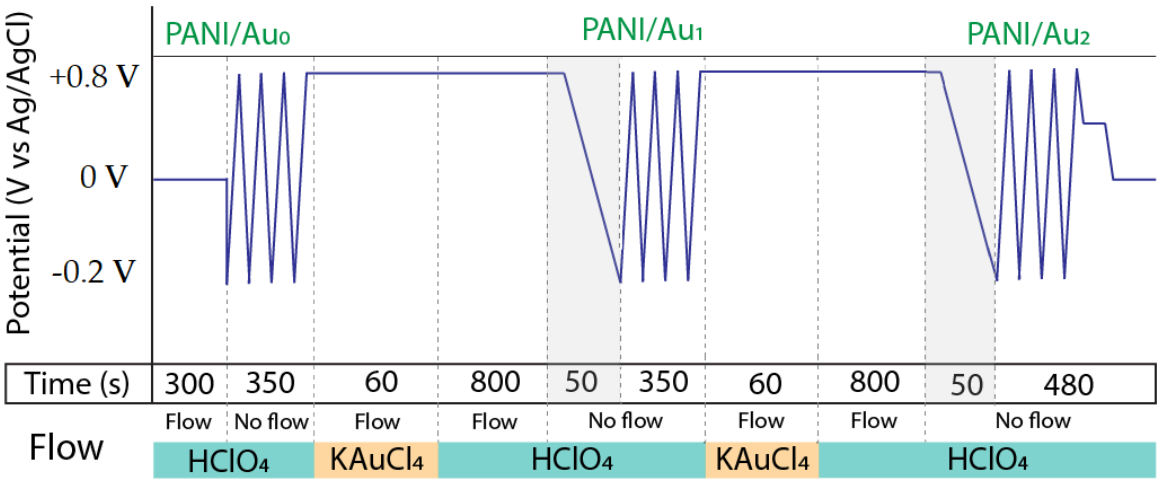

Figure 3.6: The timing diagram to fabricate the atomic gold clusters Au_N (N = 2). Reprinted from [93]

3.3 Gas delivery system

Figure 3.7 depicts the gas delivery system used in this study. The nitrogen (N_2) was used as the carrier gas. The mass flow controller (Horiba Stec, SEC-400, Mark 3) of 200 mL/min was applied to regulate the nitrogen gas flows; instead of using a high flow rate (like 1000 mL/min), the value 200 mL/min was considered sufficient because the sensor response both for QCM and IDA could be observed. If the flow rate is high then the gas flow speed also will be fast. The gas flow distributed uniformly into 16 vials of 10 mL as part of the odor delivery system (ODS), with 8 vials empty and 8 vials for analytes (liquid). Each vial was connected to a three-way solenoid valve (Takasago, EXAK-3). The field programmable gate array (FPGA, Altera Cyclone 5 SE 5CSEMA5F31C6N) was used to control on/off, the concentration variation, and the mixtures of the gaseous analytes flows in this system, the detailed information related to the ODS was available in [97].

The gas flows in this experiment were recorded by two types of sensors i.e., quartz crystal microbalance (QCM) and IDA (a miniaturized AGS sensor) where three QCMs and three IDAs can be used simultaneously. QCM is mass sensitive device, has high stability, and typically has a linear response to concentrations [98]. In this study, QCMs were coated with the same RTILs used for IDAs to complement the information related to the solubility of the analytes in the RTILs during the measurements. Since, mostly, the sensor response from QCM is

real-time (in a second), then QCMs were also used to monitor the gas flow and quantify the concentration of the analytes released by the gas delivery system during measurement. The sensor responses from three QCMs were recorded by three commercial vector network analyzers (DG8SAQ VNWA, SDR-Kits); instead of using the common oscillator circuit, the VNWA was applied because it provides more precise measurements and many parameters of QCM can be explored like the frequency, resistance, Q factor, etc. Furthermore, the sensor response from three IDAs were recorded using three commercial potentiostats using EVAL-AD5940ELCZ, Analog Devices, Middlesex County, MA, USA, that explained in more detail in the next section. The potentiostats, VNWAs, and FPGA board were connected to the computer. The volume chambers used for gas measurements for IDAs and QCMs were 5.25 cm^3 and 18 cm^3, respectively. All the measurements in this system were controlled and taken using MATLAB. The chamber for QCMs, IDAs, and the code program was available in the Appendix.

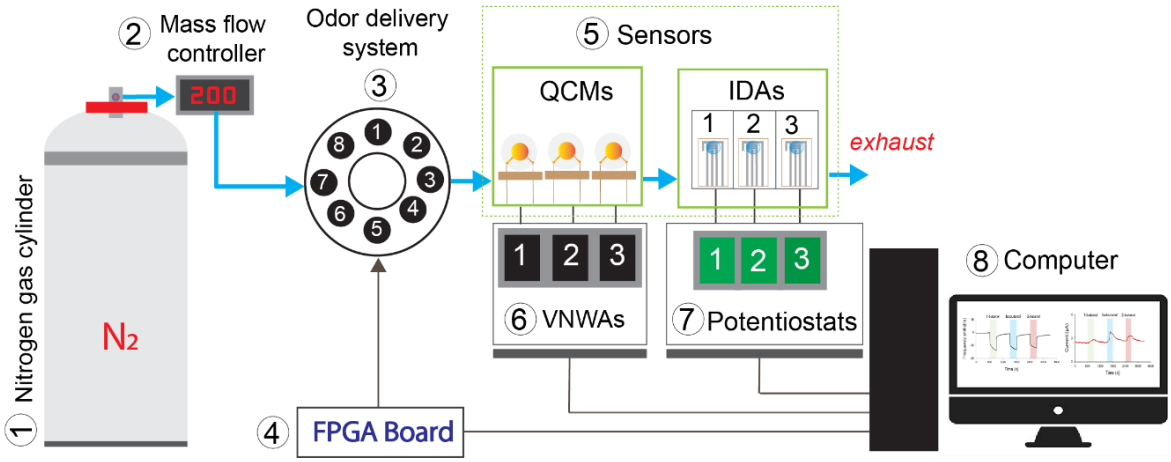

Figure 3.7: The schematic layout of gas delivery system used in this study. Reprinted from [93]

3.4 Potentiostat

The potentiostat used for gas measurement was EVAL-AD5940ELCZ from Analog Devices, Middlesex County, MA, USA. This potentiostat was chosen because it has good resolution which can measure current as small as 50 pA. It has smaller dimension size than lab fabricated potentiostat which required a bulky function generator to generate the waveform. This potentiostat has the operating voltages from -1 V to +1 V. The EVAL-AD5940ELCZ was designed specifically for the electrochemical measurements which included the EVAL-ADICUP3029 Arm® Cortex™-M3 microcontroller-based Arduino Uno as shown in Figure 3.8.a. The EVAL-AD5940ELCZ was placed on top of EVAL-ADICUP3029 as shown in Figure 3.8.b. The micro-USB cable was plugged into the USB port on the EVAL-ADICUP3029 to download the program from the computer which was written in the Keil µVision 5 software. In this study, several fixed EC potentials were fed up to the WE in the EC cell through EVAL-AD5940ELCZ. As shown in Figure 3.8.c, EVAL-AD5940ELCZ having three connectors with colors red, blue, and green, were connected to CE, RE, and WE respectively, to conduct the amperometric gas measurements. The detailed information related EVAL-AD5940ELCZ can be found in [99–102]. The code program related applying fixed EC potentials written in the Keil µVision 5 software was available in Appendix. The MATLAB code was used to record the applied EC potential and the current as sensor information was also available in Appendix.

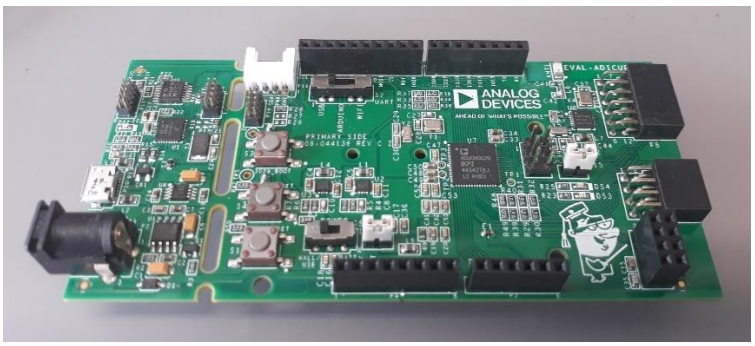

(a)

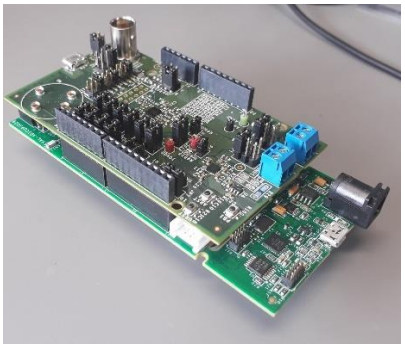

(b)

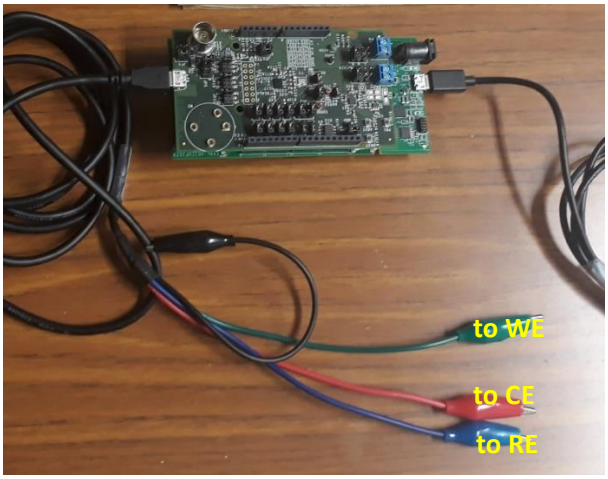

(c)

Figure 3.8: The potentiostat used for gas measurements; (a) EVAL-ADICUP3029; (b) EVAL-AD5940ELCZ placed on top of EVAL-ADICUP3029; (c) three connectors for WE, CE, and RE, respectively installed at EVAL-AD5940ELCZ for EC measurements

3.5 Discriminant analysis

The discriminant analysis was used to evaluate the separation among analytes from different combinations of several classes since this study used the isomers as target compounds which have the same molecular mass and molecular formula thus oftentimes the responses are similar. A typical statistic criterion, Wilk's lambda (Λ) was used to assess the discriminability among analytes, defined as follows [98,103,104]:

$$S_w = \sum_{k=1}^{K} \sum_{x \in C\_k} (\vec{x} - \vec{\mu}_k)(\vec{x} - \vec{\mu}_k)^T \tag{3.1}$$

$$\vec{\mu}_k = \frac{1}{n_k} \sum_{x \in C\_k} \vec{x} \tag{3.2}$$

$$S_B = \sum_{k=1}^{K} (\vec{\mu}_k - \vec{\mu})(\vec{\mu}_k - \vec{\mu})^T \tag{3.3}$$

$$\vec{\mu} = \frac{1}{n}\sum_{\forall x}\vec{x} \tag{3.4}$$

$$Wilks'\Lambda = \left|\frac{S_W}{(S_W + S_B)}\right| \tag{3.5}$$

where S_W is the variance matrix within the class, K is the number of classes, $\vec{x}$ is the measurement vector, $\vec{\mu}_k$ is the mean vector of class k, n_k is the number of measurements in class k, i.e., C_k, S_B is the variance matrix between classes, $\vec{\mu}$ is the mean vector of all measurement points, n is the total number of measurements.

Figure 3.9 illustrates the separation among three groups, i.e., group 1, group 2, and group 3 which obtained from two sensor types, e.g., sensor 1 and sensor 2. Based on the Equation 3.5, when the variation within group is small (good reproducibility) and the data variation among groups is large (good selectivity) then Wilks' lambda becomes small, therefore, good pattern separation exists. A lower value of Wilks' lambda leads a better separation.

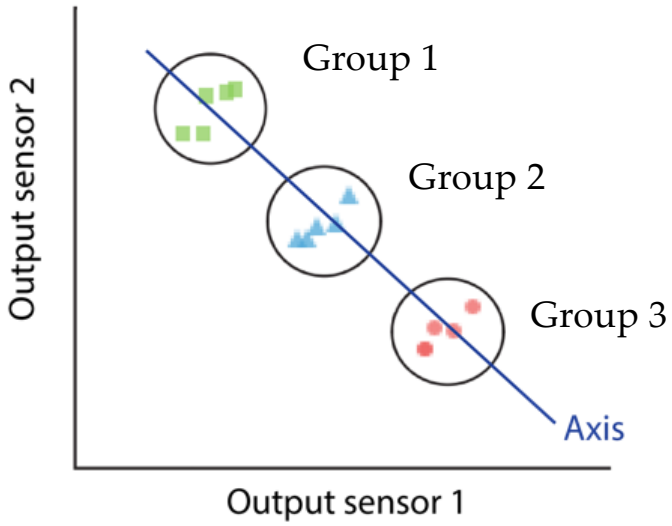

Figure 3.9: The illustration of three groups separation using two types of sensors

3.6 Summary

In this chapter, the setup for depositing sensing films (e.g., polymerization of PANI and atomic gold deposition system), gas delivery system, the potentiostat used in the gas measurement, and discriminant analysis have been explained. The atomic gold deposition system was used to fabricate the atomic gold of Au_2 clusters decorated Pt/PANI at miniaturized AGS. In the gas delivery system, nitrogen was used as the carrier gas, and the ODS system with eight channels where only three channels were used was briefly explained. In addition, besides a miniaturized AGS, the QCMs coated with the same RTILs used for IDAs were applied to complement the information related to the solubility of analytes in RTILs. The IDA used the potentiostat of EVAL-AD5940ELCZ from Analog Devices. Furthermore, the discriminant analysis used a typical statistic criterion of Wilk's lambda (Λ) to assess the gaseous butanol isomers separation numerically.

Chapter 4

Sensors using RTIL to develop miniaturized AGS

4.1 Introduction

In this chapter, the possibility of using room temperature ionic liquids (RTILs) for a miniaturized amperometric gas sensor (AGS) is investigated. Several RTILs with different cation-anion combinations are explored. The miniaturized AGS used interdigitated array electrode (IDA) where its working electrodes made of platinum (Pt) were directly used without modification since the goal in this chapter is to realize the RTIL for a miniaturized AGS. Another sensor type, i.e., quartz crystal microbalances (QCMs) were also applied to check the solubility of analytes in RTILs during gas measurement to complement the information. The gas measurement procedures, the RTILs as sensing films, and the response from QCMs and IDAs coated with the same RTILs are explained in this chapter. In addition, the sensing element selection and evaluation of the discrimination capability of butanol isomers are provided here.

4.2 Gas measurements

The gas delivery system used in this study is depicted in Figure 3.7 which consists of eight main parts, i.e., nitrogen (N_2) as carrier gas, mass flow controller (set to 200 mL/min), odor delivery system (ODS), field programmable gate array (FPGA) board, three quartz crystal microbalances (QCMs), three potentiostats (EVAL-AD5940ELCZ from Analog Devices) with the detection limit of current of 50 pA with operating voltages from -1 V to +1 V, three miniaturized AGS sensors using IDAs, three vector network analyzers (VNWAs), and a computer. The carrier gas was N_2 and the analytes were 1-butanol, iso-butanol, and 2-butanol. Herein, the gas measurements were conducted at room temperature of ~25 ^{o}C. Each measurement had 5 minutes for analyte exposure to the sensors followed by 10 minutes of recovery (only N_2 flow). The gaseous butanol concentrations released by the ODS system were also measured using the portable gas detector based on the photoionization working principle (RAE 3000 PID). Furthermore, for further study of the sensor response characteristics obtained by IDAs and QCMs coated with the same RTILs, the concentration dependency was investigated. Four different relative concentrations (RCs) of each analyte were explored (0% RC, 25% RC, 50% RC, and 100% RC) in which the relative concentration (RC) was the concentration relative to the full scale generated by ODS with 6 mL of analyte in the vial.

4.3 RTILs as sensing films

All the RTILs were purchased from Tokyo Chemical Industry Ltd. The common imidazole based RTIL was used for gas measurements. In this study, we investigated different RTILs as a thin sensing film. In this stage,

we started the RTILs selection with different cations and anions. Three RTILs were selected, the possibility of applying various RTILs for a miniaturized AGS from short to long cation chain (the order is $[EMIM]^+ < [BMIM]^+ < [HMIM]^+$) and different anions (i.e., $[Ac]^-$, $[Br]^-$, $[Cl]^-$) were investigated. Three RTILs were 1-ethyl-3-methylimidazolium acetate, 1-butyl-3-methylimidazolium bromide, and 1-hexyl-3-methylimidazolium chloride identified as [EMIM][Ac], [BMIM][Br], and [HMIM][Cl], respectively. Figure 4.1.a, b, and c shows the molecular structure of [EMIM][Ac], [BMIM][Br], and [HMIM][Cl], respectively.

Three different cation chains were included to evaluate the influence of different viscosities (or conductivities) forming RTILs against butanol isomers measurement since we know that viscosities (or conductivities) strongly depend on the cation chain. A higher alkyl chain has a higher viscosity which is more beneficial to keep its shape, moreover, if a very thin RTIL is required to apply as a coating on a miniaturized AGS. In addition, three different anions were also chosen here. A particular pair of cation-anion combination provides certain physical and chemical property, for example the electrochemical window (ECW) property. Since we used potentiostat with the operating voltages from -1 V to +1 V, hence, the RTIL has ECW more than 2 V were used. Refer to appropriate sections in Chapter 2 regarding the RTIL selections.

As shown in Table 4.1, [EMIM][Ac], [BMIM][Br], and [HMIM][Cl] have the ECWs of 3.2 V, 2.7 V, and 2.9 V, respectively. For [EMIM][Ac], the cathodic and anodic limit are -2.3 V and +0.9 V, respectively. For [BMIM][Br], the cathodic and anodic limit are -1.5 V and +1.2 V, respectively. Furthermore, [HMIM][Cl] has cathodic limit of -2.4 V with a low anodic limit of +0.5 V; the consequence of using RTIL with a high imidazolium cation length chain is that the cathodic limit tends to have a more negative potential and reduces the anodic potential [105]. Table 4.1 summarizes the basic properties of [EMIM][Ac], [BMIM][Br], and [HMIM][Cl], such as the viscosity, the density, the conductivity, and the electrochemical (EC) window.

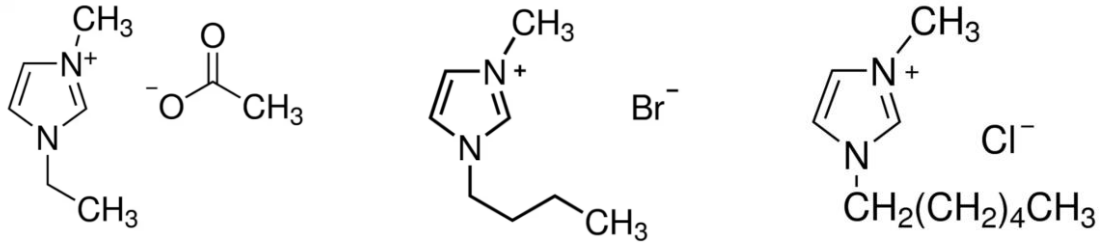

(a) (b) (c)

Figure 4.1: The molecular structure of RTILs used in this study: (a) [EMIM][Ac]; (a) [BMIM][Br]; (a) [HMIM][Cl]. Reprinted from [106–108]

Table 4.1. The basic physical and chemical properties of RTILs used in this study. Reprinted from [98]

Identifier	CAS number	Full name	Viscosity, η (P a s)	Density, ρ (Kg/m^3)	Conductivity, κ (S/m)	EC Window (V)
[EMIM][Ac]	143314-17-4	1-ethyl-3-methylimidazolium acetate	0.143 [109]	1099.3 [109]	0.2 [110]	-2.3 to +0.9 [111,112]
[BMIM][Br]	85100-77-2	1-butyl-3-methylimidazolium bromide	0.2 [113]	1300 [114]	0.1 [113]	-1.5 to +1.2 [114]
[HMIM][Cl]	171058-17-6	1-hexyl-3-methylimidazolium chloride	3.302 (a) [115]	1040 [115]	8×10^{-3} (b) [115]	-2.4 to +0.5 [116]

The information of η, ρ, and κ at 298 K (25 °C), except (a) 308.15 K (35 °C), (b) 293.15 K (20 °C)

4.4 Sensor response

4.4.1 QCMs coated with RTILs

In this study, the quartz crystal microbalance sensors (QCMs), AT-CUT (gold-electrode) which have a basic resonant frequency of 9 MHz were purchased from Seiko EG&G Ltd., Japan. The RTILs were used as the coating films on QCMs using dip-coating method illustrated in Figure 4.2 (dip coater: VLAST45-06-0100, THK Co., Ltd., Tokyo, Japan). Furthermore Table 4.2 provides the information related to dip-coating used to coat the RTILs on QCMs, i.e., the solvent, the pull-up speed, the frequency change (ΔF) and the mass loaded (ΔM) after the dip-coating process, the resistance change (Ω), and the coating's thickness (*d*). The used solvents were selected based on the solubility of RTIL. The [EMIM][Ac] is soluble in water, acetonitrile, acetone [112]. The acetone was chosen for [EMIM][Ac] because of and it has the fastest evaporation rate. The [BMIM][Br] and [HMIM][Cl] are soluble in acetonitrile, methanol, and dichloromethane [117]. Although dichloromethane has the fastest evaporation rate, it was not used because it was classified as hazardous chemical in our laboratory. Methanol was selected as solvents for [BMIM][Br] and [HMIM][Cl] because it has faster evaporation rate than acetonitrile.

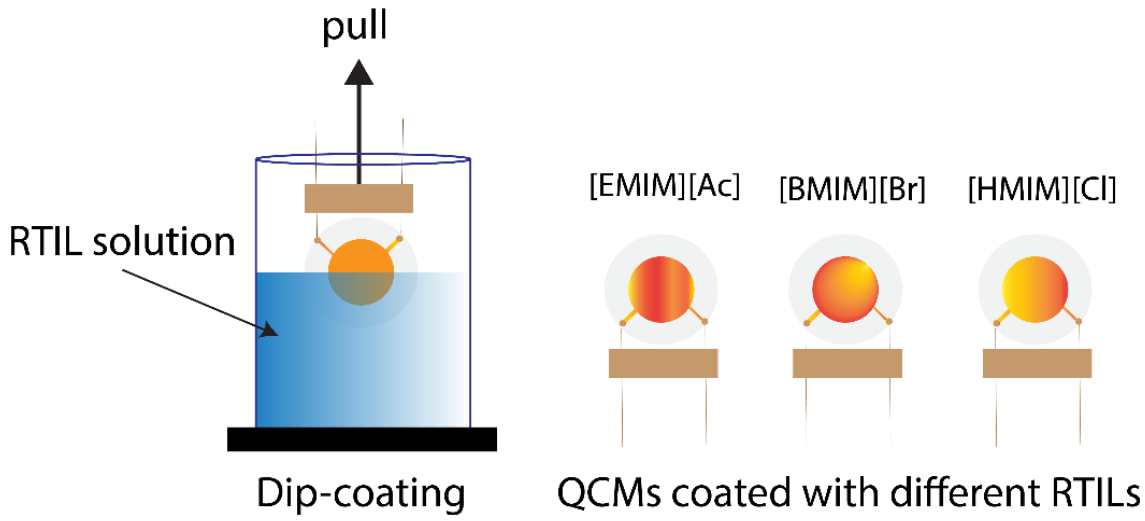

Figure 4.2: The illustration of RTILs coated on QCMs using dip-coating method

Table 4.2. The basic physical and chemical properties of RTILs used in this study. Reprinted from [98]

Identifier	QCM's coating information						
	Solvent	Concentration (mg/mL)	Pull-up speed (μm/s)	ΔF (Hz)	ΔM (μg)	ΔR (Ω)	*d* (nm)
[EMIM][Ac]	Acetone [112]	9.09	1000	577	0.62	39	28.5
[BMIM][Br]	Methanol [117]	8.72	300	675	0.72	30.8	28.3
[HMIM][Cl]	Methanol [117]	8.45	100	498	0.53	26	26.3

The coating's thickness assumed distributed uniformly on two sides of QCM's electrodes. The mass loaded after the dip-coating process calculated from Sauerbrey's formula determined in Equation 1.2

Figure 4.3 shows the sensor response from QCM coated with [EMIM][Ac] against 100% RC gaseous butanol isomers (5 minutes exposure followed by 10 minutes recovery for each analyte). QCM follows the Sauerbrey equation where the frequency shift is proportional to the adsorbed analyte's mass on its surface. In QCM, typically, the analytes having same molar mass produce a similar frequency shift. As shown in Figure 4.3, although QCM coated with [EMIM][Ac], its sensor response, i.e., frequency shift magnitudes to 1-butanol and isobutanol were almost similar.

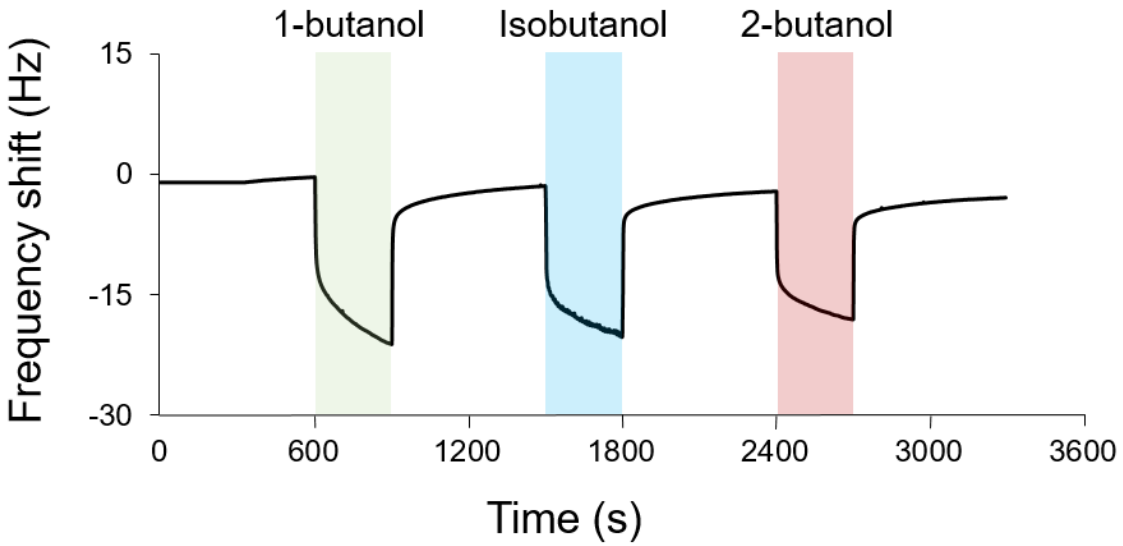

Figure 4.3: Sensor response from QCM coated with [EMIM][Ac] against 100% RC of butanol isomers. Reprinted from [98]

In this study, three RTILs having different physico-chemical properties were used as coating films on QCMs to check the solubility of butanol isomers. Table 4.3 summarizes the solubility of 100% RC butanol isomers, i.e., 1-butanol, isobutanol, 2-butanol in [EMIM][Ac], [BMIM][Br], and [HMIM][Cl] coated on QCMs. The measurements for each analyte were repeated five times with 5 minutes analyte's exposure then 10 minutes recovery time (N_2 flow); the reproducibility was assessed using mean and standard deviation (σ). As shown in Table 4.3, various frequency shifts response obtained from different sensing films RTILs coated on QCMs due to particular solubility (mass adsorption) of analyte in each RTIL mainly caused by van der Waals force effect [17].

Table 4.3. The sensor response from QCMs coated with different RTILs against butanol isomers (each measurement was repeated five times). Reprinted from [98]

Parameter	Analyte	Coating		
		[EMIM][Ac]	[BMIM][Br]	[HMIM][Cl]
Mean (Hz)	1-butanol	-20.1	-160.9	-23.0
	Isobutanol	-18.0	-165.2	-22.1
	2-butanol	-15.0	-156.2	-18.0
σ (Hz)	1-butanol	0.14	0.91	0.17
	Isobutanol	0.06	0.82	0.13
	2-butanol	0.09	0.82	0.19

The solubilities of butanol isomers in RTILs coated on QCMs were also investigated at different relative concentration level, i.e., 100%, 50%, 25%, and 0%. Each analyte vapor with certain concentration was put in a sampling bag and measured using RAE 3000 PID. The 100% RC measured by RAE 3000 PID for 1-butanol, isobutanol, and 2-butanol vapors were equal to 120 ppm, 156 ppm, and 276 ppm, respectively. Figure 4.4 shows the mean of sensor response obtained by different RTILs coated on QCMs using different concentrations. According to Figure 4.4, the solubilities of butanol isomers were detected even at low concentrations. The RTIL of [BMIM][Br] had the highest sensor response among others meaning that solubility of butanol isomers was very high in [BMIM][Br] compared to [EMIM][Ac] and [HMIM][Cl]. Furthermore, to check the linearity, the coefficient of determination (R^2) achieved from linear regression model was calculated. According to Table 4.4, the linear concentration dependency trends obtained by RTILs coated on QCM were high as determined by high R^2 (above 0.8).

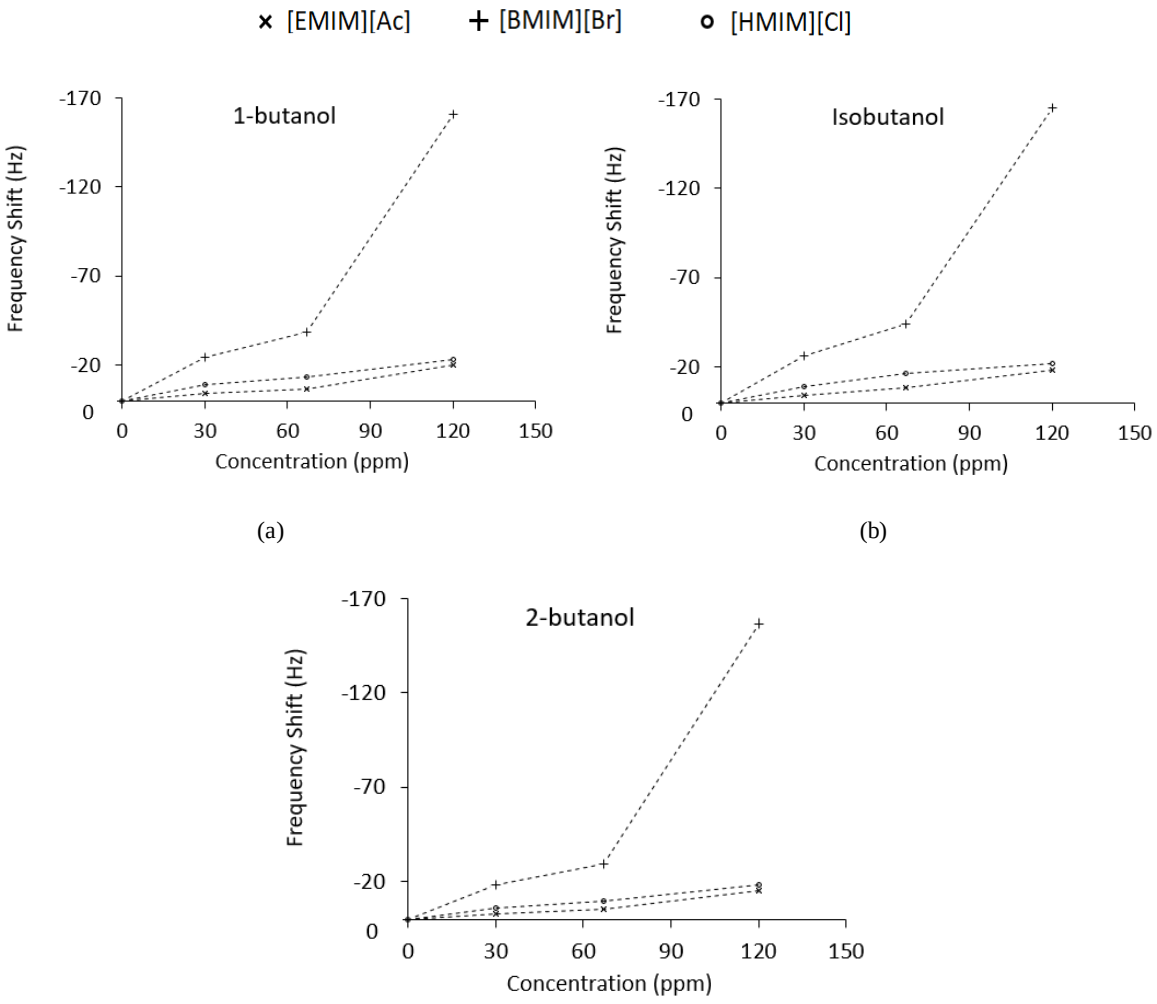

Figure 4.4: Sensor response from QCM coated with [EMIM][Ac], [BMIM][Br], and [HMIM][Cl] at different concentrations of: (a) 1-butanol; (b) Isobutanol; (c) 2-butanol. Reprinted from [98]

Table 4.4. The R^2 scores from QCMs coated with different RTILs. Reprinted from [98]

RTIL	R^2		
	1-butanol	Isobutanol	2-butanol
[EMIM][Ac]	0.96	0.99	0.97
[BMIM][Br]	0.92	0.93	0.89
[HMIM][Cl]	0.97	0.91	0.99

4.4.2 IDAs coated with RTILs

As provided by previous section, the solubilities of butanol isomers were detected using RTILs coated on QCMs. In this section, the possibility of using RTIL in a miniaturized AGS system was investigated. The different cation-anion combinations of RTILs were applied, i.e., [EMIM][Ac], [BMIM][Br], and [HMIM][Cl]. The miniaturized AGS used interdigitated array electrode (IDA). Since, the goal of this study was limited to explore the possibility using RTIL on IDA, then the working electrode (WE) of IDA made of platinum (Pt) was used without any modification. Furthermore, since the RE of IDA was made of Pt, then an Ag/AgCl ink was painted and dried for two days at RE (IDA). According to prior work, using RTIL, the Ag/AgCl ink RE exhibited enhanced sensor response over bare Pt [59]. Ag/AgCl was preferable to maintain a stable reaction during EC measurement [118]. In this experiment, RTIL of ~5 µL was dropped onto IDA surface using single channel microliter pipette (variable 2-20 µL) which was considered the minimum amount where all the electrodes were able to be covered as shown in Figure 4.5; the estimated thickness of RTIL dropped on IDA was 0.1 mm level (assumed distributed uniformly on IDA's area of 0.3 cm^2). Afterwards, the WE1, CE, and RE were connected to the potentiostat (EVAL-AD5940ELCZ from Analog Devices), whereas the WE2 was just open circuit (see Figure 4.5). The film thickness value of each RTIL dropped on the IDA was also estimated using QCM available in Table 4.5.

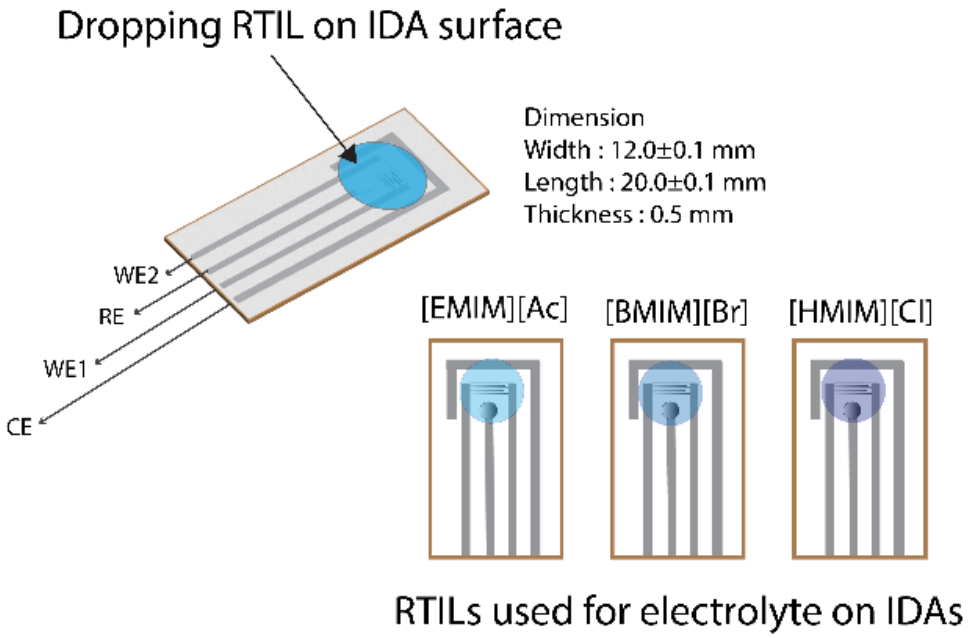

Figure 4.5: Approximately of 5 µL of RTIL used to coat the miniaturized AGS system. Reprinted from [98]

Table 4.5. The estimated thickness of RTILs dropped on IDA using QCM

Identifier	QCM's coating information			
	ΔF (Hz)	**ΔR (Ω)**	**ΔM (μg)**	***d*** **(nm)**
[EMIM][Ac]	5206.089	883.77	5.5	516.91
[BMIM][Br]	7027.606	1046.58	7.5	589.88
[HMIM][Cl]	7963.257	1229.44	8.5	837.52

The mass loaded calculated from Sauerbrey's formula determined in Equation 1.2. The RTIL thickness was assumed distributed uniformly on one side of QCM's electrodes

Figure 4.6 depicts the representative sensor response against 100% RC gaseous butanol isomers (each analyte having 5 minutes exposure followed 10 minutes recovery) from IDA coated with [EMIM][Ac] at several fixed electrochemical potential (*E*s) *vs*. Ag/AgCl, i.e., -1 V, -0.25 V, and +0.5 V. This type of sensor follows the Faraday's Law where the current produced as sensor response is proportional to the amount of analyte's concentration taking part in the EC reaction. As shown in Figure 4.6, IDA with [EMIM][Ac] at different *E*s having different sensor response against butanol isomers.

In this study, a total of six *E*s *vs*. Ag/AgCl for each RTIL were investigated. Since the potentiostat (EVAL-AD5940-ELCZ, Analog Devices) had limited operating voltages from -1V to +1V. Hence, the six *E*s selections were based on each RTIL's EC window in Table 4.1 and operating voltages from potentiostat. Three QCMs coated with RTILs were also used during the gas measurement using IDAs. Each measurement had the same procedures, i.e., five minutes of analyte exposure and 10 minutes of recovery both for QCM and IDA. The representative waveforms from QCMs with three RTILs are depicted in Figure 4.7.a. Figure 4.7.b depicts the mean of sensor responses from five repeated measurements obtained by IDAs coated with [EMIM][Ac], [BMIM][Br], and [HMIM][Cl] and those waveforms were available in Appendix. According to Figure 4.7.b, each RTIL with an *E* exhibited a certain response to butanol isomers due to a specific electrochemical reaction process shown by a current shift magnitude. From this experiment, it was concluded that three RTILs could be used for a miniaturized AGS with different solubility of butanol isomers because the different pair of cation-anion combination possessed by each RTIL provides different physical and chemical properties which affected the specific EC reaction. According to Figure 4.7.a, the [EMIM][Ac] coated on IDA had the highest solubility of isobutanol at *E* of +0.5 V *vs*. Ag/AgCl shown by the highest obtained current shift.

The different concentrations of butanol isomers were also explored in this study, i.e., 0% RC, 25% RC, 50% RC, and 100% RC. The concentration dependency trend was estimated using a linear regression where R^2 scores used to justify the linearity trend. Table 4.6 summarizes the R^2 scores against butanol isomers gas measurements for three RTILs used on IDA at several *E*s *vs*. Ag/AgCl. According to Table 4.6, mostly, obtained R^2 scores were low, approximately 0.6, except for [EMIM][Ac] at *E*s of +0.5 V and +0.9 V that had the high R^2 of 0.8. These findings indicated that a linear concentration dependency was more achieved in positive *E*s region than negative *E*s region using [EMIM][Ac]. Furthermore, the concentration dependency plot for [EMIM][Ac] on IDA at positive *E*s of +0.25 V, +0.5 V, and +0.9 V *vs*. Ag/AgCl are depicted in Figure 4.8. According to Figure 4.8, at 25% RC, the sensor response was not detected probably due to detection limits. Figure 4.9 depicts the representatives of full waveforms from different concentrations of butanol isomers using [EMIM][Ac] at +0.5 V *vs*. Ag/AgCl.

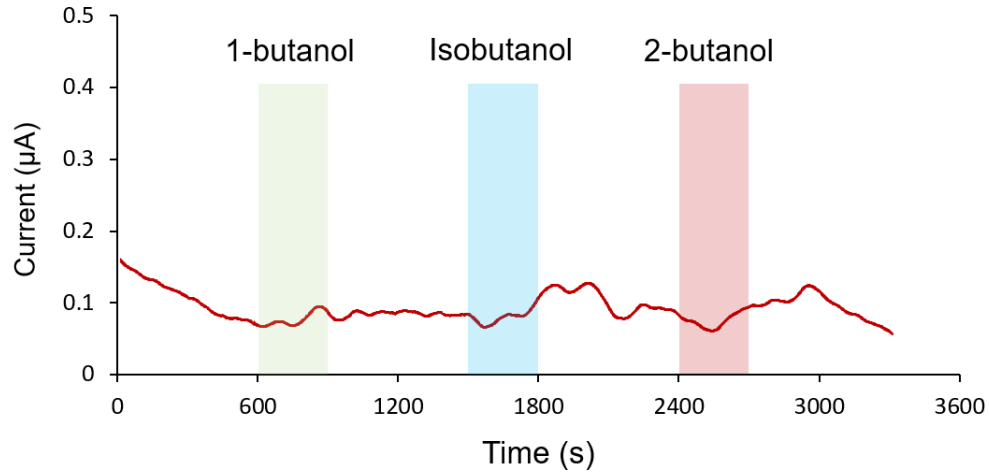

(a)

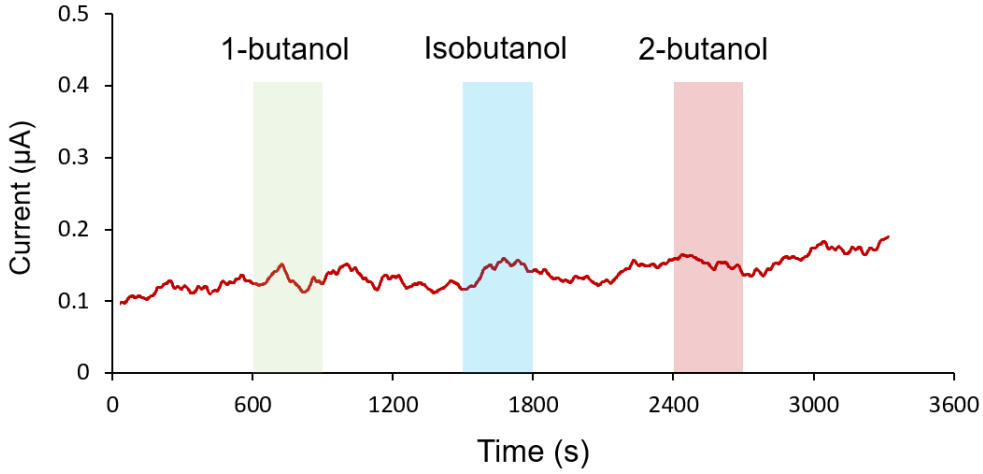

(b)

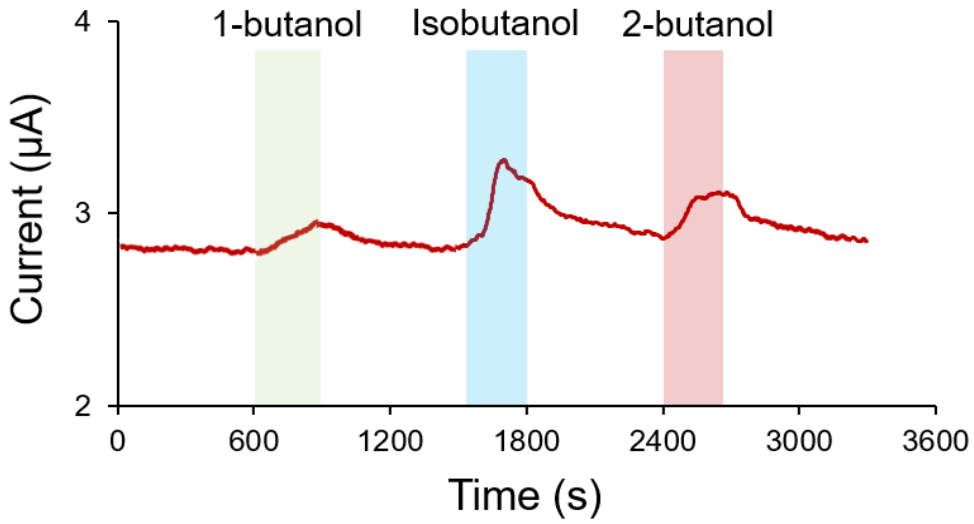

(c)

Figure 4.6: Sensor response from IDA coated with [EMIM][Ac] against 100% RC of butanol isomers at several fixed EC potential *vs.* Ag/AgCl: (a) -1 V; (b) -0.25 V; (c) +0.5 V. Reprinted from [98]

A. Sensor response from QCM coated with RTILs

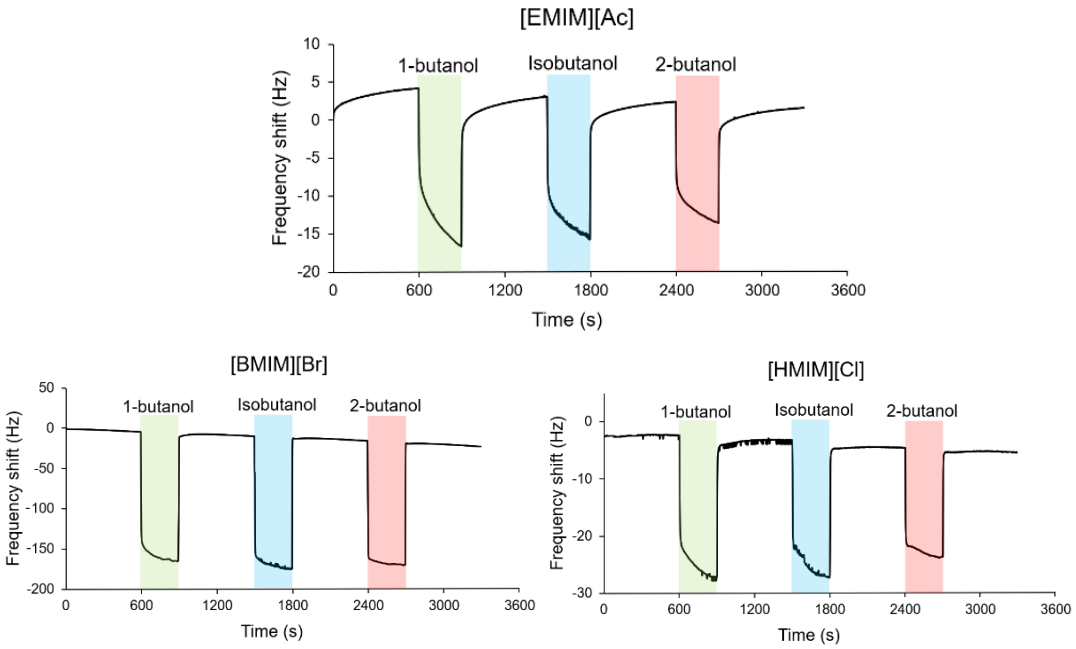

B. Sensor response from IDA coated with RTILs

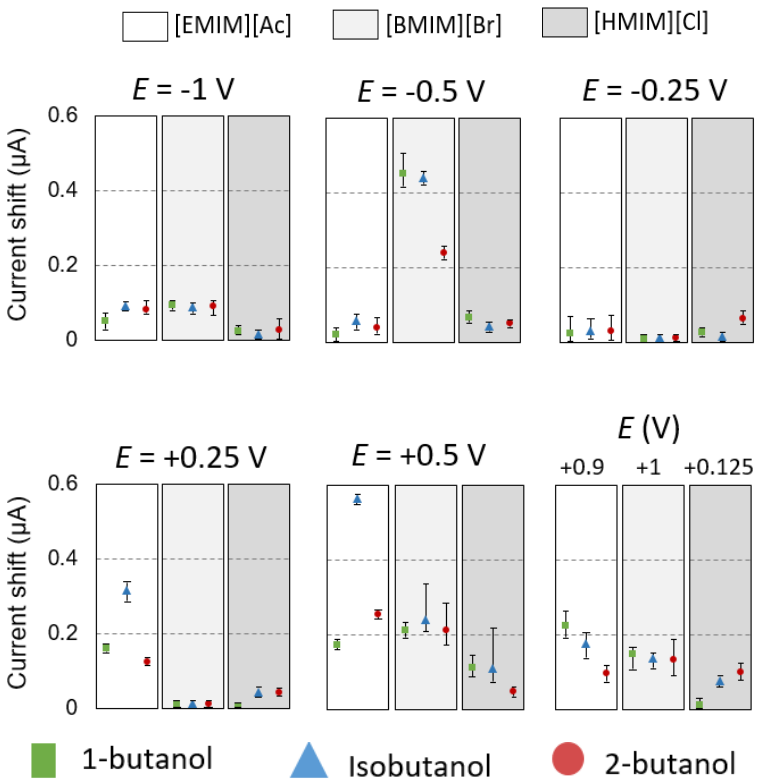

Figure 4.7: Sensor response of 100% RC butanol isomers using: (a) QCM with 3 RTILs to check the solubility of analytes during gas measurements; (b) IDAs coated with different RTILs i.e., [EMIM][Ac], [BMIM][Br], and [HMIM][Cl] at several *E*s *vs.* Ag/AgCl from 5 times measurements. Each waveform for IDAs was put in Appendix. Reprinted from [98]

Table 4.6. The R^2 scores from IDAs coated with different RTILs. Reprinted from [98]

RTIL	Fix voltage (V)	R^2		
		1-butanol	Isobutanol	2-butanol
[EMIM][Ac]	-1	0.64	0.642	0.643
	-0.5	0.60	0.61	0.60
	-0.25	0.62	0.63	0.62
	+0.25	0.61	0.62	0.63
	+0.5	0.62	0.865	0.87
	+0.9	0.872	0.877	0.882
[BMIM][Br]	-1	0.6	0.6	0.6
	-0.5	0.6	0.6404	0.6207
	-0.25	0.5	0.5	0.5
	+0.25	0.5	0.5	0.5
	+0.5	0.6857	0.508	0.647
	+1	0.65	0.62	0.6
[HMIM][Cl]	-1	0.6431	0.6433	0.6435
	-0.5	0.643	0.6431	0.6431
	-0.25	0.6432	0.643	0.643
	+0.125	0.6	0.64	0.63
	+0.25	0.67	0.64	0.643
	+0.5	0.6439	0.64	0.64

Red colour means the R^2 higher than 0.8

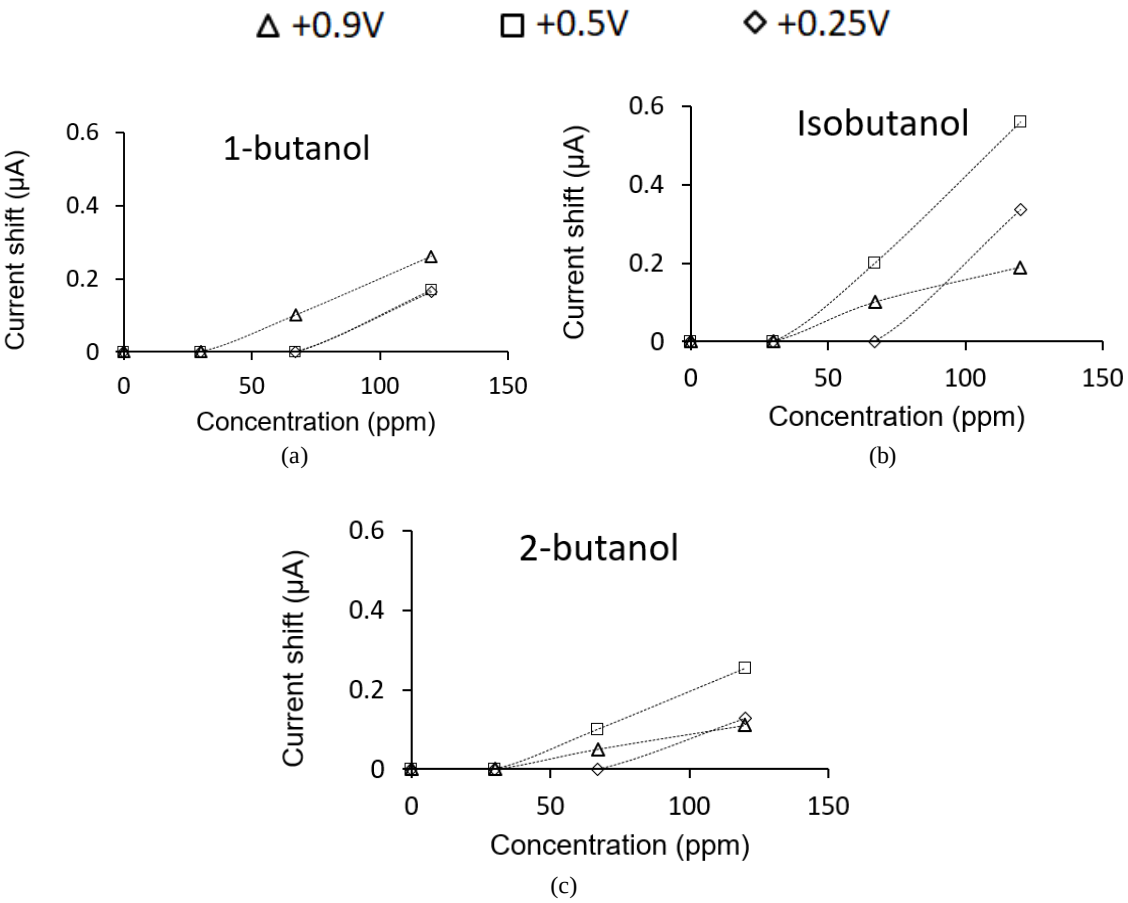

Figure 4.8: Mean sensor response for IDAs with [EMIM][Ac] at three positive *E*s (+0.25 V, +0.5 V, and +0.9 V) *vs*. Ag/AgCl against different concentrations of; (a) 1-butanol; (b) isobutanol; (c) 2-butanol. Reprinted from [98]

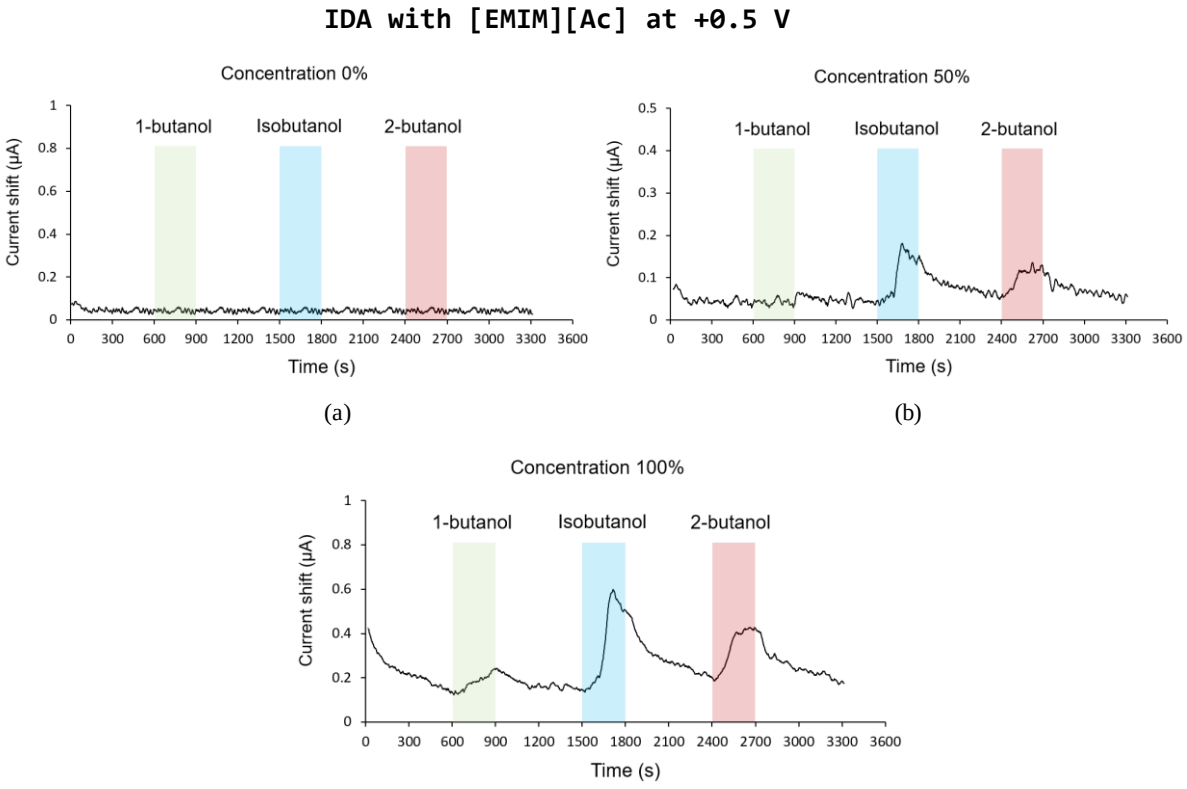

Figure 4.9: The sensor response for IDA with [EMIM][Ac] at *E* of +0.5 V *vs*. Ag/AgCl against butanol isomers at: (a) concentration of 0%; (b) concentration of 50%; (c) and concentration of 100%

4.5 Sensing element selection and evaluation of gas discrimination capability

The numerical discrimination capability among butanol isomers, i.e., 1-butanol, isobutanol, and 2-butanol, was evaluated using Wilk's lambda (Λ). Table 4.7 summarizes the representative of Wilk's Λ values from different sensor and/or *E*s combinations obtained from five repeated measurements using 100% RC. The combinations were limited up to six data dimensions. According to Table 4.7, the lowest Wilk's Λ value was 4.82×10^{-8} achieved by two sensor types loaded i.e., QCMs with three RTILs (e.g., [EMIM][Ac], [BMIM][Br], and [HMIM][Cl]) and IDAs coated with [EMIM][Ac] at positive *E*s of +0.25 V, +0.5 V, and +0.9 V *vs*. Ag/AgCl.

Furthermore, to visualize the butanol isomers' separation, the principal component analysis (PCA) was used. Figure 4.10 depicts the PCA plot from different combinations. The PCA plot using only one type of sensor is depicted in Figure 4.10.a and b for QCMs and IDAs, respectively. As shown in Figure 4.10.a, the QCMs coated with [EMIM][Ac], [BMIM][Br], and [HMIM][Cl], obtained Wilks' Λ of 5.39×10^{-5} where 2-butanol was the easiest to be distinguished among butanol isomers. Then, Figure 4.10.b shows the IDAs coated with [EMIM][Ac] at positive *E*s of +0.25 V, +0.5 V, and +0.9 V, achieved Wilks' Λ of 7.6×10^{-6} where isobutanol was the easiest to be discriminated among analytes because data points from isobutanol were not as close as the data points between 1-butanol and 2-butanol. The lowest Wilks' Λ value was achieved at 4.82×10^{-8} shown in Figure 4.10.c where two sensor types loaded with the combinations of QCMs coated with [EMIM][Ac], [BMIM][Br], and [HMIM][Cl], and IDAs coated with [EMIM][Ac] using *E*s of +0.25 V, +0.5 V, and +0.9 V *vs*. Ag/AgCl. According to Figure

4.10.c, the discrimination capability of 1-butanol, isobutanol, and 2-butanol, was enhanced as shown by a further distance between groups compared using only one sensor type. The two types of sensor enhance selectivity because it could discriminate 1-butanol, isobutanol, and 2-butanol more clearly than using one sensor type.

Table 4.7. The Wilk's lambda values obtained from different combinations. Reprinted from [98]

Data dimension	QCM	IDA	*E* (V)	Wilks' *Λ*
3	[EMIM][Ac] [BMIM][Br] [HMIM][Cl]	-	-	5.39×10^{-5}
3	-	[EMIM][Ac] [BMIM][Br] [HMIM][Cl]	-1 -1 -1	0.7815
3		[EMIM][Ac] [BMIM][Br] [HMIM][Cl]	+0.9 +1 +0.5	0.1218
3		[EMIM][Ac]	-1 -0.5 -0.25	0.185
3		[EMIM][Ac]	+0.25 +0.5 +0.9	7.6×10^{-6}
3		[BMIM][Br]	-1 -0.5 -0.25	0.037
3		[BMIM][Br]	+0.25 +0.5 +1	0.792
3		[HMIM][Cl]	-1 -0.5 -0.25	1.94×10^{-2}
3		[HMIM][Cl]	+0.125 +0.25 +0.5	4.6×10^{-3}
4	[EMIM][Ac]	[EMIM][Ac]	+0.25	8.51×10^{-8}
4	[BMIM][Br]		+0.5	2.31×10^{-6}
4	[HMIM][Cl]		+0.9	2×10^{-7}
6	[EMIM][Ac] [BMIM][Br] [HMIM][Cl]	[EMIM][Ac] [BMIM][Br] [HMIM][Cl]	-1 -1 -1	1.5×10^{-5}
6		[EMIM][Ac] [BMIM][Br] [HMIM][Cl]	+0.9 +1 +0.5	2.7×10^{-5}
6		[EMIM][Ac]	-1 -0.5 -0.25	1.30×10^{-5}
6		[EMIM][Ac]	+0.25 +0.5 +0.9	4.82×10^{-8}
6		[BMIM][Br]	-1 -0.5 -0.25	3.4×10^{-5}
6		[BMIM][Br]	+0.25 +0.5 +1	3.06×10^{-5}
6		[HMIM][Cl]	-1 -0.5 -0.25	1.78×10^{-5}
6		[HMIM][Cl]	+0.125 +0.25 +0.5	8.69×10^{-5}

Red color means the lowest Wilks' lambda

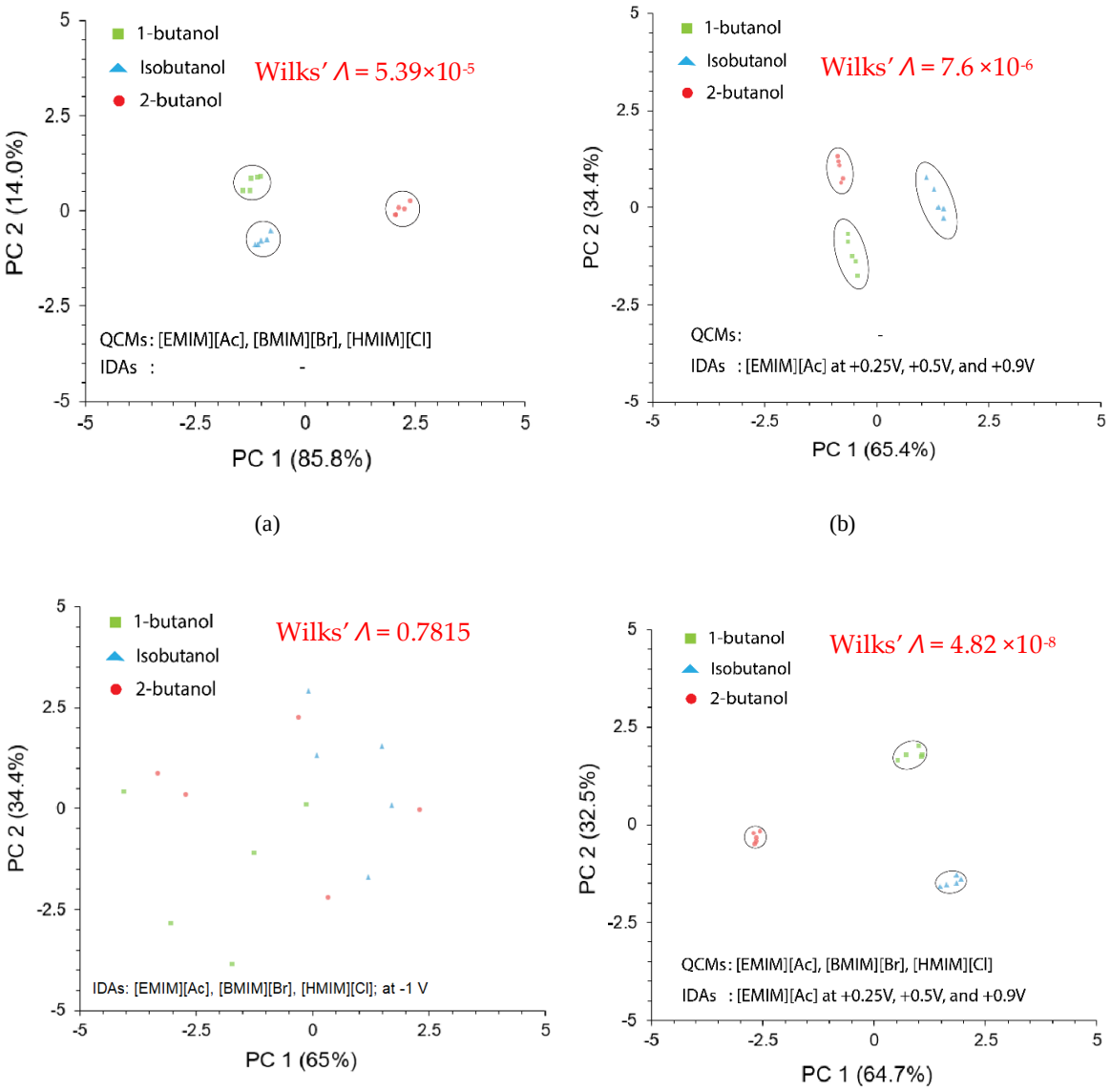

Figure 4.10: The PCA plot for; (a) QCMs with three RTILs, (b). IDAs with [EMIM][Ac] at three *E*s; (c) IDA with three RTILs at -1 V; (d) two sensor types loaded obtained from the lowest Wilks' lambda. Reprinted from [98]

4.6 Summary

In this chapter, applying RTILs in miniaturized AGS using IDA electrode was possible. Three RTILs with different cation-anion combinations were explored, i.e., [EMIM][Ac], [BMIM][Br], and [HMIM][Cl]. The solubilities of butanol isomers at 100% RC were evaluated at six fixed electrochemical potentials (*E*s) for each RTIL. Based on the results, each RTIL exhibited a specific sensor response from EC reaction due to the different physico-chemical property possessed by each RTIL. The [EMIM][Ac] had a high sensor response and exhibited a good selectivity at certain *E*s. Several concentrations were also investigated to obtain the sensor characteristics of IDA using RTILs. The [EMIM][Ac] showed promising results by achieving a high R^2 scores at several positive *E*s for gaseous butanol isomers measurement. In addition, when evaluating the sensing element selections, Although the lowest Wilk's lambda was achieved by two sensor types loaded but again incorporating the IDA coated with [EMIM][Ac] contributed to enhance the butanol isomers separation. Therefore, from all these results, next research works related to modify the working electrode of IDA with atomic gold, the RTILs having short alkyl hydrocarbon cation, i.e., 1-ethyl-3-methylimidazolium (EMIM) is selected. Probably, the diffusion transport in [EMIM][Ac] was fast because it used the short cation of [EMIM] which has the lowest viscosity among three RTILs used in this experiment; as stated in Walden's rule that the viscosity also affects the sensor response due to its relationship with conductivity.

Chapter 5

Atomic gold decorated at miniaturized AGS with selected RTILs

5.1 Introduction

In this chapter, the working electrode made of platinum in a miniaturized AGS using IDA was modified with atomic gold of Au_2 after conducting polyaniline polymerization. The verification using electrooxidation of propanol isomers in alkaline medium was used to assess the presence of Au_2 clusters decorating modified electrode of platinum-polyaniline composites. Afterward, the RTILs having short alkyl hydrocarbon cation of 1-ethyl-3-methylimidazolium (EMIM) with different anions combinations were used as a thin sensing films on modified IDA. The gaseous butanol isomers measurements were conducted and different concentrations were explored. The comparison between modified and unmodified WE of IDA were provided. The QCMs coated with RTILs were also incorporated to check the possibility of analyte's adsorption into current selected RTILs. Furthermore, the butanol isomers discrimination capability using several combinations was evaluated numerically using Wilks' lambda and visualized with linear discriminant analysis (LDA) plot.

5.2 PANI Polymerization

The PANI polymerization was conducted using 0.1 M aniline in 2 M tetrafluorobic acid and the Galvanostatic with a constant current of 0.56 mA for 260 s in the Sone Laboratory, Tokyo Institute Technology, Japan. Figure 5.1.a depicts the modified working electrode (WE) on IDA, i.e., platinum/polyaniline (Pt/PANI) composites. Furthermore, the scanning electron microscope (SEM) image of modified Pt/PANI working electrode is shown in Figure 5.1.b, which was also conducted in the Sone Laboratory, Tokyo Institute Technology, Japan. Two different magnifications were conducted to obtain a clear SEM image. The left and right SEM images had the magnification of 500 and 2000 times, respectively. As shown in Figure 5.1.b, the polyaniline nanofibers polymerized on Pt were captured using SEM (at 2000 times magnification).

The cyclic voltammogram (CV) of Pt/PANI shown in Figure 5.1.c was carried out in Nakamoto Laboratory, Tokyo Institute Technology, Japan. Ten CVs were scanned using acidic medium of 0.1 M $HClO_4$ with scan rate of 50 mV/s. The voltage was swept from -0.2 V to +0.8 V back and forth *vs.* Ag/AgCl. The Pt/PANI of IDA as working electrode, the counter electrode of IDA made of platinum, and the external Ag/AgCl as reference electrode, were used in this experiment. Furthermore, the last CV scan (the 10^{th} scan) of Pt/PANI is depicted in Figure 5.1.d. As shown in Figure 5.1.d, the CV curve of PANI in acidic medium of 0.1 M $HClO_4$ agreed with the literatures which has two redox couples, i.e., peak I and I', peak II and II' [87,119,120]. The peak I is related to the oxidation of leucoemeraldine to emeraldine, the peak II is the oxidation from emeraldine to pernigraniline, the peak II' is the reduction of pernigraniline to emeraldine, and the peak I' is the reduction of emeraldine to leucoemeraldine.

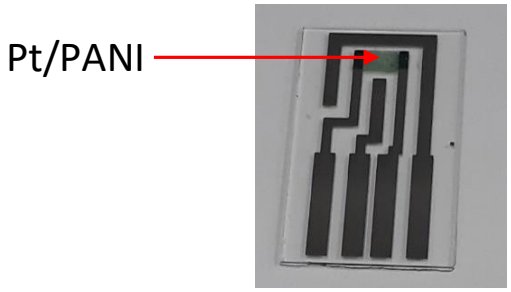

(a)

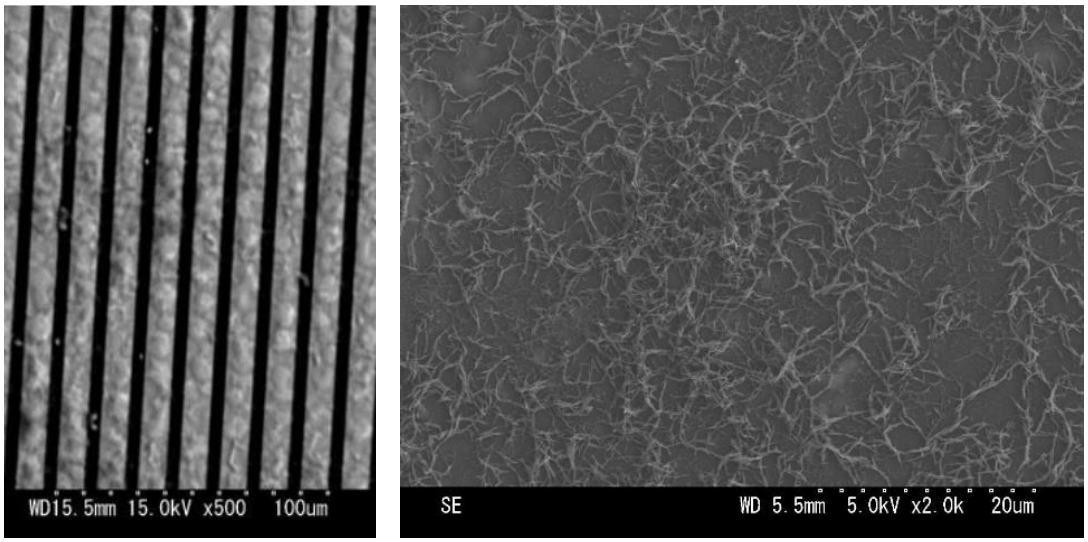

(b)

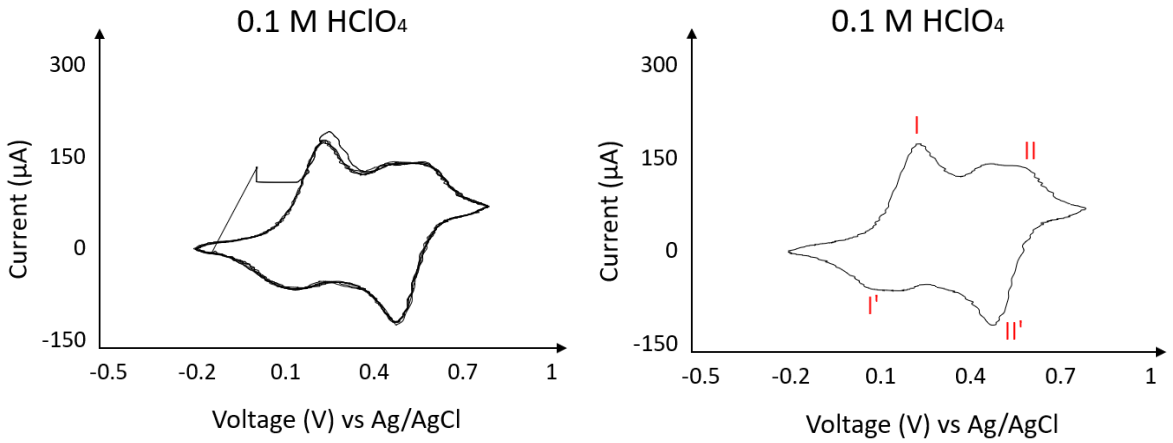

(c) (d)

Figure 5.1: The modified working electrodes at IDA: (a) Pt/PANI working electrode; (b) the SEM image of Pt/PANI composites; (c) the curves of Pt/PANI in 0.1 M$HClO_4$ with 10 CVs, (d) the last CV shown from 10 CVs scanned, scan rate was 50 mV/s. Reprinted from [93]

5.3 Atomic gold deposition

Figure 5.2.a shows the CV curve of different atomic gold formation on a same IDA electrode. The Pt/PANI/Au_0 was the modified WE at IDA without atomic gold or it was Pt/PANI. Afterward, the Pt/PANI/Au_1 followed the procedure of atomic gold deposition process with Au_N (N = 1) as shown in Figure 3.6 Furthermore,

the Pt/PANI/Au_2 was Au_2 clusters decorating Pt/PANI and the atomic gold deposition process using timing diagram shown in Figure 3.6 was completed. As shown in Figure 5.2.a, several CV curves were recorded in 0.1 M $HClO_4$ at scan rate of 50 mV/s. The CV curve of Pt/PANI/Au_2 was getting shrinkage shown by the decreased current because of degradation of PANI film due to PANI being held at a prolonged time at +0.8 V. In addition, two redox peaks at the CV curve of Pt/PANI/Au_2 were not as clear as Pt/PANI/Au_0 or Pt/PANI/Au_1. According to Alex P. Jonke et.al., the number of deposited atomic gold in PANI has a major effect on the EC properties, the CV curve with a high number of deposited atomic gold has a featureless and flat CV curve, i.e., no two redox peaks could be observed, for this points, so far, it is not clear what is causing this effect [87]. Although the degradation and flatness occurred, the performance of PANI decorated with even numbered-atomic gold showed a high catalytic activity compared to PANI without atomic gold or PANI decorated with odd-numbered atomic gold [57,87,89,91]. Furthermore, Figure 5.2.b depicts the image of the modified working electrode of Pt/PANI/Au_2 at IDA after the atomic gold deposition process.

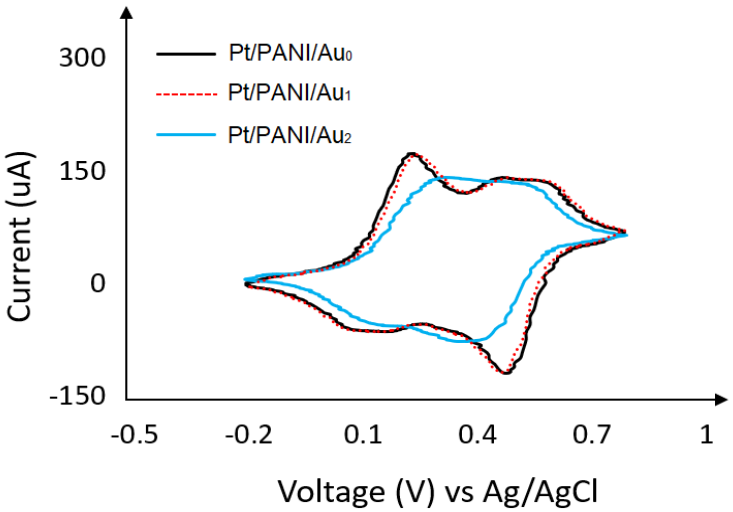

(a)

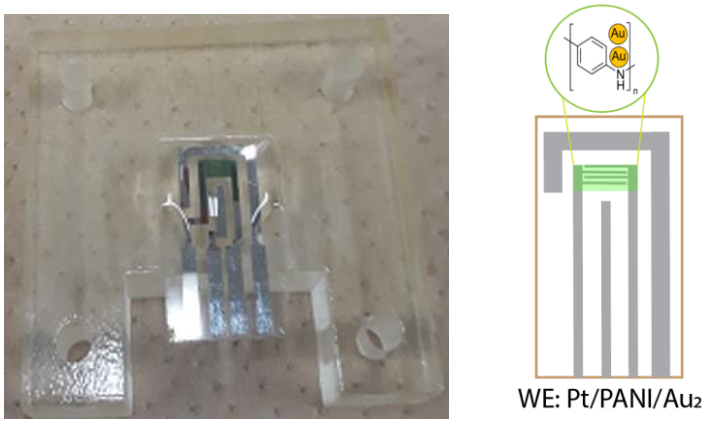

(b)

Figure 5.2: Atomic gold deposition: (a) CV curve of Pt/PANI with Au_0, Au_1, and Au_2 on the same IDA electrode in 0.1 M $HClO_4$ with scan rate of 50 mV/s; (b) Pt/PANI/Au_2 after deposition process, a thin double-sided tape was glued between IDA's substrate and acrylic chamber to maintain the IDA's position during the atomic gold deposition process. Reprinted from [93]

The current commercial SEM technology is not able to be used to capture the atomic gold in PANI due to the resolution limits. Therefore, the electrooxidation of propanol isomers in alkaline medium are massively used by researchers to confirm the presence of atomic gold clusters, such an odd-even pattern oscillation must be obtained when using the atomic gold clusters [59,60,89,120–123]. In the previous works, our group member conducted measurement of atomic gold clusters with N = 1 to 4, the odd-even patterns were obtained both for 1-propanol and 2-propanol which were explained in Chapter 2, the detailed CV curves and odd-even pattern using Pt/PANI/Au_N (N = 1 to 4) were shown in Figure 2.20. Since in this research we focused only using Pt/PANI/Au_2 for a miniaturized sensor, then the results from a bulky electrode using Pt/PANI/Au_2 is depicted in Figure 5.3. As shown in Figure 5.3, three different electrodes (e.g., EL1, EL2, EL3) were used for measurement of 0.5 M 1 propanol and 0.5 M 2-propanol in 1 M KOH against Ag/AgCl reference electrode. All the electrodes showed the same trends, i.e., two oxidation peaks obtained. For 1-propanol (red), a higher oxidation peak obtained at around –0.2 V than oxidation peak at around +0.2 V. For 2-propanol (blue), a higher oxidation peak occurred at around +0.2 V than oxidation peak at around –0.2 V.

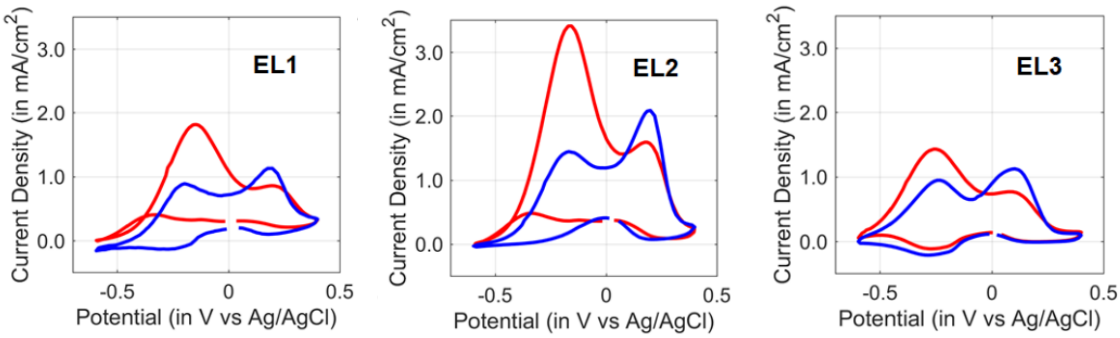

Figure 5.3: The comparison of CVs curves using three different bulky electrodes (Pt/PANI/Au_2) for electrooxidation of 0.5 M 1-propanol (red) and 0.5 M 2-propanol (blue) in 1 M KOH. The scan rate was 100 mV/s. Reprinted form [58]

In this research, the atomic gold decorated Pt/PANI was applied in a miniaturized AGS using IDA. Figure 5.4 depicts the CV curve of 1-propanol (0.5 M) and 2-propanol (0.5 M) in 1 M KOH exhibited by Pt/PANI/Au_0, Pt/PANI/Au_1, and Pt/PANI/Au_2 using IDA; 10 CVs were scanned, only the last CV shown, the scan rate was 50 mV/s. As shown in Figure 5.4, Pt/PANI/Au_2 had a catalytic activity and the highest current density both for 1-propanol (Figure 5.4.a) and 2-propanol (Figure 5.4.b), agreeing with our previous results in the bulky AGS system and with atomic gold achieved by other researchers [59,60,89,120–123]. As shown in Figure 5.4.a, for 1-propanol, at the forward scan, Pt/PANI/Au_2 had two oxidation peaks at −0.1 V and +0.25 V, while Pt/PANI/Au_1 and Pt/PANI/Au_0 only had one oxidation peak at −0.1 V. As shown in Figure 5.4.b, for 2-propanol, at the forward scan, Pt/PANI/Au_2 exhibited two oxidation peaks at −0.1 V and +0.25 V, whereas no oxidation peak was obtained using Pt/PANI/Au_0 and the Pt/PANI/Au_1 only had one oxidation peak at −0.1 V. Furthermore, using Pt/PANI/Au_2, the current density at 1st oxidation peak was higher than at the 2nd oxidation peak for 1-propanol, whereas 2-propanol showed a lower current density at the 1st peak than the 2nd peak. Thus, the deposition of Au_2 clusters on Pt/PANI was confirmed in this research study.

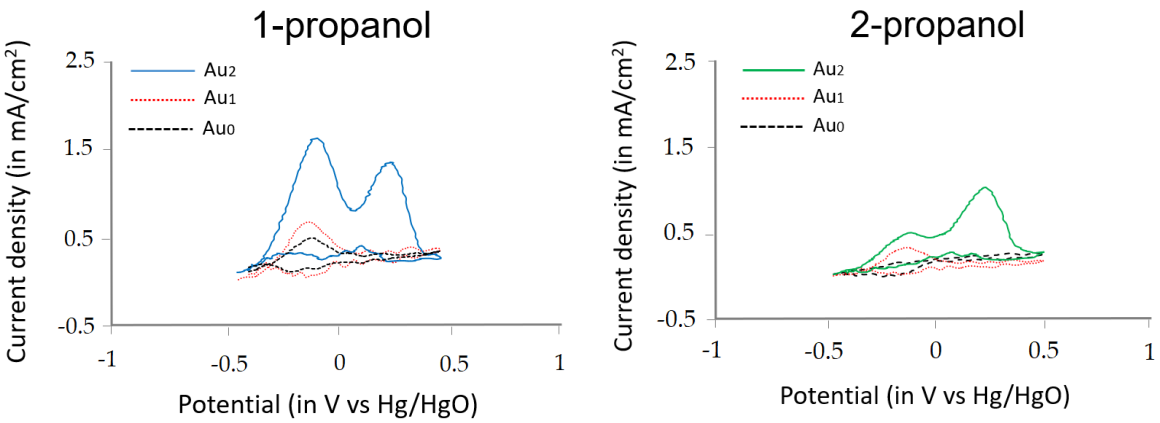

(a) (b)

Figure 5.4: The comparison using Pt/PANI/Au_2, Pt/PANI/Au_1, and Pt/PANI/Au_0 in the electrooxidation of: (a) 1-propanol; (b) 2-propanol, in alkaline medium (1 M KOH). The scan rate was 50 mV/s. Reprinted form [93]

5.4 RTILs as sensing films

In this experiment, the RTILs having short alkyl hydrocarbon cation of 1-ethyl-3-methylimidazolium (EMIM) with different anions were selected, i.e., 1-ethyl-3-methylimidazolium acetate ([EMIM][Ac]), 1-ethyl-3-methylimidazolium trifluoromethanesulfonate ([EMIM][Otf]), 1-ethyl-3-methylimidazolium chloride ([EMIM][Cl]). Although the cation was same, the anion was different, resulting a certain physico-chemical property of the RTIL. Figure 5.5 depicts the molecular structures of three RTILs as a thin sensing films in this study, i.e., [EMIM][Ac], [EMIM][Otf], and [EMIM][Cl] shown in Figure 5.5.a, b, and c, respectively. Furthermore, the detailed information regarding the basic properties possessed by each RTILs are available in Table 5.1. The anion of $[Otf]^-$ and $[Cl]^-$ were selected because their conductivities are higher and lower compared to $[Ac]^-$, respectively.

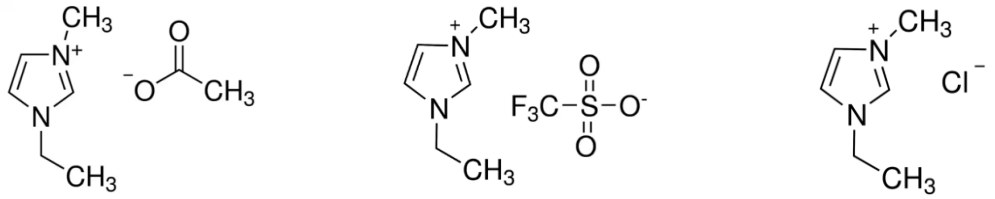

(a) (b) (c)

Figure 5.5: The molecular structures of three RTILs used in this experiment: (a) [EMIM][Ac]; (b) [EMIM][Otf]; (c) [EMIM][Cl]. Reprinted from [106,124,125]

Table 5.1. The basic physico-chemical properties of RTILs used in this study. Reprinted form [93]

Identifier	CAS number	Full name	Viscosity, η (P a s)	Density, ρ (Kg/m^3)	Conductivity, κ (S/m)	EC Window (V)
[EMIM][Ac]	143314-17-4	1-ethyl-3-methylimidazolium acetate	0.143 [109]	1099.3 [109]	0.2 [110]	-2.3 to +0.9 [111,112]
[EMIM][Otf]	145022-44-2	1-ethyl-3-methylimidazolium trifluoromethanesulfonate	0.042 [109]	1385.9 [109]	0.9 [126]	4.3 [105]
[EMIM][Cl]	65039-09-0	1-ethyl-3-methylimidazolium chloride	0.047 (a) [127]	1112 (a) [127]	0.108 [128]	-

The information of η, ρ, and κ at 298 K (25 °C), except (a) 353.15 K (80 °C)

5.5 Sensor response with selected RTILs

5.5.1 QCMs coated with RTILs

Three quartz crystal microbalance sensors (QCMs), AT-CUT used in this experiment were purchased from Seiko EG&G Ltd., Japan, which have a basic resonant frequency of 9 MHz. Three RTILs, i.e., [EMIM][Ac], [EMIM][Otf], and [EMIM][Cl] were coated on QCMs with dip-coating method depicted in Figure 5.6 (dip coater: VLAST45-06-0100, THK Co., Ltd., Tokyo, Japan). The coating information such as the solvent, the speed of pull-up, the change of frequency (ΔF), the change of mass (ΔM) after the dip-coating, and the coating's thickness (*d*), were summarized in Table 5.2. The used solvents were based on the solubility of each RTIL and the solvent's evaporation rate. The [EMIM][Ac] is soluble acetone, acetonitrile, and water [112]. Among those solvents, acetone has the fastest evaporation rate, hence we selected acetone for [EMIM][Ac]. The [EMIM][Otf] is soluble in dichloromethane, acetone, acetonitrile, water, isopropanol, ethyl acetate, and ethanol [129]; since dichloromethane was classified into hazardous chemical in our laboratory, then acetone was selected as solvent for [EMIM][Otf]. Furthermore, for [EMIM][Ac], it is soluble in acetonitrile [117], [130].

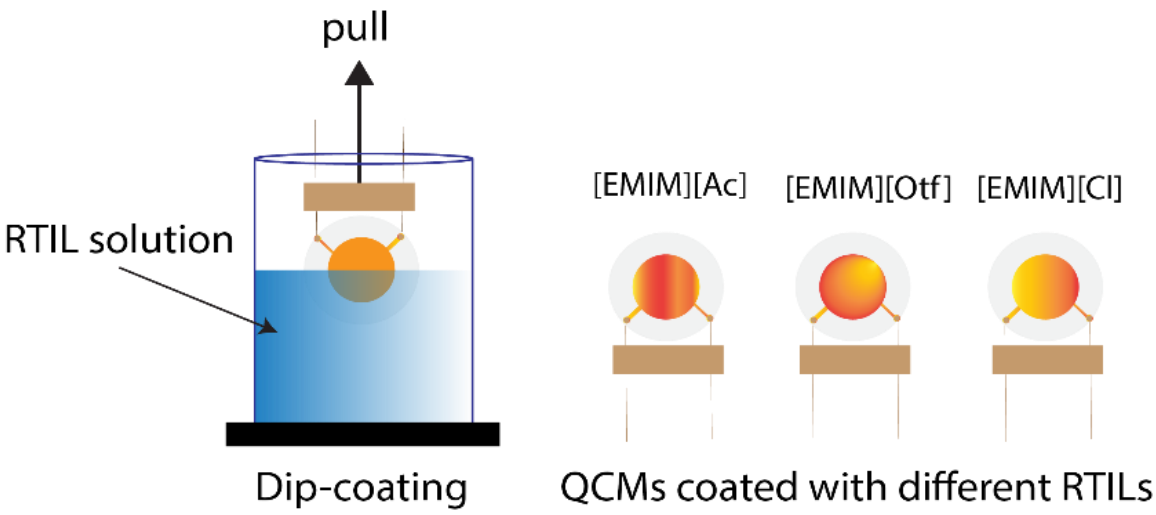

Figure 5.6: RTILs coated on QCMs using dip-coating method. Reprinted from [93]

Table 5.2. The coatings information. Reprinted from [93]

Identifier	QCM's coating information					
	Solvent	Concentration (mg/mL)	Pull-up speed (μm/s)	ΔF (Hz)	ΔM (μg)	*d* (nm)
[EMIM][Ac]	Acetone [110], [112]	10	1000	435	0.46	17.12
[EMIM][Otf]	Acetone [129]	9.09	1000	577	0.62	28.50
[EMIM][Cl]	Acetonitrile [117], [130]	9.09	100	872	0.93	33.09

The coating's thickness assumed distributed uniformly on two sides of QCM's electrodes. The mass loaded after the dip-coating process calculated from Sauerbrey's formula determined in Equation 1.2

Three QCMs coated with three RTILs, i.e., [EMIM][Ac], [EMIM][Otf], and [EMIM][Cl] were applied to check the solubility of gaseous butanol isomers with different transducer. Five relative concentrations (RCs) of butanol isomers were explored, i.e., 0%, 25%, 50%, 75%, and 100%; the relative

concentration was the amount of gaseous concentration released by ODS relative to the full scale of 6 mL analyte in the vial. The portable detector RAE 3000 PID based on photoionization, was used to quantify the equivalent amounts of RCs released by ODS as shown in Figure 5.7. Each concentration of analyte released by ODS was collected in a sampling bag and measured using RAE 3000 PID. Each analyte measurement had 5 minutes exposure time followed by 10 minutes recovery time. According to Figure 5.7.a–c, the noisy signals were obtained at 25%, 50%, and 75% RCs due to solenoid switching state (on/off) of the solenoid valve. The ODS used pulse width modulation (PWM) to control the on/off state for the solenoid valve to generate the gas concentration. When the RC was set to 100% for an analyte then the duty cycle was 100% meaning that the solenoid valve for that analyte was switched on for a given measurement time (here, 5 minutes for analyte exposure). However, for 75% RC, the duty cycle was 75%, the solenoid valve had two switching states (i.e., on and off), for example, if the period was 1 s, then solenoid valve was on for 0.75 s to generate that analyte flowing to QCMs coated with RTILs then the frequency magnitudes were decreased due to the presence of the analyte, afterward, the solenoid valve was off for 0.25 s (only N_2 flow), then the frequency magnitudes from QCMs were increased due to the absence of the analyte, this procedure was repeated during a given measurement time (this study used 5 minutes for analyte exposure). Therefore, at 25%, 50%, and 75% RCs, the decrease-increase of the frequency magnitude during the analyte exposure time was observed.

As shown in Figure 5.7.a–c, the real-time response to butanol isomers at five RCs was obtained by all QCMs coated with three RTILs. In addition, the higher concentration of butanol isomers, the higher the frequency change. Since the loaded mass of analyte on QCM surface is proportional to the frequency change, the varying frequency change magnitudes were affected by varying adsorptions occurred at each RTIL coated on QCM. Figure 5.7.d depicts the representative concentration dependency trend estimated using linear regression for 1-butanol using three RTILs. As shown in Figure 5.7.d, the coefficient of determination (R^2) scores from all RTILs coated on QCMs were high ~0.99 indicating their strong linear trend against 1-butanol. Furthermore, the mean, and standard deviation of five repeated measurements at certain RC for all analytes using three RTILs coated on QCMs are summarized in Table 5.3. In addition, the R^2 scores are also provided. Based on the Table 5.3, all obtained R^2 scores are high ~0.9, hence confirming their high linear concentration dependency trend.

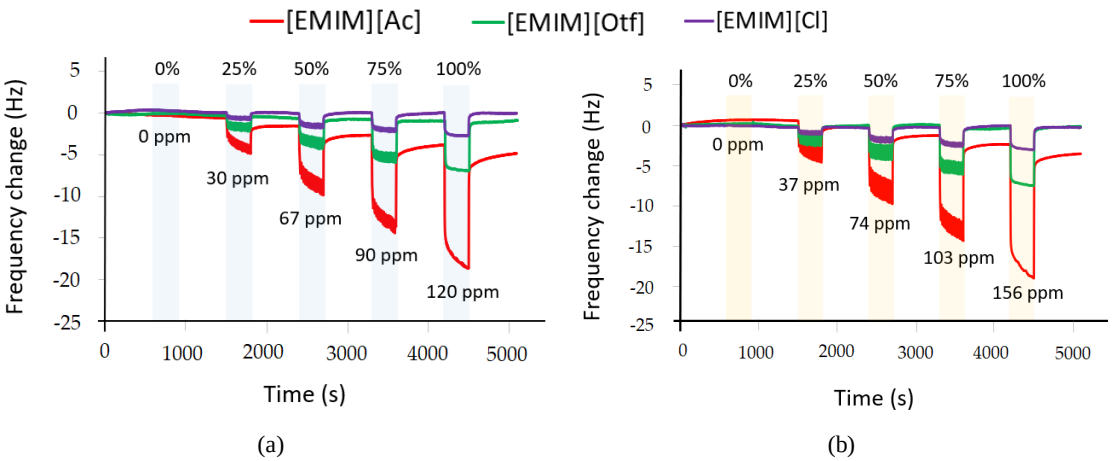

(a) (b)

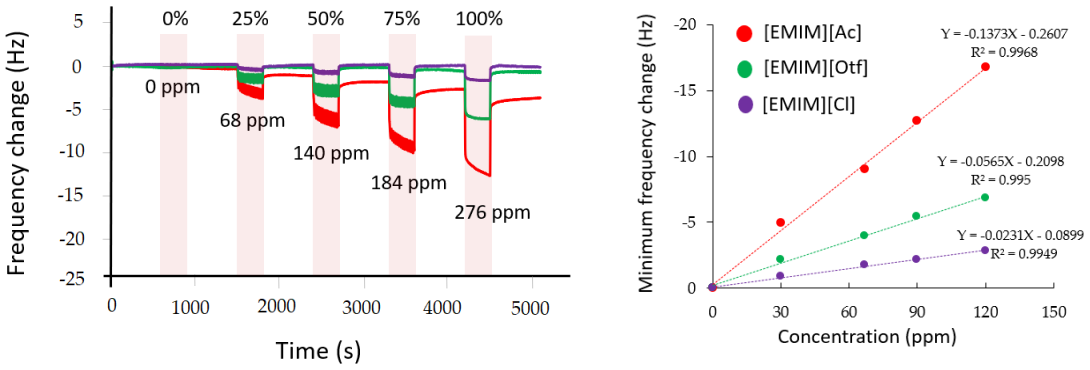

(c) (d)

Figure 5.7: Various sensor responses from QCMs coated with three RTILs using different concentrations for butanol isomers: (a) 1-butanol; (b) Isobutanol; (c) 2-butanol; (d) concentration dependency trends estimated using linear regression for 1-butanol. Reprinted from [93]

Table 5.3. The mean, standard deviation, and R^2 score from QCMs with three RTILs. Reprinted from [93]

RTIL	Analyte	Mean in Hz (Standard Deviation in Hz)					R^2
		0% RC	25% RC	50% RC	75% RC	100% RC	
[EMIM][Ac]	1-butanol	0 (0)	−4.942 (0.467)	−9.056 (0.791)	−12.7 (0.848)	−16.77 (1.532)	0.996
	Isobutanol	0 (0)	−5.08 (0.396)	−9.176 (0.548)	−13.1 (0.938)	−16.44 (1.656)	0.978
	2-butanol	0 (0)	−3.322 (0.276)	−6.102 (0.246)	−8.404 (0.620)	−10.16 (0.482)	0.971
[EMIM][Otf]	1-butanol	0 (0)	−2.138 (0.169)	−3.994 (0.148)	−5.44 (0.240)	−6.826 (0.204)	0.995
	Isobutanol	0 (0)	−2.482 (0.179)	−4.23 (0.241)	−5.782 (0.256)	−6.98 (0.258)	0.960
	2-butanol	0 (0)	−2.136 (0.276)	−3.78 (0.370)	−4.982 (0.694)	−6.22 (0.549)	0.974
[EMIM][Cl]	1-butanol	0 (0)	−0.86 (0.049)	−1.728 (0.096)	−2.146 (0.154)	−2.816 (0.093)	0.994
	Isobutanol	0 (0)	−1.04 (0.038)	−1.844 (0.104)	−2.352 (0.156)	−3.036 (0.136)	0.971
	2-butanol	0 (0)	−0.702 (0.072)	−1.31 (0.081)	−2.032 (0.167)	−2.3922 (0.183)	0.967

The value in parentheses is the standard deviation

5.5.2 IDAs coated with RTILs

In the gas sensing measurements, three selected RTILs i.e., [EMIM][Ac], [EMIM][Otf], and [EMIM][Cl] were used as thin films on a miniaturized AGS. Figure 5.8 depicts the preparation before gas sensing measurements conducted. The Ag/AgCl ink was used as RE to form a stable EC reaction which purchased from BAS Co., Ltd., Tokyo, Japan. As shown in Figure 5.8.a, the Ag/AgCl ink was painted and dried for two days to get strong adhesion to cover the Pt reference electrode at IDA. Both Pt/PANI/Au_0 and Pt/PANI/Au_2 used a dried Ag/AgCl ink. Furthermore, 5 µL of RTIL was dropped IDA surface (i.e., Pt/PANI/Au_0 and Pt/PANI/Au_2), and all the WE, CE, and RE were covered, as shown in Figure 5.8.b. After the Ag/AgCl was in contact with RTIL as shown in Figure 5.8.b, it can be used for two weeks for measurements; more than two weeks, the Ag/AgCl was peel off from platinum (weak adhesion) and soluble in RTIL. 5 µL of RTIL used for IDA was dropped on one side of QCM's electrode to estimate its thickness which was summarized in Table 5.4.

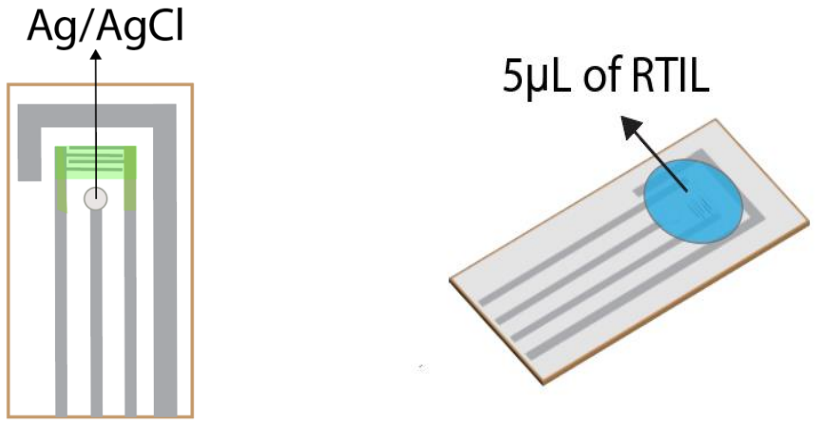

(a) (b)

Figure 5.8: The preparation before gaseous butanol isomer measurements: (a) Ag/AgCl ink painted and dried on RE of IDA; (b) 5 µL of RTIL dropped on IDA surface. Reprinted from [93]

Table 5.4. The thickness of RTILs dropped on IDA estimated using QCM

Identifier	QCM's coating information			
	ΔF (Hz)	**ΔR (Ω)**	**ΔM (µg)**	***d*** **(nm)**
[EMIM][Ac]	5206.089	883.77	5.5	516.91
[EMIM][Otf]	5921.939	945.09	6.3	467.36
[EMIM][Cl]	2186.273	871.9	2.3	215.05

The mass loaded calculated from Sauerbrey's formula determined in Equation 1.2. The RTIL thickness was assumed distributed uniformly on one side of QCM's electrodes

Two different types of IDAs were used, i.e., Pt/PANI/Au_0 and Pt/PANI/Au_2, which were coated with three RTILs [EMIM][Ac], [EMIM][Otf], and [EMIM][Cl] for butanol isomers measurements. Figure 5.9 depicts the comparison results of Pt/PANI/Au_2 and Pt/PANI/Au_0 obtained from five repeated measurements at 100% RC in which the exposure time for every analyte was 5 min followed by the recovery time of 10 min (N_2 flows). As shown in Figure 5.9, majorly, the Pt/PANI/Au_2 showed the catalytic activity by possessing a higher current density than Pt/PANI/Au_0, meaning that Au_2 deposition process was successfully conducted on modified working electrode at IDA and also active in RTILs and the different anions to form RTILs contribute to a specific EC reaction. In this experiment, three positive fixed electrochemical potentials (*E*s) *vs*. Ag/AgCl reference electrode at each RTIL were explored. The *E*s selections were based on the EC window of each RTIL (Table 5.1) and operating voltages from potentiostat (EVAL-AD5940ELCZ, Analog Devices). As shown in Figure 5.9, the magnitudes of current density owned by Pt/PANI/Au_2 using several RTILs were also varied by altering the *E*s; the highest sensitivity achieved at specific *E* indicated that the diffusion transport from the amount of analyte's concentration taking part in EC reaction was large by used that specific *E*; as shown in Figure 5.9, the high response of [EMIM][Ac] to butanol isomers were at +0.5 V whereas [EMIM][Otf] and [EMIM][Cl] were at +0.25 V.

Figure 5.10 depicts the tendency relationship between the solubility of butanol isomers in QCM and EC reaction in AGS coated with the same RTILs. Several concentrations were included in this plot, i.e., 100%, 75%, 50%, 25%, and 0%. In the AGS, the sensor data information (i.e., current shift) was obtained from modified electrodes of Pt/PANI/Au_2 using three RTILs with a certain voltage, i.e., [EMIM][Ac] at +0.5

V, [EMIM][Otf] at +0.25 V, and [EMIM][Cl] at +0.25 V. A linear regression model was used to estimate the linear tendency between the sensor information from QCM (frequency shift) and AGS (current shift) for 1-butanol, isobutanol, and 2-butanol vapors depicted in Figure 5.10.a, b, and c, respectively. As shown in Figure 5.10.a, the correlation between frequency shift (QCM) and current shift (AGS) using RTIL of [EMIM][Ac] and [EMIM][Otf] for gaseous 1-butanol exhibited a linear relationship tendency due to by achieved the high R^2 scores, i.e., 0.90 for [EMIM][Ac] and 0.98 for [EMIM][Otf]. On the other hand, for [EMIM][Cl] obtained the R^2 score of 0.79. For isobutanol vapors shown in Figure 5.10.b, the R^2 scores were in order from high to low from [EMIM][Otf] with 0.92 followed by [EMIM][Ac] with 0.89 then [EMIM][Cl] with 0.76. For 2-butanol, as shown in Figure 5.10.c, the highest R^2 with score of 0.94 was obtained by [EMIM][Otf], the RTILs of [EMIM][Ac] and [EMIM][Cl] had R^2 of 0.79 and 0.4, respectively. Based on Figure 5.10.a (1-butanol), Figure 5.10.b (isobutanol), and Figure 5.10.c (2-butanol), the highest sensor response of frequency shift (QCM) and current shift (AGS) were achieved by using same RTIL of [EMIM][Ac]. Furthermore, for the highest linear relationship between frequency shift (QCM) and current shift (AGS) for butanol isomers (i.e., 1-butanol, isobutanol, and 2-butanol) was obtained by using same RTIL of [EMIM][Otf].

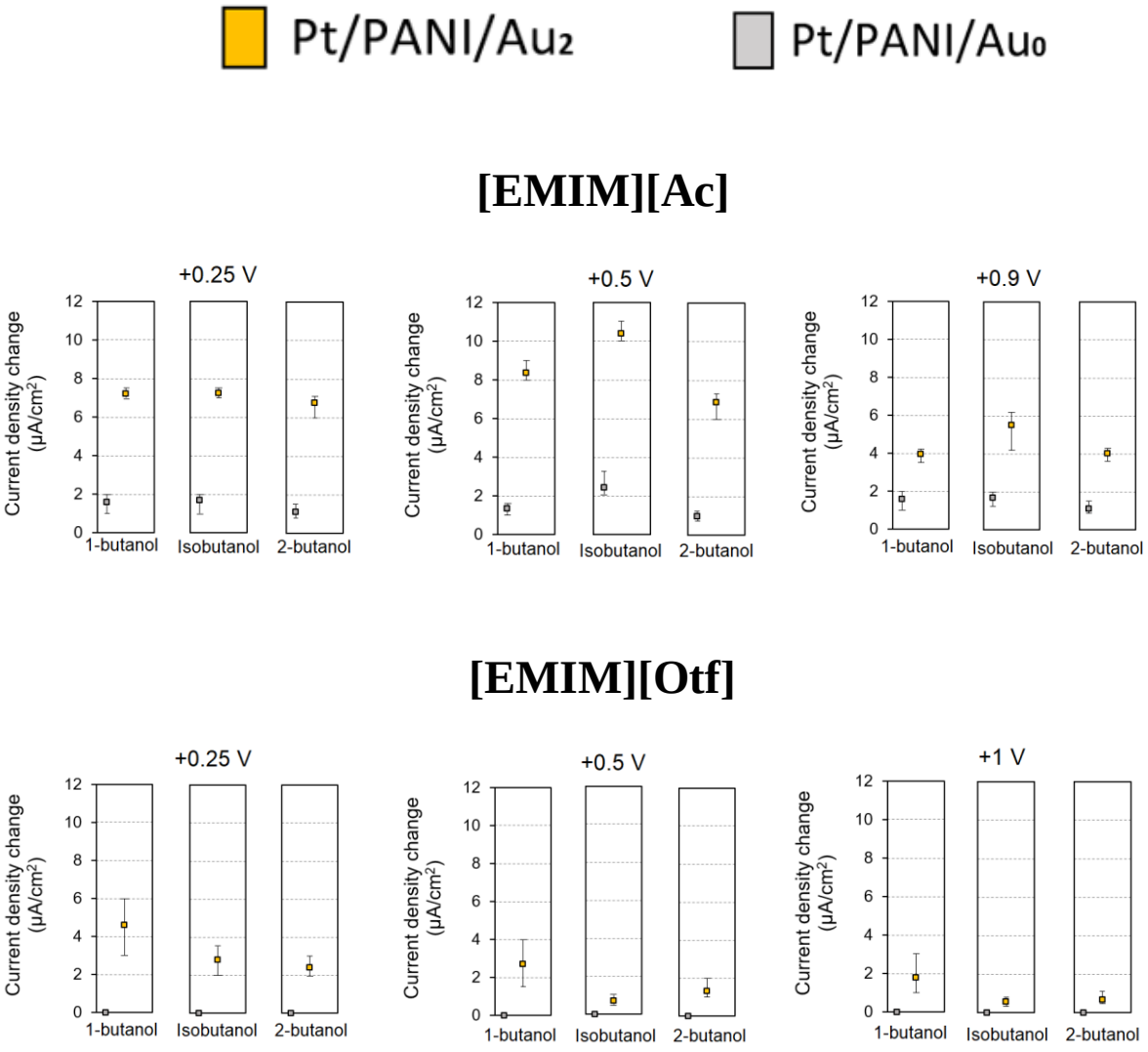

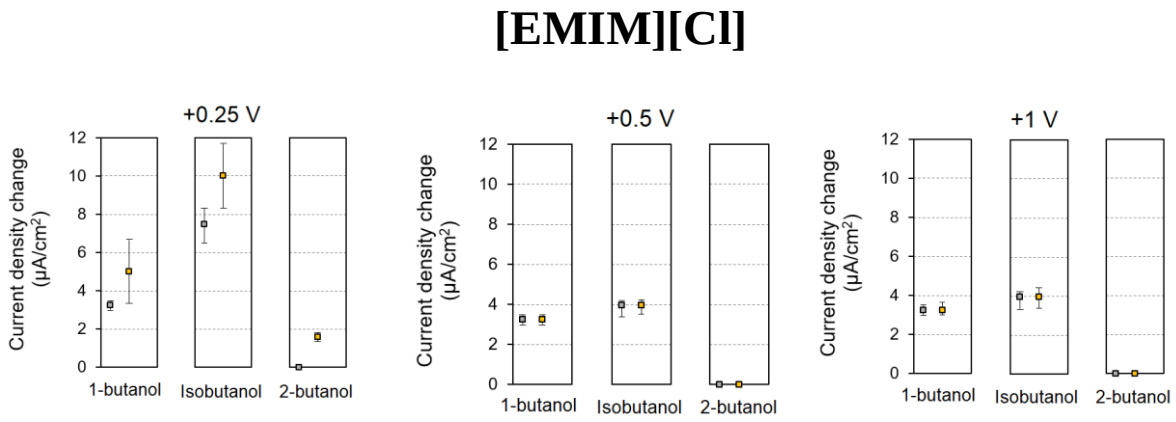

Figure 5.9: The comparison sensor response from Pt/PANI/Au_0 and Pt/PANI/Au_2 using three RTILs for butanol isomers measurement at 100% RC. Reprinted from [93]

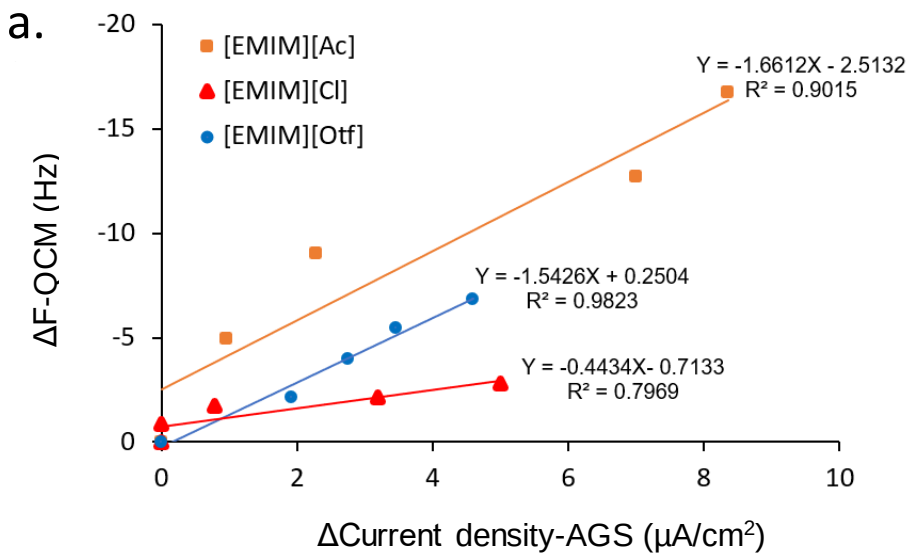

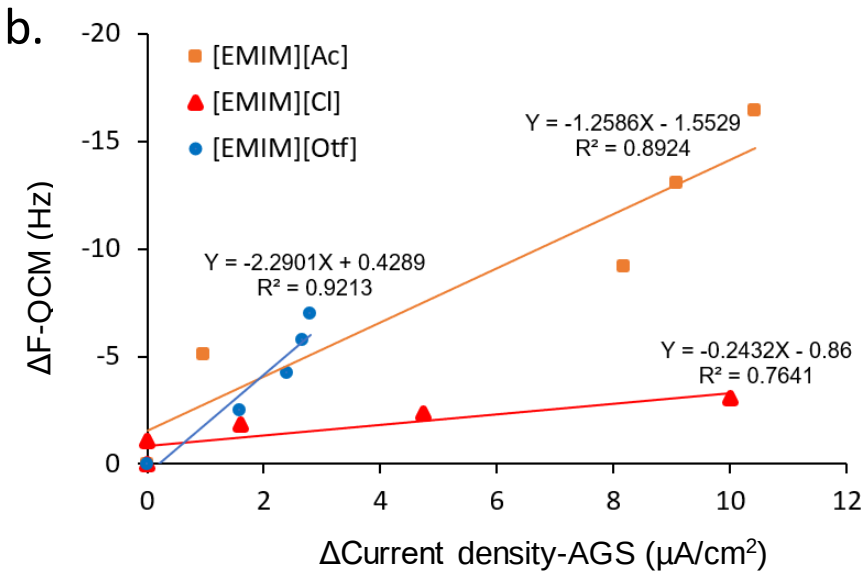

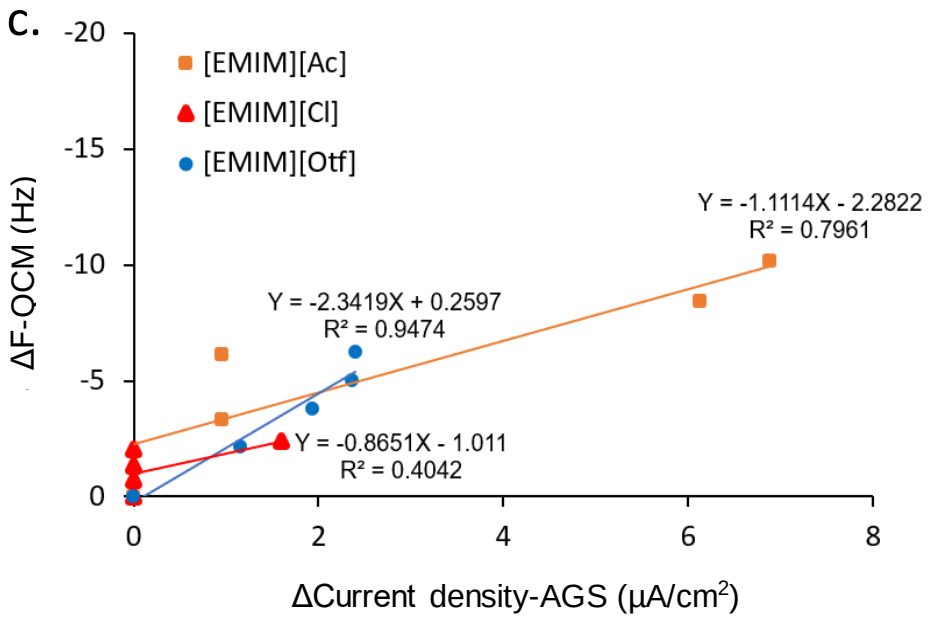

Figure 5.10: The tendency relationship between solubility of analytes in QCM and EC reaction in AGS sensor coated with the same RTIL for: (a) 1-butanol; (b) isobutanol; (c) 2-butanol. Several concentrations were included, i.e., 100%, 75%, 50%, 25%, and 0%. In AGS, the electrode was Pt/PANI/Au_2 and the current shift data was from [EMIM][Ac] at +0.5 V, [EMIM][Otf] at +0.25 V, and [EMIM][Cl] at +0.25 V

In this measurements, various concentrations of butanol isomers were explored, i.e., 0% RC, 25% RC, 50% RC, and 100% RC. Figure 5.11 depicts the comparison results from Pt/PANI/Au_2 and Pt/PANI/Au_0 against various concentrations of 1-butanol using [EMIM][Ac] at +0.5 V *vs.* Ag/AgCl. As shown in Figure 5.11.a, Pt/PANI/Au_2 had higher sensor response than Pt/PANI/Au_0 but the analytes at low RC were not able to be recorded due to the detection limit. Furthermore, the concentration dependency plot oriented to Figure 5.11.a was estimated using a linear regression model depicted in Figure 5.11.b. As shown in Figure 5.11.b, some data points from Pt/PANI/Au2 were far from the linear line, particularly for RC of 50% and 75%, probably the sensor was still far away to reach its steady state within this exposure time (5 minutes) if the exposure time is longer, then there is possibility that those points fitted at linear regression line. The detailed R^2 scores for three RTILs against butanol isomers measurements at different *E*s were summarized in Table 5.5. According to Table 5.5, mostly Pt/PANI/Au_2 showed a higher R^2 score than Pt/PANI/Au_0; these findings indicated that Pt/PANI/Au_2 could achieve more linear trends in concentration dependency than Pt/PANI/Au_0.

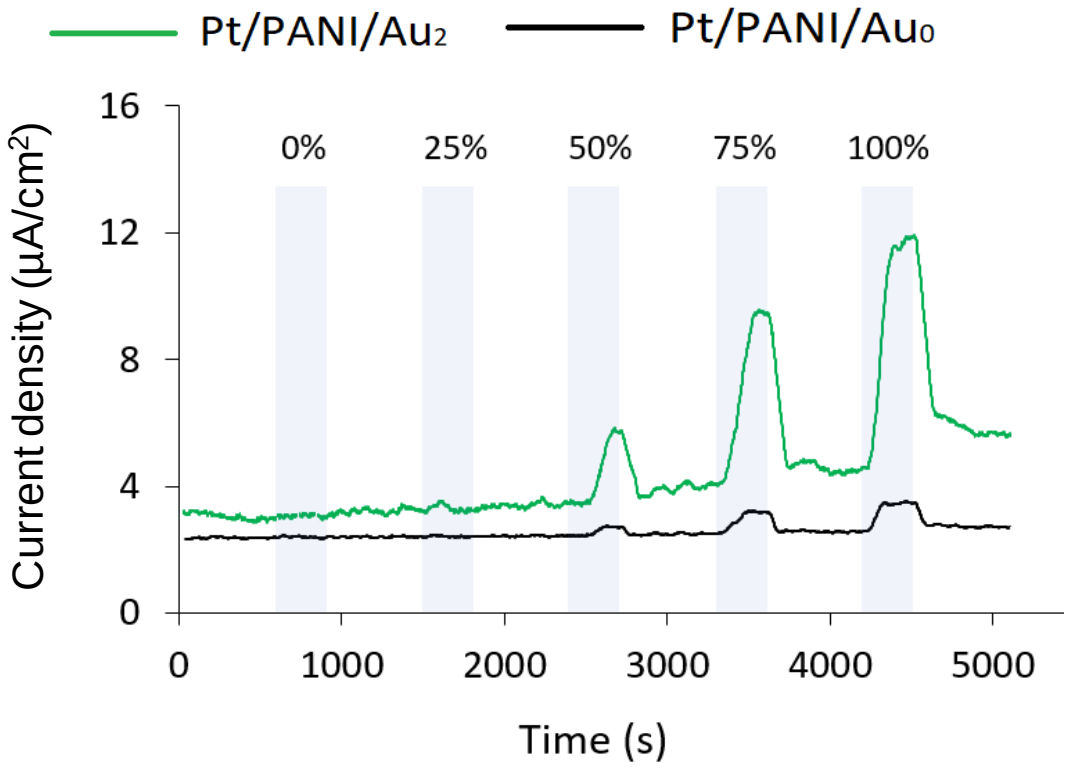

(a)

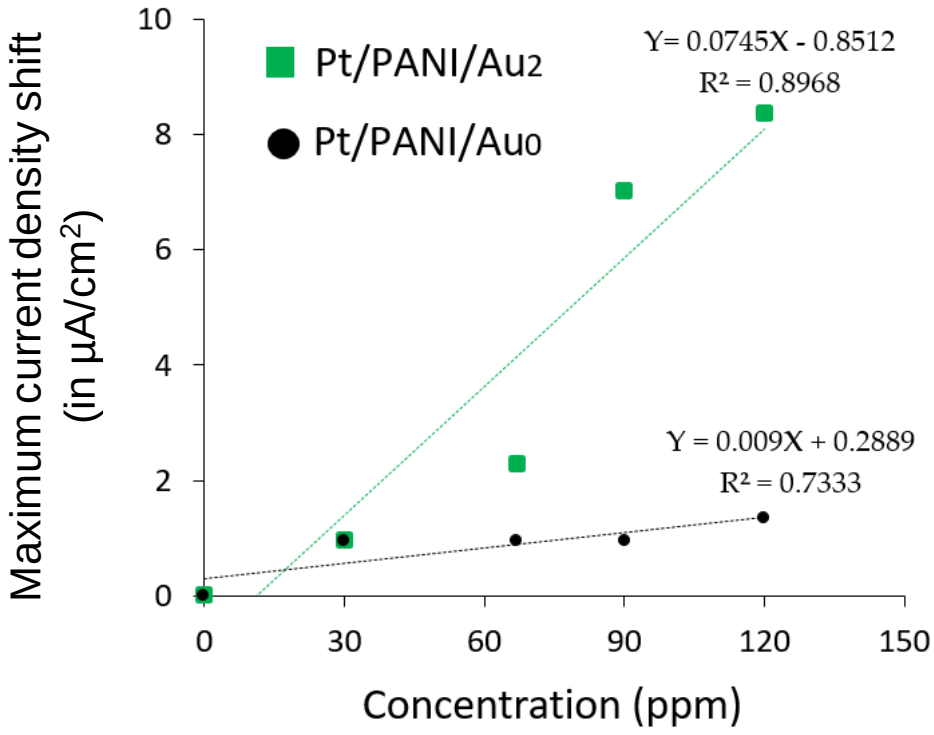

(b)

Figure 5.11: The comparison sensor response from Pt/PANI/Au_0 and Pt/PANI/Au_2 using [EMIM][Ac] at +0.5 V *vs.* Ag/AgCl for different concentrations of 1-butanol. Reprinted from [93]

Table 5.5. The R^2 scores from Pt/PANI/Au_2 and Pt/PANI/Au_0 using three RTILs. Reprinted from [93]

RTIL	Analyte	Fixed Electrochemical Potentials (*E*s) Against Ag/AgCl Ink					
		+0.25 V		+0.5 V		+0.9 V or +1 V	
		Au_2	Au_0	Au_2	Au_0	Au_2	Au_0
[EMIM][Ac]	1-butanol	0.947	0.52	0.896	0.73	0.964	0.78
	Isobutanol	0.89	0.628	0.857	0.846	0.89	0.825
	2-butanol	0.574	0.633	0.799	0.51	0.871	0.621
[EMIM][Otf]	1-butanol	0.968	0.5	0.919	0.5	0.685	0.5
	Isobutanol	0.799	0.5	0.52	0.5	0.74	0.5
	2-butanol	0.857	0.5	0.73	0.5	0.844	0.5
[EMIM][Cl]	1-butanol	0.8491	0.7	0.94	0.94	0.94	0.94
	Isobutanol	0.88	0.9	0.868	0.8	0.86	0.8
	2-butanol	0.5	0.5	0.5	0.5	0.5	0.5

Pt/PANI/Au_2 and Pt/PANI/Au_0 were labeled as Au_2 and Au_0, respectively. [EMIM][Ac] used +0.9 V while [EMIM][Otf] and [EMIM][Cl] used +1 V.

5.6 Sensing element selection and evaluation of gas discrimination capability

The array of sensors was explored to discriminate among butanol isomers. The numerical Wilk's lambda (Λ) was calculated to evaluate the discrimination capability of 1-butanol, isobutanol, and 2-butanol; the better separation can be achieved by a lower Wilks' Λ values. Table 5.6 summarizes the representative Wilks' Λ values from same or different sensing film with *E*s combinations using Pt/PANI/Au_2 obtained from five repeated measurements per analyte at 100% RC. According to Table 5.6, the lowest Wilk's Λ was achieved using different RTILs combinations, i.e., [EMIM][Ac] at +0.5 V, [EMIM][Otf] at +0.5 V, and [EMIM][Cl] at +0.5 V. Afterward, the separation power achieved by that combination was also tested using 100% RC and 75% RC.

Figure 5.12 depicts the gas discrimination among analytes visualized with linear discriminant analysis (LDA) plot. Using only one sensing film with different *E*s, i.e., [EMIM][Ac] at +0.25 V, +0.5 V, and +0.9 V, the analytes were still able to be discriminated at 100% RC shown in Figure 5.12.a; however, when 100% RC and 75% RC were loaded together, the distances between three centroid groups were getting closer, and the discrimination among butanol isomers became poor as shown in Figure 5.12.b. Furthermore, for the combination sensing films of [EMIM][Ac] at +0.5 V, [EMIM][Otf] at +0.5 V, and [EMIM][Cl] at +0.5 V; as shown in Figure 5.12.c, when 100% RC was loaded, the gas discrimination among analytes was much better than using only one sensing film. In addition, when two concentrations of 100% RC and 75% RC were mixed, the Wilks' lambda became worse due to the sensor response from selected sensing films not linear to concentration changes. However, its discrimination among butanol isomers was still achievable, and there was no overlapped between groups although the centroid distances between three analytes were closer; thus, these findings indicated that the selected sensor array could contribute to the discriminant capability among gaseous butanol isomers although different concentrations loaded.

Table 5.6 Wilk's lambda values generated from several combinations. Reprinted from [93]

Combination of Sensing Films Applied on Pt/PANI/Au_2									Wilks' Λ
[EMIM][Ac]			[EMIM][Otf]			[EMIM][Cl]			
+0.25 V	+0.5 V	+0.9 V	+0.25 V	+0.5 V	+1 V	+0.25 V	+0.5 V	+1 V	
●	●	●	×	×	×	×	×	×	2.0×10^{-1}
×	×	×	●	●	●	×	×	×	1.28×10^{-1}
×	×	×	×	×	×	●	●	●	4.8×10^{-3}
●	×	×	●	×	×	●	×	×	4.9×10^{-2}
●	×	×	●	×	×	×	●	×	5.8×10^{-3}
●	×	×	●	×	×	×	×	●	5.8×10^{-3}
●	×	×	×	●	×	●	×	×	3.3×10^{-2}
●	×	×	×	●	×	×	●	×	4.2×10^{-3}
●	×	×	×	●	×	×	×	●	4.26×10^{-3}
●	×	×	×	×	●	●	×	×	3.85×10^{-2}
●	×	×	×	×	●	×	●	×	4.8×10^{-3}
●	×	×	×	×	●	×	×	●	4.8×10^{-3}
×	●	×	●	×	×	●	×	×	2.5×10^{-2}
×	●	×	●	×	×	×	●	×	2.7×10^{-3}
×	●	×	●	×	×	×	×	●	2.75×10^{-3}
×	●	×	×	●	×	●	×	×	1.4×10^{-2}
×	●	×	×	●	×	×	●	×	1.1×10^{-3}
×	●	×	×	●	×	×	×	●	2.1×10^{-3}
×	●	×	×	×	●	●	×	×	2.3×10^{-2}
×	●	×	×	×	●	×	●	×	2.9×10^{-3}
×	●	×	×	×	●	×	×	●	2.9×10^{-3}
×	×	●	●	×	×	●	×	×	3.5×10^{-2}
×	×	●	●	×	×	×	●	×	1.78×10^{-3}
×	×	●	●	×	×	×	×	●	1.78×10^{-3}
×	×	●	×	●	×	●	×	×	3.6×10^{-2}
×	×	●	×	●	×	×	●	×	2.10×10^{-3}
×	×	●	×	●	×	×	×	●	2.10×10^{-3}
×	×	●	×	×	●	●	×	×	3.7×10^{-2}
×	×	●	×	×	●	×	●	×	2.5×10^{-3}
×	×	●	×	×	●	×	×	●	2.5×10^{-3}

In this table, labeled applying and not applying with ● and ×, respectively.

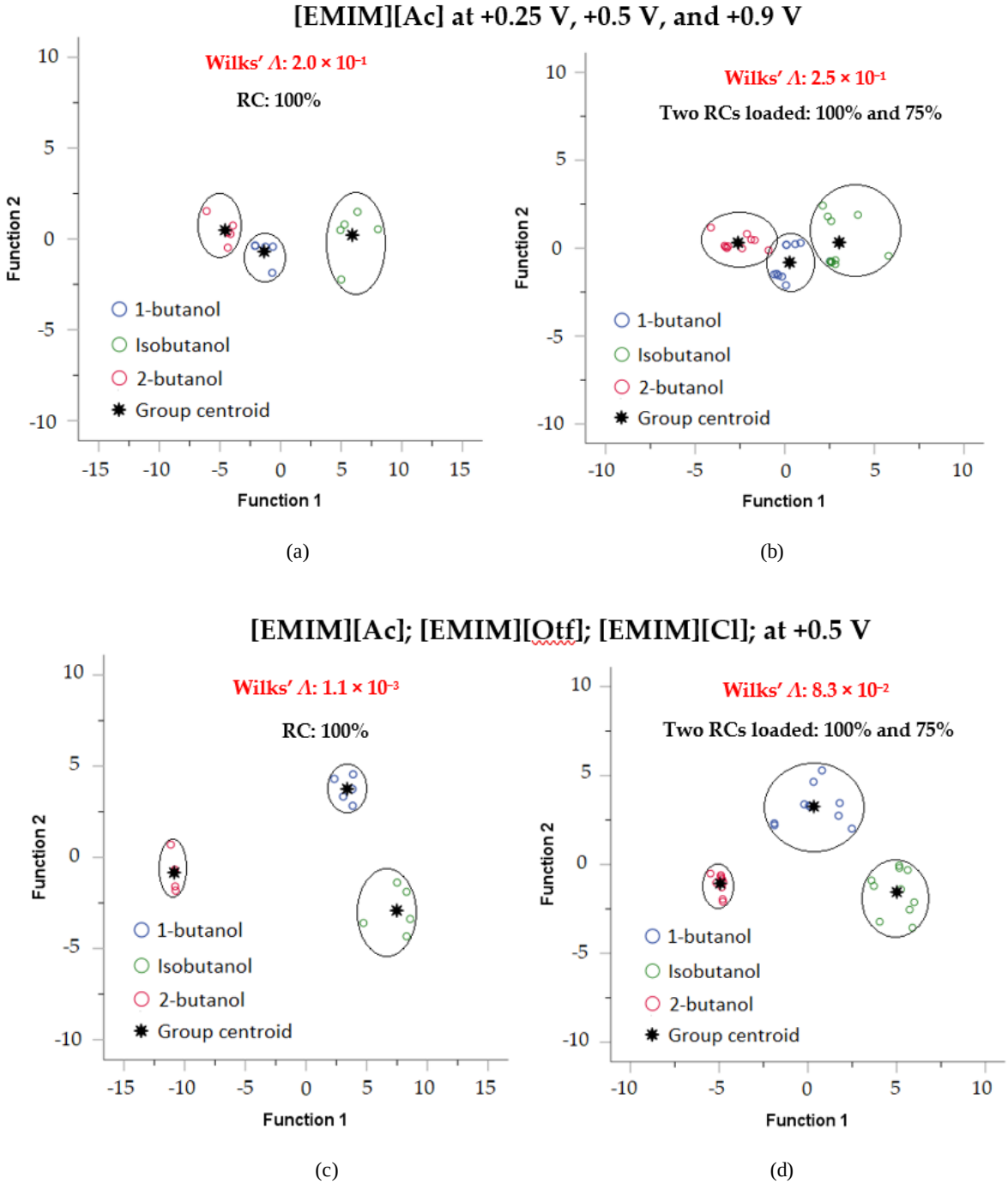

Figure 5.12: LDA was used to visualize the butanol isomers separation from different applied sensing films coated on Pt/PANI/Au_2; (a) Only 100% RC loaded (one sensing film, i.e., [EMIM][Ac] using three different *E*s *vs.* Ag/AgCl); (b). Two concentrations loaded, i.e., 100% RC and 75% RC (one sensing film, i.e., [EMIM][Ac] using three different *E*s *vs.* Ag/AgCl), (c). Only 100% RC loaded (three sensing films, e.g., [EMIM][Ac], [EMIM][Otf], and [EMIM][Cl]; at same *E* of +0.5 V *vs.* Ag/AgCl), (d). Two concentrations loaded 100% RC and 75% RC (three sensing films e.g., [EMIM][Ac], [EMIM][Otf], and [EMIM][Cl]; at same *E* of +0.5 V *vs.* Ag/AgCl). Reprinted from [93]

5.7 Butanol isomers separation using two sensor types

In this chapter, two sensor types (QCM and IDA) coated with same RTILs ([EMIM][Ac], [EMIM][Otf], [EMIM][Cl]) were used. The Wilks' lambda was calculated to evaluate butanol isomers separation. Table 5.7 summarizes the representative Wilks' lambda values for several sensing film combinations including from two sensor types. According to Table 5.7, the lowest Wilks' lambda of 7.26×10^{-4} was obtained from two sensor types combination, i.e., QCMs with 3 RTILs ([EMIM][Ac], [EMIM][Otf], [EMIM][Cl]) and IDAs using 3 RTILs of [EMIM][Ac], [EMIM][Otf], [EMIM][Cl], with the same voltage of +0.5 V vs. Ag/AgCl; here, for IDA sensor type, the sensing films combinations and voltage were same as the obtained in Table 5.6, i.e., [EMIM][Ac], [EMIM][Otf], [EMIM][Cl], at +0.5 V. The selected Wilks' lambda in Table 5.7 (7.26×10^{-4}) is lower than in Table 5.6 (1.1×10^{-3}) due to the contribution of QCM. Although same sensing films were used, but different mechanism of working principle for each sensor type indeed contributed to the enhanced butanol isomers separation. The linear discriminant analysis (LDA) plot was used to visualize the butanol isomers separation shown in Figure 5.13 achieved by selected sensing films oriented to Table 5.7. Figure 5.13.a shows the LDA plot for 100% RC of butanol isomers. According to Figure 5.13.a, the butanol isomers were separated; the distances between 1-butanol and isobutanol were close compared to 2-butanol. Figure 5.13.b depicts the LDA plot using two different concentrations loaded, i.e., 100% and 75%, here, the butanol isomers were still can be distinguished and the obtained Wilk's lambda was 4.25×10^{-3}. In Chapter 4, Wilks' lambda reached at 4.82×10^{-8} which was much lower than Wilk's lambda obtained here. Therefore, in the next section, the discrimination capability of butanol isomers from electrode with atomic gold and without atomic gold were explained.

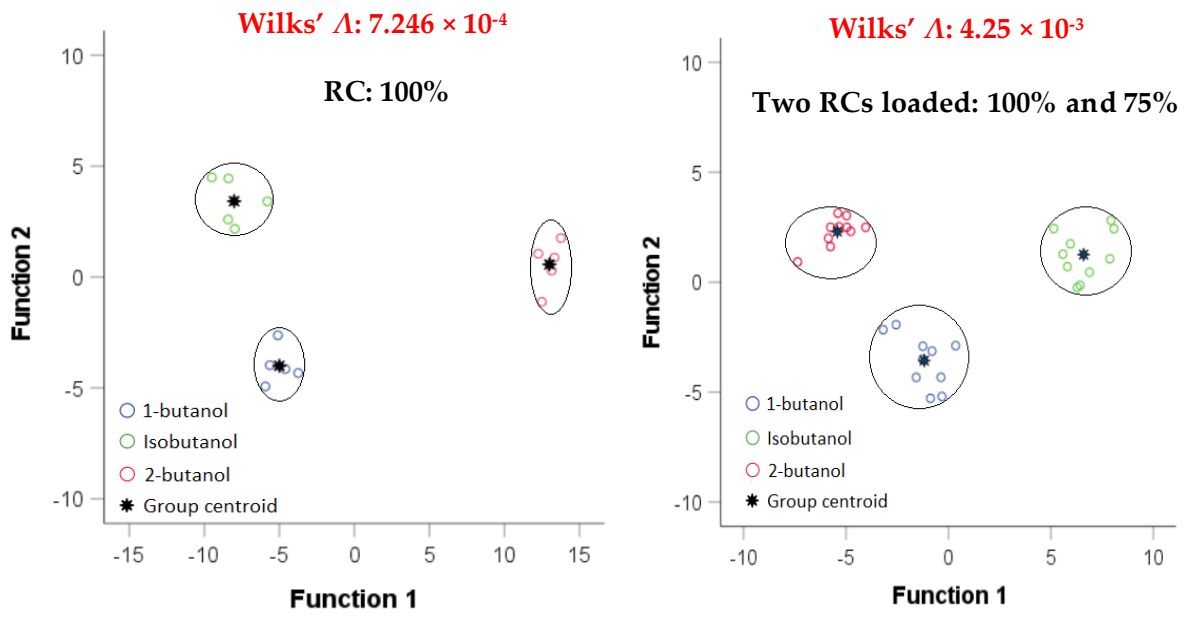

(a) (b)

Figure 5.13: The LDA plot for selected sensing films from two sensor types, i.e., QCMs coated with [EMIM][Ac], [EMIM][Otf], [EMIM][Cl], and IDAs with [EMIM][Ac], [EMIM][Otf], [EMIM][Cl] at same *E* of +0.5 V *vs.* Ag/AgCl against butanol isomers with different concentrations: (a) RC of 100%; (b) two RCs loaded, i.e., 100% and 75%

Table 5.7 Wilk's lambda values from several combination

Data dimensions	QCM film	IDA (Pt/PANI/Au_2)		Wilks' lambda
		RTIL	E (V)	
3	[EMIM][Ac]	-		1.94×10^{-2}
	[EMIM][Otf]			
	[EMIM][Cl]			
4	[EMIM][Ac]	[EMIM][Ac]	+0.25	5.4×10^{-3}
			+0.5	
			+0.9	
4		[EMIM][Otf]	+0.25	9.1×10^{-3}
			+0.5	
			+1	
4		[EMIM][Cl]	+0.25	3×10^{-3}
			+0.5	
			+1	
4	[EMIM][Otf]	[EMIM][Ac]	+0.25	2.06×10^{-2}
			+0.5	
			+0.9	
4		[EMIM][Otf]	+0.25	5.28×10^{-2}
			+0.5	
			+1	
4		[EMIM][Cl]	+0.25	3.5×10^{-3}
			+0.5	
			+1	
4	[EMIM][Cl]	[EMIM][Ac]	+0.25	1.7×10^{-2}
			+0.5	
			+0.9	
		[EMIM][Otf]	+0.25	6.9×10^{-2}
			+0.5	
			+1	
		[EMIM][Cl]	+0.25	4.3×10^{-3}
			+0.5	
			+1	
6	[EMIM][Ac]	[EMIM][Ac]	+0.5	1.803×10^{-3}
	[EMIM][Otf]	[EMIM][Otf]	+0.25	
	[EMIM][Cl]	[EMIM][Cl]	+0.25	
6	[EMIM][Ac]	[EMIM][Ac]	+0.9	1.398×10^{-3}
	[EMIM][Otf]	[EMIM][Otf]	+1	
	[EMIM][Cl]	[EMIM][Cl]	+1	
6	[EMIM][Ac]	[EMIM][Ac]	+0.5	7.26×10^{-4}
	[EMIM][Otf]	[EMIM][Otf]	+0.5	
	[EMIM][Cl]	[EMIM][Cl]	+0.5	
6	[EMIM][Ac]	[EMIM][Ac]	+0.25	2.278×10^{-3}
	[EMIM][Otf]	[EMIM][Otf]	+0.25	
	[EMIM][Cl]	[EMIM][Cl]	+0.25	

5.8 The comparison of butanol isomers measurements using electrode without the atomic gold and with atomic gold

Figure 5.14 depicts the comparison results of butanol isomers discrimination obtained in Chapter 4 and Chapter 5. Two sensor types were loaded, i.e., QCMs and IDAs. In Chapter 4, the different cation-anion of RTILs were used. In Chapter 5, RTILs having same cation but different anions were used. Furthermore, for IDAs, the WE applied in Chapter 4 and Chapter 5 were Pt only (without atomic gold) and Pt/PANI/Au_2 (with atomic gold), respectively. For QCMs, although different sensing films were used, as shown in Figure 5.14.a and Figure 5.14.b, the distance between 1-butanol group and isobutanol group were close compared to 2-butanol group.

In Chapter 4, the lowest Wilk's lambda was 4.82×10^{-8} shown in Figure 5.14.e obtained from the combination QCMs depicted in Figure 5.14.a and IDAs (Pt only, without atomic gold) depicted in Figure 5.14.c.

As shown in Figure 5.14.a, when using QCMs coated with RTILs of [EMIM][Ac], [BMIM][Br], and [HMIM][Cl], 1-butanol and iso-butanol groups were close and 2-butanol group was away from those groups. From this point, in order to obtain high separation among butanol isomers, the sensor providing a good separation between 1-butanol and isobutanol was required. As shown in Figure 5.14.c, when using the IDAs coated with [EMIM][Ac] at +0.25 V, +0.5 V, and +0.9 V, PC1 contributed to the separation between 1-butanol and isobutanol; overall, from Figure 5.14.c, the distance between 2-butanol and 1-butanol group was closer than to isobutanol group. Therefore, when combining the information from Figure 5.14.a and c, the discrimination among butanol isomers were high shown in Figure 5.14.e with obtained Wilk's lambda value reaching at 4.82×10^{-8}.

In Chapter 5, the lowest Wilk's lambda was obtained at 7.246×10^{-4} shown in Figure 5.14.f from the combination of two sensor types as shown in Figure 5.14.b and Figure 5.14.d for QCMs and IDAs ($Pt/PANI/Au_2$ or electrode with atomic gold), respectively. The sensor response from QCMs in Figure 5.14.b was similar to response obtained in Figure 5.14.a although different RTILs were used, i.e., 1-butanol and isobutanol groups were very close than 2-butanol group. Again, here, we also required the sensor which was able to differentiate 1-butanol and isobutanol. The response for IDAs ($Pt/PANI/Au_2$) with different RTILs shown in Figure 5.14.d could separate the butanol isomers, however, the distance between 1-butanol and isobutanol were close compared to 2-butanol. Therefore, when combining the sensor response from Figure 5.14.b and d, the butanol isomers were still able to be separated with achieved Wilk's lambda of 7.246×10^{-4} as shown in Figure 5.14.f, although this obtained Wilk's lambda was higher than previous result when using electrodes of Pt only (without atomic gold).

Based on Figure 5.14, IDAs contributed to the separation between 1-butanol and isobutanol to improve the discrimination capability obtained by QCMs. As depicted in Figure 5.14.c, when using Pt only (without atomic gold), isobutanol group could be separated shown by a further distance from 1-butanol and 2-butanol groups. Furthermore, when using $Pt/PANI/Au_2$ (electrode with atomic gold), the furthest distance among butanol isomers groups was obtained by 2-butanol rather than isobutanol.

Figure 5.15 shows the mean of sensor response from several electrode types using [EMIM][Ac], i.e., Pt electrode (red color), $Pt/PANI/Au_0$ (green color), $Pt/PANI/Au_2$ (yellow color). According to Figure 5.15, $Pt/PANI/Au_2$ obtained the highest sensor response to 1-butanol, 2-butanol, and isobutanol when using [EMIM][Ac] at +0.25 V, +0.5 V, and +0.9 V *vs*. Ag/AgCl. As we can see from Figure 5.15, particularly at +0.5 V, here, the blue rectangle was given to highlight the sensor response used in Figure 5.14.c and d. As shown in Figure 5.15, when using [EMIM][Ac] at +0.5 V; Pt electrode (red color) had the highest response for isobutanol and its response to 1-butanol and 2-butanol were almost same and small leading to high selectivity to isobutanol and improving the butanol isomers separation obtained by QCMs (Figure 5.14.a). However, when $Pt/PANI/Au_2$ (yellow color) was used to measure the butanol isomers, the sensitivity of each analyte was enhanced due to the catalytic activity possessing by atomic gold. As shown in Figure 5.15, using [EMIM][Ac] at +0.5 V; $Pt/PANI/Au_2$ has the highest response to isobutanol, but the difference of magnitude between isobutanol and 1-butanol was small compared with the case of Pt only. Therefore, the discrimination capability of butanol isomers was not as good as when using Pt only although the information from QCMs were also included as depicted in Figure 5.15.f. It was because $Pt/PANI/Au_2$ enhanced the sensitivity of all analytes.

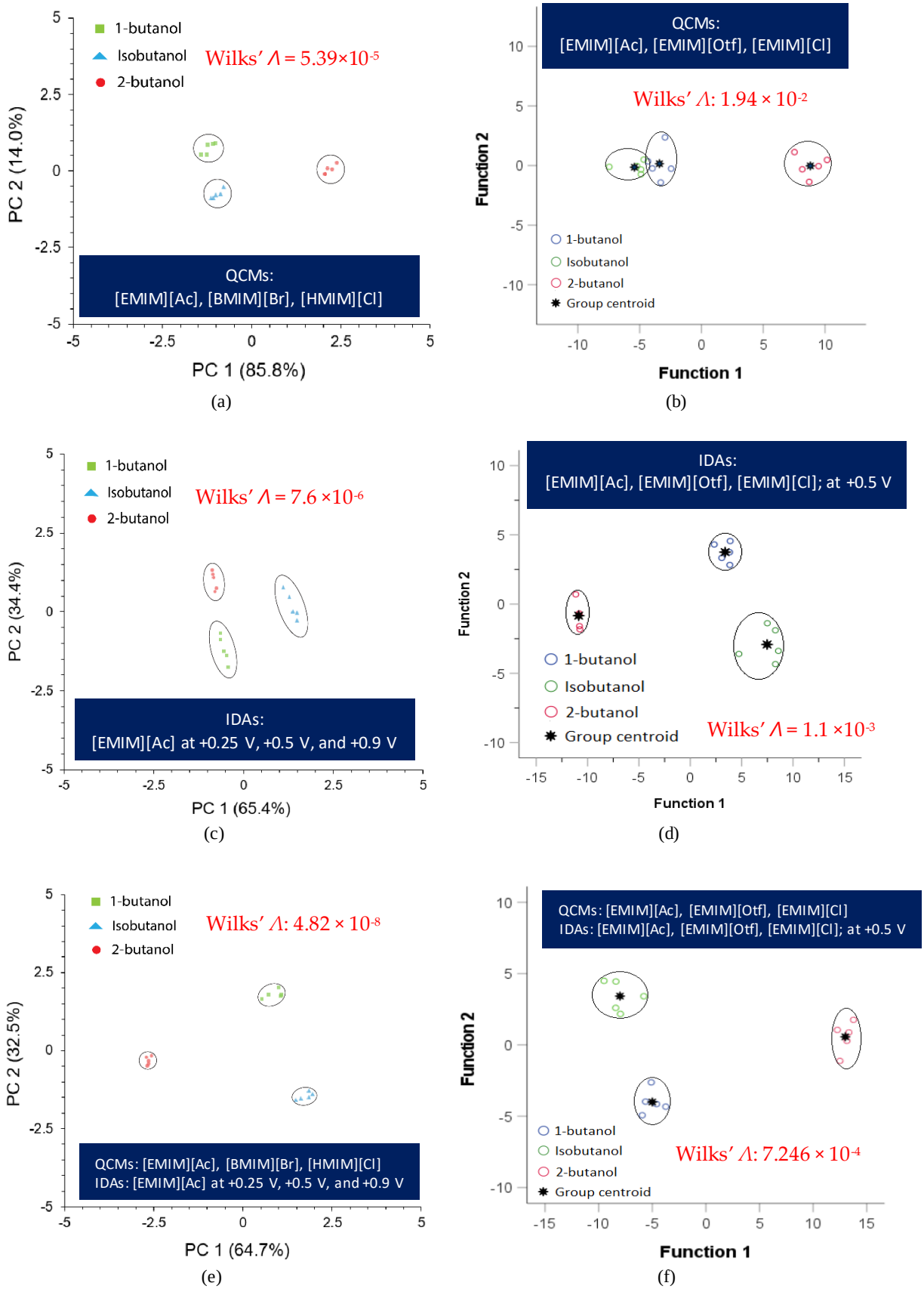

Figure 5.14: The LDA plot for: (a) QCMs coated with 3 RTILs (Chapter 4); (b) QCMs coated with 3 RTILs (Chapter 5); (c) IDAs with [EMIM][Ac] at +0.25 V, +0.5 V, and +0.9 V (Chapter 4); (d) IDAs with 3 RTILs at same *E* of +0.5 V (Chapter 5); (e) two sensor types loaded (Chapter 4); (f) two sensor types loaded (Chapter 5)

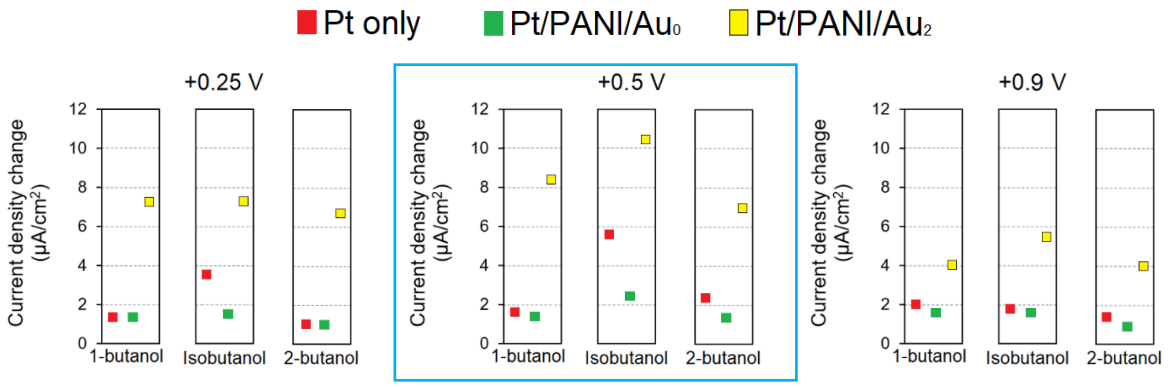

Figure 5.15: The average sensor response obtained from five repeated measurements at 100% RC 1-butanol, isobutanol, and 2-butanol using several IDAs types coated with [EMIM][Ac] at *E*s of +0.25 V, +0.5 V, and +0.9 V *vs.* Ag/AgCl). Reprinted from [93]

Figure 5.16 depicts the current from electrode with atomic gold (Pt/PANI/Au_2) and without atomic gold (Pt/PANI/Au_0) for butanol isomers at 100% RC with five repeated measurements per analyte using three RTILs. As shown in Figure 5.16.a, three fixed EC potentials using [EMIM][Ac] was used for butanol isomers measurement, i.e., +0.25 V, +0.5 V, and +0.9 V. According to Figure 5.16.a, when using RTIL of [EMIM][Ac] at three *E*s, the electrode with atomic gold (Pt/PANI/Au_2) contributed to the butanol isomers measurement because it showed a higher current than the electrode without atomic gold (Pt/PANI/Au_0). Furthermore, Figure 5.16.b depicts the result of [EMIM][Otf] used for butanol isomers measurement at three *E*s, i.e., +0.25 V, +0.5 V, and +1 V. As shown in Figure 5.16.b, electrode with atomic gold (Pt/PANI/Au_2) was the only electrode that contributed to the butanol isomers measurement while the electrode without atomic gold (Pt/PANI/Au_0) had no response at all showed by no current detected. The using of [EMIM][Cl] is depicted in Figure 5.16.c. Three *E*s were used, i.e., +0.25 V, +0.5 V, and +1 V. Based on the Figure 5.16.c, the influence of electrode with atomic gold (Pt/PANI/Au_2) in [EMIM][Cl] was not significant to enhance the sensor response from the electrode without atomic gold (Pt/PANI/Au_0). For example, the sensor response for 1-butanol and isobutanol between Pt/PANI/Au_2 and Pt/PANI/Au_0 were almost similar although different *E*s applied. For 2-butanol, at *E*s of +0.25 V and +1 V, electrode with atomic gold contributed to the enhanced sensitivity although not too much. Overall, electrode with atomic gold (Pt/PANI/Au_2) showed particular catalytic activity regarding the RTIL and applied fixed EC potentials.

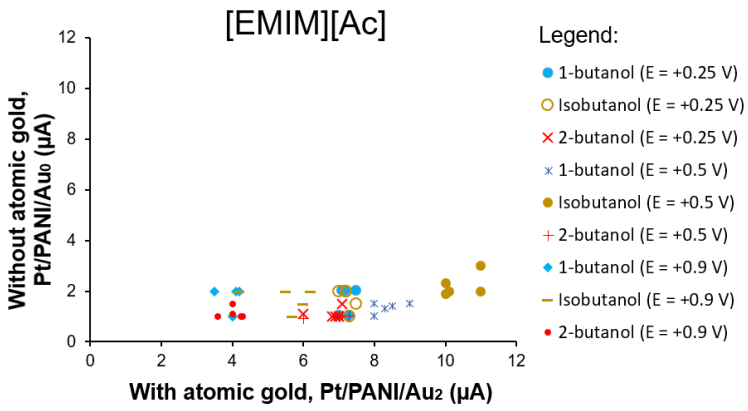

(a)

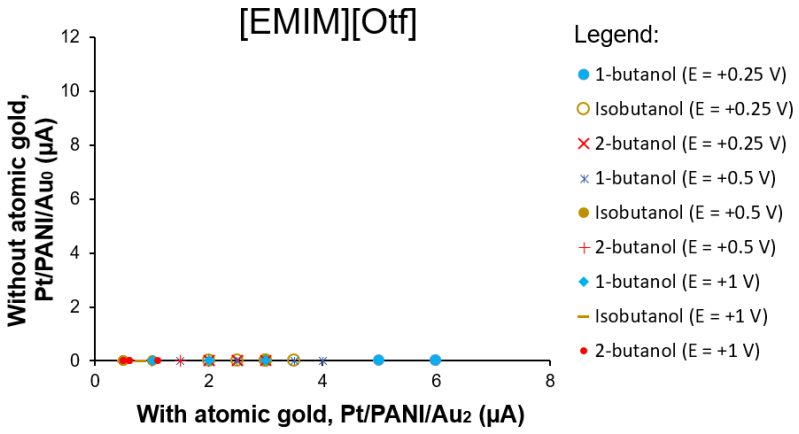

(b)

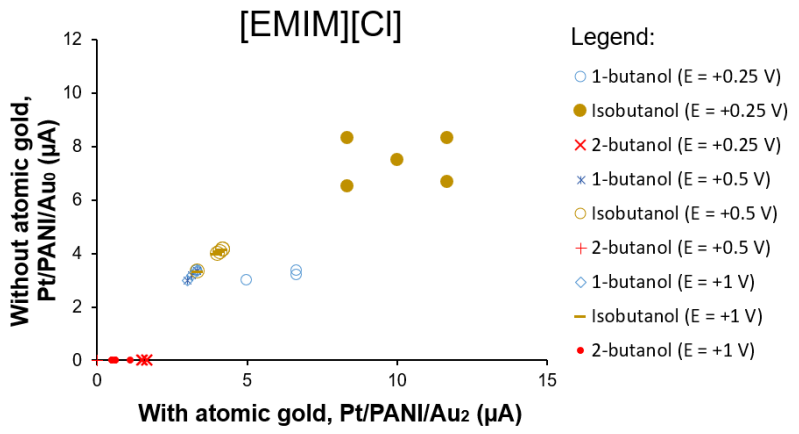

(c)

Figure 5.16: The sensor response (current) from electrode with atomic gold (Pt/PANI/Au_2) and without atomic gold (Pt/PANI/Au_0) obtained from five measurements conducted at 100% RC of butanol isomers for [EMIM][Ac], [EMIM][Otf], and [EMIM][Cl]

5.9 Summary

By using Au_2 clusters as a catalyst on IDA electrodes coated with RTILs, this study demonstrated and verified enhanced sensitivity for butanol isomers gas measurement. Using RTILs having same cation with different anions combinations, i.e., [EMIM][Ac], [EMIM][Otf], and [EMIM][Cl], Pt/PANI/Au_2 demonstrated catalytic activity. Each RTIL provide different physical and chemical properties, resulting in different catalytic activities for Pt/PANI/Au_2. It was also examined the fixed electrochemical potential against Ag/AgCl from each RTIL contributed to the certain obtained sensitivity. Furthermore, most of the obtained results indicated that Pt/PANI/Au_2 had a higher R^2 score than Pt/PANI/Au_0, which indicated that the concentration dependency trends varied more linearly with Pt/PANI/Au_2. In addition, the combinations of RTIL with EC potential were suitable for gaseous butanol isomer discrimination. The discrimination capability of butanol isomers obtained in this Chapter 5 (using electrode with atomic gold, Pt/PANI/Au_2) was not as good as in the Chapter 4 (using electrode without atomic gold, Pt only). It was due to the Pt/PANI/Au_2 enhance the sensitivity of each analyte. When using [EMIM][Ac] at +0.5 V; Pt/PANI/Au_2 obtained the highest sensor response to isobutanol, however, the magnitudes between isobutanol and 1-butanol vapors were closer than using Pt only. Therefore, it reduced the discrimination capability of butanol isomers when combining with QCMs information.

Chapter 6

Conclusion

This study successfully developed a miniaturized amperometric gas sensor (AGS) using interdigitated array (IDA) electrode and obtained several conclusions:

1. Different cation-anion of RTILs, i.e., [EMIM][Ac], [BMIM][Br], [HMIM][Cl] can be applied as the electrolyte in a miniaturized AGS system with different sensor response. Beside IDA electrodes, QCMs coated with the same RTILs were used to check the solubility of each target compound,
2. In a miniaturized AGS, from different cation-anion of RTILs, the RTIL with short alkyl hydrocarbon cation, i.e., 1-ethyl-3-methylimidazolium (EMIM) obtained the highest sensor response,
3. We also successfully modified the working electrode by doping atomic gold clusters of Au_2 on IDA electrode,
4. IDA electrodes decorated with atomic gold clusters of Au_2 were also catalytically active in these RTILs, i.e., [EMIM][Ac], [EMIM][Otf], [EMIM][Cl],
5. The sensitivity of gaseous butanol isomers measurement was more enhanced using IDA with atomic gold compared to IDA without atomic gold,
6. Different fixed EC potentials of each RTIL were also explored to obtain high sensitivity for a miniaturized AGS system,
7. The combination of several RTILs and EC potentials in miniaturized AGS system contributed to the enhanced butanol isomers' separation.

In this PhD work, we realized atomic gold doped in a miniaturized AGS with several RTILs and EC potentials to obtain a high sensitivity of gaseous butanol isomers measurement and the sensor array was also explored to achieve a good discrimination capability of butanol isomers.

Chapter 7

Future works

The commercial AGS with RTIL has not been released in the market so far. In this research work, we successfully demonstrated the enhanced butanol isomers measurement using atomic gold and several RTILs applied in miniaturized AGS. However, the response time was still very slow and the sensitivity was not improved as high as using KOH medium. There are several ways to improve the performance of the current sensor, i.e.,:

1. Applying a thin layer of RTIL,
2. Redesigning the electrode,
3. Increasing the atomic gold density,
4. The combination of the number of atomic metal clusters and metal material (atomic alloys),
5. Minimize the cavity between PANI and RTIL,
6. Applying bi-potentiostat,
7. Applying other material for working electrode.

7.1 Applying a thin layer of RTILs

As part of this experiment, we also used another sensor type, QCMs coated with RTILs, which were the same ones used for modified IDA electrodes; the results showed that QCM coated with [EMIM][Ac] was capable to quantify 1-butanol even in small RC, as shown in Figure 7.1.a. In the current EC measurement shown in Figure 7.1.b, Pt/PANI/Au_2 in [EMIM][Ac] at +0.5 V was unable to measure 1-butanol at 25% RC; this issue could be solved by applying a very thin layer of RTIL film to accelerate the diffusion transport to the AGS' working electrode since RTIL has much higher viscosity than aqueous electrolytes such as KOH and NaOH. According to this ref [131], a thin RTIL could enhance both responses and sensitivity compared a thick RTIL.

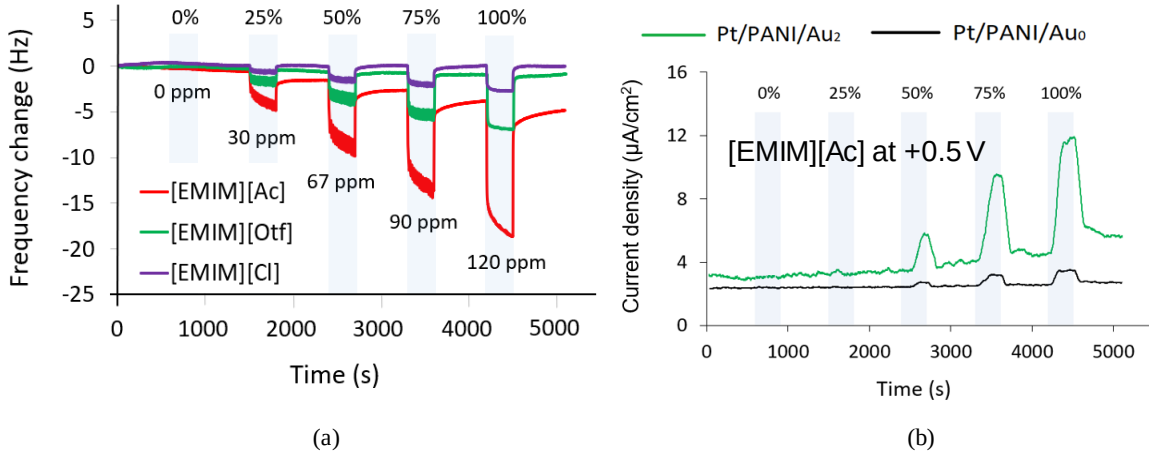

Figure 7.1: The RTIL behavior comparison against 1-butanol gas measurement using: (a) QCM; (b) IDA

7.2 Redesigning the electrode

The electrode for miniaturized AGS are required to be redesigned to apply a thin layer of RTIL. As shown in Figure 7.2, the microarray electrode (depicted in Figure 7.2.b) can be made from macro sensor (shown in Figure 7.2.a) to realize and keep a thin layer of IL. The comparison results using a bulk IL (macro IL sensor) and a thin IL (microarray sensor) are depicted in Figure 7.2.c. According to Figure 7.2.c, although the microarray sensor had smaller area than macro IL sensor, it had a higher sensitivity than macro IL because it had a thinner IL than macro sensor. There are several ways to make a microarray electrode. Figure 7.3 depicts one of the methods, i.e., partial printing, to fabricate the microarray types using a hydrophobic of 1-hexadecanethiol (HDT) as a boundary between fingers. The boundary is important to keep a thin RTIL since the aggregation of RTILs between neighbors often occurs resulting in a thick RTIL leading to decrease the sensitivity.

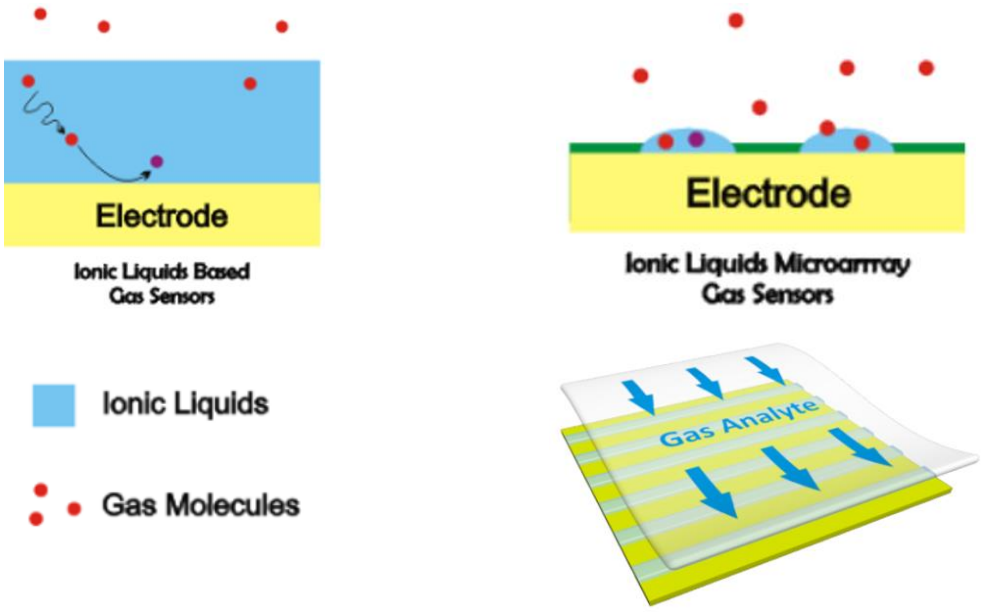

(a) (b)

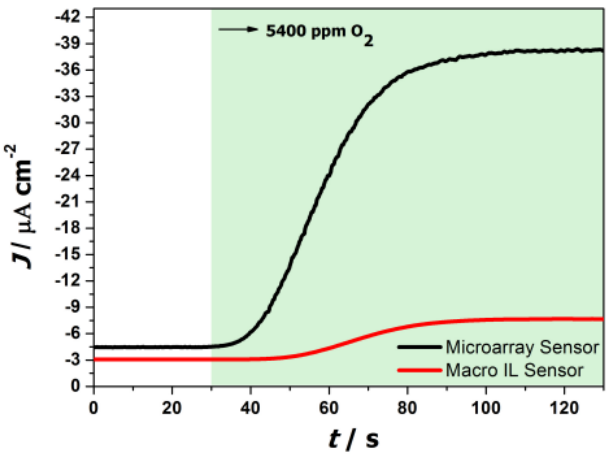

(c)

- Ionic liquid: 1-n-butyl-3-methylimidazolium bistriflimide [BMIM][NTf2]
- Area of microarray sensor: 0.012 cm^2 (30-mm-wide IL lines with 60 mm spacing)
- Area of macro IL sensor was 0.035 cm^2

Figure 7.2: The ionic liquids applied in miniaturized AGS: (a) macro sensor; (b) microarray sensor; (c) current density-time (*J-t*) responses from microarray sensor *vs.* macro IL sensor. Reprinted from [131]

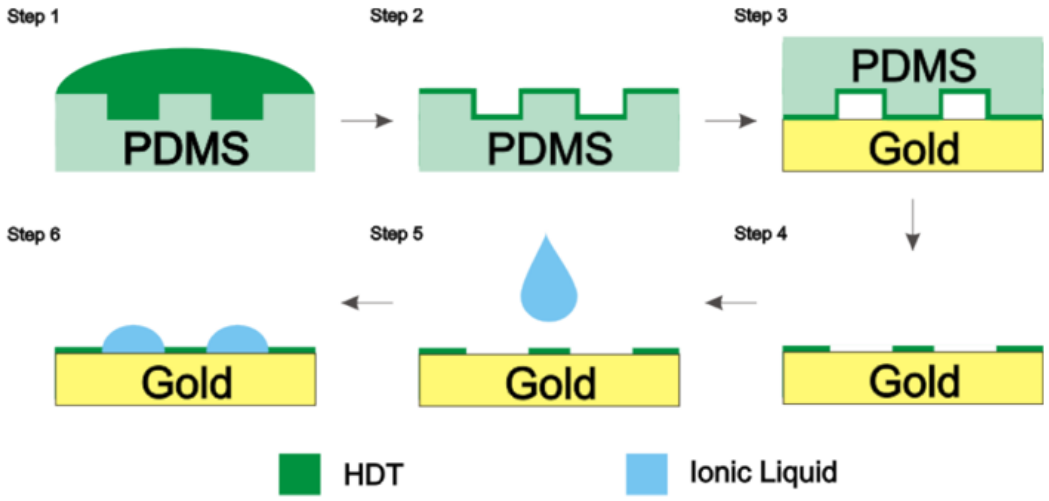

Figure 7.3: Schematic illustration of partial printing procedures. Reprinted from [131]

7.3 Increasing the atomic gold density

The atomic deposition can be increased by fabricating a porous host matrix of polyaniline (PANI). Using a porous PANI, the atomic metal can be doped not only in surface but inside the PANI. Therefore, a higher density of atomic gold can be obtained to boost a higher catalytic activity resulting to a higher sensitivity.

7.4 Atomic alloys

Atomic alloys use different atomic metal material. For example, the reported works depicted in Figure 7.4 shows different CV curve obtained from certain structure of the alloys (atomic gold and palladium) due to a particular catalytic property which contributes to the enhanced sensitivity and selectivity. Therefore, applying atomic alloy as catalyst at working electrode are essential to be explored in AGS system.

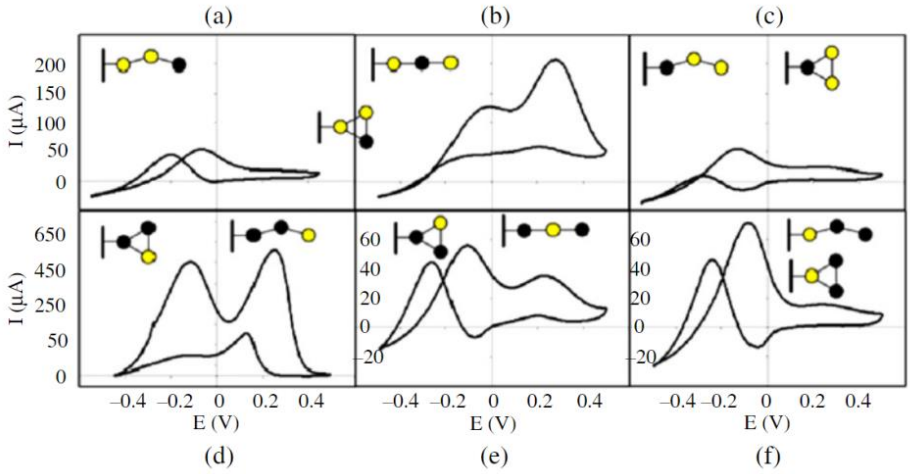

Figure 7.4: CVs for the atomic alloy, gold (Au) atom represented in yellow color, palladium (Pd) atom in black color: (a), (b), (c) are possible structures for Au_2Pd_1, (d), (e), (f) are possible structures for Pd2Au1. Reproduced from [132] with permission from Springer Nature

7.5 Minimizing the cavity between PANI and RTIL

There was a possibility that Pt/PANI was not fully in contact with RTIL, hence, some area containing atomic gold was not covered by RTIL then the atomic catalyst was not active and a high sensitivity could not be obtained. This issue could be solved by using the same RTIL (used in AGS measurement) for PANI polymerization and atomic gold deposition process [69].

7.6 Applying bi-potentiostat

To generate a high sensor response from interdigitated array (IDA) electrode, bi-potentiostat can be applied in which different voltages can be fed up to the working electrode 1 (WE1) and working electrode 2 (WE2). Figure 7.5.a depicts the illustration of redox cycling amplification mechanism for oxygen reduction using IDA. Unlike applying one potential only where the analyte undergoes oxidation or reduction only. Here, when two different potential applied, the WEs of IDA undergo the oxidation and reduction simultaneously. As shown in Figure 7.5.a, IDA had two arrays of WEs working in tandem by reducing the analyte at WE1 (here, the analyte was oxygen) and reoxidizing the anionic product at WE2. This mechanism creates an enhanced current and greater sensitivity. As shown in Figure 7.5.b, when applying different voltages to WE1 (E_{WE1} = −1.2 V *vs*. Au) and WE2 (E_{WE2} = −0.1 V *vs*. Au), the sensor response was higher than only single electrode performed (blue, WE2 disconnected).

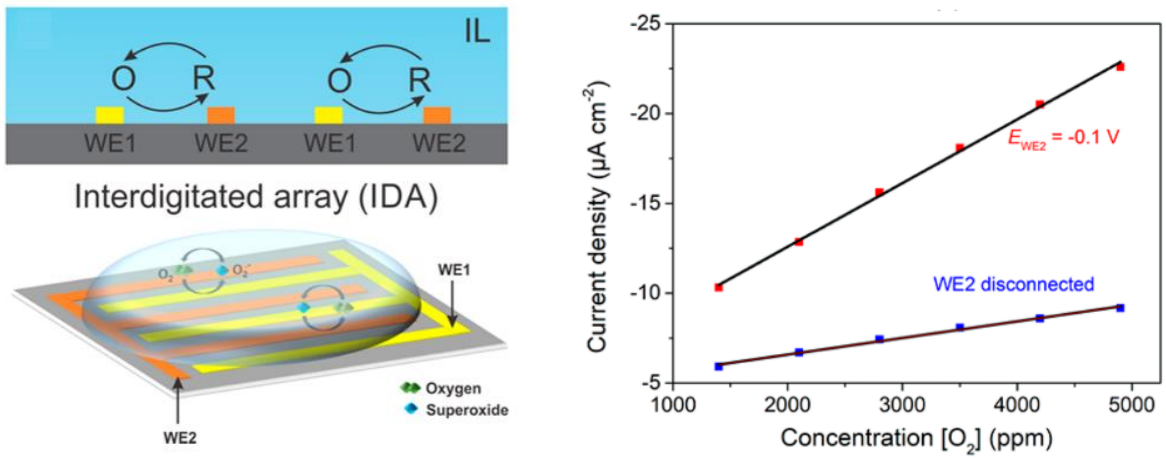

(a) (b)

Figure 7.5: AGS using IDA: (a) the illustration of redox cycling amplification, oxygen reduction takes place at WE1 (yellow) to superoxide, which diffuses to WE2 (orange) and reoxidized back to oxygen; (b) current density *vs*. concentration for the oxygen reduction from 1400 to 4800 ppm fitted with linear trend line, E_{WE1} = −1.2 V *vs*. Au and WE2 = disconnected (blue) and E_{WE2} = −0.1 V vs Au (red). Reprinted with permission from [41]. Copyright 2017 American Chemical Society

7.7 Material for working electrode

It has been known that the material of working electrode also contributes to a specific EC reaction because each material has certain physico-chemical property. Besides platinum (Pt) electrode, the electrodes materials

commonly used in AGS such as, gold (Au), glassy carbon (GC), silver (Ag), palladium (Pd) are essential to be explored with PANI/Au_2.

7.8 Closing remarks

In this research, RTILs can be used as electrolyte in miniaturized AGS system. The atomic metals decorating the modified working electrode were also active in RTILs. Therefore, atomic metal catalyst with RTIL films are the new frontier in miniaturized AGS system. There are still many rooms for improvement for current sensor. Several ways have been explained to improve the performance. If we achieve all things above, the sensor with a high sensitivity, selectivity, and a fast response time can be realized.

References

1. Gas Sensor Market Size, Share & Trends Analysis Report By Product (Oxygen /Lambda Sensors, Carbon Dioxide Sensors), By Type (Wired, Wireless), By Technology, By End-Use, By Region, And Segment Forecasts, 2023 - 2030 Available online: https://www.grandviewresearch.com/industry-analysis/gas-sensors-market.
2. Gas Sensors Market Available online: https://www.precedenceresearch.com/gas-sensor-market.
3. Gas Sensor Market Available online: https://www.gminsights.com/industry-analysis/gas-sensors-market-size.
4. Gas Sensors Market Available online: https://www.marketsandmarkets.com/Market-Reports/gas-sensor-market-245141093.html.
5. MEMS Sensors TDK Available online: https://www.tdk.com/en/news_center/press/20210108_01.html.
6. Stetter, J.R.; Li, J. Amperometric Gas Sensors - A Review. *Chem. Rev.* **2008**, *108*, 352–366, doi:10.1021/cr0681039.
7. Maleki, R.; Shams, S.M.; Chellehbari, Y.M.; Rezvantalab, S.; Jahromi, A.M.; Asadnia, M.; Abbassi, R.; Aminabhavi, T.; Razmjou, A. Materials Discovery of Ion-Selective Membranes Using Artificial Intelligence. *Commun. Chem.* **2022**, *5*, 1–13, doi:10.1038/s42004-022-00744-x.
8. Sisodia, N.; McGuinness, K.L.; Wadhawan, J.D.; Lawrence, N.S. In Situ Recalibration of Ion Selective Electrodes . *Sensors & Diagnostics* **2022**, *1*, 134–138, doi:10.1039/d1sd00003a.
9. Casans, S.; Muñoz, D.R.; Navarro, A.E.; Salazar, A. ISFET Drawbacks Minimization Using a Novel Electronic Compensation. *Sensors Actuators, B Chem.* **2004**, *99*, 42–49, doi:10.1016/j.snb.2003.09.015.
10. Janata, J. *Conductometric Sensors*;
11. Korotcenkov, G.; Brinzari, V.; Cho, B.K. Conductometric Gas Sensors Based on Metal Oxides Modified with Gold Nanoparticles: A Review. *Microchim. Acta* **2016**, *183*, 1033–1054, doi:10.1007/s00604-015-1741-z.
12. Vázquez-López, A.; Bartolomé, J.; Cremades, A.; Maestre, D. High-Performance Room-Temperature Conductometric Gas Sensors: Materials and Strategies. *Chemosensors* **2022**, *10*, doi:10.3390/chemosensors10060227.
13. Anan'eva, E.P.; Bogdanova, O.Y.; Gurina, S. V.; Sibirtsev, V.S. Using a Conductometric Method in Microbiological Control of Natural Excipients. *Pharm. Chem. J.* **2022**, *56*, 872–876, doi:10.1007/s11094-022-02721-z.
14. Jaffrezic-Renault, N.; Dzyadevych, S. V. Conductometric Microbiosensors for Environmental Monitoring. *Sensors* **2008**, *8*, 2569–2588, doi:10.3390/s8042569.
15. Songkhla, S.N.; Nakamoto, T. Overview of Quartz Crystal Microbalance Behavior Analysis and Measurement. *Chemosensors* **2021**, *9*, 1–31, doi:10.3390/chemosensors9120350.
16. Chagnard, C.; Gilbert, P.; Watkins, A.N.; Beeler, T.; Paul, D.W. An Electronic Oscillator with Automatic Gain Control: EQCM Applications. *Sensors Actuators, B Chem.* **1996**, *32*, 129–136, doi:10.1016/0925-4005(96)80121-3.
17. Aleixandre, M.; Nakamoto, T. Study of Room Temperature Ionic Liquids as Gas Sensing Materials in Quartz Crystal Microbalances. *Sensors (Switzerland)* **2020**, *20*, 1–14, doi:10.3390/s20144026.
18. Janata, J.; Nakamoto, T. Vision of New Olfactory Sensing Array. *IEEJ Trans. Electr. Electron. Eng.* **2016**, *11*, 261–267, doi:10.1002/tee.22214.
19. Yoo, E.H.; Lee, S.Y. Glucose Biosensors: An Overview of Use in Clinical Practice. *Sensors* **2010**, *10*, 4558–4576, doi:10.3390/s100504558.
20. Cho, I.H.; Kim, D.H.; Park, S. Electrochemical Biosensors: Perspective on Functional Nanomaterials for on-Site Analysis. *Biomater. Res.* **2020**, *24*, 1–12, doi:10.1186/s40824-019-0181-y.
21. Bhalla, N.; Jolly, P.; Formisano, N.; Estrela, P. Introduction to Biosensors. *Essays Biochem.* **2016**, *60*, 1–8, doi:10.1042/EBC20150001.
22. Odorant-binding protein. Available online: https://en.wikipedia.org/wiki/Odorant-binding_protein.
23. Ma, W.; Wang, Z.; Jiang, D.; Wei, J.; Yan, J.; Chen, R.; Qin, G.; Yan, S. An Odorant Receptor-Derived Peptide Biosensor for Monitoring the Migratory Locust Locusta Migratoria by Recognizing the Aggregation Pheromone 4-Vinylanisole. *Sensors Actuators B Chem.* **2023**, *375*, 132881, doi:10.1016/j.snb.2022.132881.
24. Amiri, V.; Roshan, H.; Mirzaei, A.; Neri, G.; Ayesh, A.I. Nanostructured Metal Oxide-Based Acetone Gas Sensors: A Review. *Sensors (Switzerland)* **2020**, *20*, 1–25, doi:10.3390/s20113096.
25. Liu, L.; Wang, Y.; Liu, Y.; Wang, S.; Li, T.; Feng, S.; Qin, S.; Zhang, T. Heteronanostructural Metal Oxide-Based Gas Microsensors. *Microsystems Nanoeng.* **2022**, *8*, 1–22, doi:10.1038/s41378-022-00410-1.
26. Nikolic, M.V.; Milovanovic, V.; Vasiljevic, Z.Z.; Stamenkovic, Z. Semiconductor Gas Sensors: Materials, Technology, Design, and Application. *Sensors (Switzerland)* **2020**, *20*, 1–31, doi:10.3390/s20226694.
27. Sharma, B.; Sharma, A.; Joshi, M.; Myung, J.H. Sputtered SnO2/ZnO Heterostructures for Improved NO2 Gas Sensing Properties. *Chemosensors* **2020**, *8*, 1–8, doi:10.3390/CHEMOSENSORS8030067.
28. Voc, M.; Voc, M.; Limit, P.E.; Vocs, F. Using Photoionization Detectors to Measure Toxic VOCs. **1888**, *0573*.
29. Zimmer, C.M.; Kallis, K.T.; Giebel, F.J. Micro-Structured Electron Accelerator for the Mobile Gas Ionization Sensor Technology. *J. Sensors Sens. Syst.* **2015**, *4*, 151–157, doi:10.5194/jsss-4-151-2015.
30. Wei-Hao Li, M.; Ghosh, A.; Venkatasubramanian, A.; Sharma, R.; Huang, X.; Fan, X. High-Sensitivity Micro-Gas Chromatograph-Photoionization Detector for Trace Vapor Detection. *ACS Sensors* **2021**, *6*, 2348–2355, doi:10.1021/acssensors.1c00482.
31. Tan, X.; Zhang, H.; Li, J.; Wan, H.; Guo, Q.; Zhu, H.; Liu, H.; Yi, F. Non-Dispersive Infrared Multi-Gas Sensing via Nanoantenna Integrated Narrowband Detectors. *Nat. Commun.* **2020**, *11*, 1–9, doi:10.1038/s41467-020-19085-1.
32. Jia, X.; Roels, J.; Baets, R.; Roelkens, G. On-Chip Non-Dispersive Infrared CO2 Sensor Based on an Integrating Cylinder†. *Sensors (Switzerland)* **2019**, *19*, 1–14, doi:10.3390/s19194260.

33. Jacquinot, P. The Luminosity of Spectrometers with Prisms, Gratings, or Fabry-Perot Etalons. *J. Opt. Soc. Am.* **1954**, *44*, 761–765.
34. NDIR Gas Sensor from FIGARO. Available online: https://www.figarosensor.com/technicalinfo/principle/ndir-type.html.
35. Infrared Sensor Application. Link: https://www.sgxsensortech.com/content/uploads/2014/08/AN1-%E2%80%93-A-Background-to-Gas-Sensing-by-Non-Dispersive-Infrared-NDIR.pdf.
36. Figaro 5042 Available online: https://www.figarosensor.com/product/docs/tgs5042_product infomation%28fusa%29_rev07.pdf.
37. TGS 5042-5342 Available online: https://www.figaro.co.jp/en/product/feature/tgs5042_tgs5342-2.html.
38. Alphasense Available online: https://cdn.shopify.com/s/files/1/0406/7681/files/DataSheet-AlphaSense-O2-A3-Oxygen-Sensor.pdf?v=1621008788.
39. Alphasense O2 Available online: https://www.alphasense.com/leak-free-o2/.
40. Xiong, L.; Compton, R.G. Amperometric Gas Detection: A Review. *Int. J. Electrochem. Sci.* **2014**, *9*, 7152–7181.
41. Gondosiswanto, R.; Hibbert, D.B.; Fang, Y.; Zhao, C. Redox Recycling Amplification Using an Interdigitated Microelectrode Array for Ionic Liquid-Based Oxygen Sensors. *Anal. Chem.* **2018**, *90*, 3950–3957, doi:10.1021/acs.analchem.7b04945.
42. McFarlane, D.R.; Sun, J.; Golding, J.; Meakin, P.; Forsyth, M. High Conductivity Molten Salts Based on the Imide Ion. *Electrochim. Acta* **2000**, *45*, 1271–1278, doi:10.1016/S0013-4686(99)00331-X.
43. Diederichsen, K.M.; Buss, H.G.; McCloskey, B.D. The Compensation Effect in the Vogel-Tammann-Fulcher (VTF) Equation for Polymer-Based Electrolytes. *Macromolecules* **2017**, *50*, 3831–3840, doi:10.1021/acs.macromol.7b00423.
44. Musiał, M.; Bair, S.; Cheng, S.; Wojnarowska, Z.; Paluch, M. Fractional Walden Rule for Aprotic Ionic Liquids: Experimental Verification over a Wide Range of Temperatures and Pressures. *J. Mol. Liq.* **2021**, *331*, doi:10.1016/j.molliq.2021.115772.
45. Melián-Cabrera, I. Catalytic Materials: Concepts To Understand the Pathway to Implementation. *Ind. Eng. Chem. Res.* **2021**, *60*, 18545–18559, doi:10.1021/acs.iecr.1c02681.
46. Kuretake, T.; Kawahara, S.; Motooka, M.; Uno, S. An Electrochemical Gas Biosensor Based on Enzymes Immobilized on Chromatography Paper for Ethanol Vapor Detection. *Sensors (Switzerland)* **2017**, *17*, 281, doi:10.3390/s17020281.
47. Sun, Y.F.; Liu, S.B.; Meng, F.L.; Liu, J.Y.; Jin, Z.; Kong, L.T.; Liu, J.H. Metal Oxide Nanostructures and Their Gas Sensing Properties: A Review. *Sensors* **2012**, *12*, 2610–2631, doi:10.3390/s120302610.
48. Li, H.; Meng, F.; Sun, Y.; Liu, J.; Wan, Y.; Sun, B.; Liu, J. Mesoporous SnO2 Sensor Prepared by Carbon Nanotubes as Template and Its Sensing Properties to Indoor Air Pollutants. *Procedia Eng.* **2010**, *7*, 172–178, doi:10.1016/j.proeng.2010.11.026.
49. Tonezzer, M. Single Nanowire Gas Sensor Able to Distinguish Fish and Meat and Evaluate Their Degree of Freshness. *Chemosensors* **2021**, *9*, 1–12, doi:10.3390/chemosensors9090249.
50. Jia, Y.; He, L.; Guo, Z.; Chen, X.; Meng, F.; Luo, T.; Li, M.; Liu, J. Preparation of Porous Tin Oxide Nanotubes Using Carbon Nanotubes as Templates and.Pdf. **2010**, 9581–9587.
51. Xiang, Q.; Li, F.; Wang, J.; Chen, W.; Miao, Q.; Zhang, Q.; Tao, P.; Song, C.; Shang, W.; Zhu, H.; et al. Heterostructure of ZnO Nanosheets/Zn with a Highly Enhanced Edge Surface for Efficient CO2 Electrochemical Reduction to CO. *ACS Appl. Mater. Interfaces* **2021**, *13*, 10837–10844, doi:10.1021/acsami.0c20302.
52. Zhu, L.Y.; Ou, L.X.; Mao, L.W.; Wu, X.Y.; Liu, Y.P.; Lu, H.L. *Advances in Noble Metal-Decorated Metal Oxide Nanomaterials for Chemiresistive Gas Sensors: Overview*; Springer Nature Singapore, 2023; Vol. 15; ISBN 0123456789.
53. Tsukuda, T. Toward an Atomic-Level Understanding of Size-Specific Properties of Protected and Stabilized Gold Clusters. *Bull. Chem. Soc. Jpn.* **2012**, *85*, 151–168, doi:10.1246/bcsj.20110227.
54. Liu, L.; Corma, A. Metal Catalysts for Heterogeneous Catalysis: From Single Atoms to Nanoclusters and Nanoparticles. *Chem. Rev.* **2018**, *118*, 4981–5079, doi:10.1021/acs.chemrev.7b00776.
55. Bayatsarmadi, B.; Zheng, Y.; Vasileff, A.; Qiao, S.Z. Recent Advances in Atomic Metal Doping of Carbon-Based Nanomaterials for Energy Conversion. *Small* **2017**, *13*, 1–19, doi:10.1002/smll.201700191.
56. Schwartz, I.; Jonke, A.P.; Josowicz, M.; Janata, J. Polyaniline-Supported Atomic Gold Electrodes: Comparison with Macro Electrodes. *Catal. Letters* **2012**, *142*, 1344–1351, doi:10.1007/s10562-012-0895-0.
57. Chakraborty, P.; Engineering, C. Amperometric Gas Sensor with Atomic Gold Decorated Polyaniline-Platinum Composite. **2020**.
58. Chakraborty, P.; Chien, Y.A.; Chiu, W.T.; Chang, T.F.M.; Sone, M.; Nakamoto, T.; Josowicz, M.; Janata, J. Design and Development of Amperometric Gas Sensor with Atomic Au-Polyaniline/Pt Composite. *IEEE Sens. J.* **2020**, *20*, 12479–12487, doi:10.1109/JSEN.2020.3002822.
59. Chakraborty, P.; Kawakami, H.; Faricha, A.; Chang, T.F.M.; Sone, M.; Nakamoto, T. Polyaniline-Atomic Au Modified Platinum Electrode with Ionic Liquid as Configuration for Enhanced Electrochemical Sensing. In Proceedings of the Proceedings of IEEE Sensors; Institute of Electrical and Electronics Engineers Inc., 2021; Vol. 2021-October.
60. Chakraborty, P.; Faricha, A.; Okamoto, K.; Kawakami, H.; Chang, T.-F.M.; Sone, M.; Nakamoto, T. Towards Planar Atomic-Gold Decorated Polyaniline Gas Sensors for Enhanced Electrochemical Sensing. *IEEE Sens. J.* **2023**, 1–1, doi:10.1109/JSEN.2023.3242318.
61. Guo, Z.; Li, M.; Liu, J. Highly Porous CdO Nanowires: Preparation Based on Hydroxy- and Carbonate-Containing Cadmium Compound Precursor Nanowires, Gas Sensing and Optical Properties. *Nanotechnology* **2008**, *19*, doi:10.1088/0957-4484/19/24/245611.
62. Russmayer, H.; Marx, H.; Sauer, M. Microbial 2-Butanol Production with Lactobacillus Diolivorans. *Biotechnol.*

Biofuels **2019**, *12*, 1–11, doi:10.1186/s13068-019-1594-5.
63. Timung, S.; Singh, H.; Annu, A. Bio-Butanol as Biofuels: The Present and Future Scope. *Liq. Biofuels Fundam. Charact. Appl.* **2021**, 467–485, doi:10.1002/9781119793038.ch13.
64. The properties of butanol isomers. link: https://apps.who.int/iris/bitstream/handle/10665/37266/9241542659-eng.pdf.
65. 1-Butanol Available online: https://en.wikipedia.org/wiki/1-Butanol.
66. Iso Butanol Available online: https://en.wikipedia.org/wiki/Isobutanol.
67. 2-Butanol Available online: https://en.wikipedia.org/wiki/2-Butanol.
68. Plechkova, N. V.; Seddon, K.R. Applications of Ionic Liquids in the Chemical Industry. *Chem. Soc. Rev.* **2008**, *37*, 123–150, doi:10.1039/b006677j.
69. Saheb, A.H. Sensing Materials Based on Ionic Liquids. Ph.D. Thesis, Georgia Institute of Technology, Atlanta, GA, USA, 30 June 2008.
70. Paul, A.; Muthukumar, S.; Prasad, S. Review—Room-Temperature Ionic Liquids for Electrochemical Application with Special Focus on Gas Sensors. *J. Electrochem. Soc.* **2020**, *167*, 037511, doi:10.1149/2.0112003jes.
71. Hayes, R.; Warr, G.G.; Atkin, R. Structure and Nanostructure in Ionic Liquids. *Chem. Rev.* **2015**, *115*, 6357–6426, doi:10.1021/cr500411q.
72. Hossain, M.M.; Rawal, A.; Aldous, L. Aprotic vs Protic Ionic Liquids for Lignocellulosic Biomass Pretreatment: Anion Effects, Enzymatic Hydrolysis, Solid-State NMR, Distillation, and Recycle. *ACS Sustain. Chem. Eng.* **2019**, *7*, 11928–11936, doi:10.1021/acssuschemeng.8b05987.
73. Manna, S.S.; Bhauriyal, P.; Pathak, B. Identifying Suitable Ionic Liquid Electrolytes for Al Dual-Ion Batteries: Role of Electrochemical Window, Conductivity and Voltage. *Mater. Adv.* **2020**, *1*, 1354–1363, doi:10.1039/d0ma00292e.
74. Zhang, Y.; Shi, C.; Brennecke, J.F.; Maginn, E.J. Refined Method for Predicting Electrochemical Windows of Ionic Liquids and Experimental Validation Studies. *J. Phys. Chem. B* **2014**, *118*, 6250–6255, doi:10.1021/jp5034257.
75. Zhao, C.; Burrell, G.; Torriero, A.A.J.; Separovic, F.; Dunlop, N.F.; Macfarlane, D.R.; Bond, A.M. 3-J. Phys. Chem. B 2008, 112, 6923–6936.Pdf. **2008**, 6923–6936.
76. O'Mahony, A.M.; Silvester, D.S.; Aldous, L.; Hardacre, C.; Compton, R.G. Effect of Water on the Electrochemical Window and Potential Limits of Room-Temperature Ionic Liquids. *J. Chem. Eng. Data* **2008**, *53*, 2884–2891, doi:10.1021/je800678e.
77. Chavan, S.N.; Mandal, D. Combined Effect of Ether and Siloxane Substituents on Imidazolium Ionic Liquids. *RSC Adv.* **2015**, *5*, 64821–64831, doi:10.1039/c5ra07466e.
78. Baek, B.; Lee, S.; Jung, C. Pyrrolidinium Cation-Based Ionic Liquids with Different Functional Groups: Butyl, Butyronitrile, Pentenyl, and Methyl Butyrate. *Int. J. Electrochem. Sci.* **2011**, *6*, 6220–6234.
79. Okoturo, O.O.; VanderNoot, T.J. Temperature Dependence of Viscosity for Room Temperature Ionic Liquids. *J. Electroanal. Chem.* **2004**, *568*, 167–181, doi:10.1016/j.jelechem.2003.12.050.
80. Schreiner, C.; Zugmann, S.; Hartl, R.; Gores, H.J. Fractional Walden Rule for Ionic Liquids: Examples from Recent Measurements and a Critique of the so-Called Ideal KCl Line for the Walden Plot. *J. Chem. Eng. Data* **2010**, *55*, 1784–1788, doi:10.1021/je900878j.
81. McEwen, A.B.; Ngo, H.L.; LeCompte, K.; Goldman, J.L. Electrochemical Properties of Imidazolium Salt Electrolytes for Electrochemical Capacitor Applications. *J. Electrochem. Soc.* **1999**, *146*, 1687–1695, doi:10.1149/1.1391827.
82. Silvester, D.S.; Broder, T.L.; Aldous, L.; Hardacre, C.; Crossley, A.; Compton, R.G. Using XPS to Determine Solute Solubility in Room Temperature Ionic Liquids. *Analyst* **2007**, *132*, 196–198, doi:10.1039/b700212b.
83. Keller, D.; Henninen, T.R.; Erni, R. Atomic Mechanisms of Gold Nanoparticle Growth in Ionic Liquids Studied by: In Situ Scanning Transmission Electron Microscopy. *Nanoscale* **2020**, *12*, 22511–22517, doi:10.1039/d0nr06541b.
84. Zare, E.N.; Makvandi, P.; Ashtari, B.; Rossi, F.; Motahari, A.; Perale, G. Progress in Conductive Polyaniline-Based Nanocomposites for Biomedical Applications: A Review. *J. Med. Chem.* **2020**, *63*, 1–22, doi:10.1021/acs.jmedchem.9b00803.
85. Chani, M.T.S.; Karimov, K.S.; Khalid, F.A.; Moiz, S.A. Polyaniline Based Impedance Humidity Sensors. *Solid State Sci.* **2013**, *18*, 78–82, doi:10.1016/j.solidstatesciences.2013.01.005.
86. Song, E.; Choi, J.W. Conducting Polyaniline Nanowire and Its Applications in Chemiresistive Sensing. *Nanomaterials* **2013**, *3*, 498–523, doi:10.3390/nano3030498.
87. Jonke, A.P.; Josowicz, M.; Janata, J. Polyaniline Doped with Atomic Gold. *J. Electrochem. Soc.* **2011**, *158*, E147, doi:10.1149/2.052112jes.
88. Fernández, E.M.; Soler, J.M.; Garzón, I.L.; Balbás, L.C. Trends in the Structure and Bonding of Noble Metal Clusters. *Phys. Rev. B - Condens. Matter Mater. Phys.* **2004**, *70*, 1–14, doi:10.1103/PhysRevB.70.165403.
89. Jonke, A.P.; Josowicz, M.; Janata, J. Odd-Even Pattern Observed in Polyaniline/(Au 0 – Au 8) Composites . *J. Electrochem. Soc.* **2012**, *159*, P40–P43, doi:10.1149/2.053203jes.
90. Häkkinen, H.; Landman, U. Gold Clusters and Their Anions. *Phys. Rev. B - Condens. Matter Mater. Phys.* **2000**, *62*, R2287–R2290, doi:10.1103/PhysRevB.62.R2287.
91. Chakraborty, P.; Chien, Y.A.; Chang, T.F.M.; Sone, M.; Nakamoto, T. Indirect Sensing of Lower Aliphatic Ester Using Atomic Gold Decorated Polyaniline Electrode. *Sensors (Switzerland)* **2020**, *20*, 1–10, doi:10.3390/s20133640.
92. IDA from BAS Available online: https://www.als-japan.com/1379.html#defaultTab12.
93. Faricha, A.; Yoshida, S.; Chakraborty, P.; Okamoto, K.; Chang, T.F.M.; Sone, M.; Nakamoto, T. Array of Miniaturized Amperometric Gas Sensors Using Atomic Gold Decorated Pt/PANI Electrodes in Room Temperature Ionic Liquid Films. *Sensors* **2023**, *23*, doi:10.3390/s23084132.
94. Reference Electrode E0 Available online: https://chem.libretexts.org/Bookshelves/Analytical_Chemistry/Supplemental_Modules_(Analytical_Chemistry)/Analytical_Sciences_Digital_Library/Courseware/Analytical_Electrochemistry%3A_Potentiometry/03_Potentiometric_Theory/04_Reference_Electrodes.

95. RE Ag/AgCl Available online: https://www.als-japan.com/1388.html#defaultTab13.
96. TL074 Available online: https://www.ti.com/lit/ds/symlink/tl074-ep.pdf?ts=1689741671962&ref_url=https%253A%252F%252Fwww.google.com%252F.
97. Aleixandre, M.; Nakazawa, K.; Nakamoto, T. Optimization of Modulation Methods for Solenoid Valves to Realize an Odor Generation System. *Sensors (Switzerland)* **2019**, *19*, doi:10.3390/s19184009.
98. Faricha, A.; Chakraborty, P.; Okamoto, K.; Chang, T.F.M.; Sone, M.; Nakamoto, T. Microgravimetric and Amperometric Sensor Coated with Room Temperature Ionic Liquid to Enhance Butanol Isomers Gas Separation. *IEEE Sens. J.* **2022**, *22*, 24471–24478, doi:10.1109/JSEN.2022.3221114.
99. Devices, A.; Information, C.; Devices, A. SensorPal GUI With AD5940 Evaluation Kit Eval-ADICUP3029 ► Jumpers Set as Shown – Default . **2018**, 1–13.
100. Way, O.T. EVAL-AD5940 Evaluation Kit User Guide EVAL-AD5940 Evaluation Kit User Guide. 1–27.
101. Lambe, M. Datasheet: Optimizing the AD5940 for Electrochemical Measurements, AN-1563 Application Note. *Inc., Analog Devices* **2019**, 1–16.
102. Devices, A. High Precision , Impedance , and Electrochemical Front End. *AD5940 Datasheet* **2019**.
103. Nakamoto, T.; Sasaki, S.; Fukuda, A.; Moriizumi, T. Selection Method of Sensing Membranes in Odor-Sensing System. *Sensors Mater.* **1992**, *4*, 111–119.
104. Dillon, W. R.; Goldstein, M. *Multivariate Analysis: Methods and Applications*; Wiley: New York (N.Y.), 1984;
105. Pitawela, N.R.; Shaw, S.K. Imidazolium Triflate Ionic Liquids' Capacitance-Potential Relationships and Transport Properties Affected by Cation Chain Lengths. *ACS Meas. Sci. Au* **2021**, *1*, 117–130, doi:10.1021/acsmeasuresciau.1c00015.
106. EMIM Ac Available online: https://www.sigmaaldrich.com/JP/ja/product/aldrich/689483.
107. BMIM Br Available online: https://www.sigmaaldrich.com/JP/ja/product/sial/95137%0A.
108. HMIM Cl Available online: https://www.sigmaaldrich.com/JP/ja/product/sial/87929.
109. Harris, K.R.; Kanakubo, M. Self-Diffusion Coefficients and Related Transport Properties for a Number of Fragile Ionic Liquids. *J. Chem. Eng. Data* **2016**, *61*, 2399–2411, doi:10.1021/acs.jced.6b00021.
110. Queirós, C.S.G.P.; Paredes, X.; Avelino, T.F.S.; Bastos, D.E.N.; Ferreira, M.; Santos, F.J.V.; Santos, A.F.; Lopes, M.L.M.; Lourenço, M.J.V.; Pereira, H.; et al. The Influence of Water on the Thermophysical Properties of 1-Ethyl-3-Methylimidazolium Acetate. *J. Mol. Liq.* **2020**, *297*, doi:10.1016/j.molliq.2019.111925.
111. Ghazvini, M.S.; Pulletikurthi, G.; Lahiri, A.; Endres, F. Electrochemical and Spectroscopic Studies of Zinc Acetate in 1-Ethyl-3-Methylimidazolium Acetate for Zinc Electrodeposition. *ChemElectroChem* **2016**, *3*, 598–604, doi:10.1002/celc.201500444.
112. 34. 5 EMIM Ac_EC Window.
113. Tshibangu, P.N.; Ndwandwe, S.N.; Dikio, E.D. Density, Viscosity and Conductivity Study of 1-Butyl-3-Methylimidazolium Bromide. *Int. J. Electrochem. Sci.* **2011**, *6*, 2201–2213.
114. Kim, K.; Shin, B.; Lee, H. Physical and Electrochemical Properties of 1-Butyl-3-Methylimidazolium Bromide „. *Korean J. Chem. Eng.* **2004**, *21*, 1010–1014.
115. Properties of HMIM Cl. link: https://iolitec.de/sites/iolitec.de/files/2017-05/TDS%20IL-0054%20HMIM%20Cl.pdf
116. Luca, O.R.; Gustafson, J.L.; Maddox, S.M.; Fenwick, A.Q.; Smith, D.C. Catalysis by Electrons and Holes: Formal Potential Scales and Preparative Organic Electrochemistry. *Org. Chem. Front.* **2015**, *2*, 823–848, doi:10.1039/c5qo00075k.
117. *Catalog of ionic liquids from Kanto Reagents in Nakamoto Laboratory*.
118. Saheb, A.; Janata, J.; Josowicz, M. Reference Electrode for Ionic Liquids. *Electroanalysis* **2006**, *18*, 405–409, doi:10.1002/elan.200503435.
119. Saheb, A.; Smith, J.A.; Josowicz, M.; Janata, J.; Baer, D.R.; Engelhard, M.H. Controlling Size of Gold Clusters in Polyaniline from Top-down and from Bottom-Up. *J. Electroanal. Chem.* **2008**, *621*, 238–244, doi:10.1016/j.jelechem.2007.11.025.
120. Chakraborty, P.; Engineering, C. *Amperometric Gas Sensor with Atomic Gold Decorated Polyaniline-Platinum Composite*; 2020;
121. Schwartz, I.T.; Jonke, A.P.; Josowicz, M.; Janata, J. Effect of Structured Atomic Gold on Electrooxidation of Alcohols in Alkaline Medium. *Catal. Letters* **2013**, *143*, 777–782, doi:10.1007/s10562-013-1032-4.
122. Chakraborty, P.; Chien, Y.A.; Chiu, W.T.; Chang, T.F.M.; Sone, M.; Nakamoto, T.; Josowicz, M.; Janata, J. Design and Development of Amperometric Gas Sensor with Atomic Au-Polyaniline/Pt Composite. In Proceedings of the IEEE Sensors Journal; Institute of Electrical and Electronics Engineers Inc., November 1 2020; Vol. 20, pp. 12479–12487.
123. Chakraborty, P.; Chien, Y.A.; Chang, T.F.M.; Sone, M.; Nakamoto, T. Indirect Sensing of Lower Aliphatic Ester Using Atomic Gold Decorated Polyaniline Electrode. *Sensors (Switzerland)* **2020**, *20*, 1–10, doi:10.3390/s20133640.
124. EMIM OTF Available online: https://www.sigmaaldrich.com/JP/ja/product/sial/04367.
125. EMIM Cl Available online: https://www.sigmaaldrich.com/JP/ja/product/aldrich/272841.
126. Freire, M.G.; Teles, A.R.R.; Rocha, M.A.A.; Schröder, B.; Neves, C.M.S.S.; Carvalho, P.J.; Evtuguin, D. V.; Santos, L.M.N.B.F.; Coutinho, J.A.P. Thermophysical Characterization of Ionic Liquids Able to Dissolve Biomass. *J. Chem. Eng. Data* **2011**, *56*, 4813–4822, doi:10.1021/je200790q.
127. Information of EC Window from 1-Ethyl-3-Methylimidazolium Acetate and Density of 1-Ethyl-3-Methylimidazolium Chloride. Available online: http://www.ilra.jp/docs/BASF_IL_Brochure.pdf (accessed on 1 October 2021).
128. Chen, Y.; Cai, Y.; Thomsen, K.; Kontogeorgis, G.M.; Woodley, J.M. A Group Contribution-Based Prediction Method for the Electrical Conductivity of Ionic Liquids. *Fluid Phase Equilib.* **2020**, *509*, doi:10.1016/j.fluid.2020.112462.
129. EMIM OTF Available online: https://en.solvionic.com/products/1-ethyl-3-methylimidazolium-trifluoromethanesulfonate-99.

130. Chen, T.; Chidambaram, M.; Liu, Z.; Smit, B.; Bell, A.T. Viscosities of the Mixtures of 1-Ethyl-3-Methylimidazolium Chloride with Water, Acetonitrile and Glucose: A Molecular Dynamics Simulation and Experimental Study. *J. Phys. Chem. B* **2010**, *114*, 5790–5794, doi:10.1021/jp911372j.
131. Gunawan, C.A.; Ge, M.; Zhao, C. Robust and Versatile Ionic Liquid Microarrays Achieved by Microcontact Printing. *Nat. Commun.* **2014**, *5*, doi:10.1038/ncomms4744.
132. Jonke, A.P.; Josowicz, M.; Janata, J. Polyaniline Electrodes Containing Tri-Atomic Au/Pd Clusters: Effect of Ordering. *Catal. Letters* **2013**, *143*, 1261–1265, doi:10.1007/s10562-013-1116-1.

List of publications

Journal articles

1. **A. Faricha**, P. Chakraborty, K. Okamoto, T.-F. M. Chang, M. Sone and T. Nakamoto, "*Microgravimetric and Amperometric Sensor Coated with Room Temperature Ionic Liquid to Enhance Butanol Isomers Gas Separation*," in ***IEEE Sensors Journal***, vol. 22, no. 24, pp. 24471-24478, 15 Dec., **2022**, doi: 10.1109/JSEN.2022.3221114 .

2. P. Chakraborty, **A. Faricha**, K. Okamoto, H. Kawakami, T.-F. M. Chang, M. Sone and T. Nakamoto, "*Toward Planar Atomic-Gold Decorated Polyaniline Gas Sensors for Enhanced Electrochemical Sensing*," in ***IEEE Sensors Journal***, vol. 23, no. 7, pp. 6481-6488, 1 April, **2023**, doi: 10.1109/JSEN.2023.3242318.

3. **A. Faricha**, S. Yoshida, P. Chakraborty, K. Okamoto, T.-F. M. Chang, M. Sone and T. Nakamoto, "*Array of Miniaturized Amperometric Gas Sensors Using Atomic Gold Decorated Pt/PANI Electrodes in Room Temperature Ionic Liquid Films*," in ***Sensors***, 23(8), 4132, 20 April, **2023**, https://doi.org/10.3390/s23084132.

4. **A. Faricha**, Parthojit Chakraborty, Tso-Fu Mark Chang, Masato Sone, Takamichi Nakamoto, "*Overview to Realize Amperometric Gas Sensor with Atomic Gold Decorated Platinum/Polyaniline Composites*," invited review paper at ***Chemosensors*** (on writing process).

International conferences

1. **Anifatul Faricha**, Parthojit Chakraborty, Tso-Fu Mark Chang, Masato Sone, Takamichi Nakamoto, *Gas Sensor Array System Using Microgravimetric and Amperometric Sensors Coated with Room Temperature Ionic Liquid to Enhance Isomers Separation*, in Conf. Advances in Functional Materials (AFM), January **2023**, Kyushu, Japan.

2. P. Chakraborty, H. Kawakami, **A. Faricha**, T. -F. M. Chang, M. Sone and T. Nakamoto, *Polyaniline-atomic Au modified platinum electrode with ionic liquid as configuration for enhanced electrochemical sensing*, 2021 IEEE Sensors, Sydney, Australia, **2021**, pp. 1-4, doi: 10.1109/SENSORS47087.2021.9639545.

Domestic conferences:

1. **Anifatul Faricha,** Shohei Yoshida, Parthojit Chakraborty, Keisuke Okamoto, Tso-Fu Mark Chang, Masato Sone, Takamichi Nakamoto. Modified Planar Electrodes with Polyaniline and Atomic Gold to Enhance Butanol Isomers Gas Sensing, 令和 5 年電気学会全国大会, Mar. **2023**.

2. **Faricha Anifatul**, Chakraborty Parthojit, Tso-Fu Mark Chang, Masato Sone, Takamichi Nakamoto. Gas Sensing Measurement for Propanol Isomers Using Microgravimetric and Electrochemical Sensor Coated with Room Temperature Ionic Liquid, 電気学会全国大会, Mar. **2022**. (Award: winner of oral presentation)

3. Chakraborty Parthojit, Kawakami Hiroki, **Faricha Anifatul**, Okamoto Keisuke, Chang Tso-Fu Mark, Sone Masato, Nakamoto Takamichi. Characterization of planar electrochemical gas sensor based on atomic gold decorated polyaniline nanocomposite, IEEJ workshop, Mar. **2022**.
4. **Anifatul Faricha**, Parthojit Chakraborty, Tso-Fu Mark Chang, Masato Sone, and Takamichi Nakamoto, *Study of Gas Sensing Measurement Using Room Temperature Ionic Liquid Coated on Interdigitated Array Electrodes and Quartz Crystal Microbalance*, IEEJ Sensor Symposium, **2021**, 9P2-SS2-1.「センサ・マイクロマシンと応用システム」 シンポジウム論文集 電気学会センサ・マイクロマシン部門 [編] 38 6p-, 2021-11.